



University of
Nottingham

PhD Thesis

**Quantum Coherence Control
for Radio-Frequency Dressed
Cold Atom Systems**

Author:
Bethany Foxon

Supervisor:
Dr Thomas Fernholz

Ultracold Atoms Group
School of Physics and Astronomy
University of Nottingham

*A thesis presented for the degree of
Doctor of Philosophy*

January 2021

Abstract

The ability to understand and control the internal state of the atom is essential to cold atom schemes. From quantum memories and fundamental physics experiments to timekeeping and inertial sensing, precise state manipulation is a key element. The use of static and AC-dressing fields can generate complex potential geometries, such as optical lattices, shell traps and toroidal shapes. However, the increased complexity of these topologies presents a number of complications which need to be addressed.

The first question is one of control. The use of radio-frequency dressing to couple between magnetic sublevels in the ground state of an alkali atom can enable multi-photon transitions between arbitrary pairs of energy levels. In this thesis, we study the structure of rubidium 87 with such a dressing, with its many emergent quasi-energy levels. Of particular interest are the couplings between hyperfine levels, which are studied both theoretically and experimentally. We measure the relative population in each of the hyperfine levels utilising the linear birefringence properties of the atom. A common-path, homodyne interferometer is used to convert polarisation change into a measure of population. We can thus determine the internal state of the atom, as well as measuring transition frequencies and coupling strengths, including their dependence on static magnetic field. Pure magnetic substates can be produced and studied using a series of optical and microwave pulses. State labelling can also be performed, as the sign of the polarisation shift differs between states. The introduction of a common mode suppressed state detection scheme provides an improved method of measurement.

Building on this knowledge of the dressed level system, this thesis also presents work towards the generation of robust, trappable pairs of clock states for use in quantum technology. We begin with a pair of trappable states whose potentials have a similar response to static magnetic field. The frequency of the transition between these two states will still exhibit field dependence however, due to differences in the magnitude of the Landé g -factors between hyperfine manifolds. In order to coherently control these states, for use in state dependent guiding or quantum memories, this mismatch in the potentials needs to be cancelled. By use of the AC-Zeeman effect to tune the relevant level energies, increased robustness is demonstrated. The reduction in field dependence can be achieved to higher orders using a number of dressings at different frequencies and powers, with data using dressings to second order presented here. We demonstrate a reduction in field dependence to less than the resolution-limited linewidth over our trappable range.

“I like the cover,” he said. “Don’t Panic. It’s the first helpful or intelligible thing anybody’s said to me all day.”

Douglas Adams

Acknowledgements

I'd like to thank the many people who have helped me throughout my PhD. Firstly my supervisor Thomas Fernholz, for his support and extensive knowledge, which have been invaluable during my time at Nottingham. To Sindhu Jammi, for her friendship and endless patience in the lab. I'd also like to thank Konstantinos Poullos, Igor Lesanovsky and our collaborators at the University of Sussex and the Foundation for Research and Technology-Hellas for their scientific input and work on the joint parts of this project.

For their advice on the thesis and viva, thank you to Vilius Atkocius, Nathan Cooper, Charu Mishra and Jamie Johnson. I'd also like to thank the whole group, for being so supportive and always willing to help, and for making my time at Nottingham such a pleasure. I'm grateful to my parents and whole family for their help and encouragement all these years. My appreciation to Rachel Cook, Annie Caley-Renn and my tabletop group for providing some much needed distraction. Most of all, thank you to Joe Foxon, for helping me stay somewhat sane.

Contents

Contents	i
List of Figures	iii
List of Tables	vi
List of Symbols	vii
1 Introduction	1
1.1 Scientific Background	2
1.1.1 History of Light and Matter	2
1.1.2 Cold Atom Tools	4
1.1.3 Quantum Technology	6
1.1.4 Radio-Frequency Dressed Traps	9
1.2 This Work	10
1.2.1 Thesis Aims	10
1.2.2 Outline and Publications	13
2 Radio-Frequency Dressed Alkali Atoms	17
2.1 Alkali Atoms	17
2.1.1 Atomic Structure	17
2.1.2 Static Magnetic Field Dependence	20
2.2 Radio-Frequency Dressing	22
2.2.1 Spin Precession and Driving	22
2.2.2 Rotating Wave Approximation	24
2.2.3 Dressed State Spectrum	27
3 Preparing the Atoms	31
3.1 The Atom Cloud	31
3.1.1 Magneto-Optical Trapping	31
3.1.2 Imaging for Optimisation	34
3.2 Preparing a Pure Quantum State	37
3.2.1 Bare Microwave Transitions	37
3.2.2 Shelving and State Cleaning	40

3.2.3	Optical Pumping	43
4	Birefringent Detection	45
4.1	Linear Birefringence	45
4.1.1	Effective Hamiltonian	47
4.1.2	Stokes Operator Form	51
4.2	Two Colour Method	53
4.2.1	Two State Detection	53
4.2.2	Signal Analysis	56
4.2.3	Common Mode Suppression	59
5	Experimental Apparatus	67
5.1	Laser System	67
5.1.1	Generating the Beams	67
5.1.2	Optical Bench and Chamber Optics	75
5.2	Other Apparatus	80
5.2.1	Vacuum Equipment and Dispensers	80
5.2.2	Magnetic Field Generation	82
5.2.3	Microwave-Dressing Generator	85
6	Microwave Spectroscopy	87
6.1	Theoretical Formulation	87
6.1.1	Dressed Microwave Transitions	89
6.1.2	Rotating Wave Approximation	91
6.1.3	Bare Microwave Couplings	96
6.2	Microwave Frequency Spectra	97
6.2.1	Signal Normalisation	98
6.2.2	Transition Frequencies	101
6.2.3	Broadening Effects	104
6.2.4	Rabi Cycle Distortion	109
6.3	Coupling and Field Dependence Data	110
6.3.1	Static Field Dependence	110
6.3.2	Coupling Coefficient Measurements	113
6.3.3	Ramsey Interferometry	120
7	Coherence Control	125
7.1	Theoretical Model	125
7.1.1	Coherence and the AC-Zeeman Effect	125
7.1.2	Choice of Dressing Frequency	129
7.1.3	Treatment of Quasi-Energy Levels	133
7.1.4	Treatment of Bare Energy Levels	136
7.2	Coherence Data	139

7.2.1	Measurement Method	139
7.2.2	First Order Dressing	143
7.2.3	Second Order Dressing	153
8	Conclusion and Outlook	161
8.1	Conclusion	161
8.1.1	Microwave Spectroscopy	161
8.1.2	Coherence Control	162
8.2	Outlook	163
8.2.1	Interferometric Sensing	163
8.2.2	Experimental Improvements	165
	Appendix	167
A	Angular Momentum	167
A.1	Magnitudes and Commutation	167
A.2	Matrix Forms	169
A.3	Wigner $3j$ -Symbols	170
A.4	Wigner d -Matrices	172
B	Coupling Coefficients	173
B.1	Individual Coupling Coefficients	173
B.2	Coefficients of Degenerate Groups	180
	Bibliography	183

List of Figures

2.1	Energy Levels in ^{87}Rb	18
2.2	Breit-Rabi Diagram	21
2.3	Laboratory Frame Energy Levels	23
2.4	Rotating Frame Energy Levels	27
3.1	MOT Principles	32
3.2	AOM Frequency Calibration	34
3.3	Absorption Imaging	35
3.4	MOT Characterisation	36
3.5	Bloch Sphere and π -Pulses	38
3.6	MW π -Pulse Calibration	39
3.7	State Preparation Transitions	41
3.8	State Preparation Sequence	42
3.9	Optical Pumping	44
4.1	Birefringent Detection	46
4.2	Detection Scheme and Equipment	54
4.3	Detection Sequence	55
4.4	Modulated Signals	58
4.5	Mach-Zehnder Interferometer	60
4.6	EOM Spectroscopy	61
4.7	Common Mode Suppressed Sequence	63
4.8	Common Mode Suppressed Signals	65
4.9	Signal Demodulation	66
5.1	External Cavity Diode Laser	68
5.2	Laser Frequencies	70
5.3	Lock Signals and Spectroscopy	72
5.4	Optical Bench Laser Set-Up	76
5.5	Main Chamber Optics	77
5.6	Two Laser Detection Set-Up	79
5.7	Vacuum Chamber	80

5.8	Coils and Oscillation Damping	83
5.9	Field Angle Calibrations	84
5.10	Microwave Dressing Generator	86
6.1	Dressed Transition Groups	88
6.2	Resonant Coupling Coefficients	95
6.3	Normalising Atom Number	99
6.4	Signal Decay Due to Free-Fall	100
6.5	Full Spectrum Transition Data	102
6.6	Group 1 Transition Data	103
6.7	Group 3 Transition Data	103
6.8	Peak Width Analysis	105
6.9	Gaussian Versus Lorentzian	106
6.10	Broadening vs Power	107
6.11	Rabi Cycle Peak Distortion	108
6.12	Clock Power Dependence	110
6.13	Clock Static Field Dependence	111
6.14	Group 1 Static Field Dependence	112
6.15	Rabi Cycle Power Dependence	114
6.16	Coupling Coefficient Fits	115
6.17	Coupling Measurements	117
6.18	Clock Coupling Field Dependence	118
6.19	Group 1 Coupling Field Dependence	119
6.20	Trappable Clock Rabi Frequency	119
6.21	Two Pulse Ramsey Data	121
6.22	Ramsey Pulse Sequence	122
6.23	Ramsey Detuning Scan	124
6.24	Cuts through Ramsey Data	124
7.1	AC Zeeman Effect	127
7.2	Three Level System Zeeman Shift	129
7.3	Coupling Strengths for Dressing	132
7.4	Zeeman Shifts on Quasi-Energy Levels	134
7.5	Bare Dressing Theory	138
7.6	Calibrating MW-Dressing Strength	139
7.7	Detection Strength Field Minima	141
7.8	MW-Dressing Frequencies	144
7.9	MW-Dressing Colourmaps	145
7.10	Derivative at Resonance	146
7.11	MW-Dressing Strength Scans	147
7.12	Comparison of Theoretical Models	149

7.13	MW-Dressed Potentials	150
7.14	Trap Depth Predictions	152
7.15	Second MW-Dressing Strength Scans	155
7.16	Second Order Dressing	156
7.17	MW-Dressed Potentials For Multiple Dressings	158
8.1	Sagnac Interferometry	164
8.2	Improving Interaction Time	165
B.1	All σ_- -Polarised Transitions	174
B.2	All σ_- -Coupling Graphs	175
B.3	All π -Polarised Transitions	176
B.4	All π -Coupling Graphs	177
B.5	All σ_+ -Polarised Transitions	178
B.6	All σ_+ -Coupling Graphs	179
B.7	All σ_{\pm} -Polarised Transitions	180
B.8	All σ_{\pm} Combined Coupling Graphs	182

List of Tables

4.1	State Dependent Detection Strengths	58
5.1	Laser Frequencies and Powers	69
5.2	Laser Locking Details	71
5.3	Calibration of Static Field Coils	82
6.1	Relative Resonant Static Field Couplings	95
6.2	MW-Dressing Coupling Coefficients	97
6.3	Measured Clock Couplings	116
7.1	Choice of Dressing Transition	132
B.1	All σ_- -Polarised Coupling Equations	174
B.2	All π -Polarised Coupling Equations	176
B.3	All σ_+ -Polarised Coupling Equations	178
B.4	Relative Resonant Degenerate Couplings	181

List of Symbols

This section provides a comprehensive list of symbols used throughout this thesis (these are also defined when first used in the main text). Symbols unique to a single calculation or which have multiple meanings are not included in this list. Standard mathematical symbols are also assumed. Values of fundamental constants are as given in [38].

\hat{a}	Annihilation Operator
α	Polarisability Coefficient
A	Amplitude
\mathcal{A}	Hyperfine Magnetic Dipole Constant
A	Area
B	Magnetic Field
c	Speed of Light in Vacuum ($2.997925 \times 10^8 \text{ m s}^{-1}$)
d	Wigner d -Matrix
d	Dipole Moment
Δ	Angular Frequency Detuning
\hat{e}	Unit Vector
e	Elementary Charge (1.602×10^{-19})
ϵ_0	Vacuum Permittivity ($8.854 \times 10^{-12} \text{ Fm}^{-1}$)
E	Energy
E	Electric Field
F	Total Angular Momentum
g	Landé g -Factor
h	Plank Constant ($6.62559 \times 10^{-34} \text{ m}^2 \text{ kg s}^{-1}$)
\hbar	Reduced Plank Constant ($h/(2\pi)$)
h.c.	Hermitian Conjugate
H	Hamiltonian
I	Nuclear Angular Momentum
I	Current
\mathcal{I}	Light Intensity
$\mathbb{1}$	Identity Matrix
J	Total Electron Angular Momentum

\mathcal{J}	Components of Electron Angular Momentum
$\tilde{\mathfrak{J}}$	Bessel Function
k	Angular Wavenumber
l	Length
λ	Wavelength
L	Orbital Angular Momentum
m	Magnetic Sublevel
μ	Magnetic Dipole Moment
μ_B	Bohr Magneton ($9.2732 \times 10^{-24} \text{ J T}^{-1}$)
n	Dressed Group Number
n	Nuclear Shell Number
η_σ	Polarisation Normalisation Factor
N	Atom Number
$\hat{\rho}$	Density Operator
ϱ	Density
P	Power
\mathcal{P}	Electron Shell $L = 1$
φ	Phase
ψ	Wave Function
Ψ	Total Wave Function
r	Radial Coordinate
R_c	Rydberg Constant ($1.0973731 \times 10^7 \text{ m}^{-1}$)
$\hat{\mathbf{R}}$	Rotation Matrix
σ	Polarisation
ς	Angular Momentum of Photon
S	Spin Angular Momentum
\mathbf{S}	Stokes Operator
\mathcal{S}	Electron Shell $L = 0$
t	Time
τ	Time Constant
θ_F	Rotation Angle in Manifold
T	Temperature
Θ	Static Magnetic Field Angle
u	Mode Function
U	Rotation Operator
v	Velocity
V	Voltage
w	Width
ω	Angular Frequency
Ω	Rabi Angular Frequency
x, y, z	Cartesian Coordinates

Subscripts

Listed below are the abbreviations used solely in subscripts. Other symbols and abbreviations from this section, as well as full words used in subscripts, are not listed. Also note that superscripts d and p are used to differentiate between MW-dressings and the MW-probe once MW-dressing has been introduced.

co	Cooler Beams
det	Detection Beam (both $F = 1$ and 2)
eff	Effective
$F1$	Detection Beam for $F = 1$
$F2$	Detection Beam for $F = 2$
ic	Imaging and State Cleaning Beams
int	Interaction
mod	Modulation
norm	Normalised
offs	Offset
op	Optical Pump Beam
pot	Potential
quad	Quadrupole Field
res	Resonance
rot	Rotating Frame
rp	Repump Beams
tot	Total

Abbreviations

AC	Alternating Current
AOM	Acousto-Optic Modulator
BPD	Balanced Photodetector
BR	Breit-Rabi
BT	Bias Tee
CCD	Charge-Coupled Device
CMOT	Compressed Magneto-Optical Trap
CS	Coarse Structure
DC	Direct Current, Static Field
ECDL	External-Cavity Diode Lasers
EOM	Electro-Optic Modulator
FWHM	Full Width Half Maximum
GPS	Global Positioning System

HFS	Hyperfine Splitting
IR	Infrared
MOT	Magnto-Optical Trap
MW	Microwave
OD	Optical Density
PD	Photodetector
Rb	Rubidium
RF	Radio-Frequency
RMSE	Root Mean Squared Error
SO	Spin-Orbit
UHV	Ultra-High Vacuum

Colours

Figures in this thesis use a standardised colour legend so all data and diagrams may be easily cross-referenced. Given below are the colours which correspond to all magnetic fields. Colour definitions are also included in the figure legends and/or captions. Data sets where such a scheme is not applicable are coloured using an extended version of the default MATLAB colour palette. The meaning of the colour black differs between figures.

Static Fields

All static fields are shown in the same colour, with line-styles differentiating field components and types where applicable.

 Static Field

Infrared Fields

Colours corresponding to different frequencies of infrared light.

 Cooler
 Repumper
 Imaging and State Cleaning
 $F = 1$ Detection
 $F = 2$ Detection
 $F = 1$ and 2 Combined Detection
 Optical Pumping

Radio-Frequency Fields

Colours corresponding to different polarisation components of radio-frequency light.

-  σ_- -Polarised RF
-  σ_+ -Polarised RF
-  σ_{\pm} -Polarised RF

Microwave Fields

Colours corresponding to different microwave fields. Sets of MW data are grouped by detuning. There are three separate ways of grouping fields used in this thesis. In order to be clear which figures cannot be directly cross-referenced due to using different categorisation methods, different shades of red and blue are used for separate methods of grouping relative red and blue detuning. Fixed colours are used for combined and non-detuned data sets.

-  /  σ_- / σ_+ -Polarised
-  /  Lower/Higher Group Number
-  /  Lower/Higher Hyperfine Sublevel Number
-  Non-Detuned (π -polarised/central group/central hyperfine sublevel)
-  Mixed Groupings (σ_{\pm} -polarised/combined low and high group or magnetic sublevel number)

Chapter 1

Introduction

The aim of this work is to improve our understanding of and ability to manipulate dressed ultracold atoms, with the experimental focus on radio-frequency-dressed rubidium 87. ^{87}Rb is commonly used in cold atom sensors, although the methods developed are applicable to other alkali atoms. Two key emergent questions from such schemes are: how can we control the external and internal state of the atom, and how can we make the state robust against changes in external fields? The study of and solution to both of these problems, using microwave spectroscopy and coherence control, forms the basis of this thesis.

Oscillating magnetic fields play a vital role in forming a wide range of trapping geometries, broadening the range of possibilities for cold atom systems. By the application of a radio-frequency dressing field, multi-photon transitions between arbitrary pairs of states can be permitted. Such external control thus enables precise manipulation of the internal state of the atom. The structure of the dressed rubidium 87 atom can be analysed using microwave spectroscopy, in order to measure transition frequencies and coupling coefficients. This data is required for the development of a method of producing a pair of robust magnetically trappable clock states, for trapped interferometry and other systems. Due to the static field dependence of the coupling coefficients, the AC-Zeeman effect enables the use of detuned MW-dressings to tune the field sensitivities of magnetic sublevels. This technique is theoretically formulated and experimentally verified in this work, providing the general method for manipulating the field-sensitivities of transitions in the ground state of dressed alkali atoms.

In this introductory chapter we will begin with the scientific context for this work: the emergence of quantum mechanics is explained, as well as applications and sensing devices currently in use or under development (Section 1.1). In Section 1.2 the specific questions considered in this thesis are outlined,

giving both the initial problem to be addressed and a brief explanation of possible methods of doing this. A summary of the content of this thesis, as well as associated publications, is also given.

1.1 Scientific Background

This section provides an overview of the historical research which led to the theoretical and technical developments which my work builds on, as well as the present day work motivating my research. In Section 1.1.1 we take a look at the history of our understanding of light and matter, culminating in the discovery of the wave-particle duality and the advent of quantum mechanics. Note that dates given in brackets in this section are the publication dates of the relevant papers; the research performed will in many cases have occurred prior to the stated year. We then move onto some of the applications and techniques utilising quantum mechanics (Section 1.1.2), before providing an overview of the current areas of research in quantum sensing (Section 1.1.3). Context on the specific technique of radio-frequency dressing is given in Section 1.1.4.

1.1.1 History of Light and Matter

The idea that the physical world can be discretised into a multitude of individual pieces goes at least as far back as 400 BCE, with Democritus and his contemporaries proposing the idea of the atom, from ‘indivisible’. This model states that there are an infinite number of atoms of infinitely many types, separated by empty space. These indestructible pieces are of a specific shape and undergo a specific type of motion which determines the properties of the material they make up [180].

The extrapolation from this and later revisions of the atomisation theory led many physicists to consider light as a stream of particles. Arguably a precursor to the wave theory of light, Aristotle’s description several decades later of light as a disturbance in the atoms which made up the air provided the basis for a competing theory [150]. René Descartes (1637 [56]) later refined this idea to state that light propagated through a universal medium called the plenum. Further work followed by Robert Hooke (1665 [92]) comparing mechanical water waves with light, and Christiaan Huygens (1690 [95]) mathematically formulating the wave theory of light. In spite of this, the theory of light as a flow of particles or ‘corpuscles’ still remained dominant throughout much of this century, due to work by Pierre Gassendi (1658 [73]) and Isaac Newton (1687 [133]).

A turning point came when Thomas Young (1802 [188]) illustrated the wave nature of light with his experiment which showed that a beam of light

sent through two slits in an opaque sheet produces a diffraction pattern, and therefore must be explained with a wave model. Further work on diffraction and other results on the wave nature of light followed by Augustin Fresnel (1868 [72]) and others. In the meantime, in the study of the nature of the atom, Antoine Lavoisier (1789 [112]) had developed the theory of conservation of mass, which led to John Dalton's work (1803 [44]) formalising the basis of molecular chemistry. This solidified the theory that all matter is formed of some combination of constituent elements at the same time as a consensus towards the wave nature of light was forming. Further developments of note include James Clerk Maxwell's formulation (1865 [37]) of the equations of electromagnetism, and the indication by Albert Michelson and Edward Morley (1887 [129]) of the lack of an aether, the hypothesised substance through which light would propagate, similar to Descartes' plenum.

The development of physics working from the principles of matter being discrete and energy being unquantised was progressing unhindered until Gustav Kirchoff's work (1860 [109]) on thermal radiation led to a problem. The solution to the energy emission of a black-body formulated by Lord Rayleigh (1898 [146]) was not accurate for short wavelengths. The prediction stated that a black-body would emit infinite energy at infinitely short wavelengths. Sometimes referred to as the ultraviolet catastrophe, this proved a major sticking point. An explanation was presented by Max Planck (1901 [137]) using the assumption of the quantisation of energy. Although providing a solution to the problem at hand, this development led to a large number of questions, and laid the groundwork for a new field of research known as quantum mechanics.

Meanwhile in the study of the atom, further paradigm change was occurring with the discovery of radioactivity by Henri Becquerel (1896 [11]) and follow up work by Pierre Curie and Marie Skłodowska Curie (1898 [43]) necessitating a rethink of Dalton's indivisible atom. The first subatomic particle, the electron, was discovered by Joseph John Thomson (1905 [175]) with the use of a cathode ray tube and alkali atoms. This led to a model of the atom as a sphere of positively charged matter with electrons contained inside. This model turned out to be short-lived, as a later theory of the atom by Ernest Rutherford (1911 [152]), predicting a dense positively charged core, was verified by an experiment using gold foil and alpha particles, showing collisions and deflections from the atomic nucleus. Rutherford's initial assumption was that the electrons were located in a cloud around the nucleus, but this was later revised by Niels Bohr (1913 [19]) into an orbital model which explained the existence of spectral lines.

Now that the orbital structure of the atom was beginning to be understood, the next step was to gain an understanding of the interplay between atoms and light. The splitting of atomic spectral lines in the presence of a magnetic

field had already been noted by Pieter Zeeman (1896 [190]); a similar effect was later discovered for electric fields by Johannes Stark (1913 [170]). This field dependence provided the basis for a theory and experiment by Otto Stern and Walther Gerlach (1922 [76]) which demonstrated the quantisation of angular momentum using silver atoms which separated into groups when passed through a spatially varying magnetic field.

The boundaries between atoms and light had already been blurred by Albert Einstein's (1905 [61, 62]) mass-energy equivalence principle, and his work on the photoelectric effect had given strong evidence of the wave-particle duality of light. As such it was logical that attention turned to the wave nature of matter, as postulated by Louis de Broglie (1923 [51]). Erwin Schrödinger's work (1926 [161]) treated atoms as having a wavefunction, and he went on to mathematically demonstrate the Stark effect, amongst other phenomena. At the same time Werner Heisenberg (1925 [90]) was working on an alternative formulation using matrix mechanics which was found to be equivalent to Schrödinger's method. An experimental observation of the wave nature of matter was soon provided by Clinton Davisson and Lester Germer (1928 [48]) with the observation of electron diffraction. Further important steps in the development of quantum mechanics include Max Born's (1926 [22]) statistical interpretation of the wavefunction and Paul Dirac's (1926 [58]) relativistic quantum mechanics.

1.1.2 Cold Atom Tools

Many results and possible applications emerged from the newly formulated field of quantum mechanics. In this section we take a look at a few of these general areas of development which provide the tool-set needed for more complete sensing possibilities to be discussed in Section 1.1.3. Only a brief overview of the development of these ideas is given here; a number of these techniques will be discussed in more detail later in this work.

Laser Cooling

The idea that radiation could exert a force was an emergent result of the Maxwell equations, and this was experimentally demonstrated in the early 1900s [113]. The first proposal of using this as a mechanism to cool atoms required the use of both quantum mechanics and the invention of the laser [80], and was introduced in 1975 [85]. Exploitation of the Doppler effect and radiation pressure enabled laser cooling, which was initially demonstrated with bound ions [187], and the deceleration of a beam of neutral atoms followed shortly after [128]. The first realisation of an optical molasses was with sodium atoms [34], using 3 pairs of counter-propagating laser beams to provide cooling

in all spatial dimensions.

Magneto-Optical Traps

Although an effective means of forming a cloud of cold atoms, optical molasses have the disadvantage that they provide no spatial confinement. The addition of a magnetic field with a field zero at the centre of the optical molasses allows for the trapping cold atoms, initially with sodium [143]. Magneto-optical traps (MOTs) provide a relatively simple method of producing a cloud of cold atoms, but are limited in the lowest temperature that can be reached. As such, MOTs are now often used to provide an initial cloud of cold atoms before further cooling and trapping techniques are utilised.

Magnetic Trapping

One issue with the quadrupole field used for a simple magneto-optical trap is the trapping at a field zero. Spin-flips at the field zero cause losses from the trap when the laser cooling is switched off. The use of, for example, a Z-shaped wire in addition to external field coils allows the formation of a Ioffe-Pritchard trap [64], which provides confinement in all three dimensions, but also has a non-zero minimum. The Z-wire configuration has the advantage that it can be used to generate cigar-shape traps for use in the study of 1D physics [189], although other methods of generating such a trap are possible, including purely coil based designs [20]. The use of current carrying wires for the spatial guiding of atoms [55] is also a component of a number of quantum sensors.

Bose-Einstein Condensates

One interesting application of these laser cooling and trapping techniques was the ability to produce a new state of matter, the Bose-Einstein condensate. The theoretical formulation of the Bose gas [23], a quantum mechanical form of matter, led to the hypothesis that a whole new state of matter could be reached at sufficiently low temperatures [63]. In this state, all bosons in the gas lie in the lowest energy level of the atom. To achieve this, the atoms must be sufficiently cool that their de Broglie wavelength is larger than the atomic spacing, causing the gas to be a quantum system described by a single wavefunction. This was first observed in 1995 using rubidium atoms [5].

Atom Chips

A simple way of making tight, compact traps is miniaturisation. Microfabrication of gold wires [110] has allowed for more complex designs known as atom chips. Traditional large coil systems require high currents to generate strong fields, but the use of an atom chip allows for the formation of a cloud much

closer to the field generating wires, and as such much tighter traps are easily attainable. Multi-layer chips [178] allow complex configurations of wires, simple switching between multiple trap types and integrated atom guiding possibilities [53]. In addition to these advantages, purely chip based sensors are much more portable and therefore useful in industrial sensors. For more applications of atom chips, see [147].

Interferometry

As mentioned previously, interferometers were initially conceived in order to measure the existence of an aether [129]. The basic principle of a double path interferometer is that a beam of photons (or later particles) is split into two parts which take separate paths before being recombined. If there is some difference between the two paths, destructive interference will occur in the combined beam, and the effect causing the path difference may be measured. Common-path interferometers are also possible assuming there is some difference between the two beams, for example in polarisation. The first atom interferometer was realised in 1991 with helium atoms [30], followed shortly after by sodium atoms [107]. As an alternative to the basic Michelson interferometer used with light, for cold atom applications one common method is Ramsey interferometry [145]. This involves the use of AC-fields to put atoms in an equal superposition of two states at the input and recombine the atoms at the output. A central pulse to flip the states of the atoms at the midpoint of the sequence is typically included to remove the effects of the free evolution of the states over time. Assuming the two paths are equal, the atoms will end purely in their initial state after the final pulse; otherwise the population fraction in the second state gives the phase measurement.

1.1.3 Quantum Technology

For any external parameter which an atom is sensitive to, it is possible to envisage a scheme where an atomic response can be used as a measurement device. Here we take a look at some of the numerous possibilities for cold-atom based quantum systems using alkali atoms. Our particular focus is on quantum sensing, although other applications are also briefly detailed. Quantum sensing can also be achieved with charged ions, molecules, superconducting materials and elementary particles, although these are not covered in this work; a summary of such applications can be found in [52].

Atomic Clocks

Ramsey interferometry in action can be seen in the *Système International* definition of a second. Time was initially measured only as a fraction of a

day, using sun-dials. Accuracy was later improved by mechanical quartz-oscillator clocks, measuring the second as a fraction of a year [125]. Atomic clocks provide a much more stable timebase, and as such the definition of the second was set as the time it takes to make 9.193×10^9 oscillations between the hyperfine levels in ground state of caesium 133, measured using the Ramsey method [123]. The robustness of an atomic clock is usually considered in terms of the Allan deviation [3], a measure of the frequency stability. For caesium this deviation is 10^{-13} [185], although strontium optical lattice clocks can outperform this by four orders of magnitude [179]. Navigation systems, both globally and in space, rely heavily on highly accurate timekeeping. For instance, the ability of the global positioning system (GPS) to determine location is highly dependent on accurate time measurement, as the location of a GPS device relative to three satellites is measured using the time it takes a signal to reach the device for each satellite. For more details on atomic clocks see [118].

Inertial Navigation

Inertial navigation systems are devices which measure the motion of an object. Although GPS can provide accurate global positioning to < 10 m [7], this is only possible if a signal connection to a satellite can be achieved. Sufficiently far underground or under the sea this is not usable, and as such there is interest in a different method of navigation. Inertial navigation systems rely on the fact that if your initial location is sufficiently well known, an accurate integration of how much you have turned by and how fast you were moving over time will give your location without reference to any external device. This would not provide a replacement to GPS, as this is still required for the initial localisation, but would for example reduce the regularity with which a submarine would have to resurface to know its current location. A complete system consists of two components, rotation sensors to measure orientation and accelerometers to measure spatial movement.

Rotation Sensors

A key component of atomic rotation sensors is the Sagnac effect used in ring interferometers, where counter-propagating beams travel in opposite directions around the ring and are recombined at a detector. This will produce an interference pattern if one arm is effectively longer than the other due a rotation of the system. Originally conceived in the early 20th century as an attempt at finding the existence of an aether [153] (similarly to the emergence of the Michelson interferometer) this is now a useful tool in cold atom experiments. Optical gyroscopes are already used in high precision measurements of relativistic effects [15]. One method of forming a Sagnac interferometer is

with the use of a ring trap [68], which has been demonstrated [132]. Further work towards a robust rotation sensor is ongoing [172].

Accelerometers

Airborne atom interferometers use atoms in the presence of retro-reflected laser beams, pulsed three times with alternating-current magnetic fields to split the atoms, redirect them and finally recombine them [74]. These devices measure the movement of the retro-reflecting mirror relative to an optical phase ruler. Prototypes have been tested on aeroplanes [10], and current development of such devices is in progress with the aim of commercialisation. In addition to the applications in a complete inertial navigation system, accelerometers are also useful in the recent field of gravimetry. By measuring the acceleration due to gravity, dense objects underground can be detected, including for archaeological, geophysical and geodesic purposes. Classical gravimeters measuring the displacement of a mass on a spring are highly sensitive to vibrational noise, unlike cold atom vertical-accelerometers [192]. Compact systems are being developed [50] for field based applications, with satellite applications [21] having potential in improving geodesic measurements taken from space.

Magnetometry

We recall that the sensitivity of atoms to magnetic fields has been known since the late 19th century [190]. The ability to measure magnetic fields has applications in a number of areas, such as in archaeology and mineral surveying [149]. Optically pumped magnetometers have an advantage over prior systems in that they can measure weak magnetic fields without the need for cryogenic cooling, allowing for miniaturisation [100]. A significant medical use is magnetoencephalography, the study of the magnetic fields produced by the brain, used for research and diagnostic purposes. Cold atom systems are in development [24] which generate compact brain scanners which can be placed closer to the head than the current generation of models which require sizable cryogenic cooling equipment. Magneto-cardiology, the study of the magnetic field of the heart, is another medical application which cold atom sensors are being developed for [101]. The scanners utilise optically pumped magnetometry, where optical pumping is used to prepare a magnetically sensitive state. The Larmor frequency of the atom can then be measured, giving a value for the magnetic field strength. One method of measuring this is using linear birefringence detection [142]. Other uses include in detection of submarines, and investigation of magnetic fields in space [28]. In addition to magnetometry, electric field sensing can be performed using Rydberg atoms [65].

Further Applications

Cold atoms systems have substantial potential for further research into fundamental physics, in studying topology [191], 1D gases [36] and the search for dark energy [29] to name but a few examples, for more possibilities see [183]. Another area of interest utilising cold atoms is for computation purposes. First proposed in 1980 [12], quantum computing relies on the use of superpositions of atomic states to provide data storage. Storage and retrieval of quantum bits has been experimentally demonstrated [134, 169], although much work is still necessary before these provide a viable mass market means of computing. Potential implementations involve using hot vapours [93] and nitrogen-vacancy centres [182]. Networks for the quantum transmission of data utilising entanglement also have the potential to revolutionise data transfer [35], although this will require more development of quantum memories before this proves efficient. The ability of quantum systems to provide secure communications [158] is also of interest.

1.1.4 Radio-Frequency Dressed Traps

The specific field of study in this thesis is radio-frequency (RF) dressed potentials. Radio-frequency fields were originally used in cold atom systems for evaporate cooling purposes [47], where an ‘RF-knife’ is used to effectively cut through a potential and remove the more energetic atoms, generating a cooler cloud. However, the applications of non-static fields in magnetic trapping are numerous, significantly diversifying the geometric possibilities. The application of an RF-field to couple the potentials of two or more spin states can allow the formation of a potential barrier, enabling the generation of additional minima [88]. As the power of the RF-dressing can be ramped slowly up and down, this can be used as a form of beam splitter. Such a method generated the first coherent splitting of a BEC on an atom chip [91, 163], enabling interferometry. A potential barrier between two BECs also allows for the study of tunneling [96].

Shell traps, where atoms are confined to the outside of a hollow spheroid, can be generated using RF-dressing in order to increase the trapping strength in one direction [40, 194]. Due to the influence of gravity, currently atoms will mostly fall to the bottom of such a trap, although generating the trap in microgravity would remove this issue [120]. The study of a 2D BEC is of topological interest, and also shell traps can be used for trapped interferometry [124]. Combining slowly varying static fields with radio-frequency dressings can permit the generation of complex potentials. Using a static field varied at higher than the trapping frequency, but lower than the Larmor frequency, this allows the potential to be altered without the atoms either

following the field modulation or becoming subject to spin-flips [114]. Such potentials have been realised [78], and can also be used as a loading stage for other types of trap.

Optical lattices are already used for a number of purposes, including as clocks [118], and to form a variety of many-body and spin-dependent systems [18]. Radio-frequency dressing allows for a higher level of control [121, 165] over the potential shape, including facilitating the investigation of 1D lattices [119] and qubit manipulation [166]. One further RF-dressed trap of interest is rings [140], and the extension to toroidal potentials [68], enabling state-dependent, trapped Sagnac interferometry [193]. For more details on RF-dressed trapping possibilities, see [135].

1.2 This Work

Prior to the start of my PhD, a system for the state dependent detection of radio-frequency dressed rubidium 87 had been developed using the linear birefringence properties of the atom. The first aim of my project was to use this method to spectroscopically measure the energy level system in the dressed atom. This knowledge of the internal atomic structure allows for the preparation of pure dressed states, as well as facilitating further manipulation. Robustness against spatial and slow temporal variations in external static field strength can be problematic when requiring transitions between pairs of states with differing dependencies on static field. A method of reducing these discrepancies in pairs of clock states involves utilising the AC-Zeeman effect. More detail on the aims of this thesis is given in Section 1.2.1.

This thesis carries on from the work of previous PhD students, most recently Dr Sindhu Jammi [97], who set up the vacuum and laser system, as well as developed the detection technique. A number improvements to the experiment have been made during the course of my PhD, most notably a re-working of the laser system, as well as the implementation of multi-frequency microwave generation and improvements to the detection system. An outline of the content of this thesis is given in Section 1.2.2. Details on the dispersive detection method (without common mode suppression) are given in the previous paper on this experiment [98].

1.2.1 Thesis Aims

Dressing and Detection

As discussed in Section 1.1.2, radio-frequency dressing can facilitate a range of complex potential geometries. In this work we focus on the case where ^{87}Rb atoms are dressed such that all magnetic sublevels within a given hyper-

fine manifold are coupled. These dressed states permit multi-photon transitions between levels which are forbidden in the undressed scenario, as photons from the dressing field can be combined with MW-probe photons to permit direct transitions between any arbitrary pair of states. This is particularly useful in the case of trapped schemes, as it enables the probing of pairs of trappable clock states, with applications in state-dependent sensors.

This RF-dressing also has the advantage of enabling a state dependent dispersive detection method, which allows detection of the atom fraction in each of the two ground state hyperfine manifolds. This is a method of polarisation homodyning, common-path interferometry which gives a relative measure of the atom number in each state by utilising the birefringence properties of the atomic cloud [98]. Initially two lasers were used to detect population in the two hyperfine states, but the system has since been improved by using a single laser and an electro-optic modulator to provide both required frequencies. This allows the common mode suppression of power fluctuations, facilitating more reliable measurements of the population fraction in each of the two states. The direction of polarisation change is negative for certain magnetic sublevels, which is an advantage when attempting state labelling. One use of RF-dressed traps of particular interest in my group is state-dependently guided rotation sensors utilising the Sagnac effect, as was briefly discussed in Section 1.1.3. Such closed-path, fully guided interferometers can provide increased control over freely propagating atoms, and remove wave-packet dispersion. The use of trappable clock states is a requirement of such a scheme, enabled by RF-dressing as previously described. RF-fields also form the basis of a toroidal ring-trap, which enables state guiding.

Spectroscopy and State Selection

Controlling the internal state of the atom is essential in many applications, especially if state-dependent trapping is desired. Optical pumping using infrared (IR) light can prepare a number of atomic states [86], so long as it is possible to form an appropriate dark state using standard angular momentum selection rules. This is of course limited in the number of states possible to prepare, as well as in the number of possible transitions. In order to allow the preparation of a pure atomic state in any chosen sublevel, and the probing of any arbitrary transition, we turn to microwave fields. Microwave probing between undressed hyperfine sublevels for use in state control is already an established technique for atoms [126], ions [2] and even molecules [57]. Atoms can be prepared in a pure bare state, using our ‘shelving’ technique similar to that in use for trapped ions [42]. This involves a series of MW and IR pulses used to maximise the population in our chosen state, and selectively remove atoms in other states.

Once we have produced a bare state, this can be adiabatically RF-dressed, and a MW-probe used to drive transitions. As our dressing scheme permits multi-photon transitions between hyperfine magnetic sublevels, this facilitates direct transitions between any arbitrary pair of states. The nature of the groups of quasi-energy levels which appear due to the RF-dressing field can thus be analysed. In this thesis the theoretical formulation of the MW-coupling between radio-frequency dressed energy levels in the ground state of alkali atoms is shown, with corresponding data for ^{87}Rb . Using our state labelling technique we can experimentally verify these results, including by finding the transition frequencies and their coupling strengths, which can be both measured as a function of static field strength. This data is necessary for our next aim: manipulating field dependencies of transitions.

Coherence Control

An emergent issue in the dressed scenario is the matter of retaining the coherence of an atomic state. The static magnetic field dependence of atomic energy levels is a necessary component of many atomic sensing schemes, but also leads to complications. Clock-states are pairs energy levels which have a reduced transition frequency dependence on external parameters, in this case static magnetic field, and are so called because of their initial use in atomic clocks. Unfortunately, no pair of trappable states in ^{87}Rb has identical static field dependence, due to the mismatch in the Landé g -factors of the hyperfine levels. Choosing the pair of trappable states with the minimum mismatch in potentials, it is then desirable to engineer a clock transition by manipulating the static field dependence of one or both of the states involved. One method of controlling the static field sensitivity of transitions in ^{87}Rb , using MW-dressing, has been shown to be effective in the case of the undressed atom [157]. This relies on the use of the AC-Zeeman effect [33], which, analogously to the AC-Stark effect for electric fields [116], causes a change in the energy separation of two levels in the presence of an oscillating magnetic field.

In the RF-dressed case, the increased complexity of the energy level system makes engineering the field-dependencies of the energy levels considerably more complicated. The magnitude of the AC-Zeeman shift will be roughly proportional to the square of the coupling strength of the transition. The RF-dressing causes the coupling coefficients between energy levels to also display static field dependence. By locating a transition from one of the two clock states with an appropriate coupling dependence on static field, the energy level may be engineered to match the static field dependence of the other the clock state, and hence remove the transition frequency dependence. Increasing numbers of different MW-frequencies and powers can be combined to cancel the field dependence to higher order. Other methods have been used

to engineer robust clock transitions in specific field scenarios. For instance it has been shown that such a transition can be formed by adjusting the ellipticity of the RF-dressing field [168], although this method is not compatible with trapping systems with different requirements of the RF-ellipticity, such as toroidal traps [68]. RF-dressing as a means of increasing the coherence of atoms in Ioffe-Pritchard traps has also been proposed [106].

The production of a controlled, coherent state is a necessity in a number of atomic physics experiments. For instance, in a state-dependent, guided matter-wave interferometer the spatial path taken by the atoms is determined by their static field dependence. A mismatch in the path length of the two clock states, and imperfect overlap of the two states at the detection site, will lead to errors in the measured Sagnac phase. Even if spatial state manipulation is not required, mismatches in the static field dependence of a transition, for instance in quantum memories, will lead to decoherence of the atoms if external stray magnetic fields are present. Magnetic shielding can be impractical due to size constraints, and as such MW-based coherence control could be a useful tool in the development of compact devices.

1.2.2 Outline and Publications

A chapter by chapter list of the content of this thesis is given below, as well as a breakdown of the appendices and details of associated publications.

Chapter 1: In this introductory chapter we have considered the historical development of our knowledge of the nature of light and matter, up to and including the establishment of the field of quantum mechanics. We have considered some of the main experimental tools used in cold atom systems, as well as a few of the nascent technologies in systems which utilise these. We have then considered the need for increased control over the internal state of the atom, which provides the motivation for this thesis.

Chapter 2: In this chapter the energy level structure of alkali atoms is detailed, starting from the basic shell structure, followed by the spin-orbit coupling and the coupling to nuclear angular momentum. The interaction between the atom and an external static magnetic field is then explored for different field strength regimes. Finally we consider the effects of applying a radio-frequency dressing field to couple between magnetic sublevels, and the energy level structure of the dressed atom in the rotating frame is derived.

Chapter 3: The experimental method used for generating a cloud of atoms in an appropriate initial state is given in this chapter. We go through the various experimental stages from cooling the atoms to characterising and optimising the cloud, followed by a description of the shelving and state-cleaning

method used to prepare the atoms in a pure magnetic substate.

Chapter 4: In order to detect the population fraction of atoms in a given energy level, a simultaneous detection measurement for separate F -levels is required; a method of doing this by exploiting the birefringent properties of the atom is studied. A description of our polarisation homodyning, common-path interferometer is given in this chapter, as well as details on the required experimental set-up and signal processing. Improvements on the original system using electro-optic modulation to achieve common mode suppression of laser power fluctuations are also detailed.

Chapter 5: This chapter focuses on the physical experimental set-up used in this work. The laser system, including the frequency stabilisation method and optical bench set-up is detailed, including upgrades to improve the state detection as well as broader system reliability. The ultra-high vacuum system is also described, along with the equipment for generating static and oscillating magnetic fields. The design of the new generator used to create multi-order MW-dressings is also given.

Chapter 6: In this chapter we analyse and demonstrate the effects of an applied microwave field on the RF-dressed atom. We begin by formulating the couplings between energy level manifolds, considering the coupling strengths and dependence on magnetic fields. Data is then given using this method as a tool for spectroscopy, including measuring the energy level structure of the dressed atom, as well as demonstrating state-dependent control. Measurements of Rabi frequencies and their static field dependencies are also shown. We then demonstrate the possibility of using the RF-dressed atom for interferometry purposes.

Chapter 7: The use of microwave dressing fields to control the static field dependence of energy levels is studied in this chapter. Both the theoretical formalism and data showing the technique in action are given for first and second order dressings. A number of different frequencies and powers of MW-dressings are investigated. The general method for optimising the dressing for any arbitrary pair of levels is also described.

Chapter 8: In this concluding chapter the work detailed so far is summarised. Potential improvements on the method are detailed, as well as useful applications of the results so far, including its implementation in a rotation sensing experiment. An overview of the future experimental direction is also provided, most notably the plan for the use of an optical dipole trap and cavity enhanced detection.

Appendix: Two appendixes are also included for additional detail. In Appendix A angular momentum matrices and equations used throughout this

thesis are defined, as well as the specific cases of Wigner d -matrices and $3j$ -symbols necessary in calculating the couplings between hyperfine sublevels. In Appendix B the full set of equations and plots describing the coupling coefficients between transitions in the ground state of RF-dressed ^{87}Rb are given.

Publications

There are three publications relating to my time working on this experiment. The first is a collaboration with the University of Sussex and the Institute of Electronic Structure and Laser, Foundation for Research and Technology-Hellas. This paper by G. Sinuco-León et al. [A] sets out the theoretical calculation of the MW-coupling coefficients between RF-dressed levels, including their static field dependence. Our data gives an experimental verification of the theoretically predicted spectrum of all possible transition frequencies, as well as data on atoms in optical dipole and shell traps from our collaborators for a number of trappable substates.

The second paper with J. Johnson et al. [B] relates to atomic inertial sensing, specifically the development of a Sagnac interferometric rotation sensor. The sensor is being developed by my colleagues at the University of Nottingham, utilising techniques developed in my experiment; RF-dressing and MW-probing are both essential features of the scheme. My data confirms the ability to perform Ramsey interferometry using RF-dressed clock states. The paper also includes details on the use of MW-dressing for coherence control of the necessary trappable clock states, including preliminary data from my experiment and details on how such a technique will be a necessary component of the final rotation sensor design.

In our most recent paper [C] we show data on the use of such a dressing technique to completely remove the static field dependence of specific transitions to first order, and consider how higher order dependencies may be cancelled using multi-order MW-dressings. The paper gives the theoretical formulation of the coherence control method, and describes how the technique can be generalised for use with any transition in the ground state of RF-dressed alkali atoms. Working from the coupling coefficients of the RF-dressed level system, the method for choosing an appropriate MW-dressing frequency to cancel an arbitrary field dependence is described. The static field dependence of the trappable clock transition in ^{87}Rb is shown to be reduced to less than the resolution-limited linewidth.

- [A] G.A. Sinuco-León, B.M. Garraway, H. Mas, S. Pandey, G. Vasilakis, V. Bolpasi, W. von Klitzing, B. Foxon, S. Jammi, K. Poullos, and T. Fernholz. Microwave spectroscopy of radio-frequency-dressed ^{87}Rb . *Physical Review A*, 100:053416, 2019.
- [B] J. Johnson, B. Foxon, V. Atkocius, F. Gentile, S. Jammi, K. Poullos, and T. Fernholz. Hafele and Keating on a chip: Sagnac interferometry with a single clock. In S.M. Shahriar and J. Scheuer, editors, *Optical, Opto-Atomic, and Entanglement-Enhanced Precision Metrology II*, volume 11296, pages 224–237. International Society for Optics and Photonics, SPIE, 2020.
- [C] B. Foxon, S. Jammi, and T. Fernholz. Multi order controlled synthetic clock transitions. *In preparation*.

Chapter 2

Radio-Frequency Dressed Alkali Atoms

In this chapter we derive the energy level structure of radio-frequency (RF) dressed alkali atoms, with additional detail for rubidium 87. After reviewing the basic structure and static field dependence of the alkali atom (Section 2.1), we then look at how an RF-dressing field changes this dependence in the weak field regime, and introduces new couplings (Section 2.2). The angular momentum relations and forms in Appendix A are assumed throughout.

2.1 Alkali Atoms

We begin here with the energy level structure of the alkali atom (Section 2.1.1), then move onto the effects of static magnetic fields in the various regimes of field strength (Section 2.1.2). This section is provided in order to give a detailed picture of the undressed atom as a basis on which to build our dressed case model.

2.1.1 Atomic Structure

In this section we go through the contributions to the energy level structure of alkali atoms, starting with the coarse structure energy shells, followed by the fine structure which arises from spin-orbit coupling, and finally the hyperfine structure due to the coupling with the nuclear angular momentum, providing a complete picture of the undressed atom. Specific values and diagrams are given for ^{87}Rb , as this is the element used in the experimental part of this work. This section is standard theory from textbooks such as [69].

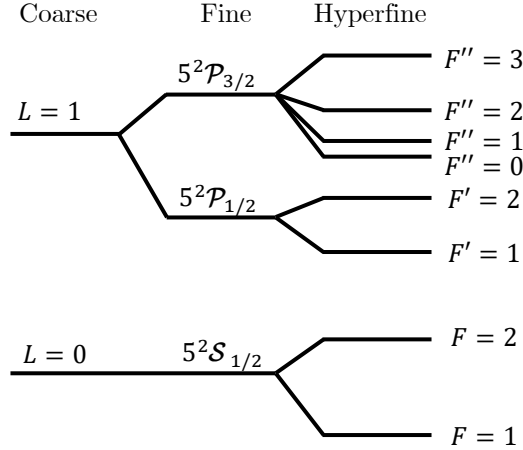


Figure 2.1: The diagram shows the energy levels of ^{87}Rb due to the coarse, fine and hyperfine structure for electronic angular momenta $L = 0$ and 1 (adapted from [171]). Energy levels are spaced vertically by energy, with arbitrary spacing between sets of F -levels.

Coarse Structure

Alkali elements have a single electron with zero net angular momentum in their outermost shell. As all of the innermost electron sub-shells are full, these have only a minor net effect on the dynamics of the atom, and as such the Hamiltonian will be given primarily by the interaction between the nucleus and the outermost electron in the $n = 5$ shell. In the case of ^{87}Rb there are four full inner shells. As the atoms are hydrogen-like, the Bohr formula for the energy of a charged particle in a $\frac{1}{r^2}$ potential

$$E_{\text{CS}} = -hc \frac{R_c}{n^*} \quad (2.1)$$

(where R_c is the Rydberg constant, r is the radial coordinate) holds, with the minor adjustment that the effective shell number is now given by $n^* = n - \delta_L$, where δ_L is the quantum defect, which accounts for imperfect charge-screening of the nucleus by inner shell electrons. The electron angular momenta L of interest in this work are labelled \mathcal{S} for $L = 0$ and \mathcal{P} for $L = 1$, and the associated quantum defects are $\delta_{\mathcal{S}} = 3.19$ and $\delta_{\mathcal{P}} = 2.64$ in the case of ^{87}Rb [117]. We name the Hamiltonian associated with the shell energy \hat{H}_{CS} . For a full derivation of nuclear shell structure see [31, 41].

Fine Structure

As electrons have intrinsic spin $\frac{1}{2}$, their motion within a potential will lead to a coupling between the spin and orbital angular momenta $\hat{\mathbf{S}}$ and $\hat{\mathbf{L}}$. This

spin-orbit interaction is responsible for the fine structure splitting of the coarse energy levels. The spin-orbit interaction is given by

$$\hat{H}_{\text{SO}} \propto \hat{\mathbf{L}} \cdot \hat{\mathbf{S}} = \frac{1}{2} \left(\hat{\mathbf{J}}^2 - \hat{\mathbf{L}}^2 - \hat{\mathbf{S}}^2 \right), \quad (2.2)$$

where $\hat{\mathbf{J}} = \hat{\mathbf{L}} + \hat{\mathbf{S}}$ is the total angular momentum of the electron. This will therefore cause an energy contribution of

$$E_{\text{SO}} \propto J(J+1) - L(L+1) - S(S+1). \quad (2.3)$$

For ^{87}Rb in the $L = 0$ ground state, denoted $5^2\mathcal{S}_{\frac{1}{2}}$ ($n^{2S+1}L_J$), $E_{\text{SO}} = 0$ as there is no orbital angular momentum. In the $L = 1$ case the energy level branches into the $5^2\mathcal{P}_{\frac{1}{2}}$ and $5^2\mathcal{P}_{\frac{3}{2}}$ levels (see Figure 2.1) due to the two possible values of J given by $|L - S| \leq J \leq L + S$. The transition between the \mathcal{S} and \mathcal{P} levels is called the D -line, with $5^2\mathcal{S}_{\frac{1}{2}} \rightarrow 5^2\mathcal{P}_{\frac{1}{2}}$ and $5^2\mathcal{S}_{\frac{1}{2}} \rightarrow 5^2\mathcal{P}_{\frac{3}{2}}$ labelled the $D1$ and $D2$ -lines respectively. We refer to the F -levels of the excited states of the $D1$ and $D2$ lines as F' and F'' respectively, and the ground state as F .

Hyperfine Structure

Another factor which needs to be accounted for in the Hamiltonian is the nuclear angular momentum $\hat{\mathbf{I}}$, and its coupling to the electron angular momentum. This term, known as the Fermi contact interaction, generates the hyperfine structure (HFS). Similarly to the spin-orbit case (Eq. 2.2), this coupling is given by

$$\hat{H}_{\text{HFS}}^F = \mathcal{A}_{\text{HFS}} \hat{\mathbf{I}} \cdot \hat{\mathbf{J}} = \frac{\mathcal{A}_{\text{HFS}}}{2} \left(\hat{\mathbf{F}}^2 - \hat{\mathbf{I}}^2 - \hat{\mathbf{J}}^2 \right), \quad (2.4)$$

where $\hat{\mathbf{F}} = \hat{\mathbf{J}} + \hat{\mathbf{I}}$ is the total angular momentum of the atom and \mathcal{A}_{HFS} is the magnetic dipole constant for a given level. From this we obtain an energy dependence of

$$E_{\text{HFS}}^F = \frac{\mathcal{A}_{\text{HFS}}}{2} (F(F+1) - I(I+1) - J(J+1)). \quad (2.5)$$

This equation only holds true for $J = \frac{1}{2}$ states, as in the $5^2\mathcal{P}_{\frac{3}{2}}$ case the electric quadrupole contribution needs to be accounted for, which contains terms proportional to $(\hat{\mathbf{I}} \cdot \hat{\mathbf{J}})^2$ [171]. As can be seen in Figure 2.1, the Fermi contact interaction causes the energy to branch into separate levels with the possible F values $|I - J| \leq F \leq I + J$. For our $5^2\mathcal{S}_{\frac{1}{2}}$ ground state, $\frac{\mathcal{A}_{\text{HFS}}}{h} = 3.1417$ GHz in ^{87}Rb [16]. We can now define the total Hamiltonian as

$$\hat{H}_0^F = \hat{H}_{\text{CS}} + \hat{H}_{\text{SO}} + \hat{H}_{\text{HFS}}^F, \quad (2.6)$$

in the absence of external magnetic fields. All energy levels which can be addressed on the D -line are shown in Figure 2.1, independent of static field.

2.1.2 Static Magnetic Field Dependence

In this section we study the coupling between alkali atoms and static magnetic fields in the strong, weak and intermediate regimes. This section is standard theory found in textbooks such as [69]. The change in energy of an atomic level in the presence of an external magnetic field is known as the Zeeman shift, which introduces a field dependent term into our Hamiltonian

$$\hat{H}_{\text{tot}} = \hat{H}_0^F + \hat{H}_{\text{DC}}. \quad (2.7)$$

To calculate this shift, the coupling between each of the angular momenta and the magnetic field needs to be accounted for. This provides a contribution to the Hamiltonian of

$$\hat{H}_{\text{DC}} = -\hat{\boldsymbol{\mu}}_{\text{tot}} \cdot \hat{\mathbf{B}}_{\text{DC}} = \mu_B (g_I \hat{\mathbf{I}} + g_L \hat{\mathbf{L}} + g_S \hat{\mathbf{S}}) \cdot \hat{\mathbf{B}}_{\text{DC}}, \quad (2.8)$$

where the total magnetic dipole moment $\hat{\boldsymbol{\mu}}_{\text{tot}} = \hat{\boldsymbol{\mu}}_I + \hat{\boldsymbol{\mu}}_J + \hat{\boldsymbol{\mu}}_L$. The Landé g -factors account for the different magnitudes of the magnetic moments, with $\hat{\boldsymbol{\mu}}_I = \mu_B g_I \hat{\mathbf{I}}$ and similarly for $\hat{\mathbf{L}}$ and $\hat{\mathbf{S}}$. Alternatively the definition $\hat{\boldsymbol{\mu}}_I = \mu_N g_I \hat{\mathbf{I}}$ can be found in literature, which requires a different value for g_I . The magnetic field is chosen to be in the z -direction, $\hat{\mathbf{B}}_{\text{DC}} = B_{\text{DC}} \hat{\mathbf{e}}_z$, without loss of generality. The form of the energy dependence is determined by whether the hyperfine splitting or the magnetic field dependence is the dominant effect.

Strong Field Dependence

In the strong field regime where the $E_{\text{DC}} \gg E_{\text{HFS}}$, J and its associated magnetic sublevels m_J (as well as I and m_I) are good quantum numbers and the simplification $g_J \hat{\mathbf{J}} = g_L \hat{\mathbf{L}} + g_S \hat{\mathbf{S}}$ is valid, meaning

$$\hat{H}_{\text{DC}} = \mu_B (g_I \hat{\mathbf{I}} + g_J \hat{\mathbf{J}}) \cdot \hat{\mathbf{B}}_{\text{DC}}. \quad (2.9)$$

The value $g_J \gg g_I$, differing by a factor given by the ratio of the electron to proton mass ($\approx 1/1836$ [81]), which is the same as the ratio of the nuclear to Bohr magneton. This means that the $g_J \hat{\mathbf{J}}_z$ contribution is dominant, and $\hat{\mathbf{J}}$ can be considered to be precessing around $\hat{\mathbf{B}}_{\text{DC}}$. This will provide an energy contribution of

$$E_{\text{DC}} = \mu_B \langle J, m_J | g_J \hat{\mathbf{J}} \cdot \hat{\mathbf{B}}_{\text{DC}} | J, m_J \rangle = \mu_B g_J m_J B_{\text{DC}}. \quad (2.10)$$

The factor g_J is derived starting from $g_J \hat{\mathbf{J}} \cdot \hat{\mathbf{J}} = g_L \hat{\mathbf{L}} \cdot \hat{\mathbf{J}} + g_S \hat{\mathbf{S}} \cdot \hat{\mathbf{J}}$, substituting in $\hat{\mathbf{J}} = \hat{\mathbf{L}} + \hat{\mathbf{S}}$ on the right hand side then rearranging to obtain

$$g_J = g_L \frac{J(J+1) + L(L+1) - S(S+1)}{2J(J+1)} + g_S \frac{J(J+1) - L(L+1) + S(S+1)}{2J(J+1)}. \quad (2.11)$$

Note that even for what we consider to be strong magnetic fields, the fine structure splitting is still dominant ($E_{\text{SO}} \gg E_{\text{DC}}$). For extremely high mag-

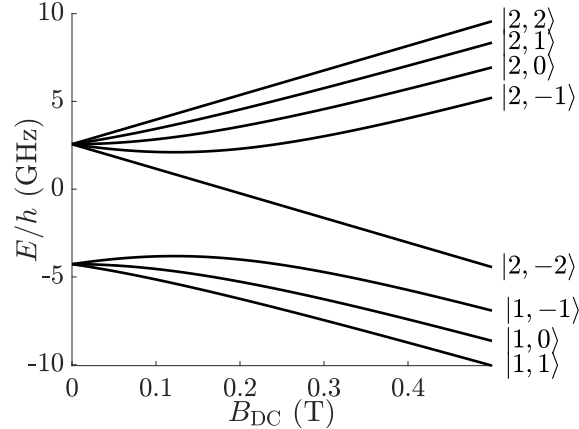


Figure 2.2: The energy dependence of the magnetic sublevels levels of ^{87}Rb on static magnetic field in the $5^2\mathcal{S}_{\frac{1}{2}}$ state is shown in the figure, as given by Eq. 2.15 [25]. States are labelled by their $|F, m_F\rangle$ values.

netic fields we enter the Paschen-Bach regime where $\hat{\mathbf{L}}$ and $\hat{\mathbf{S}}$ individually couple to $\hat{\mathbf{B}}_{\text{DC}}$ [156].

Weak Field Dependence

In the weak field regime where the magnetic field dependence is much smaller than the hyperfine splitting ($E_{\text{HFS}} \gg E_{\text{DC}}$), the total angular momentum of the atom $\hat{\mathbf{F}}$ can be treated as precessing around $\hat{\mathbf{B}}_{\text{DC}}$, allowing for the simplification $g_F\hat{\mathbf{F}} = g_I\hat{\mathbf{I}} + g_J\hat{\mathbf{J}}$, and therefore

$$\hat{H}_{\text{DC}} = \mu_B g_F \hat{\mathbf{F}} \cdot \hat{\mathbf{B}}_{\text{DC}}. \quad (2.12)$$

As F and m_F are now good quantum numbers, this provides the energy contribution

$$E_{\text{DC}} = \mu_B \langle F, m_F | g_F \hat{\mathbf{F}} \cdot \hat{\mathbf{B}}_{\text{DC}} | F, m_F \rangle = \mu_B g_F m_F B_{\text{DC}}, \quad (2.13)$$

where the static field is in the z -direction. In ^{87}Rb the factor g_F has values $g_{F=1} = -0.50182671$ and $g_{F=2} = 0.49983642$ in the $5^2\mathcal{S}_{\frac{1}{2}}$ ground state, as given by

$$g_F = g_J \frac{F(F+1) + J(J+1) - I(I+1)}{2F(F+1)} + g_I \frac{F(F+1) - J(J+1) + I(I+1)}{2F(F+1)}, \quad (2.14)$$

derived in the same manner as g_J in Eq. 2.11. As can be seen from Eq. 2.12, at weak fields the energy dependence of the levels is linear with magnetic field, and for the $m_F = 0$ case the energy is independent of magnetic field.

Intermediate Fields

For intermediate magnetic fields where $E_{\text{DC}} \sim E_{\text{HFS}}$ the energies will be in a superposition of the $|F, m_F\rangle$ and $|J, m_J, I, m_I\rangle$ bases, requiring a full diagonalisation of the Hamiltonian $H_{\text{HFS}} + H_{\text{DC}}$ to extract the energy eigenvalues, where H_{DC} is as in Eq. 2.9. In the simple case of $J = \frac{1}{2}$ the solution is given by the Breit-Rabi equation [25]

$$E_{\text{BR}} = E_{\text{HFS}} \left(-\frac{1}{2(2I+1)} + \frac{1}{2} \sqrt{1 + \frac{4m_F}{2I+1} \mathbf{x} + \mathbf{x}^2} \right), \quad (2.15)$$

where

$$\mathbf{x} = \frac{(g_J - g_I)\mu_B B(t)}{E_{\text{HFS}}}. \quad (2.16)$$

From our previous definitions of F and its constituents, we see that the $I = \frac{3}{2}$ [67] nucleus of ^{87}Rb will have $F = 1, 2$ in the ground state $5^2\mathcal{S}_{\frac{1}{2}}$. As F has magnetic sublevels $-F \leq m_F \leq F$, the $F = 1, 2$ states split into 3 and 5 levels respectively, as can be seen in Figure 2.2.

2.2 Radio-Frequency Dressing

In this section we study the effects of an applied radio-frequency (RF) dressing field on the atom. We begin with the basic form of the RF-field and the couplings this will invoke (Section 2.2.1), followed by moving to the rotating frame (Section 2.2.2) and examining the resulting energy levels (Section 2.2.3). This section is based on previous theoretical work from [97, 98].

2.2.1 Spin Precession and Driving

From this point on we shall be purely working in the weak field regime, studying the $L = 0$ ground state of alkali atoms, where the factor g_J will be approximately that of a free electron $g_e \approx 2$ [84]. This state has two possible values of total angular momentum $F = I \pm 1/2$. Recalling that $g_I \ll g_J$, we can approximate $g_I = 0$, and using Eq. 2.14 we can obtain that the corresponding two g_F -factors will be

$$g_F \approx \pm g_J / (2I + 1) \approx \pm 2 / (2I + 1). \quad (2.17)$$

We therefore see that the two sets of magnetic sublevels $|F, m_F\rangle$ will have approximately opposite coupling to static magnetic field. This means that the sublevels in both manifolds can be near-resonantly coupled with the same radio-frequency. Due to the different sign of the g_F -factors between F -levels, an RF of linear polarisation σ_{\pm} is necessary to couple between all sublevels

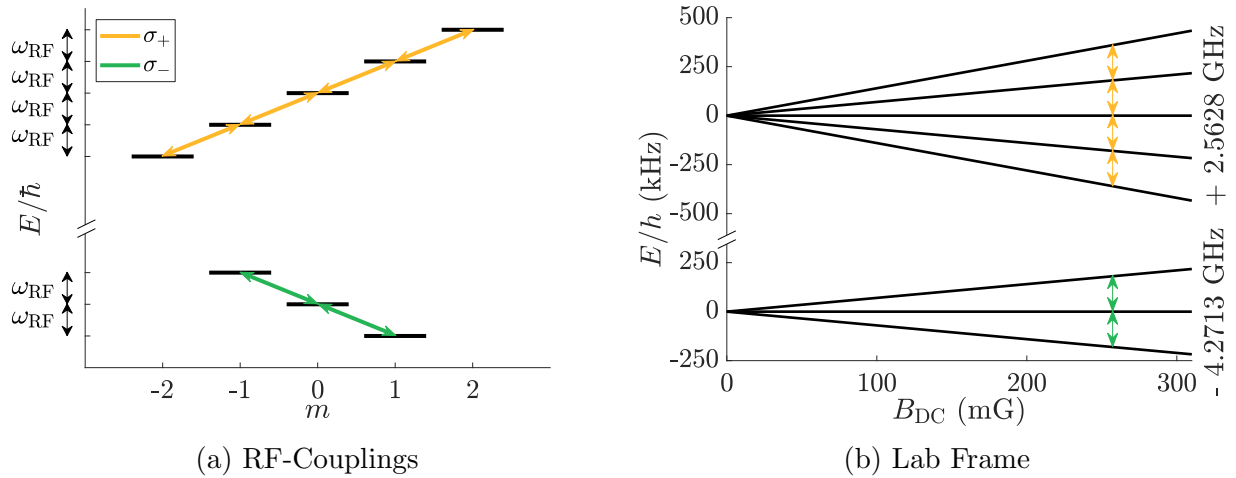


Figure 2.3: The energy level diagram for the magnetic substates in the ground state of ^{87}Rb are shown in (a), with the RF-dressing frequencies indicated. The static magnetic field dependence of these states in the laboratory frame is a linear Zeeman shift (Eq. 2.13), shown in (b). The arrows indicate the frequencies of the applied RF-dressing, which couples the magnetic sublevels at the resonant static field. Hyperfine structure frequencies are indicated on the right hand side. Adapted from our paper [167].

in each of the two manifolds, as illustrated on the energy level diagram Figure 2.3a for $I = 3/2$. The magnetic field dependence of each sublevel is given by Eq. 2.13, exhibiting the linear Zeeman shift shown in Figure 2.3b for ^{87}Rb . The two manifolds of m_F -levels are separated by a fixed energy determined by the hyperfine splitting. Note that in this thesis we will be referring to the set of states $|F, m_F\rangle$ within a single hyperfine F -level as one manifold. Therefore more explicitly we mean a ‘hyperfine’ manifold, rather than the alternative ‘fine’ manifold sometimes found elsewhere in literature. As alkali atoms have an odd number of protons, they have a non-zero nuclear angular momentum [177], and as such g_F will always be positive in the upper $F = I + 1/2$ manifold and negative in the lower $F = I - 1/2$ case. Differently polarised fields are therefore required to couple between sublevels in the two manifolds.

If we apply a σ_{\pm} -polarised RF-dressing, we can enable couplings between magnetic sublevels in both manifolds. In general, transitions between energy levels are restricted to only those possible via the standard selection rules for magnetic dipoles:

$$\Delta F = 0, \pm 1, \quad \Delta m_F = 0, \pm 1 \quad \text{and} \quad F = 0 \not\leftrightarrow 0. \quad (2.18)$$

In the dressed case however these rules no longer apply, because of multi-

photon transitions, i.e. a single input spectroscopy photon in combination with the dressing field can drive transitions between any pair of sublevels. Such a coupling changes the energy dependence of the levels, as we shall derive below, following the same method as detailed in a previous paper on this experiment [98]. For the purposes of the rotating frame calculation we will be using the notation $B_{\text{RF}}^{\pm} = B_{\pm}$, $B_{\text{RF}}^{\pi} = B_{\pi}$ and $\omega_{\text{RF}} = \omega$. Later we will revert to using the unsimplified labels, to avoid confusion with MW-fields once these are introduced.

To fully formulate the equation for the dressed case, we need to split the magnetic field into its constituent parts:

$$\hat{\mathbf{B}}_{\text{tot}}(t) = \hat{\mathbf{B}}_{\text{DC}} + \hat{\mathbf{B}}_{\text{RF}}(\omega t). \quad (2.19)$$

The static field can be defined to be in the z -direction ($\hat{\mathbf{B}}_{\text{DC}} = B_{\text{DC}}\hat{\mathbf{e}}_z$) without loss of generality. Considering that σ_{\pm} -polarisation is required for the RF-field, it is convenient to define this in terms of spherical coordinates. The Cartesian and spherical unit vectors are related by

$$\hat{\mathbf{e}}_{\pm} = \frac{1}{\sqrt{2}}(\hat{\mathbf{e}}_x \pm i\hat{\mathbf{e}}_y), \quad \hat{\mathbf{e}}_{\pi} = \hat{\mathbf{e}}_z. \quad (2.20)$$

The RF-field in this basis will be given by

$$\begin{aligned} \hat{\mathbf{B}}_{\text{RF}}(\omega t) &= \hat{\mathbf{B}}_{\text{RF}}e^{-i\omega t} + \hat{\mathbf{B}}_{\text{RF}}^*e^{i\omega t}, \\ \hat{\mathbf{B}}_{\text{RF}} &= B_+\hat{\mathbf{e}}_+ + B_-\hat{\mathbf{e}}_- + B_{\pi}\hat{\mathbf{e}}_{\pi}, \end{aligned} \quad (2.21)$$

giving the full equation for the magnetic field:

$$\hat{\mathbf{B}}_{\text{tot}}(t) = B\hat{\mathbf{e}}_z + (B_+\hat{\mathbf{e}}_+ + B_-\hat{\mathbf{e}}_- + B_{\pi}\hat{\mathbf{e}}_{\pi})e^{-i\omega t} + \text{h.c.}, \quad (2.22)$$

where h.c. is the Hermitian conjugate. We now modify our total Hamiltonian to account for the contribution from RF-fields

$$\hat{H}_{\text{tot}} = \hat{H}_0^F + \hat{H}_{\text{DC}} + \hat{H}_{\text{RF}}. \quad (2.23)$$

2.2.2 Rotating Wave Approximation

To analyse the effect of the RF-dressing on the energy levels, we move into a rotating frame to simplify our Hamiltonian. Using Eq. 2.12, and accounting for all polarisations, we see that our RF Hamiltonian will be given by

$$\hat{H}_{\text{RF}} = \sum_{\sigma \in -,\pi,+} \eta_{\sigma} \mu_B g_F (B_{\sigma} e^{-i\omega t} \hat{F}_{\sigma} + B_{\sigma}^* e^{i\omega t} \hat{F}_{-\sigma}), \quad (2.24)$$

where η_σ are the polarisation normalisation factors $\eta_\pm = \mp \frac{1}{\sqrt{2}}$ and $\eta_0 = 1$. This can be generalised to

$$\eta_\sigma = \text{sign}(1 - 2\varsigma) \left(\frac{1}{\sqrt{2}}\right)^\varsigma, \quad (2.25)$$

where the angular momentum of the photon $\varsigma = \pm 1, 0$ for $\sigma = \sigma_\pm, \pi$ respectively. This factor is necessary to account for the constant values in Eq. 2.20. In subscripts we are using \pm to represent σ_\pm , and also the notational simplification $\sigma_- = -\sigma_+$ and $\pi = -\pi$, i.e. that the different values σ relate in the same way as their associated angular momenta ς . Using Eq. 2.22 and \hat{F} in the spherical form with raising and lowering operators \hat{F}_\pm (see Appendix A.1) provides the total field-dependent laboratory frame Hamiltonian

$$\hat{H}_{\text{tot}} = \frac{\mu_B g_F}{2} \left(\hat{F}_z B_{\text{DC}} + \left(\frac{1}{\sqrt{2}} (\hat{F}_+ B_+ + \hat{F}_- B_-) + \hat{F}_\pi B_\pi \right) e^{-i\omega t} \right) + \text{h.c.} \quad (2.26)$$

We now move to the rotating frame of the RF using the rotation operator

$$\hat{U}_\pm = e^{i(\varphi \pm \omega t) \hat{F}_z}, \quad (2.27)$$

where the sign of ωt is given by the sign of the g_F -factor which determines the direction of rotation, and φ is the phase which determines the RF-field orientation. As transitions between m_F -levels require σ_\pm -polarisation, the field must be oriented in the $x - y$ plane. The field orientation is then given by

$$\hat{\mathbf{B}}_{\text{RF}}(\omega t) / |\hat{\mathbf{B}}_{\text{RF}}(\omega t)| = \hat{\mathbf{e}}_x \cos \varphi + \hat{\mathbf{e}}_y \sin \varphi. \quad (2.28)$$

Starting from the time dependent Schrödinger equation $\hat{H}\psi = i\hbar\dot{\psi}$, and defining $\phi = \hat{U}_\pm \psi$ we obtain:

$$i\hbar\dot{\phi} = \dot{\hat{U}}_\pm \phi + \hat{U}_\pm \dot{\psi} = i\hbar\dot{\hat{U}}_\pm \psi + \hat{U}_\pm \hat{H}\psi = i\hbar\dot{\hat{U}}_\pm \hat{U}_\pm^\dagger \phi + \hat{U}_\pm \hat{H} \hat{U}_\pm^\dagger \phi, \quad (2.29)$$

where a dot denotes a derivative with respect to time. $i\hbar\dot{\hat{U}}_\pm \hat{U}_\pm^\dagger = -\hbar\omega F_z$ as F_z commutes with \hat{U}_\pm ($[\hat{U}_\pm, \hat{F}_z] = 0$), and this gives the rotating frame Hamiltonian

$$\hat{H}_{\text{rot}} = i\omega F_z + \hat{U}_\pm \hat{H} \hat{U}_\pm^\dagger. \quad (2.30)$$

Time independent Hamiltonian components will be unaffected, as these commute with \hat{F}_z , so we apply this equation only to our Hamiltonian from Eq. 2.26. Using the previous commutation relation this gives the result

$$\begin{aligned} \hat{H}_{\text{rot}} = & \frac{\mu_B g_F}{2} \left((B_{\text{DC}} - \frac{\hbar\omega}{\mu_B |g_F|}) \hat{F}_z + (B_\pi e^{i\mp\omega t} + B_\pi^* e^{i\pm\omega t}) \hat{F}_\pi \right. \\ & \left. + \hat{U}_\pm \left(\frac{1}{\sqrt{2}} (\hat{F}_+ B_+ + \hat{F}_- B_-) e^{-i\omega t} \right) \hat{U}_\pm^\dagger \right) + \text{h.c.}, \end{aligned} \quad (2.31)$$

which includes the resonant magnetic field

$$B_{\text{res},F} = \frac{\hbar\omega}{\mu_B |g_F|}. \quad (2.32)$$

In this thesis we will also use the approximation of a single resonant field at

$$B_{\text{res}} = (B_{\text{res},F=I-1/2} + B_{\text{res},F=I+1/2})/2 \quad (2.33)$$

for simplicity in some circumstances.

The choice of the RF to be in the x -direction necessitates that $B_\pi = B_\pi^* = 0$. To simplify the \hat{U}_\pm terms, we apply the Baker-Hausdorff lemma [1]

$$e^{k\hat{F}_z} \hat{F}_\pm e^{-k\hat{F}_z} = e^{\pm k} \hat{F}_\pm, \quad (2.34)$$

which gives the Hamiltonian:

$$\begin{aligned} \hat{H}_{\text{rot}} = & \frac{\mu_B g_F}{2} \left((B_{\text{DC}} - B_{\text{res},F}) \hat{F}_z \right. \\ & + \frac{1}{\sqrt{2}} \left(e^{\mp i\varphi} F_+ B_+ (1 + e^{2i\omega t}) + e^{\pm i\varphi} F_- B_- (1 + e^{-2i\omega t}) \right. \\ & \left. \left. + e^{\pm i\varphi} F_+ B_-^* (1 + e^{-2i\omega t}) + e^{\mp i\varphi} F_- B_+^* (1 + e^{2i\omega t}) \right) \right). \end{aligned} \quad (2.35)$$

Using the rotating wave approximation, we can then discount terms oscillating at 2ω . This approximation is valid so long as these terms are far from resonance, $\hbar\omega \gg \mu_B g_F |B_{\text{eff}}|$, where B_{eff} is the effective magnetic field. Due to the signs of the g_F -factors, only σ_+ -polarised RF can directly couple magnetic sublevels in the $F = I + 1/2$ manifold and σ_- for $F = I - 1/2$. As such, we can disregard terms which are counter-rotating with respect to the Larmor precession, which necessitates separating the Hamiltonians for different F -levels. This gives the result

$$\hat{H}_{\text{rot}}^\pm = \frac{\mu_B g_F}{2} \left((B_{\text{DC}} - B_{\text{res},F}) \hat{F}_z + \frac{1}{\sqrt{2}} (e^{\pm i\varphi} F_\pm B_\pm + e^{\mp i\varphi} F_\mp B_\pm^*) \right), \quad (2.36)$$

where \hat{H}_{rot}^+ applies to the upper manifold with $F = I + 1/2$ and \hat{H}_{rot}^- applies to the lower manifold $F = I - 1/2$. The effective magnetic field will then be given by

$$\hat{\mathbf{B}}_{\text{eff}}^\pm = (B_{\text{DC}} - B_{\text{res},F}) \hat{\mathbf{e}}_z + \frac{1}{2} (e^{\pm i\varphi} B_\pm + e^{\mp i\varphi} B_\pm^*) \hat{\mathbf{e}}_\pm, \quad (2.37)$$

with the effective Hamiltonian

$$\hat{H}_{\text{eff}}^\pm = \frac{\mu_B g_F}{2} \hat{\mathbf{F}} \cdot \hat{\mathbf{B}}_{\text{eff}}^\pm \quad (2.38)$$

of the same form as in the DC case in Eq. 2.12, but adapted for a time

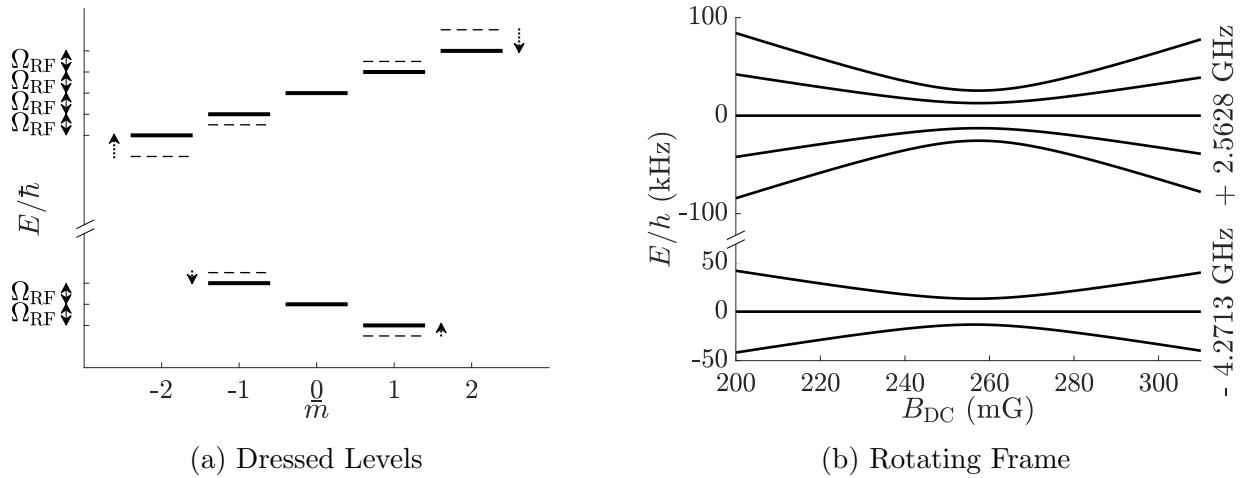


Figure 2.4: The shifts on the energy of the magnetic sublevels in the ground state of ^{87}Rb in the presence of an RF-dressing field is shown in (a). Dashed lines indicate the undressed levels from Figure 2.3a, and arrows show the shift in energy caused by the RF-dressing field. The corresponding energy dependence in the rotating frame, as given by Eq. 2.43, is shown in (b). Hyperfine structure frequencies are indicated on the right hand side. Adapted from our paper [167].

dependent field. Using our chosen RF-dressing of the form

$$B_{\pm} = \frac{1}{\sqrt{2}} e^{\mp i\varphi} B_{\text{RF}}, \quad (2.39)$$

this simplifies to

$$\hat{\mathbf{B}}_{\text{eff}}^{\pm} = (B_{\text{DC}} - B_{\text{res},F}) \hat{\mathbf{e}}_z + \frac{1}{2} e^{\pm i\varphi} B_{\text{RF}} \hat{\mathbf{e}}_x + \text{h.c.} \quad (2.40)$$

2.2.3 Dressed State Spectrum

To obtain the full Hamiltonian and eigenvalues of the RF-dressed atom we will be using the F -matrices found in Appendix A.2. The reduced Hamiltonian for the $|\uparrow\rangle|\downarrow\rangle$ basis, given by Eq. 2.36 with the appropriate F -matrices is

$$H_{\text{tot},F} = \begin{pmatrix} \mu_B g_F (B_{\text{DC}} - B_{\text{res},F}) & \frac{\hbar \Omega_{\text{RF}}^{\pm}}{2} \\ \frac{\hbar \Omega_{\text{RF}}^{\pm*}}{2} & -\mu_B g_F (B_{\text{DC}} - B_{\text{res},F}) \end{pmatrix}, \quad (2.41)$$

where Ω_{RF}^{\pm} are the Rabi angular frequencies of the inter-manifold couplings

$$\hbar \Omega_{\text{RF}}^{\pm} = \mu_B g_F |B_{\text{eff}}^{\pm}| \approx \frac{\mu_B g_F |B_{\text{RF}}^{\pm}|}{\sqrt{2}}. \quad (2.42)$$

This approximation is only true near the resonant static field. Taking the eigenvalues of this Hamiltonian gives the static field dependence of the energy levels

$$E_{F,\bar{m}} = \mu_B g_F \bar{m} \sqrt{\frac{|B_{\text{RF}}^\pm|^2}{2} + (B_{\text{DC}} - B_{\text{res},F})^2}, \quad (2.43)$$

where we have reintroduced the m dependence from Eq. 2.13. We are now using \bar{m} instead of m because we are discussing dressed levels. Figure 2.4b shows the static field dependence of the full set of magnetic sublevels in the rotating frame. Static field independent energy components from Eq. 2.6 are not considered here.

The associated energy level picture Figure 2.4a shows that the separation of the energy levels relates to the Rabi frequency of the RF, which is proportional to the RF-field strength. As the Rabi frequency is proportional to the magnitude of the RF-field, we can see that in the limit of zero RF-power the energy spectrum would be of the same form as the linear undressed (Figure 2.3b) case, only with the zero field point shifted to the static field resonance due to the rotating frame. In the undressed case the energy levels within an F -manifold are degenerate at zero field, because of the symmetry of the system, but the application of RF-fields removes the degeneracy. Increasing the RF-field strength leads to avoided crossings and non-degenerate eigenvalues, in accordance with the von Neumann-Wigner theorem [54, 186] which states that in non-symmetric systems a degeneracy cannot be created by varying a single parameter. The repulsion between levels is generated when a coupling field is applied, and increases with the field strength.

For completeness, the full Hamiltonians for each sub-manifold in the bare state basis transformed into the rotating frame will be

$$H_{\text{tot},F=1} = \hbar \begin{pmatrix} -\omega_{\text{tot}} & \frac{1}{\sqrt{2}} \frac{\Omega_{\text{RF}}^-}{2} & 0 \\ \frac{1}{\sqrt{2}} \frac{\Omega_{\text{RF}}^{*-}}{2} & 0 & \frac{1}{\sqrt{2}} \frac{\Omega_{\text{RF}}^-}{2} \\ 0 & \frac{1}{\sqrt{2}} \frac{\Omega_{\text{RF}}^{*-}}{2} & \omega_{\text{tot}} \end{pmatrix}, \quad (2.44)$$

$$H_{\text{tot},F=2} = \hbar \begin{pmatrix} -2\omega_{\text{tot}} & \frac{\Omega_{\text{RF}}^+}{2} & 0 & 0 & 0 \\ \frac{\Omega_{\text{RF}}^{*+}}{2} & -\omega_{\text{tot}} & \sqrt{\frac{3}{2}} \frac{\Omega_{\text{RF}}^+}{2} & 0 & 0 \\ 0 & \sqrt{\frac{3}{2}} \frac{\Omega_{\text{RF}}^{*+}}{2} & 0 & \sqrt{\frac{3}{2}} \frac{\Omega_{\text{RF}}^+}{2} & 0 \\ 0 & 0 & \sqrt{\frac{3}{2}} \frac{\Omega_{\text{RF}}^{*+}}{2} & \omega_{\text{tot}} & \frac{\Omega_{\text{RF}}^+}{2} \\ 0 & 0 & 0 & \frac{\Omega_{\text{RF}}^{*+}}{2} & 2\omega_{\text{tot}} \end{pmatrix}, \quad (2.45)$$

where

$$\hbar\omega_{\text{tot}} = (-1)^F \mu_B g_F (B_{\text{DC}} - B_{\text{res},F}) + \hbar\omega_{\text{RF}}. \quad (2.46)$$

As our initial state $|F, F_z\rangle$ is an eigenstate of \hat{U}_\pm , this is the same in both laboratory and rotating frames, assuming we can discount any evolution of the dynamical phase.

When applying our RF-dressing field, adiabaticity is an important consideration. It is therefore necessary to ramp the dressing field strength sufficiently slowly that the atoms adiabatically follow the orientation of the effective field, whilst simultaneously reducing the static field strength in order to tune the Larmor frequency near resonance. This method thus conserves the total magnitude of the collective spin. The angle of the effective magnetic field given in Eq. 2.40 relative to the z -axis is

$$\theta_F = \frac{\pi}{2} - \tan^{-1} \left(\frac{B_{\text{DC}} - B_{\text{res},F}}{\sqrt{2}B_{\text{RF}}^\pm} \right). \quad (2.47)$$

In order to adiabatically change the effective field it is required that

$$|\dot{\theta}_F| \ll \frac{\mu_B g_F |B_{\text{eff}}|}{\hbar}, \quad (2.48)$$

meaning that any of the three magnetic fields which determine θ_F cannot change faster than the effective field, in which case the state would not remain an eigenstate of the Hamiltonian. The state can now be obtained using a rotation around the rotating y -axis, given by

$$|\psi_{\text{rot}}\rangle = \hat{U}_y(\theta_F) |F, F_z\rangle = e^{i\theta_F \hat{F}_y} |F, F_z\rangle. \quad (2.49)$$

To get to the laboratory frame we must reintroduce the rotation operator from Eq. 2.27, which gives

$$|\psi(t)\rangle = \hat{U}_\pm^\dagger |\psi_{\text{rot}}\rangle = e^{i(\varphi \pm \omega t) \hat{F}_z} e^{i\theta_F \hat{F}_y} |F, F_z\rangle. \quad (2.50)$$

Our rotating \hat{F} will be given by

$$\hat{\mathbf{F}} = \hat{U}_y^\dagger(\theta_F) \hat{U}_\pm^\dagger(t) \hat{\mathbf{F}} \hat{U}_\pm(t) \hat{U}_y(\theta_F), \quad (2.51)$$

which can be put into matrix form by defining the full rotation operator

$$\hat{\mathbf{R}}_\pm(t) = e^{i(\varphi \mp \omega t) \hat{F}_z} e^{i\theta_F \hat{F}_y} = \hat{\mathbf{R}}_z(\varphi \pm \omega t) \hat{\mathbf{R}}_y(-\theta_F), \quad (2.52)$$

which has the constituent rotation matrices

$$\hat{\mathbf{R}}_z(\pm\omega t) = \begin{pmatrix} \cos(\varphi \pm \omega t) & -\sin(\varphi \pm \omega t) & 0 \\ \sin(\varphi \pm \omega t) & \cos(\varphi \pm \omega t) & 0 \\ 0 & 0 & 1 \end{pmatrix}, \quad (2.53)$$

$$\hat{\mathbf{R}}_y(-\theta_F) = \begin{pmatrix} \cos \theta_F & 0 & -\sin \theta_F \\ 0 & 1 & 0 \\ -\sin \theta_F & 0 & \cos \theta_F \end{pmatrix}. \quad (2.54)$$

This gives the result

$$\hat{\mathbf{R}}_{\pm}(t) = \begin{pmatrix} \cos(\varphi \pm \omega t) \cos \theta_F & -\sin(\varphi \pm \omega t) & -\cos(\varphi \pm \omega t) \sin \theta_F \\ \sin(\varphi \pm \omega t) \cos \theta_F & \cos(\varphi \pm \omega t) & -\sin(\varphi \pm \omega t) \sin \theta_F \\ \sin \theta_F & 0 & \cos \theta_F \end{pmatrix}, \quad (2.55)$$

which, again using the Baker-Hausdorff lemma (Eq. 2.34), allows the simplification

$$\hat{\mathbf{F}} = \hat{\mathbf{R}}_{\pm} \hat{\mathbf{F}} \hat{\mathbf{R}}_{\pm}^{-1} = \hat{\mathbf{R}}_{\pm} \hat{\mathbf{F}}, \quad (2.56)$$

thus completing the formulation for the individual F -manifolds.

The study of the RF-dressed atom described here provides the foundation for the remainder of the work in this thesis. The method used to generate a pure dressed state is addressed in Chapters 3. Our dispersive detection method (Chapter 4) requires RF-dressing, and provides the means of measuring the internal state of the atom necessary for performing microwave spectroscopy (Chapter 6). The theory of the coupling coefficients between hyperfine manifolds detailed in the spectroscopy chapter builds directly on the RF Hamiltonians formulated above. The addition of MW-dressing fields for coherence control then logically develops from this (Chapter 7).

Chapter 3

Preparing the Atoms

In this chapter we will go through the steps involved in generating a cloud of cold atoms in a pure initial state. In Section 3.1, the method of cooling the atoms using magneto-optical trapping is detailed, as well as the absorption imaging method used to characterise the cloud. A description of our method of preparing a pure quantum state using a combination of microwave and laser pulses in a shelving procedure is then provided (Section 3.2).

3.1 The Atom Cloud

The first step of any standard cold atoms experiment is the production of an atomic cloud with an appropriate atom number and temperature. We first cover the basics of magneto-optical trapping and compression (Section 3.1.1). The principle of absorption imaging, for measuring the properties of the cloud, is then detailed (Section 3.1.2). Temperature and atom number measurements are also shown and optimal laser frequencies determined.

3.1.1 Magneto-Optical Trapping

A magneto-optical trap (MOT) uses Doppler cooling and position dependent magnetic fields to cool and trap atoms. For Doppler cooling, light detuned by a small amount from an allowed energy transition in the atom is used. The atoms absorb photons of momentum $\hbar k$ from a directional laser beam, and then emit a photon of the same energy in a random direction. As after many such interactions the momentum gain from spontaneous emission will average zero, the net effect is a force due to radiation pressure in the direction of travel of the laser beam. In order to cool atoms in one dimension, a pair of counter-propagating laser beams must be used. The frequency must be red-detuned from (lower frequency than) the transition such that the atom sees the photons

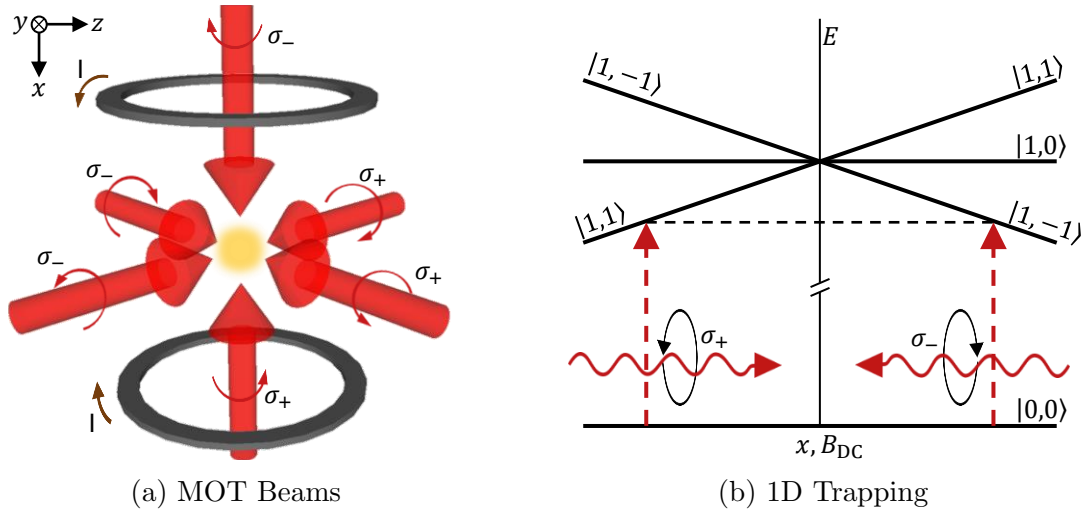


Figure 3.1: In (a) the light beams and currents I used for generating a 3D MOT are shown, with appropriate polarisations labelled. Due to perspective, axes are only indicative. The graph (b) illustrates the basic principle of a 1D MOT, showing the energy splitting of the different $|J, m_J\rangle$ levels as a function of position (which is proportional to static field), and the required counter-propagating laser beams. Adapted from [69].

at closer to its resonance frequency when moving in the opposite direction to the beam. As the likelihood of an atom absorbing a photon increases the closer the photon energy is to that of the atomic transition, atoms will preferentially absorb photons from the counter-propagating beam, giving the net effect of slowing the atom. The force in an optical molasses is given by

$$\mathbf{F} \approx -\mathbf{a}v, \quad \mathbf{a} = \frac{16\hbar k^2 \Omega^2 \Delta}{(\Gamma^2 + 4\Delta^2)^2}, \quad (3.1)$$

where Δ is the laser detuning, k is the angular wavenumber, Ω is the Rabi frequency and Γ is the damping coefficient [69, 128]. Applying three pairs of orthogonal laser beams will cool the atoms in all three dimensions, see Figure 3.1a. This will produce an optical molasses within the region of the laser beam overlap, but atoms will be lost over time due to diffusion from this region.

The application of a position dependent magnetic field allows the confinement of the cooled atoms, forming the MOT. The magnetic field gradient can be formed using anti-Helmholtz coils, which are a pair of identical circular coils centred on the same axis, running counter-propagating currents. The static field dependence of the magnetic sublevels m_F for weak B_{DC} is given by Eq. 2.13, and is of the form shown in Figure 3.1b for $J = 0, 1$. As σ_{\pm}

light excites transitions of $\delta m_J = \pm 1$ respectively, counter-propagating beams must be polarised with opposite rotational senses (but the same helicity) in order to excite the lowest energy transition either side of the field minimum. The magnetic field has the effect of breaking the symmetry of the molasses and significantly reducing the likelihood of atoms escaping from the cloud. The chosen transitions are used as their energies become closer to resonance with a red-detuned beam further from the field minimum, and are therefore more likely to receive a kick towards the centre of the cloud the further they are from this. Mathematically, this means the force in the MOT is position dependent according to

$$\mathbf{F}_{\text{MOT}} \approx -a\mathbf{v} - \frac{a\mathbf{b}}{k}x, \quad \mathbf{b} = \frac{g\mu_B}{\hbar} \frac{dB}{dx}. \quad (3.2)$$

For more details on the principles of a MOT, see [69, 128].

Other methods of generating a MOT are possible, including different magnetic field geometries and even blue-detuned methods [99], but the technique described here is arguably the simplest, and therefore the one used in this experiment. The only slight change from what is described previously is that ^{87}Rb has a more complicated level structure, although the basic principles are the same. For the cooling light, we require a closed transition, i.e. a transition where atoms excited to this level must decay back to their original state. Therefore the transition $F = 2 \rightarrow F'' = 3$ on the $D2$ -line is chosen for cooling, which is optimal due to the selection rules (Eq. 2.18) disallowing decay from $F'' = 3$ to $F = 1$ and therefore prohibiting direct losses from the cooling cycle. In a small fraction of instances, scattering can still allow the atoms to decay into the $F = 1$ state. Although the probability of this happening in a given cycle is low, the many cycles involved in cooling make the atom losses to the $F = 1$ dark state significant. The application of a repump beam resonant at the frequency of $F = 1 \rightarrow F'' = 2$ allows lost atoms to be readmitted to the cooling cycle by the possibility of decay back to $F = 2$.

The temperature of the MOT can be lowered further by changing the detuning of the cooler beam, forming a compressed MOT (CMOT) [136]. As the detuning increases, the near-resonant photon rescattering is reduced, causing the cloud to collapse and cool. Polarisation gradient cooling [115] may also play a part in reducing the temperature. The CMOT phase is a short (in our case 2 ms) ramp at the end of the much longer (~ 2 s) MOT time, so we begin with a sufficient number of atoms in the trap. Although a number of techniques can be used to lower the temperature of atom clouds much further, atoms from a MOT are sufficient for our purposes. Over the course of the CMOT phase, the cooler frequency detuning is ramped. The optimal final cooler detuning is found by scanning this value and maximising

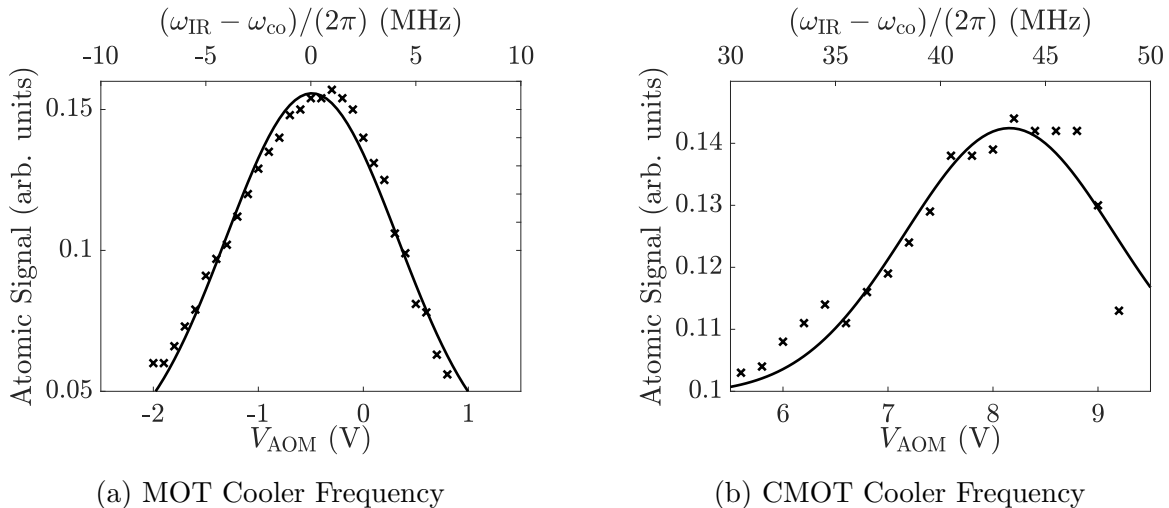


Figure 3.2: A scan of the frequency of the cooler beam during both the MOT and CMOT stages are shown in (a) and (b) respectively. The measured atomic signal is proportional to the atom number in the cloud. The repump laser frequency is similarly calibrated.

the final atom number, detected using the method described in Chapter 4. The initial cooler frequency ω_{co} is also calibrated in the same manner. An acousto-optic modulator (AOM, discussed in more detail in Section 5.1.1) allows the adjustment of the frequency of a laser beam. Figure 3.2a shows the calibration of the cooler frequency, with both the AOM control voltage and the corresponding frequency change marked. In Figure 3.2b we see that the final cooler frequency in the CMOT phase is measured to be (43 ± 2) MHz detuned from the initial cooler frequency, leading to an atom number decrease of $\sim 9\%$ in exchange for a reduction in cloud temperature, which will be measured in Section 3.1.2.

3.1.2 Imaging for Optimisation

Absorption imaging is the method of shining resonant light through an atomic cloud and imaging the outgoing light using a camera, in our case a charge-coupled device (CCD). As resonant light will be absorbed and then scattered by any atoms the beam path, the CCD will measure the shadow of the cloud. We use this technique in order to measure the temperature of the cloud and the number of atoms being trapped. In our experiment, this method is used for set-up purposes only, and does not form part of the main experimental sequence used for data taking; our more sophisticated two-state detection scheme used for these purposes is detailed in Chapter 4. The advantage of

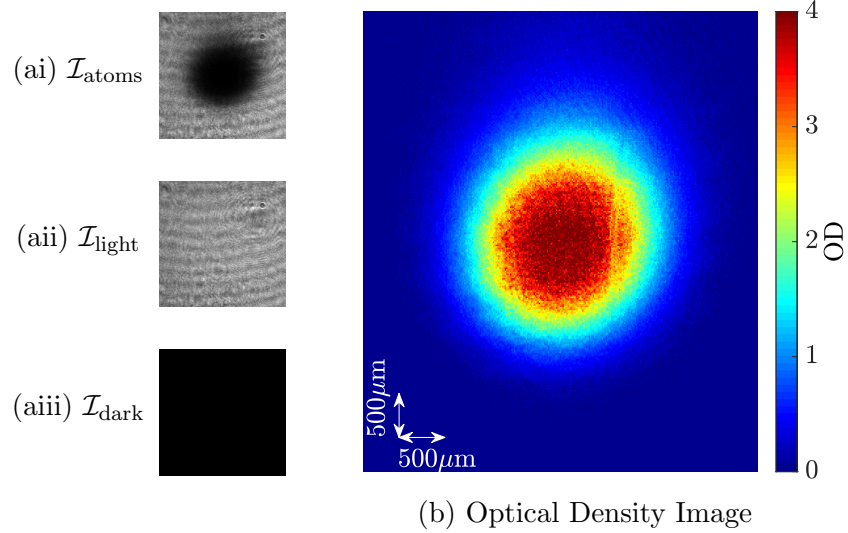


Figure 3.3: The absorption image (b) is calculated using Eq. 3.5, which combines the data in (ai), the image with atoms present, (aai) the image with light but no atoms and (aiii) the dark image. The colourmap of optical density in (b) runs from dark blue (no absorption) to red (maximum absorption).

absorption imaging is that it allows a 2D spatial image of the cloud, unlike the method described later which only gives the total atom fraction in a given state. In our experiment absorption imaging is performed using light on the $F = 2 \rightarrow F'' = 2$ $D2$ -line transition. This is the same transition as the cooler beams, but with no detuning.

A beam of light of intensity \mathcal{I} will be attenuated by $\frac{d\mathcal{I}}{dz} = -N\sigma_{sc}\mathcal{I}$ whilst travelling through a section of cloud with column density \mathbf{N} and scattering cross-section σ_{sc} . Integrating this over the length of the beam, we see that intensity of light hitting the CCD will be given by

$$\mathcal{I} = \mathcal{I}_0 e^{-\text{OD}} = \mathcal{I}_0 e^{-N\sigma_{sc}}, \quad (3.3)$$

where \mathcal{I}_0 is the initial intensity of the beam and OD is the optical density. Note that the latter equality is only true in the case where the image is not saturated, i.e. some fraction of light must be reaching the CCD through all regions of the cloud. The scattering cross section is given by

$$\sigma_{sc} = \frac{\sigma_0}{1 + 4(\Delta/\Gamma)^2 + \mathcal{I}/\mathcal{I}_{\text{sat}}}, \quad (3.4)$$

where σ_0 is the resonant cross-section, Δ is the detuning, \mathcal{I}_{sat} is the saturation intensity and Γ is the damping factor [69].

We measure the initial and final intensity of the beam using a CCD to take multiple images. The first image is taken with the imaging beam turned

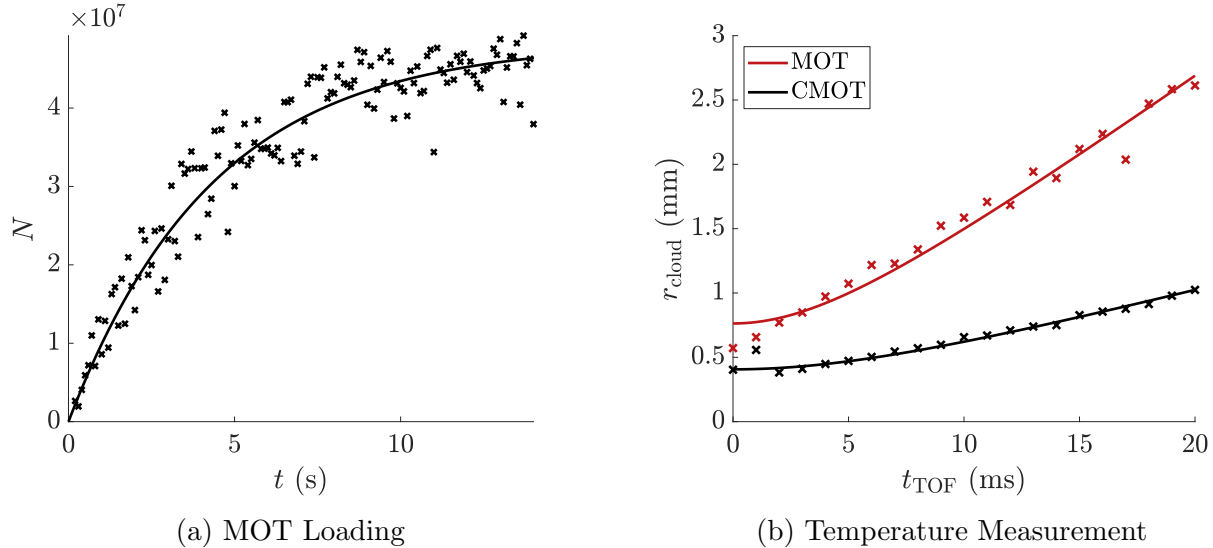


Figure 3.4: The final atom number after the CMOT phase is plotted in (a) as a function of the MOT duration, with a fit to Eq. 3.7 giving a maximum atom number of $N_{\max} = (4.83 \pm 0.08) \times 10^7$. The horizontal radius of the free-falling cloud is plotted as a function of time in (b), extracting the temperature $(170 \pm 30) \mu\text{K}$ for the MOT and $(23 \pm 1) \mu\text{K}$ for the CMOT using Eq. 3.8.

on whilst atoms are in the beam path, which has intensity $\mathcal{I}_{\text{atoms}}$. The second is after the atoms have fallen out of the beam path, with the imaging beam still on, giving $\mathcal{I}_{\text{light}}$. There may be some photons incident on the detector when the beam is off, so we also take an image of this $\mathcal{I}_{\text{dark}}$. We now have our optical density

$$\text{OD} = \ln \left(\frac{\mathcal{I}_{\text{light}} - \mathcal{I}_{\text{dark}}}{\mathcal{I}_{\text{atoms}} - \mathcal{I}_{\text{dark}}} \right) \quad (3.5)$$

for a single pixel. For more details see [148]. To obtain the atom number we then need to integrate over all pixels which have width $x_{\text{px}} = 5.6 \mu\text{m}$, accounting for the magnification $M = 1/3$, giving

$$N = \frac{x_{\text{px}}^2}{\sigma_0 M^2} \sum_{x,y} \text{OD}_{x,y}. \quad (3.6)$$

The three images: atoms, light and dark are shown in Figures 3.3ai-3.3aiii respectively, with the processed density image in Figure 3.3b. Using this method on the image, we calculate the atom number to be 1.28×10^8 . This was a particularly high atom number taken with relatively new ^{87}Rb dispensers, and most data in this thesis was taken with an atom number of the order of 10^7 , due to the ^{87}Rb dispensers reaching the end of their lifetime.

We can also use our absorption imaging technique to measure the MOT loading rate. The number of atoms will increase over time by

$$N = N_{\max}(1 - e^{-t/\tau}), \quad (3.7)$$

where N_{\max} is the maximum atom number reached after infinite time and τ is one over the loading rate. A graph of MOT loading time is shown in Figure 3.4a, with a value $N_{\max} = (4.83 \pm 0.08) \times 10^7$ and $\tau = (4.4 \pm 0.4)$ s. We choose a MOT time of ~ 2 s to have a sufficient atom number for most measurements, although this is increased when measuring particularly weak signals.

The temperature T of the cloud can then be obtained from the expansion rate of its horizontal radius r_{cloud} in free-fall [138], given by

$$r_{\text{cloud}} = \sqrt{\frac{k_B T t^2}{m} + r_0^2}. \quad (3.8)$$

For $r_{\text{cloud}} \gg r_0$ this can be obtained by setting the equipartition energy $\frac{1}{2}k_B T$ equal to the kinetic energy $\frac{1}{2}mv^2$; the full equation also accounts for the initial radius r_0 . In Figure 3.4b we plot r_{cloud} against t and measure a cloud temperature of (170 ± 30) μK for the MOT and (23 ± 1) μK for the CMOT.

3.2 Preparing a Pure Quantum State

The method of producing a pure $|F, \bar{m}\rangle$ substate is detailed in this section. The basics of microwave driving bare transitions is detailed in Section 3.2.1, along with appropriate calibrations. How microwave pulses are used in combination with infrared beams to produce the required atomic state is described in Section 3.2.2. Optical pumping, used for increasing the final atom number, is detailed in Section 3.2.3.

3.2.1 Bare Microwave Transitions

Transitions between different sublevels in the ground state of ^{87}Rb can be driven using multiple frequency regimes. Indirect transitions using infrared light, which occur via an excitation to and decay from an excited state in a different L -manifold, have already been explained in the context of a MOT (Section 3.1.1). Transitions and superposition states using radio-frequencies for couplings between magnetic sublevels for a fixed value F were the subject of Section 2.2. Now we consider driving bare transitions between F -levels $|1, m\rangle \leftrightarrow |2, m'\rangle$ using MW-frequencies (for coupling constants for these transitions see Table 6.2). When close enough to resonance with the transition,

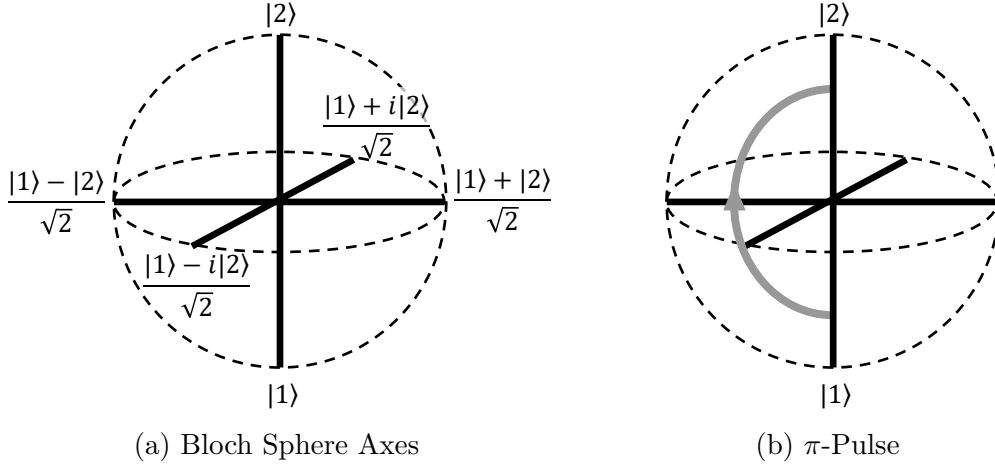


Figure 3.5: The Bloch sphere is a way of representing two level quantum systems. The axes of the sphere represent different superpositions of states, labelled in (a). In (b) we represent a π -pulse as a transition from the state represented by the dashed arrow to the state represented by the solid black arrow. The grey arrow indicates the MW-pulse which is driving this transition. Adapted from [69].

any such pair of sublevels can be treated as a two level system.

The Bloch sphere, shown in Figure 3.5, represents transitions between states in a quantum two level system as a geometric motion along the surface of a sphere. Each of the mutually orthogonal three axes through the sphere intersect with the surface at a location which represents a combination of the two states: $|1\rangle$, $|2\rangle$, $\frac{1}{\sqrt{2}}(|1\rangle \pm |2\rangle)$, $\frac{1}{\sqrt{2}}(|1\rangle \pm i|2\rangle)$, labelled in Figure 3.5a. The full surface represents all possible combinations of the two states, and as such can be used to represent transitions and superpositions. A transition which moves the atomic spin π radians about the Bloch sphere is known as a π -pulse (not to be confused with π -polarisation). This is shown Figure 3.5b, moving all atoms in $|1, m\rangle$ to $|2, m\rangle$ (in practice there will still be a negligible number of atoms remaining in the initial state), with atoms in other $F = 1$ sublevels unaffected.

In order to drive a single transition from each of the $|1, m\rangle$ states, we choose the set of π -polarised transitions $|1, m\rangle \leftrightarrow |2, m\rangle$. The transition frequency for $|1, 0\rangle \leftrightarrow |2, 0\rangle$ will be of fixed energy $E = \hbar\omega_{\text{HFS}}$, as both of the sublevels involved are independent of static field. Our static field is set as high as safely possible, in order to maximise the frequency difference between the three possible transitions. The initial frequency calibration for these transitions is performed by preparing the atoms in $F = 1$ using only the repump beam after the MOT phase. A MW-pulse is then applied, calibrated by scanning

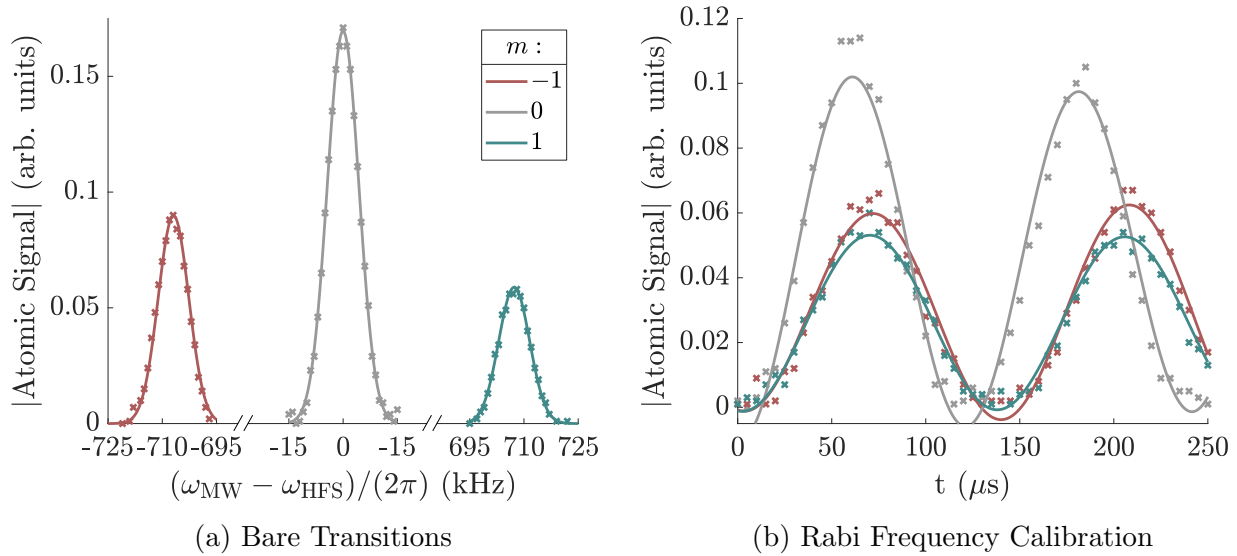


Figure 3.6: The transition frequency of the three bare π -polarised transitions is measured in (a) from a Gaussian fit to their spectroscopic peaks. The bare $m = -1, 0, 1$, $|1, m\rangle \leftrightarrow |2, m\rangle$ transitions are centred on the frequencies $(-707.0 \pm 0.1, 0.0 \pm 0.1$ and $707.3 \pm 0.2)$ kHz respectively, corresponding to $B_x = 0.51$ G. In (b) the Rabi-frequency is calibrated using a sine fit to the oscillation, giving the respective frequencies $\omega_{\text{Rabi}}/(2\pi) = (7.3, 8.3$ and $7.4)$ kHz, all ± 0.1 kHz. For all data $B_{\text{MW}} = 6$ mG.

the frequency and detecting the fraction of atoms transferred to $F = 2$. Using our two state detection method (described in Chapter 4) we can measure the atom fraction in $F = 2$. The peaks corresponding to the transitions can be seen in Figure 3.6a, at $(\omega_{\text{MW}} - \omega_{\text{HFS}})/(2\pi) = (\pm 707, 0)$ kHz, for the transitions $|1, m\rangle \leftrightarrow |2, m\rangle$ for $m = \pm 1, 0$ respectively. In the bare state only three π -polarised MW-transitions are possible, so we know these are the correct peaks. It should be noted that the data in this figure was taken with the full state preparation method described in the following section, but this only causes an increase in peak amplitude, and does not alter the frequencies.

With the MW-power set to the maximum safe value in our system, the length of the MW-pulse must also be calibrated in order to achieve maximum transfer of atoms into the desired state. We do this by measuring Rabi cycles between the two states, as shown in Figure 3.6b. We vary the length of the MW-pulse and detect the fraction of atoms in each of the F -levels over time, again using our two state detection method. We can fit a sinusoidal function to this variation, and the first peak, where the highest fraction of atoms is in $F = 2$, is our π -pulse duration. We measure from our data that the required

π -pulse time is (68, 60, 67) μs , all $\pm 0.1 \mu\text{s}$, for the transitions $|1, m\rangle \leftrightarrow |2, m\rangle$ for $m = -1, 0, 1$ respectively at the highest available output MW-probe power.

3.2.2 Shelving and State Cleaning

Now that we have calibrated the bare state π -polarised transitions, these can be used in combination with laser pulses in order to prepare a pure $|F, m\rangle$ state. In order to do this, we make use of a variant of a technique used in ion experiments [9, 131] known as ‘shelving’. Effectively, this means transferring some fraction of atoms into a non-interacting state for use later. In our case, such a procedure is performed using MW-transitions, combined with laser pulses for state cleaning. The internal state of the atoms at each point in the sequence is shown in energy level form in Figure 3.7. We begin with atoms in a MOT, followed by the CMOT phase, which both require a cooler and repumper beam (Figure 3.7a), as described in Section 3.1.1. This leaves atoms purely in $F = 2$, spread across all m -levels. We typically prepare atoms in $F = 1$ in our experiment, and to achieve this we then leave the cooler beam on but turn off the repump beam (Figure 3.7b) so all atoms accumulate in $F = 1$, as this is now a dark state. We then select the $|1, m\rangle$ level we wish to prepare, and apply a π -polarised MW-pulse resonant with $|1, m\rangle \leftrightarrow |2, m\rangle$, as calibrated in the previous section.

Our next step (Figure 3.7d) is to remove all atoms remaining in $F = 1$. We do this by reapplying the repump laser, transferring all atoms out of $F = 1$ and into $F = 2$, see Figure 3.7e. We then apply a second MW π -pulse, Figure 3.7e, so that we now have atoms only in $|1, m\rangle$ and the $F = 2$ sublevels. In order to make a pure $|1, m\rangle$ substate we must finally apply a single state cleaning beam, on the same $F = 2 \rightarrow F'' = 3$ transition as the cooler but now resonant with the transition. This beam causes multi-photon scattering, which will heat and accelerate the atoms in the $F = 2$ state and cause them to exit the atomic cloud region (Figure 3.7f).

We note that the cooler pulse and first π -pulse are not essential to be able to create a pure $|F, m\rangle$ state; simply starting with the atoms spread evenly over the $F = 2$ sublevels (i.e. turning off the cooler beam before the repumper at the end of the MOT stage) and then performing a single MW π -pulse followed by the $F = 2$ state cleaning will still produce the required state. The full procedure is used to increase the final atom number in the desired state, improving the value by at least a factor of 2. The choice of π -polarisation was made because the individual components of σ_{\pm} -polarisations cannot be produced separately, and so due to degenerate transitions we cannot drive atoms from the single state $|1, 0\rangle$ to a single $F = 2$ sublevel using this polarisation.

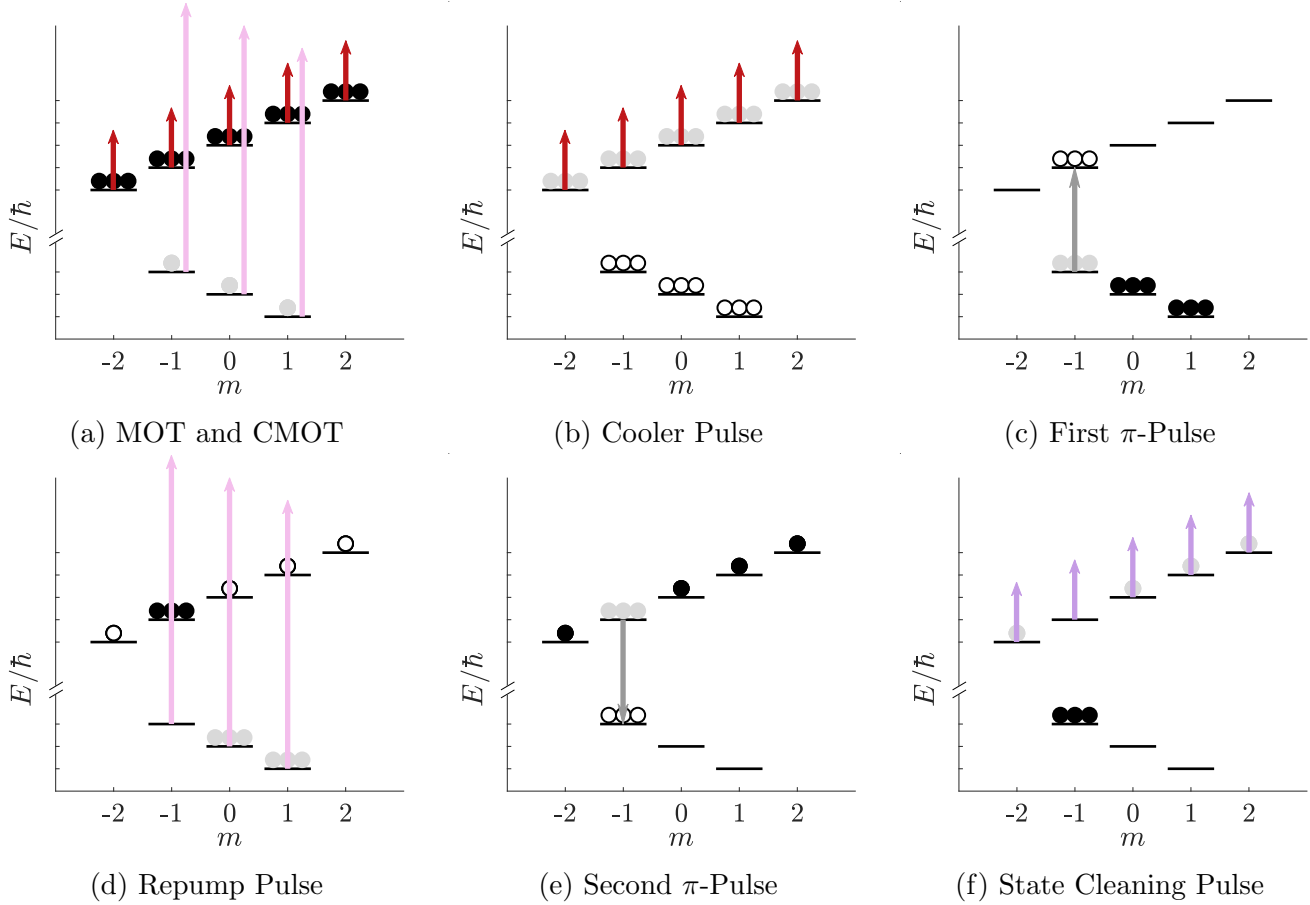


Figure 3.7: Stages of preparing a pure $|1, m\rangle$ state. White circles indicate atoms arriving a given state, and grey circles indicate atoms leaving the state during this step. The black circles represent levels which are populated both before and after this stage in the sequence, although in some cases atoms may move between populated levels. The first stage is the MOT and CMOT (a), which requires cooler (red) and repumper (pink) light, as described in Section 3.1.1. In (b) the repump light is turned off and the cooler transfers all atoms into $F = 1$. Next a $\pi/2$ MW-pulse (c) with π -polarisation is applied to transfer atoms $|1, m\rangle \rightarrow |2, m\rangle$. The repump beam (d) is then applied to move all atoms into $F = 2$. A second MW-pulse (e) identical to the first then transfers atoms $|2, m\rangle \rightarrow |1, m\rangle$, followed by (f) a resonant state cleaning beam (purple) which removes all atoms in $F = 2$ leaving only atoms in $|1, m\rangle$. The sequence is shown for preparing a $|1, -1\rangle$ state, but $m = 0, 1$ states can be generated in the same manner. Stages (b) and (c) are not compulsory, but are used to increase the final atom number in the desired state. An optional optical pump beam can be added in step (b) for increased atom number if preparing a $|1, 0\rangle$ state, see Figure 3.9. Adapted from [97].

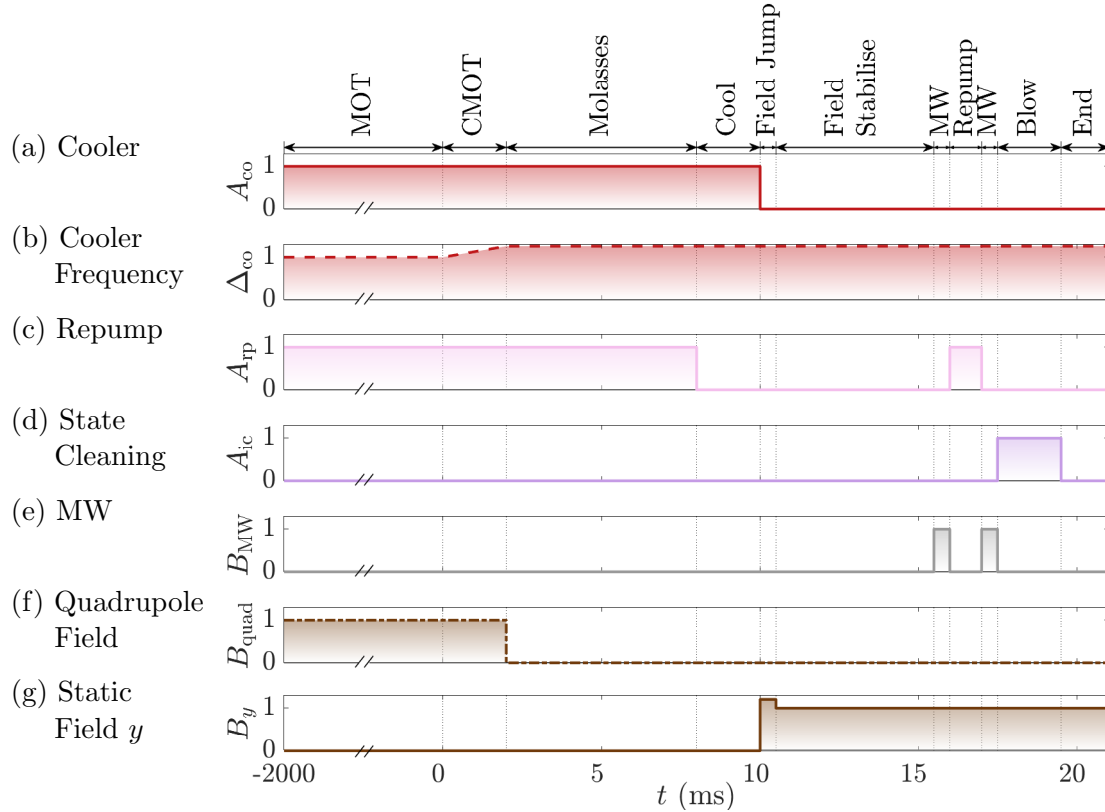


Figure 3.8: The figure shows when the various fields and beams are active during the state preparation process. The fields indicated are the set values, but ramping or jumping static fields will lead to oscillations in the output field amplitude. We start with a 2 s MOT phase with both the cooler and repumper active, before increasing the detuning of the cooler laser to form a CMOT. The quadrupole coils which are on during the MOT stages are then turned off, a gap of a few milliseconds allows the fields stabilise. We then turn off the repumper to produce an $F = 1$ state, followed by jumping the static field in the y -direction and allowing this to stabilise. This then puts us in the correct field orientation to perform the rest of the state preparation sequence as given in Figures 3.7c-3.7f. Adapted from [97].

If we wish to produce a pure $|2, m\rangle$ substate, we can produce a $|1, m\rangle$ state as described previously, then perform a MW π -pulse to $F = 2$. For a state $|2, |m| \leq 1\rangle$ a π -polarised MW is still applicable using the transition $|1, m\rangle \rightarrow |2, m\rangle$, but for a state $|2, \pm 2\rangle$ we must instead use σ_{\pm} -polarised MW on either the transition $|1, -1\rangle \rightarrow |2, -2\rangle$ or $|1, 1\rangle \rightarrow |2, 2\rangle$. There may still be some small residual population in the $|1, m\rangle$ state however, due to slight MW-power or static field fluctuations leading to an imperfect π -pulse.

A full graph summarising the stages of the state preparation sequence is given in Figure 3.8, showing all non-zero fields. The sequence is performed using a custom LabView control program, connected to a National Instruments field-programmable gate array, which has a large number of both analog and digital outputs used to control all triggered electronics. In addition to the transitions discussed above, it is important to be able to control the magnetic fields during the sequence. The colours of the lines in the figure correspond to those in Figure 3.7, with the addition of brown lines for static fields. The cooler (solid red) and repumper (pink) are on during the 2 s MOT time, as are the quadrupole coil fields (dot-dashed brown). The cooler frequency (dashed red) is then ramped closer to resonance during the 2 ms CMOT stage. The quadrupole fields are then shut off, and the static field allowed to stabilise for 6 ms. For a further 2 ms the cooler beam is left on to pump the atoms into $F = 1$, with the repumper switched off. We then also turn off the cooler and jump the static field in y (solid brown) for 0.5 ms before dropping this down to the desired value in order to damp field oscillations (this will be explained in Section 5.2.2). The fields are then allowed to stabilise for 5 ms before the first MW π -pulse. This is a purely π -polarised MW-field as the static field in z is zero. Axes are as defined in Figure 3.1a, and field orientations and their relevance to MW-polarisation will be discussed in Section 6.1.1.

In our state preparation sequence, short (60 μ s) MW-pulses are used at the maximum safe MW-probe power. However a lower power, longer (0.5 ms) MW-pulse (grey) is shown in Figure 3.8e for ease of viewing. The first pulse is then followed by 1 ms of repumping into $F = 2$, and then another identical MW-pulse. We then pulse the state cleaning beam (purple) to remove the remaining $F = 2$ population. A pure state $|F, m\rangle$ is then prepared and ready for state probing and detection, as desired. The method of pulsing the laser powers will be discussed in Section 5.1.

3.2.3 Optical Pumping

Another method of improving the final atom number during the state preparation sequence is optical pumping. This is the process of transferring atoms between energy levels by the application of light, typically of visible or near visible frequencies, in order to couple between L -manifolds. In this case we are using IR light on the ^{87}Rb $D1$ -line, specifically the $F = 1 \rightarrow F' = 1$ transition. In contrast to the single MW-transitions driven during our state preparation sequence, optical pumping can address multiple m -levels simultaneously, and relies on the presence of atomic dark states. Dark states are generated by applying light which can only cause transitions from certain states, leaving others unaffected. For instance σ_+ or σ_- polarised light can be

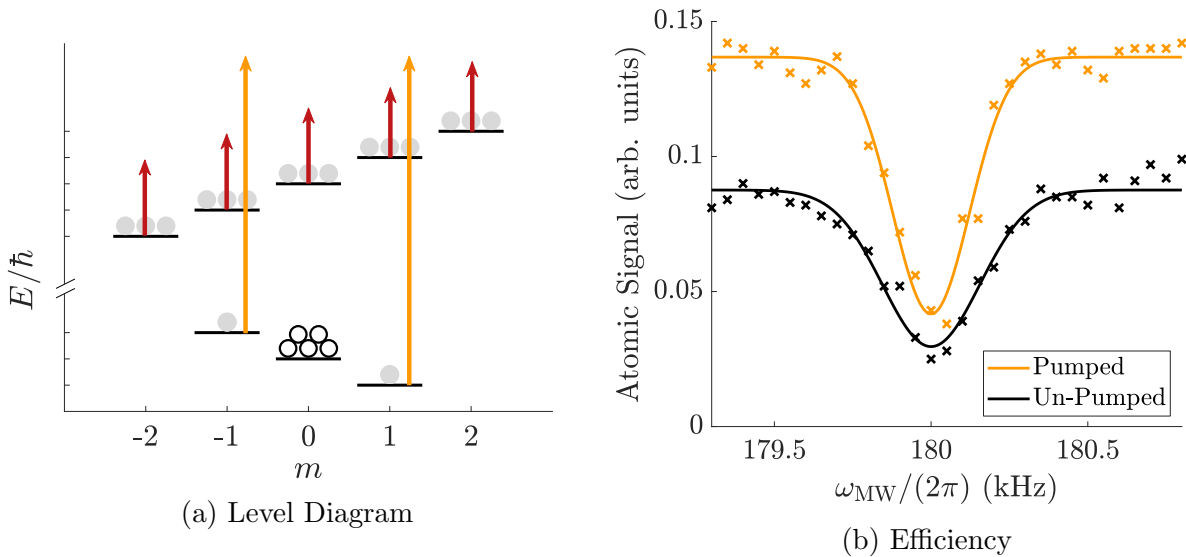


Figure 3.9: In the energy level diagram (a) the optical pump (orange) and cooler (red) transitions are marked. Grey circles indicate levels atoms are being removed from, and white circles show the final location of the atoms, which accumulate in the $|1, 0\rangle$ dark state. This replaces the Figure 3.7b in the full preparation sequence if preparing an $m = 0$ state. Adapted from [97]. In (b) a scan of the transition between dressed levels $|1, 0\rangle \rightarrow |2, 0\rangle$ is shown, illustrating the increase in atom number in the initial prepared $|1, 0\rangle$ state of $(56 \pm 5)\%$ and in the amplitude of the detected peak by $(64 \pm 8)\%$.

used for optically pumping into a state $|m_2| > \max(|m_1|)$ [87]. The method we are using relies on the fact that transitions $|F = 1, m = 0\rangle \leftrightarrow |F' = 1, m' = 0\rangle$ are forbidden by selection rules. We pump atoms with a π -polarised laser from $|F = 1, m = \pm 1\rangle$ into $|F' = 1, m' = \pm 1\rangle$, where some fraction of the time they will decay into the dark state $m = 0$. Figure 3.9a is the optical pumping energy level diagram, where the optical pump beam is shown in orange. The cooler beam (red) must also be active to prevent the formation of a dark state in $F = 2$. The improvement in atom number in the desired state is illustrated in Figure 3.9b, which shows the $F = 1$ detected signal when scanning the frequency of the probe MW across the dressed transition $|1, -1\rangle \rightarrow |2, 1\rangle$, starting with a pure $|1, -1\rangle$ state. We see in the figure that the amplitude of the optically pumped signal is now bigger by $(56 \pm 2)\%$.

Chapter 4

Birefringent Detection

In this chapter our two state detection method is described, as enabled by the radio-frequency dressing. This detection scheme was developed by the previous PhD student working on this experiment, and is detailed in her thesis [97], as well as in a paper on the topic [98]. An overview of the principles of the scheme, including the light-matter interaction and subsequent signal processing, is given in Section 4.1. The practicalities of the experimental method are detailed in Section 4.2. How we have upgraded the system in order to provide common mode suppression, cancelling the effects of laser power noise, is also described in the section.

4.1 Linear Birefringence

A material is birefringent if it has a refractive index that varies depending on both the polarisation and the direction of propagation of light passing through it. By utilising the linear birefringence properties of an atomic cloud, the number of atoms in a given F -level can be measured. Measuring the population of atoms in each of the possible hyperfine sublevels, we can establish the internal state of the atom. Such a detection method enables a dispersive measurement of the atomic state. In Section 4.1.1 the interaction between light and matter is described. With the use of Stokes vectors (Section 4.1.2), we can find the strength of the polarisation change caused by individual atomic states.

The circular birefringence properties of a material have been understood since the 1840s, with the discovery of the Faraday effect [159], the rotation of the polarisation of a beam of light when passed through a material in the presence of a magnetic field. Specifically, the magnetic field must be aligned in the direction of light propagation for this effect to occur. Many sensing schemes have been developed which utilise this circular birefringence [49, 108], including for taking quantum non-demolition measurements [111]. Correspondingly

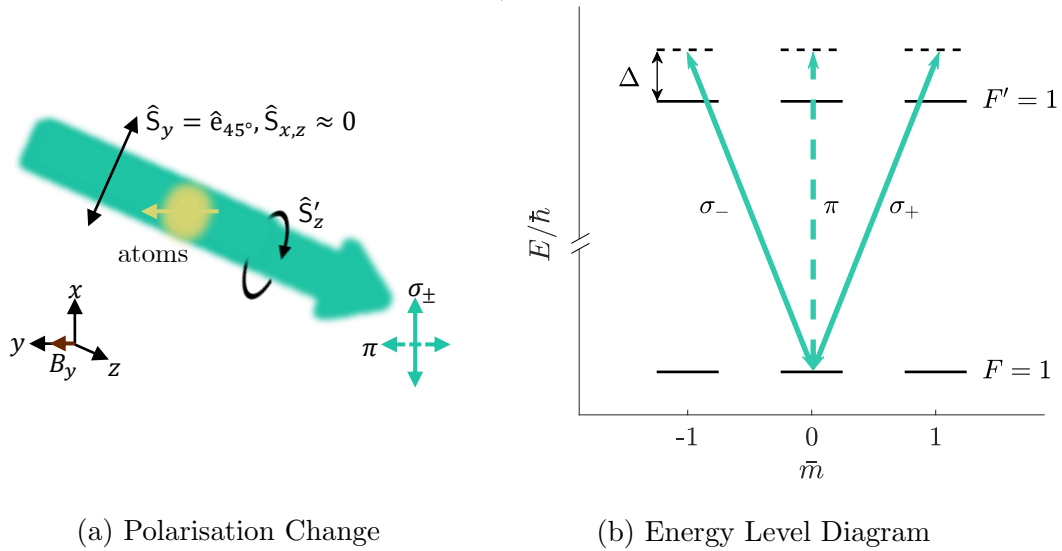


Figure 4.1: Passing detuned light through a cloud of atoms, a shift in the polarisation can occur. This is illustrated for the Voigt effect in (a), where light linearly polarised in a 50 : 50 superposition of σ_{\pm} and π passes through the atomic cloud and shifts to elliptical polarisation. \hat{S} are the Stokes vectors, which define the polarisation state of the light. A simplified level scheme is shown in (b) illustrating how an atom can display linear birefringence with light detuned by Δ from a D -line transition. The π -polarised transition in the figure is forbidden by the standard selection rules, so light of this polarisation does not interact with the atoms, whereas the orthogonally polarised σ_{\pm} light may, leading to a shift in polarisation. Adapted from [98].

for perpendicularly polarised light, the Voigt effect relies on linear birefringence [162]. In this section, the basic principles of the linear birefringence detection method are explained, and the relevant Hamiltonian and detection strengths shown.

The principle of atomic linear birefringence is illustrated in Figure 4.1a, where light polarised in an equal superposition of π and σ_{\pm} passes through a medium, in this case an atomic cloud, and shifts from linear to elliptical polarisation. A simple energy level scheme is shown in Figure 4.1b to illustrate how this is possible. Recalling the standard selection rules (Eq. 2.18), we know that the transition $|F = 1, 0\rangle \rightarrow |F' = 1, 0\rangle$ is forbidden. Therefore, if we have atoms prepared in a pure $|F = 1, 0\rangle$ state and apply π -polarised light, this cannot interact with a transition and therefore is unaffected by the atomic cloud. However, the σ_{\pm} -transitions to $m = \pm 1$ are not forbidden, and therefore near resonant light will interact with the cloud. As only a part of the light can interact with the atoms, the polarisation of the beam will shift

from linear to elliptical polarisation, and from this shift we can establish the atom number in the relevant state. In order to establish the dependence of the polarisation change on both atom number and atomic state, we must study the atom-light interaction. This is a relatively brief explanation of the topic, as it has been described in more detail in [98, 104], from which we will be working in this section.

4.1.1 Effective Hamiltonian

A laser beam passing through an atomic cloud can be described by summing over the Hamiltonian of all atoms j in the beam path

$$H_{\text{int}} = - \sum_j \hat{\mathbf{d}}_j \cdot \hat{\mathbf{E}}(\hat{\mathbf{r}}_j), \quad (4.1)$$

where $\hat{\mathbf{d}}$ is the atomic dipole moment and $\hat{\mathbf{E}}$ is the electric field. In order to calculate this Hamiltonian, we require the quantised electric field [39]

$$\mathbf{E} = \mathbf{E}_0 \left(\hat{a}_+ \hat{\mathbf{e}}_+ + \hat{a}_+^\dagger \hat{\mathbf{e}}_+^* + \hat{a}_- \hat{\mathbf{e}}_- + \hat{a}_-^\dagger \hat{\mathbf{e}}_-^* \right), \quad (4.2)$$

where \hat{a}_\pm are the creation and annihilation operators, which are dependent time and position. \mathbf{E}_0 is the electric field amplitude and $\hat{\mathbf{e}}_\pm$ are the unit vectors as defined in Eq. 2.20. We define the beam to be travelling in the z -direction without loss of generality. The dipole moment is given by

$$\hat{\mathbf{d}} = -e\hat{\mathbf{r}} = -e(\hat{\mathbf{e}}_+ \hat{r}_+ + \hat{\mathbf{e}}_0 \hat{r}_0 + \hat{\mathbf{e}}_- \hat{r}_-), \quad (4.3)$$

with $r_\pm = (-iy \pm x)/\sqrt{2}$ and $r_0 = z$. For the transition $|F, m\rangle \rightarrow |F', m'\rangle$, the separate components of the dipole moment can be defined as

$$\mathbf{d}_{F,m,F',m'}^\sigma = -e \langle F, m | r^{-\sigma} | F', m' \rangle \quad (4.4)$$

for each of $\sigma = \sigma_\pm, \pi$. Only atoms in the relevant states where the light is sufficiently near resonance with a transition will interact. We therefore need to include terms dependent on the density matrix $\hat{\rho}_{F,m,F',m'}$, which accounts for the probability of the atom being in such a state, and is a function of both z and t . This gives a total dipole operator

$$\hat{\mathbf{d}} = \sum_{\mathbf{k}} (\mathbf{d}_{\mathbf{k}}^- \hat{\mathbf{e}}_+^* + \mathbf{d}_{\mathbf{k}}^0 \hat{\mathbf{e}}_0^* + \mathbf{d}_{\mathbf{k}}^+ \hat{\mathbf{e}}_-^*) \hat{\rho}_{\mathbf{k}} + \text{h.c.}, \quad (4.5)$$

where the sum \mathbf{k} is over all two level systems $|F, m\rangle \leftrightarrow |F', m'\rangle$. In order to simplify the calculation we can move from individually summing over each atom to summing over regions of space, i.e.

$$\hat{\rho}_{\mathbf{k}} = \frac{1}{\varrho \text{Ad}z} \sum_j \hat{\rho}_{\mathbf{k}}^j(t), \quad (4.6)$$

where ρ is the density of atoms, A is the area of the beam and j is all atoms in the region from z to $z + dz$. The interaction Hamiltonian can therefore be calculated to be

$$\hat{H}_{\text{int}} = E_0 \sum_{\mathbf{k}} \int_0^l (\mathbf{d}_{\mathbf{k}}^+ \hat{a}_+ + \mathbf{d}_{\mathbf{k}}^- \hat{a}_-) \hat{\rho}_{\mathbf{k}} \rho A dz + \text{h.c.}, \quad (4.7)$$

with \mathbf{k} as in Eq. 4.5 and l as the length of the atomic cloud in the z -direction. The non-interacting part of the Hamiltonian must also be accounted for, which integrating over the whole region of the cloud will be given by

$$\hat{H}_{\text{atoms}} = \sum_{F', m'} \int_0^l \hbar \omega_{F', m'} \hat{\rho}_{F', m', F', m'} \rho A dz, \quad (4.8)$$

where the energy of the upper level of the atom $\hbar \omega_{F', m'}$ can be calculated from Eq. 2.6, and can be written as $\hbar \omega_{F', m'} = \hbar(\omega_{\text{IR}} + \Delta_{F'})$, where $\Delta_{F'}$ is the relevant detuning. The interaction and atomic Hamiltonians are then combined to obtain the total Hamiltonian

$$\hat{H}_{\text{tot}} = \hat{H}_{\text{int}} + \hat{H}_{\text{atoms}}. \quad (4.9)$$

We are working in the off-resonant limit, i.e. the laser light is sufficiently far detuned from any transition so as to not drive population transfer. Considering the coherence $\hat{\sigma}_{F, m-1, F', m}$, the time evolution can be calculated using the Heisenberg equation [127]

$$\frac{\partial \hat{\rho}_{F, m-1, F', m}}{\partial t} = \frac{1}{i\hbar} \left[\hat{\rho}_{F, m-1, F', m}, \hat{H} \right], \quad (4.10)$$

recalling that all values $\hat{\rho}$ and \hat{a}_{\pm} are functions of z and t . Using $\langle m | m' \rangle = \delta_{m, m'}$ and the definition of the density operator $\hat{\rho}_{m_1, m_2} = |m_1\rangle \langle m_2|$, we see that

$$\hat{\rho}_{m_1, m_2} \hat{\rho}_{m_3, m_4} = \hat{\rho}_{m_1, m_4} \delta_{m_2, m_3}. \quad (4.11)$$

This allows us to calculate

$$\begin{aligned} \frac{\partial \hat{\rho}_{F, m-1, F', m}}{\partial t} = & -i(\omega_0 + \Delta_{F'}) \hat{\rho}_{F, m-1, F', m} - \frac{E_0}{\hbar} \left(i \mathbf{d}_{F, m-1, F', m}^+ \hat{a}_+ \hat{\rho}_{F, m-1, F', m-1} \right. \\ & \left. + i \mathbf{d}_{F, m+1, F', m}^- \hat{a}_- \hat{\rho}_{F, m-1, F', m+1} \right), \end{aligned} \quad (4.12)$$

where terms with population in the excited states have been set to zero. To move to the rotating frame, we require the definition of our slowly varying operators

$$\hat{\rho}_{F, m-1, F', m} = \bar{\rho}_{F, m-1, F', m} e^{-i\omega_0 t} \quad \hat{a}_{\pm} = \bar{a}_{\pm} e^{-i\omega_0 t}. \quad (4.13)$$

The only difference between the time dependence of $\hat{\rho}$ and $\bar{\rho}$ is that the term $-i\omega_0 \hat{\rho}$ is not present in the latter, as it is included in the definition. As the

oscillation of $\bar{\rho}$ is much slower than that of $\Delta_{F'}$, this allows the adiabatic approximation $\partial\hat{\rho}_{F,m-1,F',m}/\partial t = 0$. We then rearrange Eq. 4.12 to get the result

$$\begin{aligned}\hat{\rho}_{F,m-1,F',m} &= -\frac{E_0}{\hbar\Delta_{F'}}(\mathbf{d}_{F,m-1,F',m}^+\bar{a}_+\hat{\rho}_{F,m-1,F,m-1} + \mathbf{d}_{F,m+1,F',m}^-\bar{a}_-\hat{\rho}_{F,m-1,F,m+1}), \\ \hat{\rho}_{F,m+1,F',m} &= -\frac{E_0}{\hbar\Delta_{F'}}(\mathbf{d}_{F,m+1,F',m}^-\bar{a}_-\hat{\rho}_{F,m+1,F,m+1} + \mathbf{d}_{F,m-1,F',m}^+\bar{a}_+\hat{\rho}_{F,m+1,F,m-1}),\end{aligned}\tag{4.14}$$

where we have treated $\partial\hat{\rho}_{F,m+1,F',m}/\partial t$ in the same manner. These values can now be substituted into Eq. 4.9. Assuming negligible population in the upper state, we find that

$$\begin{aligned}\hat{H}_{\text{tot}} &= \hbar \sum_m \int_0^l \left((C^+ \hat{a}_+^\dagger \hat{a}_+ + C^- \hat{a}_-^\dagger \hat{a}_-) \hat{\rho}_{F,m,F,m} \right. \\ &\quad \left. + \mathbf{b} \left(\hat{a}_-^\dagger \hat{a}_+ \hat{\rho}_{F,m+1,F,m-1} + \hat{a}_+^\dagger \hat{a}_- \hat{\rho}_{F,m-1,F,m+1} \right) \right) \varrho \mathbf{A} dz.\end{aligned}\tag{4.15}$$

This is only true for time scales $t \gg 1/\Delta_{F'}$ due to our adiabatic elimination. The new coefficients

$$C^\pm = -2\frac{E_0^2}{\hbar} \sum_{F'} \frac{(\mathbf{d}_{F,m,F',m\pm 1}^\pm)^2}{\Delta_{F'}}, \quad \mathbf{b} = -2\frac{E_0^2}{\hbar} \sum_{F'} \frac{\mathbf{d}_{F,m,F',m-1}^+ \mathbf{d}_{F,m,F',m+1}^-}{\Delta_{F'}},\tag{4.16}$$

have been introduced. In order to calculate these, we require the definition of the relevant dipole moment

$$\begin{aligned}\mathbf{d}_{F,m\pm 1,F',m}^\pm &= (-1)^{J+I-F'-F+m\pm 1} \sqrt{(2F+1)(2F'+1)(2I+1)} \\ &\quad \times \begin{pmatrix} F & 1 & F' \\ m \pm 1 & \pm 1 & -m \end{pmatrix} \begin{Bmatrix} F & F' & 1 \\ J' & J & I \end{Bmatrix} \langle J \| e\hat{r} \| J' \rangle.\end{aligned}\tag{4.17}$$

The term in the large round brackets is the Wigner 3j symbol, as defined in Eq. A.26, and the term in curly brackets is the Wigner 6j symbol, defined in [127]. In this work, we are only interested in the relative strength of the detected signal for each magnetic sublevel m , and therefore only concern ourselves with the Wigner 3j symbol, bundling all other factors into a value only dependent on F . The m dependent terms are

$$\begin{pmatrix} F & 1 & F' \\ m \pm 1 & \pm 1 & -m \end{pmatrix} \propto \begin{cases} (F \pm m + 1)(F \pm m + 2) & : F' = F - 1 \\ (F \mp m)(F \pm m + 1) & : F' = F \\ (F \mp m)(F \mp m - 1) & : F' = F + 1 \end{cases}\tag{4.18}$$

We now only consider possible transitions on the ^{87}Rb $D1$ -line, which has possible values $F = 1, 2$ and $F' = 1, 2$. For a full derivation of the constants for

^{87}Rb , see [97]. In calculating \mathcal{C}^\pm , we treat the $F = 1$ and 2 values separately, and only consider population in the ground state F -manifold. Therefore, introducing the new constants \mathcal{C} we obtain

$$\begin{aligned}\mathcal{C}_{F=1}^\pm &= \mathcal{C}_F((F(F+1) \mp m - m^2) \\ &\quad + \mathcal{C}_{F+1}((F+1)(F+2) \pm (2F+3)m + m^2)) \\ \mathcal{C}_{F=2}^\pm &= \mathcal{C}_{F-1}(F(F-1) \mp (2F-1)m - m^2) \\ &\quad + \mathcal{C}_F(F(F+1) \mp m - m^2)\end{aligned}\quad (4.19)$$

for the ground state of ^{87}Rb , where \mathcal{C}_F depend only on the value F . In order to simplify further, we can treat this purely as a sum of terms in m :

$$\mathcal{C}_F^\pm = -\alpha_0(\alpha_F^{(0)} + \alpha_F^{(\pm 1)}m + \alpha_F^{(2)}m^2), \quad (4.20)$$

where α_F are the polarisability coefficients, and the value α_0 is an overall scale factor. The polarisability of a medium is defined as the magnetic dipole moment induced per unit applied electric field [174]. In our case this is effectively a measure of how much an atomic cloud is altered by an applied laser beam, and is a function of the detuning of the laser from a transition. The coefficient \mathbf{b} can also be established using Eq. 4.18. Regardless of whether $F' = F \pm 1$ or F , the proportionality

$$\mathbf{d}_{F,m,F',m-1}^+ \mathbf{d}_{F,m,F,m+1}^- \propto \sqrt{\frac{(F+m)(F+m+1)}{(F-m)(F-m+1)}} \quad (4.21)$$

is true. We therefore obtain the value

$$\mathbf{b} = -\alpha_0 \alpha_F^{(2)} \sqrt{(F+m)(F+m+1)(F-m)(F-m+1)}, \quad (4.22)$$

where the values α_0 and $\alpha_F^{(2)}$ are the same as in Eq. 4.20. This is because we have extracted the m dependent terms in Eq. 4.17, and other terms in the dipole moments \mathbf{d}^\pm are identical.

Substituting in for these values in Eq. 4.15 gives the Hamiltonian

$$\begin{aligned}\hat{H}_{\text{tot}} &= -\alpha_0 \int_0^l \left(\alpha_F^{(0)} (\hat{a}_+^\dagger \hat{a}_+ + \hat{a}_-^\dagger \hat{a}_-) \sum_m \hat{\rho}_{m,m} \right. \\ &\quad + \alpha_F^{(1)} (\hat{a}_+^\dagger \hat{a}_+ - \hat{a}_-^\dagger \hat{a}_-) \sum_m m \hat{\rho}_{m,m} \\ &\quad + \alpha_F^{(2)} ((\hat{a}_+^\dagger \hat{a}_+ + \hat{a}_-^\dagger \hat{a}_-) \sum_m m^2 \hat{\rho}_{m,m} \\ &\quad + \sqrt{(F+m)(F-m)(F+1+m)(F+m-1)} \\ &\quad \left. \times (\hat{a}_-^\dagger \hat{a}_+ \sum_m \hat{\rho}_{m+1,m-1} + \hat{a}_+^\dagger \hat{a}_- \sum_m \hat{\rho}_{m-1,m+1}) \right) \rho \text{Ad}z,\end{aligned}\quad (4.23)$$

where we have used the notational simplification $\hat{\rho}_{F,m,F',m'} = \hat{\rho}_{m,m'}$ and the values α_F can be found in [97]. We now have the total Hamiltonian of the atom-light interaction. As our observable is the polarisation of the detection beam, this requires conversion to a more appropriate form.

4.1.2 Stokes Operator Form

We now introduce the Stokes operators \hat{S} , which are vector representations of the polarisation of light, of the same form as \hat{F} in Eq.s A.24 and A.25. We can also represent these in the alternative form

$$\begin{aligned}\hat{S}_x &= \frac{\hbar}{2}(\hat{a}_-^\dagger \hat{a}_+ + \hat{a}_+^\dagger \hat{a}_-), \\ \hat{S}_y &= \frac{i\hbar}{2}(\hat{a}_-^\dagger \hat{a}_+ - \hat{a}_+^\dagger \hat{a}_-), \\ \hat{S}_z &= \frac{\hbar}{2}(\hat{a}_+^\dagger \hat{a}_+ - \hat{a}_-^\dagger \hat{a}_-),\end{aligned}\tag{4.24}$$

where the ladder operators are given by $\hat{a}_+^\dagger = (1, 0)$ and $\hat{a}_-^\dagger = (0, 1)$. We also require the operators in circular form

$$\begin{aligned}\hat{S}_+ &= \hat{S}_x + i\hat{S}_y = -\hat{a}_+^\dagger \hat{a}_-, \\ \hat{S}_- &= \hat{S}_x - i\hat{S}_y = -\hat{a}_-^\dagger \hat{a}_+,\end{aligned}\tag{4.25}$$

and the atom number

$$N = \hat{a}_+^\dagger \hat{a}_+ + \hat{a}_-^\dagger \hat{a}_-.\tag{4.26}$$

If we wish to convert the Hamiltonian for our atom-light interaction into purely vector form, and hence establish the dependence of the Stokes operators on total angular momentum, we also require the relationships between \hat{F} and $\hat{\rho}$, quantising along the z -axis. Working from the definition of the ladder operators \hat{F}_\pm (Eq. A.5) and their eigenvalue (Eq. A.16), we can work backwards to obtain the eigenvalues of the Cartesian \hat{F} values. \hat{F}_z comes from rearranging Eq. A.18. Combining and rearranging these two pairs of equations, and simplifying using Eq. 4.11, gives

$$\begin{aligned}\hat{F}_x &= \frac{\hbar}{2} \sum_m \sqrt{F(F+1) - m(m+1)} (\hat{\rho}_{m+1,m} + \hat{\rho}_{m,m+1}), \\ \hat{F}_y &= -\frac{i\hbar}{2} \sum_m \sqrt{F(F+1) - m(m+1)} (\hat{\rho}_{m+1,m} - \hat{\rho}_{m,m+1}), \\ \hat{F}_z &= \hbar \sum_m m \hat{\rho}_{m,m}\end{aligned}\tag{4.27}$$

and

$$\hat{F}_\pm = i\hbar \sum_m \sqrt{F(F+1) - m(m\pm 1)} \hat{\rho}_{m\pm 1, m}, \quad (4.28)$$

where in the \hat{F}_- component we have redefined $m \rightarrow m-1$, as we are summing over all values of m regardless.

Substituting for the relevant Stokes operators and $\hat{f} = \hat{F}/\hbar$ vectors into Eq. 4.23, this simplifies to

$$\hat{H}_{\text{tot}} = -\alpha_0 \int_0^l \left(\alpha_F^{(0)} N + \alpha_F^{(1)} \hat{S}_z \hat{f}_z + \alpha_F^{(2)} (N \hat{f}_z^2 - \hat{S}_- \hat{f}_+^2 - \hat{S}_+ \hat{f}_-^2) \right) \rho \text{Ad}z. \quad (4.29)$$

We can then obtain the Cartesian form

$$\begin{aligned} \hat{H}_{\text{tot}} = -\alpha_0 \int_0^l \left(\alpha_F^{(0)} N + \alpha_F^{(1)} \hat{S}_z \hat{f}_z + \alpha_F^{(2)} (N \hat{f}_z^2 \right. \\ \left. - \hat{S}_x (\hat{f}_x^2 - \hat{f}_y^2) - \hat{S}_y (\hat{f}_x \hat{f}_y - \hat{f}_y \hat{f}_x) \right) \rho \text{Ad}z, \end{aligned} \quad (4.30)$$

by substituting in for $\hat{f}_\pm = \hat{f}_x \pm i\hat{f}_y$ and \hat{S}_\pm from Eq. 4.25.

In order to find the change in the z component of the Stokes operator, we once again require the use of the Heisenberg equation $\partial \hat{S}/\partial z = [\hat{S}, \hat{H}]/(i\hbar c)$ and the commutation relations, the same as for F in Eq. A.2. We are approximating the time dependence as zero, and are only considering spatial variation. This gives us

$$\frac{\partial \hat{S}_z}{\partial z} = \alpha_0 \alpha_F^{(2)} (\hat{S}_y (\hat{f}_x^2 - \hat{f}_y^2) - \hat{S}_x (\hat{f}_x \hat{f}_y + \hat{f}_y \hat{f}_x)) \quad (4.31)$$

for the polarisation change in the relevant direction. In order to observe the Voigt effect, we use light polarised with $\hat{S}_{x,z} \approx 0$ and at 45° in \hat{S}_y . As our shift is purely on \hat{S}_z , we see that

$$\hat{S}'_z = \hat{S}_z + \mathbf{g}_F^{(2)} \int_0^l (\hat{f}_x^2 - \hat{f}_y^2) \rho \text{d}z, \quad (4.32)$$

where the constant $\mathbf{g}_F^{(2)} = \omega \mathbf{s}_y \alpha_F^{(2)} / (2\epsilon_0 c)$ is calculated in [98], and includes the photon flux of light of the relevant polarisation \mathbf{s}_y . The total polarisation change due to the atomic cloud will therefore be given by

$$\langle \hat{S}'_z \rangle = \mathbf{g}_F^{(2)} N_m \langle \hat{F}_x^2 - \hat{F}_y^2 \rangle, \quad (4.33)$$

where N_m is the atom number in the relevant state and we have discounted the \hat{S}_z term due to our choice of initial polarisation. From Eq. 4.27, we calculate

that

$$\begin{aligned}\hat{F}_x^2 &= \frac{\hbar^2}{2} \sum_m (F(F+1) - m^2) \hat{\rho}_{m,m}, \\ \hat{F}_y^2 &= \frac{\hbar^2}{2} \sum_m (F(F+1) - m^2) \hat{\rho}_{m,m}, \\ \hat{F}_z^2 &= \hbar^2 \sum_m m^2 \hat{\rho}_{m,m}\end{aligned}\tag{4.34}$$

where we have used the same trick with redefining m as in the previous equations. The quantity $\langle \hat{F}_x^2 - \hat{F}_y^2 \rangle$ is therefore calculated to be

$$\langle \hat{F}_x^2 - \hat{F}_y^2 \rangle = \frac{\hbar^2}{2} (F(F+1) - 3m^2).\tag{4.35}$$

We see from this that the magnitude of the polarisation change depends on the internal state of the atom, as well as the total atom number in the cloud.

4.2 Two Colour Method

In this section the equipment and procedure used to measure the internal state of the atom are detailed. In Section 4.2.1, the method of using different lasers to detect the population in each of the two F -levels is described, as was in place at the start of my PhD. The signal demodulation required to obtain a measure of the internal state of the atom is the subject of Section 4.2.2. In Section 4.2.3 our new method of detecting the signal using a single laser and an electro-optic modulator to provide the two components is discussed, which is used in order to stabilise against power fluctuations and provide a more accurate relative measure of population in the two F -levels.

4.2.1 Two State Detection

Two different frequencies of light are required to detect the population of atoms in each of the two ground state F -levels. The detection scheme, using two lasers to provide the required frequency components of the beam, is shown in Figure 4.2b. The polarisation change at each stage in the sequence is shown in Figure 4.2a. The two beams are overlapped using a Wollaston prism, which can combine beams of opposite polarisation, or separate a single beam into orthogonal polarisations. After the first prism, the detection light is π and σ_{\pm} -polarised for $F = 1$ and 2 respectively, as marked at ① in the figures. As an equal combination of π and σ_{\pm} polarisation is required, a half-waveplate is then used to adjust this to $\pm 45^\circ$ for $F = 1$ and 2 respectively ②. After passing through the atomic cloud, this will shift to some polarisation with an ellipticity

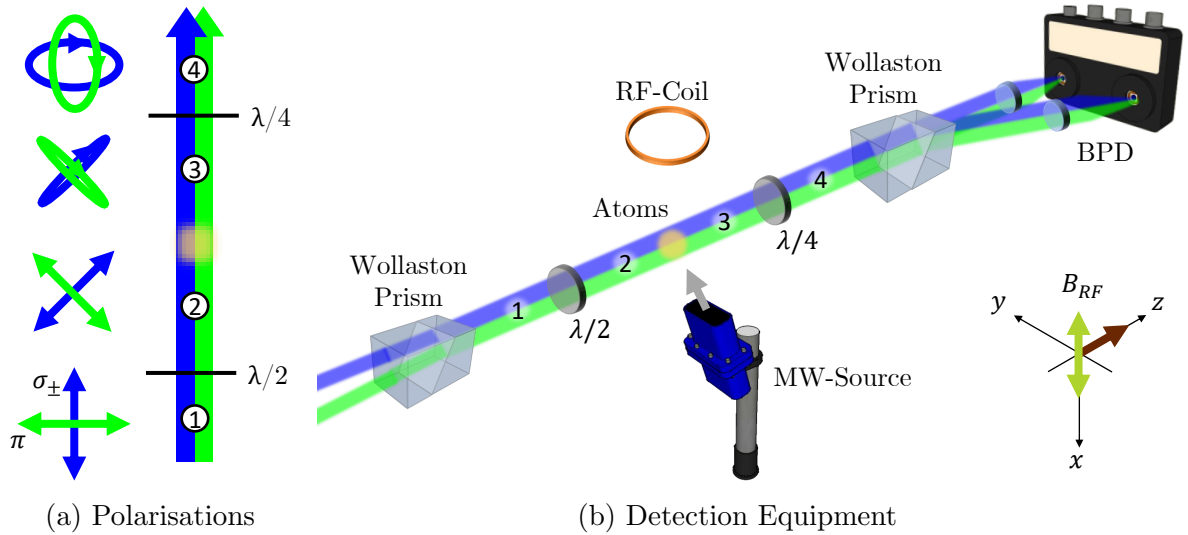


Figure 4.2: The figure shows the schematic of the experimental set-up facilitating our two-state detection method, in the case where two lasers are used to provide the beam. The two frequencies of detection light, for $F = 1$ and $F = 2$ state detection, are shown in green and blue respectively. Two Wollaston prisms are used to combine the two beams, and then decompose these into separate polarisations after passage through the atomic cloud. The polarisation of the beam at various stages is shown in (a) and the necessary equipment shown in (b). Adapted from [98].

proportional to the atom number in the relevant state ③. In order to split correctly into its constituent polarisations at the second Wollaston prism, a quarter waveplate is required to adjust this to the polarisation shown at ④. After passing through the prism, these are now separated into the two linear polarisation components. A balanced photodetector (BPD) takes these two components as its input, and measures the difference in power between them. As we have correctly set-up our waveplates, the signal sent out by the BPD will be zero in the case of no atoms, such that in the presence of atoms the signal will be proportional to the atom number in the relevant state. Also shown in Figure 4.2b are the RF-coil, providing the dressing required for the signal demodulation, and the MW-horn, which is required for the preparation of atoms in the desired state.

In Figure 4.3, the procedure for probing and detecting the atom cloud is shown, following directly on from the state preparation sequence in Figure 3.8. We begin by ramping our static field in the y -direction from the value required during the state preparation procedure to the value required for our measurement. In the sequence shown, an example of a static field at an arbitrary magnitude, at some angle in the $y - z$ plane is shown. For fully π

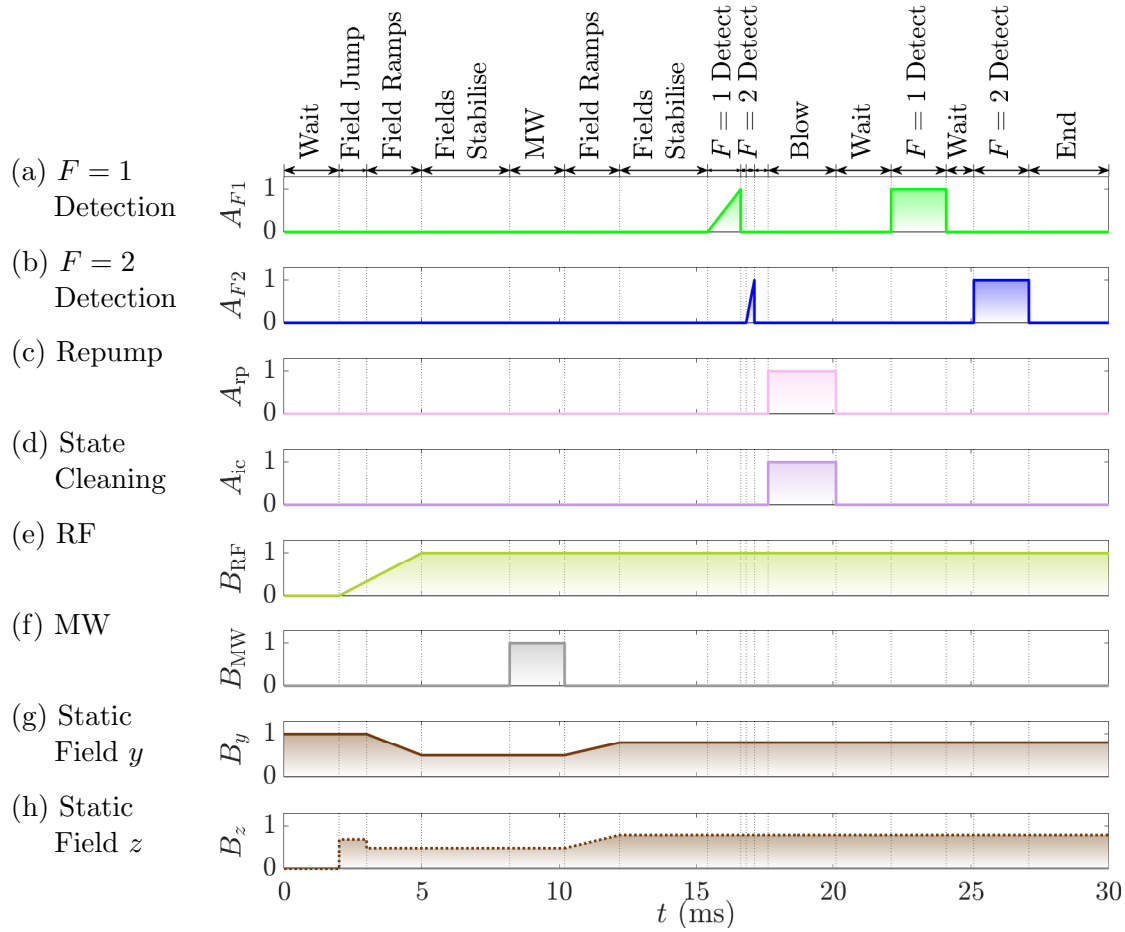


Figure 4.3: Graph of the fields active during the MW-probing and detection process. Fields indicated are only the nominal values those fields are set to, as ramping or jumping static fields will lead to oscillations in the output field amplitude until this is allowed to stabilise. The detection sequence is preceded by the state preparation procedure from Figure 3.8. After the state is prepared, we ramp or jump our fields to the required values and allow this to stabilise, before pulsing the MW in the desired manner (single pulse of arbitrary duration shown for illustrative purposes). We then ramp to the static field resonance, and perform our imaging using the two state detection beams, which are ramped in power then switched off in sequence. All atoms are then blown away and the power of the beams detected. The ratio of y to z -direction field amplitudes is dependent on the desired MW-polarisation to be experienced by the atoms. Adapted from [97].

or σ_{\pm} -polarised MW, the field is required to be purely in the y or z -direction respectively. As the field $B_z = 0$ during the state preparation sequence, this is jumped to a high field value before being reduced to the necessary value, for reasons given in Section 5.2.2. During the field ramps, the RF is also adiabatically ramped to the desired magnitude, with the atoms following the orientation of the effective field.

After a wait of a few milliseconds to ensure that all fields have stabilised, MW-probing is carried out. In Figure 4.3f a single MW-pulse of arbitrary power and duration is applied. For optimal detection strength, the static fields are then ramped to the resonant static field in both y and z for the field angle chosen. Once this field change has been given time to stabilise, our detection pulse sequence is carried out. The $F = 1$ detection beam is switched on and ramped linearly in amplitude for 1 ms before being switched off and the $F = 2$ beam enabled and ramped likewise. These two pulses register consecutive measurements at the balanced photodiode. The $F = 2$ pulse is shorter due to additional pumping processes in $F = 2$ causing problems with the level assignment. Once the $F = 2$ beam has also been switched off, the atoms are blown away. One beam transfers atoms from $F = 1$ to $F = 2$ via transitions on the $D2$ -line (using the repump laser), and a resonant state cleaning beam removes atoms in $F = 2$ from the cloud. Consecutive pulses of each of the detection beams are then required in order to obtain the power of the light in each beam, for the purposes of demodulation. A relative measure of atom number is then obtained by analysing the BPD signal.

Note that the detection pulse for $F = 2$ is shorter. Only in the case $\theta_1 = \pi/2$ is the RF-dressed state $|1, 0\rangle$ fully a quantum non-demolition measurement; no other states are eigenstates of the measurement. As such, sufficiently long detection pulses can destroy the atomic state. We find that the $F = 2$ states are more strongly affected by this, and as such there is a trade off between detection pulse length increasing signal strength and decreasing state purity. Noise due to such effects is characterised fully in [98].

4.2.2 Signal Analysis

Now that we understand the effect of an atom cloud on the polarisation of light passing through, we can consider how we may exploit this to gain information on the nature of the atomic state. In order to measure the polarisation change, we require splitting the light which has passed through the cloud into its separate polarisation components and measuring the imbalance. We consider the resultant signal, the difference between the σ_{\pm} and π -components, which our system is set-up to measure as zero difference in the absence of an atomic cloud. The signal is required to be demodulated in order to extract

the polarisation difference from the carrier wave, see [141].

In the simple case, the total balanced signal will be given by

$$u = \frac{1}{\sqrt{t_p}} \int_0^{t_p} U e^{2i(\omega_{\text{RF}}t \pm \varphi)} dt, \quad (4.36)$$

for a square pulse of duration t_p , where the term $1/\sqrt{t_p}$ is the normalisation factor given by $1/\sqrt{\int_0^{t_p} F^2(t)dt}$ for an arbitrary pulse of shape $F(t)$. U is the signal due to polarisation change, and the exponential term accounts for the RF-dressing. This is a simplification, however, as it does not account for the decay in signal strength over time $e^{-\gamma t}$. When we account for this we need to use a more complex mode function \tilde{u} , giving the signal strength

$$u = \sqrt{\frac{2\gamma}{1 - e^{-2\gamma t_p}}} \int_0^{t_p} U e^{2i(\omega_{\text{RF}}t \pm \varphi) - \gamma t} dt = \int_0^{t_p} U \tilde{u} e^{2i(\omega_{\text{RF}}t \pm \varphi)} dt \quad (4.37)$$

for times $0 \leq t \leq t_p$. For all other times $u = 0$, as there is no applied probe light and/or atomic cloud. γ is an experimentally determined decay factor. The polarisation dependent signal strength will be given by

$$U = c_{\text{PD}} \langle \hat{S}'_z \rangle = c_{\text{PD}} g_F^{(2)} N_{\bar{m}} \langle \hat{F}_x^2 - \hat{F}_y^2 \rangle, \quad (4.38)$$

where we have used Eq. 4.33 and included a constant dependent on the properties of the detector c_{PD} . This, in combination with Eq. 4.35, allows the demodulation of the function.

One issue when applying a square pulse of detection light is that the jumping in light power causes a sudden spike in the detected signal. This can be discounted by only processing the function in the region of stable beam power, but a more efficient detection method is to slowly increase the laser power. A linear ramp in power gives a mode function

$$\tilde{u} \propto e^{-2\gamma t + r t^2}, \quad (4.39)$$

where the value r accounts for the rate of increase in power. The constant of proportionality for the normalisation is considerably more complicated than in Eq. 4.37, but can be experimentally determined. A plot of these mode functions for the two different F -levels is shown in Figure 4.4a, along with the total modulated signal. The large spikes in signal due to fast switching of laser power can be seen to be substantial when the light is switched off at the end of the detection pulse, but are much smaller at the beginning of the detection time. The signal after switching off the light is not important, and therefore the final spikes can be safely discounted. In this figure the two frequencies of laser light are pulsed and analysed separately, but simultaneous detection is possible. For each state, the signal is only analysed for the interval between the end of the first large oscillation after switching on the detection light, up

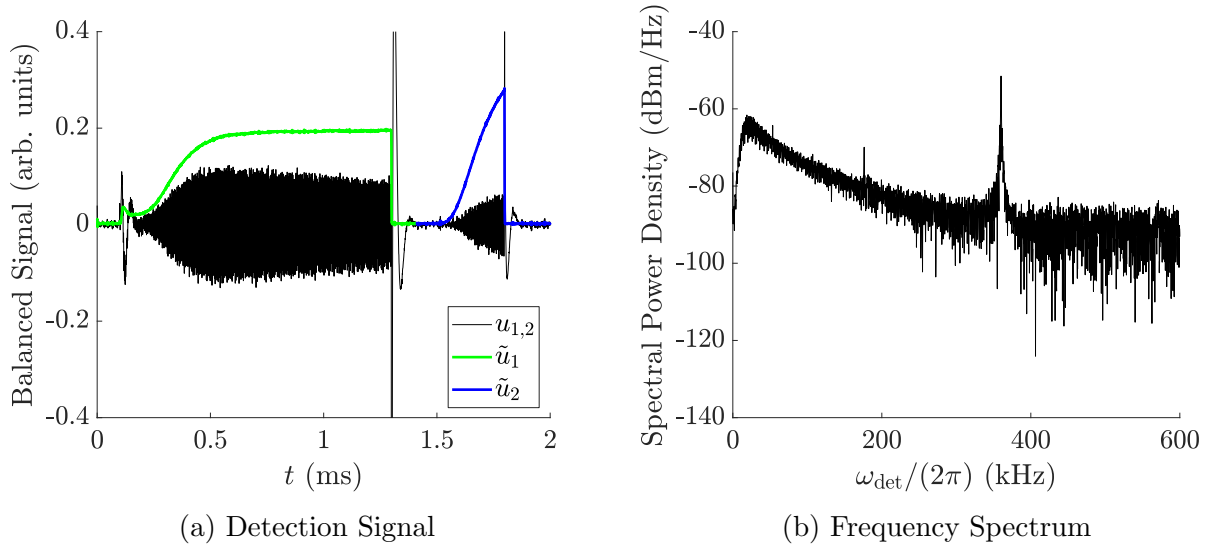


Figure 4.4: An example unprocessed signal detected by the balanced photodiode is shown in (a), where we have some population in both $F = 1$ and 2 . $u_{1,2}$ is the total signal from both F -levels combined, and $\tilde{u}_{1,2}$ are the mode functions for the signal from the two levels, as given by Eq. 4.39. In (b) the frequency spectrum of this signal is plotted, showing a large amount of power at $2 \times \omega_{\text{RF}}/(2\pi) = 360$ kHz, and a smaller $1 \times \omega_{\text{RF}}$ component.

until the time when the the detection light is toggled off.

We recall from Eq.s 4.35 and 4.38 that

$$\mathbf{U} \propto (F(F+1) - 3\bar{m}^2), \quad (4.40)$$

where we have switched to using \bar{m} as we are in the RF-dressed scenario. This means that depending on the state $|F, \bar{m}\rangle$, the detected signal strength will vary in overall scale. The relative signal strengths are given in Table 4.1. We see that certain states have negative signal strengths, which correspond to a polarisation change in the opposite direction. This sign change can be used for state labelling in spectroscopic measurements.

F	\bar{m}	-2	-1	0	1	2
1			-1	2	-1	
2		-6	3	6	3	-6

Table 4.1: The table shows the relative strengths of the signals detected in each of the $|F, \bar{m}\rangle$ sublevels, as given by Eq. 4.40. Negative magnitudes indicate a polarisation rotation in the opposite direction.

The detection method is a form of single-path homodyne interferometry; the two polarisation components of the light provide the requisite equivalent of having multiple paths. Although two different frequencies of light are used, the method counts as homodyning as the component frequencies do not mix, and make separate measurements. Signals at integer multiples of the RF-dressing frequency are generated. It transpires that the signal at $1 \times \omega_{\text{RF}}$ disappears entirely at 45° polarisation relative to the quantisation axis, and as such we use side-band detection of the $2 \times \omega_{\text{RF}}$ signal, which is maximal at this point. The frequency spectrum of an example modulated signal is shown in Figure 4.4b. We see a large amount of power at $2 \times \omega_{\text{RF}}/(2\pi) = 360$ kHz, and small signal at $1 \times \omega_{\text{RF}}$, indicating that the polarisation of the detection light is close to 45° ; this reduces cross-talk with from the $1 \times \omega_{\text{RF}}$ component. Before demodulation, the signal must be low pass filtered to remove the low frequency noise. For more details on the detection system see [98].

4.2.3 Common Mode Suppression

In order to accurately obtain the atom fraction in each of the F -levels, a comparison between the detected signals from both states is required. This can of course be achieved by the afforested method of using two separate lasers for detection of the two states, but this has the disadvantage that fluctuations in the power output from either laser, or due to any other optical components, will be different for the two beams. In order to eliminate this power noise, we can instead use an electro-optic modulator (EOM), producing multiple frequencies in a single laser beam. This will enable the common mode suppression of power noise. The simultaneous detection of the two states $F = 1$ and 2 is possible due to the difference in the sign of the g_F -factors, meaning that they counter-precess with respect to each other in the presence of a magnetic field. The difference in the polarisation dependence of their respective signals can be used to distinguish the states.

The application of a static or slowly varying electric field to certain materials facilitates a change in its optical properties. One manifestation of such an electro-optic effect is the Pockels effect, in which the induced birefringence in a material is proportional to the applied electric field. Materials which have the correct crystal structure, lacking inversion symmetry, display this effect [155]. One such material is lithium niobate (LiNbO_3), which is commonly used in optical devices, and is the medium used in the iXblue EOM in this experiment. A laser beam of frequency ω_{IR} can acquire a component oscillating at $\beta \sin(\omega_{\text{mod}} t)$ on passing through the crystal. This gives a light

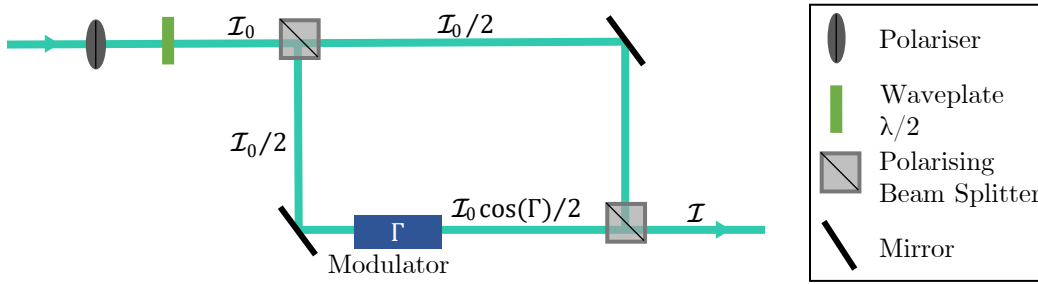


Figure 4.5: A Mach-Zehnder interferometer splits a single beam into two equal parts and sends these along different paths, then recombines them to obtain an interference pattern dependent on the path difference. In an EOM of this type, the path difference is generated by a modulator which varies the light intensity in one of the paths by an amount dependent on the retardation of the material Γ . Adapted from [122].

amplitude of

$$\begin{aligned}
 A &= A_0 e^{i\omega_{\text{IR}}t + i\beta \sin(\omega_{\text{mod}}t)} \\
 &\approx A_0 e^{i\omega_{\text{IR}}t} (1 + i\beta \sin(\omega_{\text{mod}}t)) \\
 &\approx A_0 \left(e^{i\omega_{\text{IR}}t} + \frac{\beta}{2} e^{i\omega_{\text{IR}}t + i\omega_{\text{mod}}t} - \frac{\beta}{2} e^{i\omega_{\text{IR}}t - i\omega_{\text{mod}}t} \right),
 \end{aligned} \tag{4.41}$$

where, assuming β to be small, we have expanded e^x for $x = i\beta \sin(\omega_{\text{mod}}t)$, and then replaced sine with its exponential form. This shows that, in addition to the carrier frequency, there are two main sidebands at frequencies of $\omega_{\text{IR}} \pm \omega_{\text{mod}}$. In full, this can be expanded using the Jacobi-Anger identity [45] to give the complete solution

$$A = A_0 e^{i\omega_{\text{IR}}t} \left(\mathfrak{J}_0(\beta) + \sum_{k=0}^{\infty} \mathfrak{J}_k e^{ik\omega_{\text{mod}}t} + \sum_{k=0}^{\infty} (-1)^k \mathfrak{J}_k e^{-ik\omega_{\text{mod}}t} \right) \tag{4.42}$$

as a sum of Bessel functions \mathfrak{J} . We therefore also obtain sideband frequencies at $\omega_{\text{IR}} \pm k\omega_{\text{mod}}$ for all integer values k [94].

A Mach-Zehnder interferometer splits an input light beam of intensity \mathcal{I}_0 into two equal parts, and sends these down separate paths to recombine at an output, producing an interference pattern if there is a difference between the two paths taken. We can achieve amplitude modulation by inserting a phase modulator into one of these paths. The retardance of this material Γ causes an amplitude modulation of $\cos(\Gamma)$. In a material which displays the Pockels

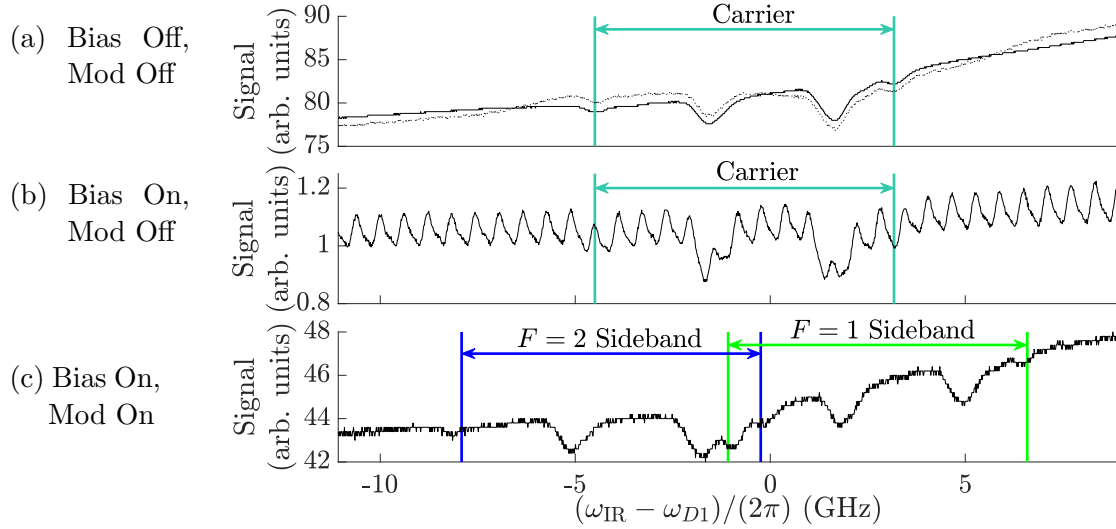


Figure 4.6: Scanning the full frequency range of the $D1$ -line, spectroscopy using the light through the EOM is shown with no modulation or bias in (a). The spectroscopy with a bias voltage but no modulation is shown in (b) and both bias and modulation are enabled in (c). The regions between the transitions $F = 2 \rightarrow F' = 1$ and $F = 1 \rightarrow F' = 2$ are marked with arrows to indicate the spectroscopy peaks for both the carrier and the sideband frequencies. The horizontal axis shows the carrier frequency. The solid line in (a) is a time averaged waveform, with an example single shot shown as a dashed line. All graphs display signals in the same arbitrary units.

effect, the retardance changes proportionally to an applied voltage,

$$\Gamma = \Gamma_0 + \frac{\pi V_{\text{mod}}}{V_{\pi}}, \quad (4.43)$$

where Γ_0 is the initial retardance of the material, and V_{π} is the half wave voltage of the modulator.

Figure 4.5 shows a schematic of a Mach-Zehnder interferometer used for intensity modulation. Summing the light in the two paths after one arm has been subjected to a modulation gives a total intensity output of

$$\mathcal{I}_{\text{out}} = T \frac{\mathcal{I}_0}{2} \left(1 + \cos \left(\frac{\pi}{V_{\pi}} V(t) - \varphi \right) \right), \quad (4.44)$$

where we have included a phase φ to account for any initial mismatch between the two optical paths, and T is the optical transmission [122]. Substituting in for the time dependent voltage

$$V(t) = V_{\text{DC}} + V_{\text{mod}} \cos(\omega_{\text{mod}} t) \quad (4.45)$$

and expanding as Bessel functions in the same manner as Eq. 4.42 shows that different frequency components have different dependencies on the bias voltage V_{DC} , and as such the carrier and/or specific sidebands can be suppressed depending on the bias [82]. In our case carrier suppression is chosen, as we require two frequencies to detect population in the two different F -levels, using both first order sideband frequencies. Equal power in both frequency components is desirable, as the optimal power for detecting both states is similar. Therefore two sidebands, rather than for instance one sideband and the carrier, achieves this straightforwardly. A third frequency would also interfere with the atoms, as well as the shot-noise limited photodetection. We input a laser of frequency roughly equidistant between that of the two transitions $F = 1 \rightarrow F' = 1$ and $F = 2 \rightarrow F' = 2$, and then modulate at slightly over half the frequency difference between that of the two transitions, in order to achieve the two detection frequencies with appropriate detunings. The carrier suppression will not be 100%, but a small amount of light far (~ 3 GHz) detuned from any ^{87}Rb transition will have a negligible effect on the atoms.

Light from the detection laser is input to the EOM, and for testing purposes the output light was passed through a Rb cell to a photodiode (PD). In Figure 4.6a, where neither bias nor modulation was applied, we see the typical $D1$ -line spectroscopy at the PD, which will be discussed further in Section 5.1.1. As the EOM is highly temperature sensitive and can heat up quickly when light or modulation is applied, the intensity of light through the EOM is unstable. The solid line in the figure is a time average of the signal, but an example single shot of the spectroscopy is shown by the dashed line, indicating how much the intensity fluctuates over the 33 ms scan. This is partially due to a 50 Hz oscillation in intensity of light through the EOM by $\pm 2\%$, as measured with a fixed laser frequency, likely due to mains noise. As the laser frequency is scanned over time, the measured time has been converted to carrier frequency in the data using the measured locations of the $F = 2 \rightarrow F' = 1$ and $F = 1 \rightarrow F' = 2$ transitions. This region has been marked in the figure.

The effect of using the bias controller, which adjusts the bias voltage to minimise the intensity of the light in the carrier frequency, is shown in Figure 4.6b. We see that the intensity of the output light drops by a factor of ≈ 80 , although this oscillates in intensity by $\pm 5\%$ every 1 ms, showing the response time of the device. Spectroscopy peaks are still roughly discernible in the measurement, although demodulation would be required to recover these reliably. In Figure 4.6c, the spectroscopy is shown with both the bias and the modulation applied, at 3.417 GHz and 16.5 dBm input power. The final EOM modulation frequency differs slightly from this value, but as a test case this is

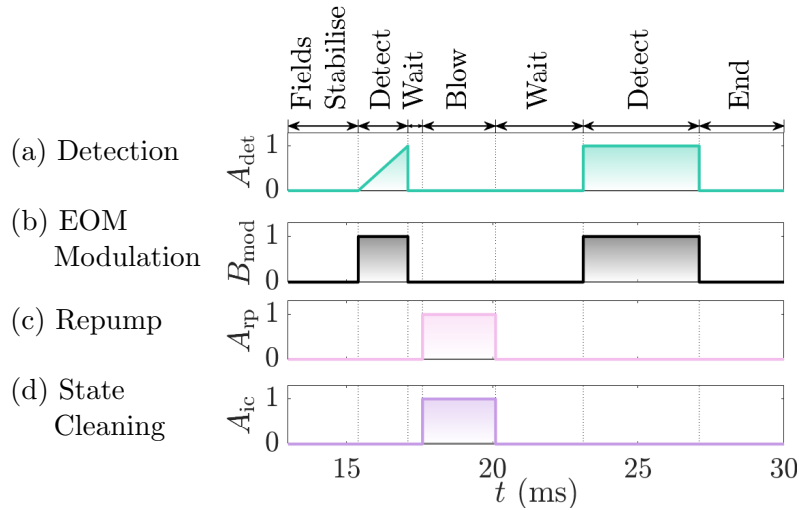


Figure 4.7: The graph shows the detection sequence using common mode suppression, plotting only the period where the sequence differs from the prior sequence shown in Figure 4.3. (a-d) in this figure directly replaces (a-d) in the prior sequence, with the corresponding fields off at times (0 – 13) ms. The previous two separate beams for detecting $F = 1$ and 2 are now no longer present. All other fields are unaffected, i.e. the RF and static field are both enabled and constant in amplitude during the period shown in this figure.

successful in showing the two sets of spectroscopic peaks measured using the two main frequency components of the output light. The regions indicating spectroscopy peaks measured by each sideband are marked using the carrier region, shifted by minus and plus the modulation frequency for $F = 1$ and 2 detection light respectively. Although the peaks do not align perfectly with the marked locations, considering that this is using only a crude frequency calibration, and the frequency scan is not necessarily wholly linear, this is a good verification of the capability of the device. We see no indication of the carrier spectroscopy, showing a good level of suppression, although due to overlap in carrier frequency with sideband transition peaks we cannot reliably say by how much this has been suppressed. As there are no ^{87}Rb transitions in the region of the carrier frequency, a lack of complete carrier suppression should not alter the state of the atoms in any case.

Sending the output light from the EOM through the main chamber, after a small fraction is picked off to send to a bias controller, we can now perform common-mode suppressed two state detection. As the bias controller requires continuous light, a low intensity beam is always provided to the EOM, but this light power is increased during the detection pulse (using an AOM, see Section 5.1.1), and also the MW-modulation is triggered. The detection se-

quence used is the same as in Figure 4.3, only with a single detection laser rather than two used sequentially. The altered part of the sequence is shown in Figure 4.7. Note that although in the long term we will wish to use a shorter detection pulse due to pumping processes in $F = 2$ causing issues with level assignment, atom number issues mean this will have to wait until after the ^{87}Rb dispensers are replaced to be viable, due to our weak signal strength. In Figure 4.8a a Rabi cycle is shown, with atoms prepared in the bare state $|1, 0\rangle$ and driven to $|2, 0\rangle$ using a MW-probe, with the data taken using a single detection laser for both states. An example modulated signal, with the atoms in a 50 : 50 superposition of the two states, is shown in Figure 4.8b. Due to the maximum input power of the EOM, allowing through only 0.25 mW of detection light for each state rather than the 0.5 mW used previously, the mean amplitude of the detected signal will be lower than that of the signal from the two laser system, Figure 4.4a. However the main difference is in atom number, as depleted dispensers at the time the common-mode suppressed data was taken make the signal size much reduced. Replacing the dispensers will give a much better indication of the shape of the signal, and reduce the relative noise level, although time constraints have meant that this has not yet been achieved.

Signal analysis has been performed in the same manner as in the two laser case, described in Section 4.2.2. The only difference is that it is the phase of the signal, rather than the individual detection pulses, which labels the states. As $F = 1$ and 2 have opposite signs of Landé g -Factors, these will precess in opposite directions. This means that when the incoming light is at 45° to the quantisation axis, adjusted using a half-waveplate, the two F -signals will be 90° out of phase. This will manifest as real and imaginary parts of the demodulated signal obtained using Eq. 4.37. Similarly to when demodulating the signal in Figure 4.4a, we consider only the region of balanced signal between the large spikes caused by switching the detection light on and off. Shown in Figure 4.9bi for a state where the atoms are primarily in $F = 1$, and Figure 4.9bi for atoms primarily in $F = 2$, these signals are extracted from the region (60 – 200) ms in data such as Figure 4.8b. The figure is a plot of the imaginary and real parts of U from Eq. 4.36, which correspond to signals from population in $F = 1$ and 2 respectively. We can clearly see that the signal in $F = 1$ is strong in the first figure, with the $F = 2$ signal showing only noise around zero signal, and vice versa in the second figure. An alternative way to display this same data is using phasor graphs, which plot the real versus imaginary signal at all times. Figures 4.9ai and 4.9aii show the corresponding phasor plots for the two cases. The noise level, measured before the detection beams are triggered, is also plotted in both phasor graphs. We see that for the largely $F = 1$ state, the signal is purely imaginary, aside from

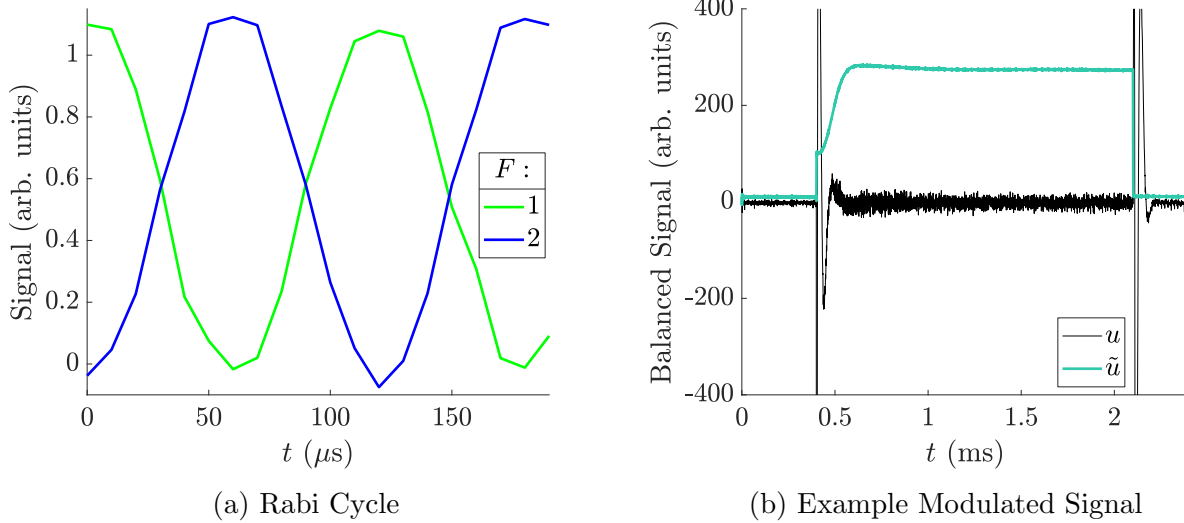


Figure 4.8: Using a single laser passed through an EOM in order to simultaneously detect population in both F -levels, (a) shows a Rabi cycle on the bare transition $|1, 0\rangle \leftrightarrow |2, 0\rangle$. An example modulated detection signal u is shown in (b), along with its mode function \tilde{u} for a 50 : 50 superposition of population in both F -levels. The reduced signal strength compared to Figure 4.4a is partially due to a 50% reduction in the intensity of the detection light, but primarily due to a reduced atom number in the cloud caused by ^{87}Rb dispenser depletion.

a real component which is comparable to the noise level, and likewise the $F = 2$ signal is purely real when we discount the noise. The pairs of figures (i) and (ii) show analysis of the signals at 60 ms and 120 ms in Figure 4.8a respectively. The $F = 1$ signal is a factor of ~ 3 smaller than the $F = 2$ signal, as predicted by Table 4.1, although this is accounted for in the analysis.

Ideally the relative signal to noise ratio for both the original system and the common-mode suppression would be analysed, when measuring the atom fraction in a given state. However, in order to do this accurately we require a larger signal strength, achievable with a higher atom number. Currently we see from Figure 4.8b that the signal strength is much diminished compared to the previous case of Figure 4.4a, due to a reduction in achievable atom number by a factor of more than 10 in the nearly two years between measurements. Replacing the ^{87}Rb dispensers is therefore the next major step in the experimental plan, at which point it will be possible to access the scientific benefits of the common mode suppressed scheme. Practical benefits of the single detection laser method in the day to day running of the experiment are given in Section 5.1.2.

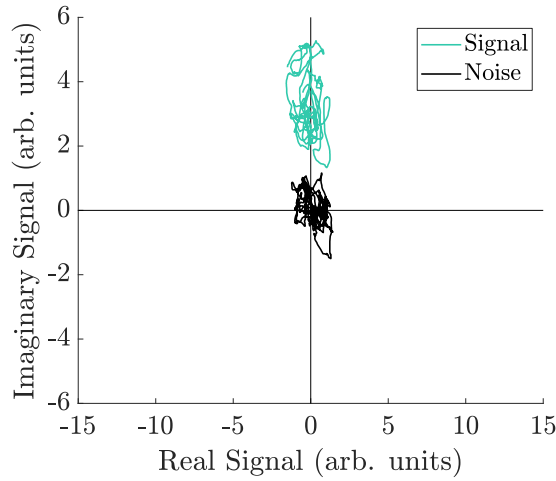
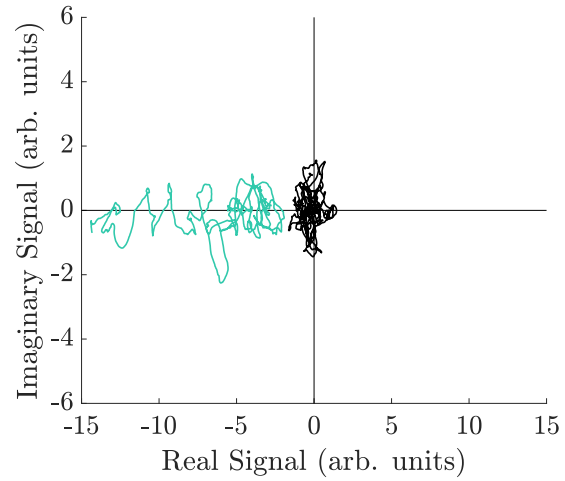
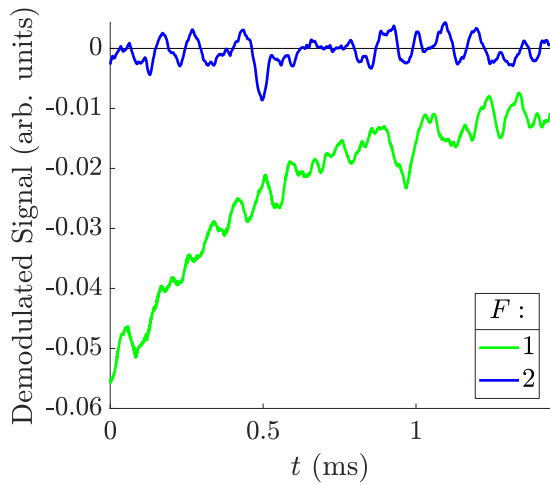
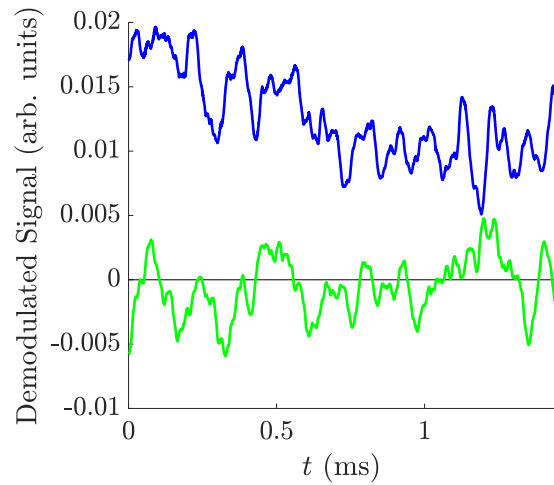
(ai) Phasor Plot, State $F = 1$ (aii) Phasor Plot, State $F = 2$ (bi) Temporal Plot, State $F = 1$ (bii) Temporal Plot, State $F = 2$

Figure 4.9: The overall phase of a detection signal denotes the internal state of the atom. In (a) phasor graphs, decomposing the detection signal into real and imaginary parts, show that when atoms are prepared in $F = 1$ the signal is imaginary, and for $F = 2$ the signal is real. A noise measurement is also shown for reference, taken from signals such as Figure 4.8b at < 35 ms (i.e. before the detection beam is triggered). At (60 – 200) ms the detection beam is enabled, and this is the region of interest in (b). The demodulated signal in this region is plotted as a function of time, with the real and imaginary parts showing the population in $F = 1$ and 2 separately.

Chapter 5

Experimental Apparatus

In this chapter, the equipment and experimental set-up used to take the data in thesis are detailed. The laser system which generates the required powers and frequencies of infrared (IR) light is described in Section 5.1. Other necessary equipment to generate the static and oscillation magnetic fields and vacuum system are detailed in Section 5.2.

5.1 Laser System

This section describes the laser system used for cooling, manipulating and detecting the atoms in our experiment. The original system was developed by previous PhD students, most recently Dr Sindhu Jammi, and is detailed in her thesis [97]; the cooler and repumper laser system remains unchanged from this time. The original system used six lasers, although we have since upgraded to require only four lasers to provide the same functionality with increased robustness. In this section we first go through the method of generating the required IR powers and frequencies (Section 5.1.1), before describing the layout of the optical components and beam paths in the experiment (Section 5.1.2).

5.1.1 Generating the Beams

The IR frequencies used in this experiment are generated using external cavity diode lasers (ECDLs). Starting with the basics of how these work, we then state the requirements on the powers of each of the beams. Details of the required frequencies and the laser locking methods used for frequency stabilisation are then given.

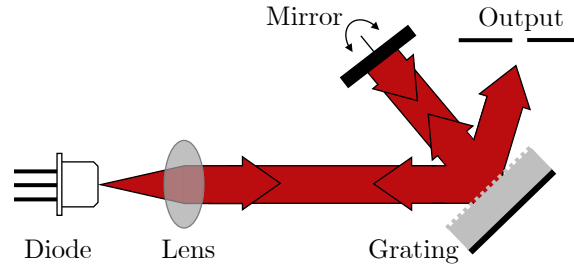


Figure 5.1: The figure shows a schematic of the workings of an external-cavity diode-laser in the Littmann-Metcalf configuration. A semiconductor diode provides IR light, collimated by a lens, and adjusted in frequency using a diffraction grating. An adjustable mirror allows for cavity length and hence resonant wavelength adjustment whilst also providing robustness against changes in the output beam angle. Adapted from [154].

Diode Lasers

Conventional IR lasers operate using an anti-reflection coated semiconductor laser diode and an external cavity. For details of such diodes, see [4]. Light output from the diode passes through a collimating lens, before hitting an optical grating. The diffraction grating has a periodically structured reflective surface, the orientation of which determines the resonant frequency of the cavity, and hence the output wavelength of the laser. Optical feedback to the laser diode due to the external cavity improves the frequency stability of the output light, hence reducing the linewidth of the laser [66]. A simple (Littrow) set-up consisting of a diode pointing at an adjustable grating has the downside that the angle of the output light is highly dependent on the grating position. This is the set-up used by our standard home-build ECDLs. A configuration which is robust against such changes, known as a Littmann-Metcalf set-up, has an additional mirror opposite the grating which is adjusted instead of the grating itself [32]. This is shown in Figure 5.1, and is the configuration used by our Toptica ECDLs.

Optical isolators are required after this stage in order to only allow light in one direction and prevent unwanted feedback from undesired reflections later in the set-up. Beams output from simple ECDLs will not necessarily be Gaussian in profile. In order to adjust the beam shape, a pair of anamorphic prisms is used. These (right-angled) triangular prisms can be arranged such that the relative width of the beam in the horizontal direction, in comparison with the vertical direction, can be adjusted to achieve a circular profile [173]. Further sets of spherical lenses may also be necessary to change the area of this Gaussian beam. Commercial lasers typically have inbuilt optical isolators and beam shaping optics before the output, so such components are not nec-

essary externally to the laser package. With the home-built lasers, external components are required.

Beam Requirements

A number of different IR wavelengths and powers are required to operate the experiment, as described in Chapters 3 and 4, for preparing and detecting the atomic state respectively. A total of six different frequencies of light are needed, of appropriate powers. Discussion of the required powers and frequencies follows below, and is summarised in Table 5.1. In general, the higher the cooler beam power the better, as this will provide faster cooling due to a stronger molasses force. This is because the amplitude of the beam is proportional to the Rabi frequency of the transition, which changes the damping factor as seen in Eq. 3.1. Our cooler power is limited by the output power of our TA Pro laser. Approximately 200 mW of power is output from the main optical bench after frequency shifts, which is then divided into 3 equal power orthogonal beams, and can obtain a MOT of $\sim 2 \times 10^7$ atoms after 2 s, which could be increased substantially using new Rb dispensers. The repump power is required to be sufficient to prevent sizable losses to the $F = 1$ dark state. As we obtain diminishing returns on increases in atom number with repump power (due to the finite number of atoms in the dark state), our 30 mW repump beam is sufficiently close to saturation. The absorption imaging power must not exceed ~ 0.5 mW to avoid saturation at the camera, which would prevent accurate measurement of the atom number, as described in Section 3.1.2. The state cleaning power needs to be high enough to remove all atoms in $F = 2$ in a reasonable time frame, and we find that 0.5 mW of

Beam	Transition	Detuning/ (2π) (MHz)	Power (mW)
Optical Pump	$F = 1 \rightarrow F' = 1$	$\Delta_{\text{op}} = -30$	0.8
Detect $F = 1$		$\Delta_{F1} = 60$	0.25
Detect $F = 2$	$F = 2 \rightarrow F' = 2$	$\Delta_{F2} = -200$	0.25
Repump	$F = 1 \rightarrow F'' = 2$	0	30
Cooler	$F = 2 \rightarrow F'' = 3$	$\Delta_{\text{co}} = -20$	200
State Cleaning		0	0.5
Imaging		0	0.5

Table 5.1: The table shows the frequencies of the beams in the experiment, with the transition and detuning given, as well as the power in each beam.

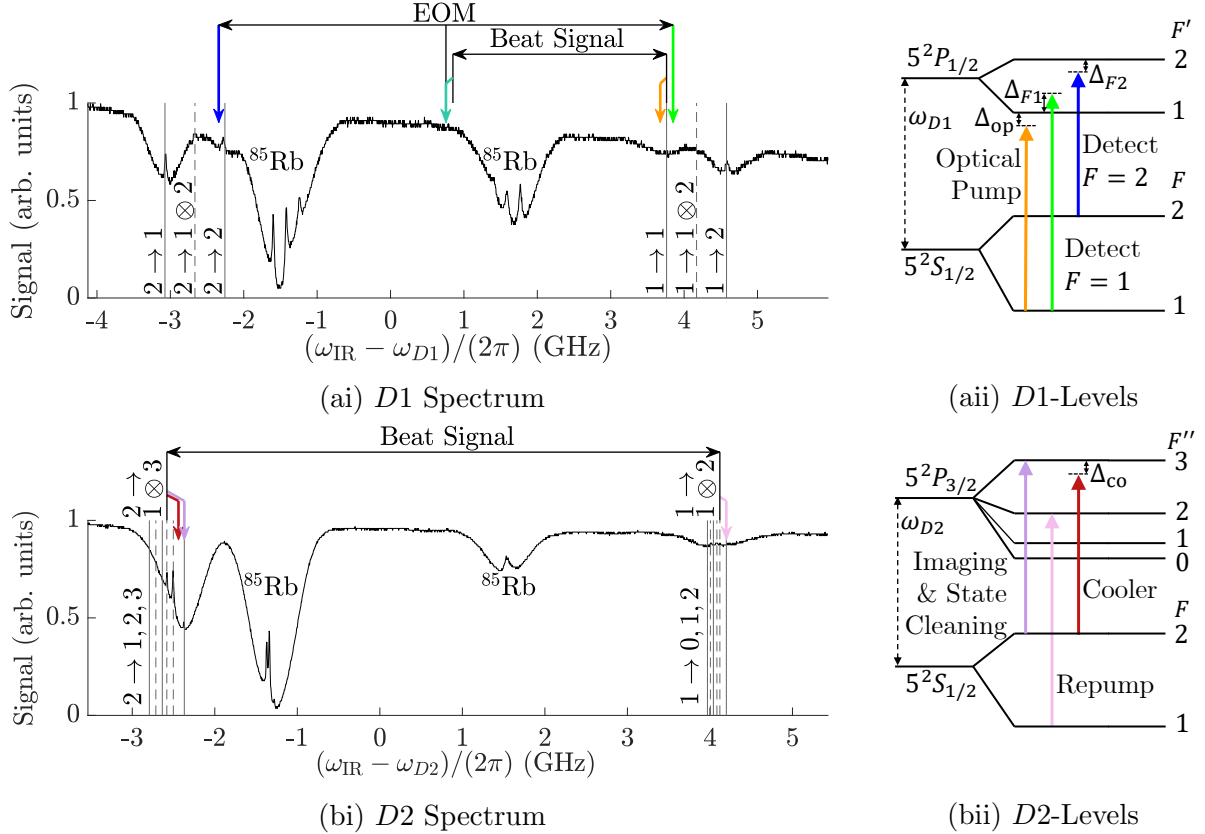


Figure 5.2: The figures (a) and (b) show the frequencies of the lasers on the *D1* and *D2*-lines respectively. The spectroscopic data in (ai) and (bi) were taken using the detection and the cooler laser respectively. Solid and dashed lines indicate transitions and crossover transitions. Black vertical lines indicate the frequencies the lasers are locked to (or receive as an input to the EOM). The turquoise arrow marks the detection laser frequency before the EOM, and other coloured arrows indicate the frequencies of the beams labelled on the relevant transitions in (aia) and (bia). All coloured arrows in (ai) and (bi) are AOM shifts, aside from the blue and green which are EOM sidebands. Adapted from [97] with frequency calibrations from [171].

power for 2.5 ms is sufficient. Likewise an optical pump power of 0.8 mW is sufficient to pump the majority of the atoms to the desired state in 2 ms. Both frequencies of detection light are required to be ~ 0.5 mW for optimal detection strength, as too high a power will saturate the balanced photodiode. Due to limitations on the maximum light power which can be pushed through the EOM, the output power is only ~ 0.25 mW per frequency component, which although not optimal is still sufficient for our purposes.

Beam	Laser	Line	Locking	$\omega_{\text{AOM}}/(2\pi)$ (MHz)	$\omega_{\text{EOM}}/(2\pi)$ (GHz)	Figure
Optical Pump	DL Pro (1)	$D1$	Spectroscopy $F = 1 \rightarrow F' = 1$ Lamb Dip	-30^*	-	5.3a
Detect $F = 1$	DL Pro (2)	$D1$	2890 MHz Beat to Optical Pump	-80	3.14	5.3b
Detect $F = 2$					-3.14	
Repump	DL 100	$D2$	Spectroscopy $F = 1 \rightarrow F'' = 1 \otimes 2$	+78.5	-	5.3c
Cooler	TA Pro	$D2$	6745 MHz Beat to Repump	$2 \times +110$	-	5.3d
State Clean- ing/Imaging						

* Beam split from laser into lock to +140 MHz, output to +110 MHz

Table 5.2: The table shows how the multiple beams used in the experiment are produced at the correct frequencies from the four Toptica Photonics lasers. This includes details of the locking, either to spectroscopy or a beat signal, as well as the AOM frequencies and EOM frequencies where applicable. The final column shows the figure number where the spectroscopy and lock signals can be seen in Figure 5.3. The spectroscopic signals for the $D1$ and $D2$ -lines are shown in Figure 5.2ai and 5.2bi respectively, with locking frequencies labelled.

Table 5.1 details the relevant transitions and detunings for each of the beams, and the frequencies are also marked in Figure 5.2. In Figures 5.2ai and 5.2bi the saturated absorption spectroscopy signal of the detection and cooler lasers are shown respectively, with both the frequencies of the final beams and the frequencies the lasers are directly locked to indicated above. Features in the spectrum are also labelled, with grey solid lines indicating transitions from F to F' or F'' ($D1$ or $D2$ -line transitions respectively), and grey dashed lines indicating the associated crossover transitions. In Figures 5.2aai and 5.2bii the final frequencies of the beams are shown, with the colours of the arrows labelled in (ii) corresponding to the same beams in (i). The method of locking the lasers to the correct frequencies is described in the following section, along with further description of the absorption spectrum.

Laser Locking

In this section the method of generating the correct frequencies of IR light for each of the required beams is detailed. Typically the required frequencies of laser light are resonant or near resonant with an atomic transition, but are locked relative to a different transition. This is because for fast

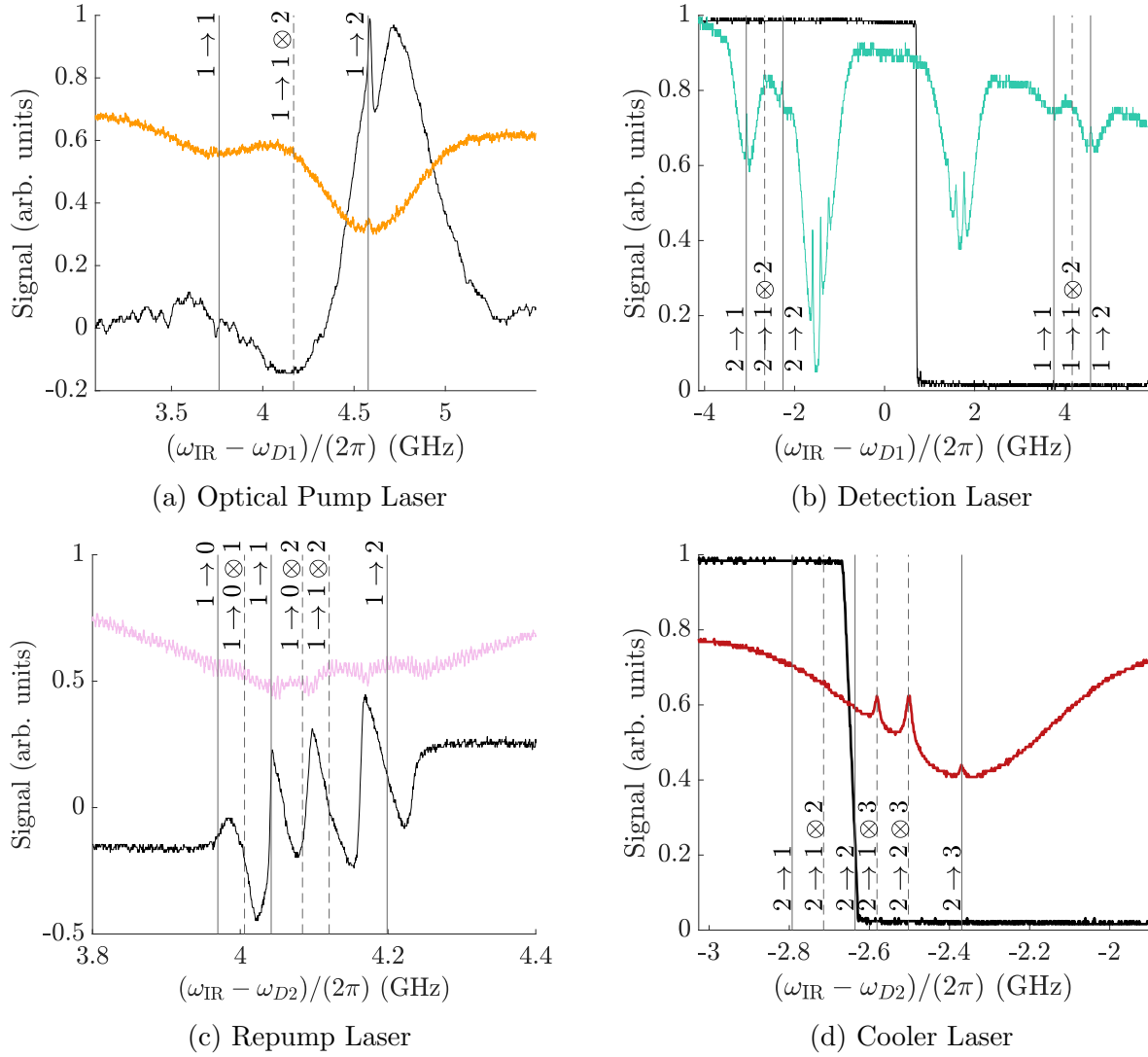


Figure 5.3: The spectroscopy signals for the four different lasers are marked with coloured lines, with the optical pump, detection, repump and cooler shown in (a-d) respectively. Their respective lock signals are shown in black in the same figures. In (a) and (c) this is a derivative lock signal, and in (b) and (d) the square waves are generated using beats to the respective derivative signals. The transitions from $F \rightarrow F'$ on the $D1$ -line are labelled in (a) and (b) and the $F \rightarrow F''$ transitions on $D2$ are labelled in (c) and (d). Solid and dashed vertical lines mark transitions and crossover transitions respectively. Some transition peaks are not visible as not all spectroscopy measurements are properly saturated. Frequency calibrations are from [171].

(\sim microsecond) switching times we require the use of acousto-optic modulators (AOMs). These devices consist of a crystal, in our case tellurium dioxide, and a piezo-electric transducer to provide radio-frequency modulation, which causes diffraction of the light at multiples of an angle proportional to the wavelength (for small angles). As each of these orders of light (save for the zeroth order) are being scattered from a moving plane, they gain a change in frequency given by the scattering order multiplied by the radio-frequency. This allows fast switching of light through non-zero orders, by toggling whether the modulation signal is provided. AOMs can also be used for changing output light power, by controlling the amplitude of the modulation signal. For more details on AOMs, see [59].

The locking frequencies and AOM shifts were shown in Figure 5.2 relative to the absorption spectroscopy data. When the light is near-resonant with a transition it will be absorbed and scattered, causing a reduction in the transmitted light intensity, as measured using a photodiode (PD). Measuring the PD signal as a function of laser frequency will give a spectrum which is representative of the internal structure of the atom. Naturally occurring Rb contains both isotopes ^{85}Rb and ^{87}Rb , and as such we see peaks relating to transitions in both isotopes in the spectroscopy. Figure 5.3 shows the relevant sections of the spectroscopy taken with each of the four lasers in the vicinity of the locking frequencies. The main peaks are Doppler broadened, as atoms in the hot vapour cell are moving at a range of velocities, and as such will experience different frequencies of laser light as being resonant.

The use of two beams, a high power pump and a low power probe, leads to the emergence of sharper lines known as Lamb dips. Due to the fixed detuning, these counter-propagating beams will excite atoms moving in opposite directions, aside from on resonance with a transition, where both beams will affect atoms which have roughly zero velocity parallel to the laser beam. The pump beam excites these atoms to a saturation state where the population in the ground and excited state are roughly equal. The probe beam will therefore be less attenuated by the atoms at this point, and will appear as a peak in the spectroscopic frequency scan. This is not the only form of spectral feature: as counter-propagating beams will have an equal and opposite Doppler shift relative to the atom, at halfway between two transition frequencies (from the same initial energy level) some atoms will see both beams as being resonant, meaning that atoms of this frequency are excited by the pump beam, and therefore do not absorb the probe. These are crossover transitions which also manifest as peaks in the spectrum, for more details see [139].

The method of locking each of the lasers is given in Table 5.2. Two lasers, one on each of the D -lines, are locked to spectroscopy using a derivative lock signal. A description of the method of generating a derivative lock signal

and using proportional-integral-derivative control to stabilise the frequency of lasers is given in my Master's thesis [70]. In Figure 5.3a the spectroscopy and derivative signal for locking to the $F = 1 \rightarrow F' = 1$ Lamb dip are shown for the optical pumping laser. In Figure 5.3c the spectroscopy and lock signal for the repump laser are shown, locking on the $F = 1 \rightarrow F' = 1 \otimes 2$ crossover peak. Derivative locks require demodulation of a signal with an applied frequency; in the case of the repump beam the laser itself is modulated, and in the case of the optical pumping laser the spectroscopy cell is modulated.

A mechanical shutter is placed on the cooler beam, as it is such high power that any light from incorrect orders through the AOM which are not fully cropped by the iris could affect the state of the atoms. As the imaging and state cleaning light are switched using the same AOM, a further mechanical shutter on the imaging beam ensures the state cleaning beam can be used separately. The detunings of the beams can be optimised by altering the radio-frequency applied to the AOM, adjusting the frequency to ensure optimal signal size at the end of the sequence, either in the absorption signal or the state-dependent detection signal as appropriate. This is performed using the same method as was shown in Figure 3.2b for the MOT frequency, and we note that the optical pumping must be calibrated using the appropriate initial m -level, and calibrating the absorption imaging frequency also ensures the state cleaning beam frequency is correct.

The other two lasers are beat-locked, although the spectroscopy for both the detection (Figure 5.3b) and cooler (Figure 5.3d) lasers are still measured so as to be able identify the frequency of the beatlock signal. In all spectroscopy plots (orange for optical pumping, turquoise for detection, pink for repump and red for cooler) the colours are the same as the labels in Figure 5.2. When two frequencies of light are combined using a mixer, the output light will be at two frequencies, the sum and the difference of the two inputs. With the use of appropriate low-pass filters to keep only the difference between the two signals, we can then use a mixer to combine the detected beat signal with a reference signal from an oscillator which is set at the desired frequency difference between the two lasers. The difference between these two signals can be minimised with the use of beat-lock electronics, as described in [6]. Such electronics provide a reference step-function signal shown in Figures 5.3b and 5.3d, which is high when the frequency difference is positive and low when negative, or visa versa. We therefore lock the laser to the edge of the function, where the frequency difference is zero. Only details of the common-mode suppressed, single detection beam laser set-up are given in Table 5.2 and associated figures, but originally two separate detection lasers were individually beat-locked to the optical pumping beam.

5.1.2 Optical Bench and Chamber Optics

In this section the paths taken by all beams on the optical bench and through the main chamber are explained. Firstly, the current system using four lasers to produce all beams is detailed, followed by the original six-laser system. Both systems have been used to take sets of data shown in this thesis, and some of the data was taken by the system at interim stages during the upgrade. The advantages of using the current system for common-mode suppression in the detection system were given in Section 4.2.3. Other changes to the system were made to increase its robustness and reduce experimental downtime.

Four Laser System

We see from Figure 5.4 that there are four lasers forming the six different frequencies of light. The correct laser frequencies are all generated on the main optical bench, and then taken to the main chamber set-up by six optical fibres and one periscope. The optical pumping and repump lasers both only provide a single frequency to be output to the main chamber. The detection laser provides both the $F = 1$ and $F = 2$ detection beams, using an EOM. The cooler laser provides the cooling light, as well as the absorption imaging and detection beams. This is the only laser with multiple outputs from the main optical bench (as both frequencies of detection beam are output through the same fibre). A periscope takes the high power cooler beam to the main set-up, and two optical fibres take each of the state cleaning and imaging beams, which are of the same frequency but require different paths through the chamber.

Figure 5.5 shows three different cuts through the main chamber optical set-up. A single cooler beam arrives in this region on the lower level below the chamber (Figure 5.5a), and is then split into three beams using two beam splitters. The vertical cooler beam is combined with repump light in order to provide all the necessary frequencies for locking. All MOT beams are retro-reflected, with waveplates providing the correct polarisations for trapping. As the spherical octagon main chamber has a total of five pairs of viewports, this allows the horizontal plane 3D MOT beams to be at 45° from both the detection beams in the z -direction and the imaging beam in the x -direction. Both the CCD and the balanced PD shown in Figure 5.5c allow for the relaying of data to the laboratory computer. The final two beams, for state cleaning and optical pumping, are mounted at a small angle from vertical, in order to pass through the region of the atomic cloud without requiring components blocking the x -direction MOT beam (Figure 5.5b).

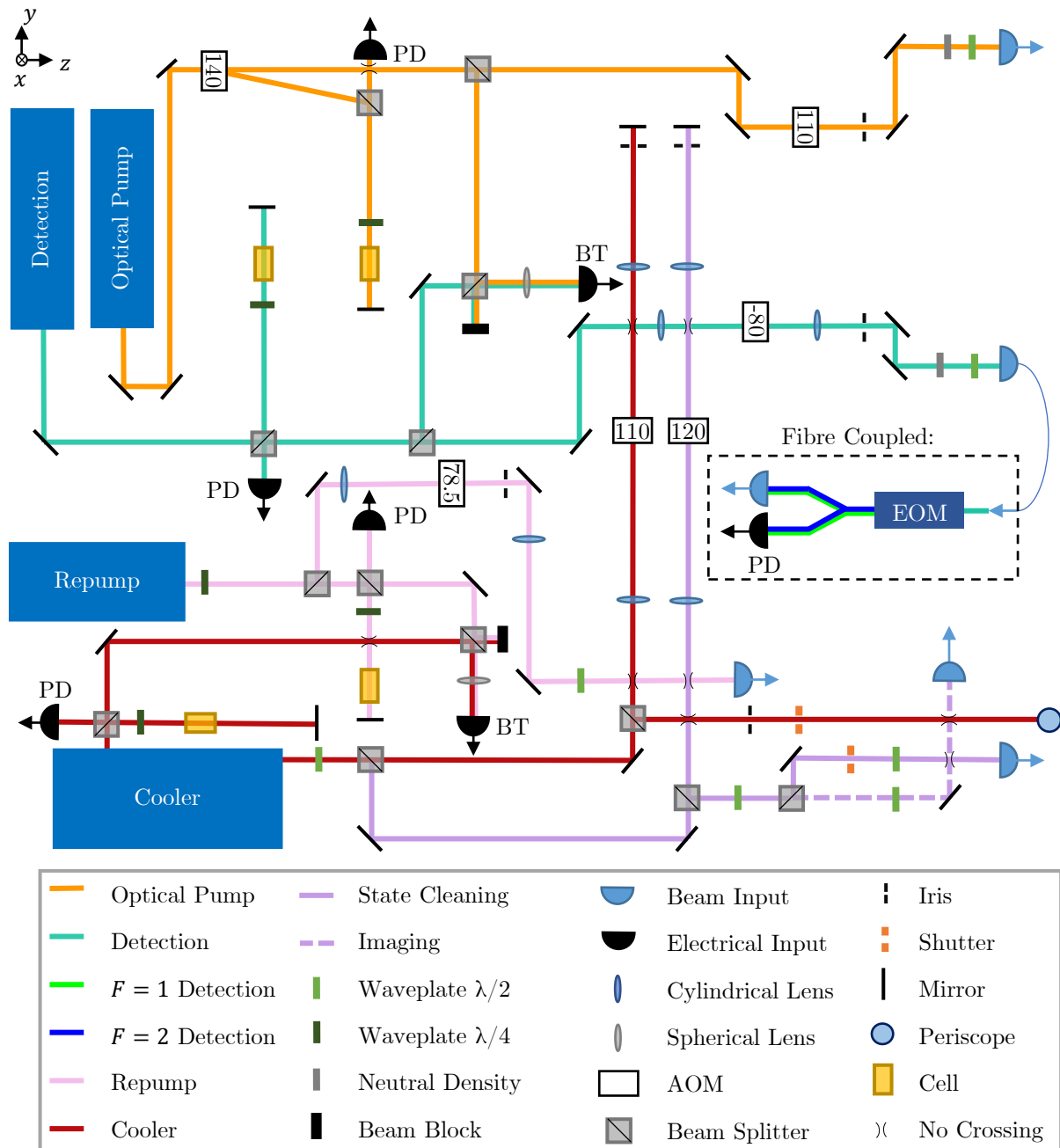


Figure 5.4: The figure shows the layout of the optical bench used in this experiment. The four lasers generate six beams of the correct frequency and power for output to the main chamber (Figure 5.5). Electronics labelled BT and PD are bias-tees and photodiodes respectively. AOMs display their modulation frequency $\omega_{\text{AOM}}/(2\pi)$ in MHz.

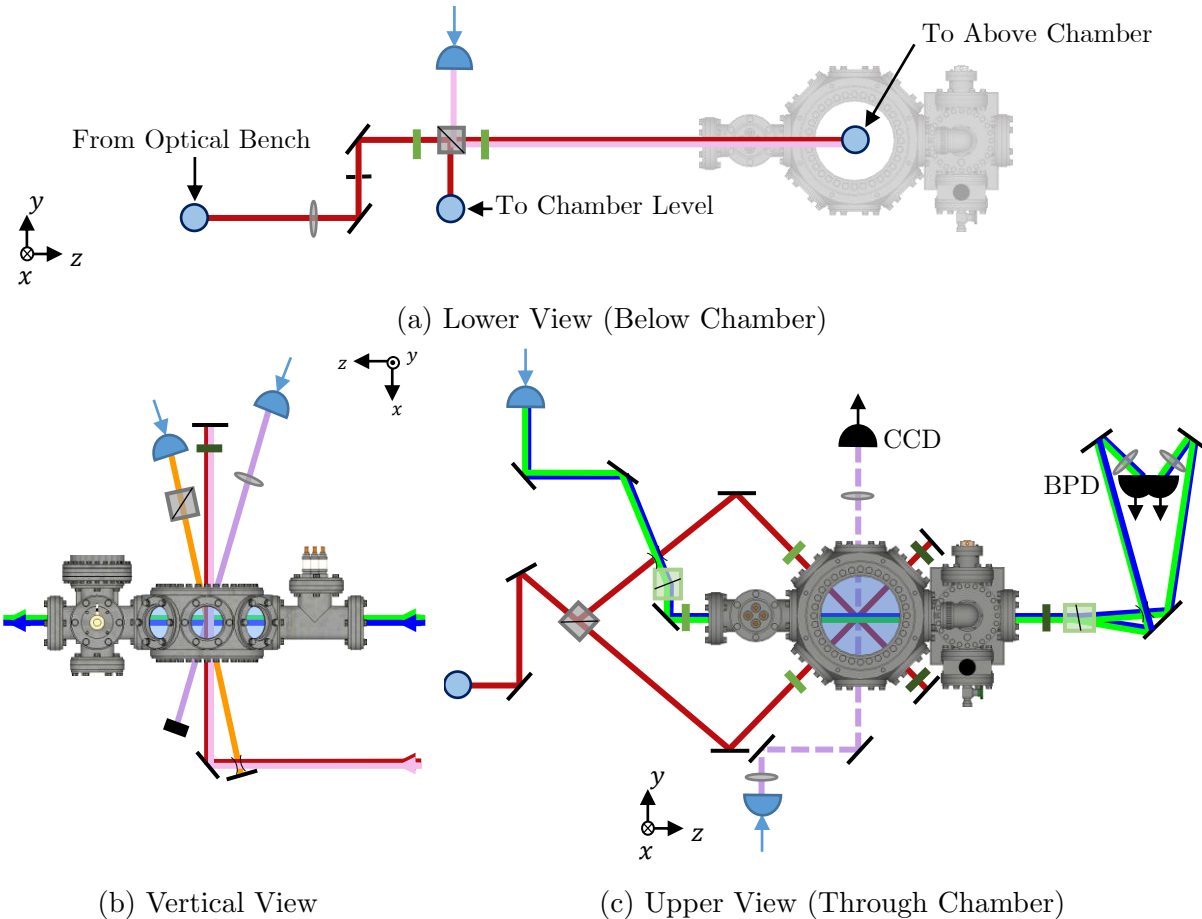
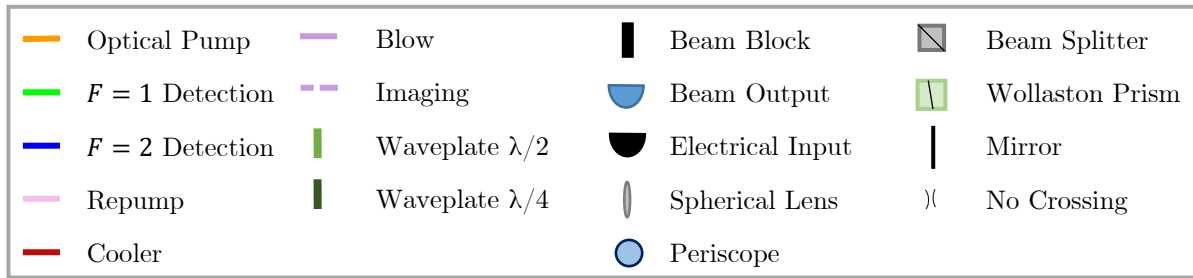


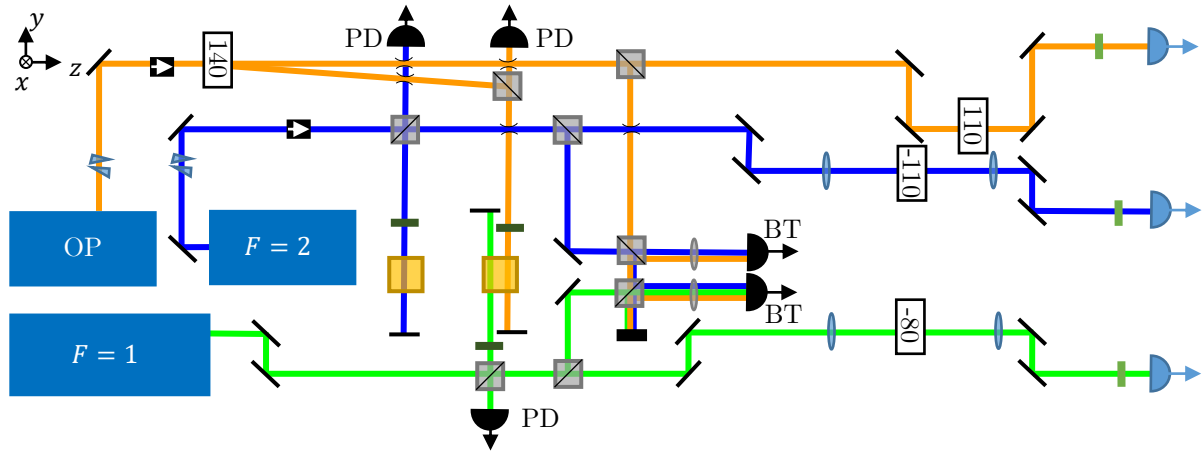
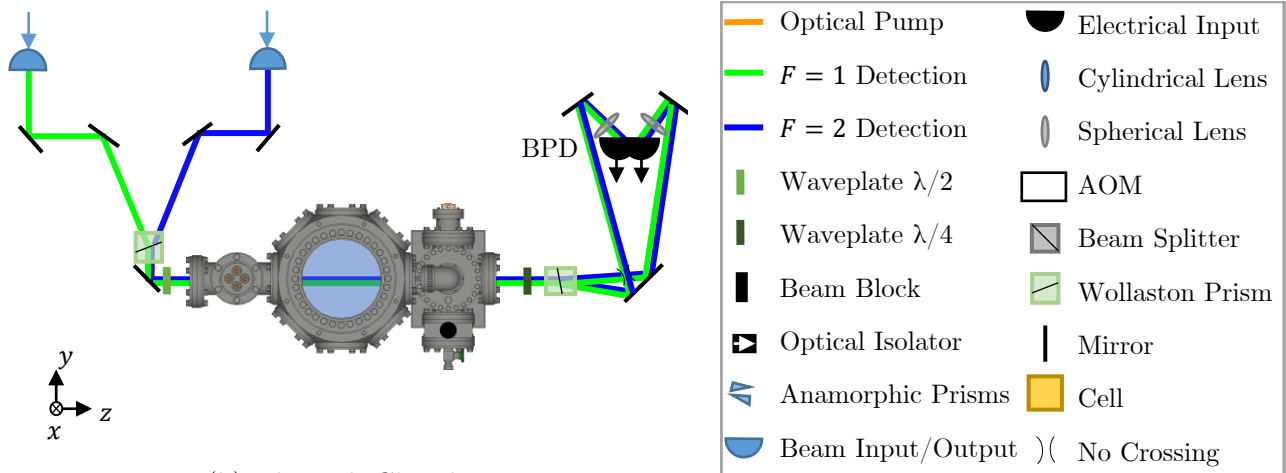
Figure 5.5: Beam paths cross through the main chamber from all three Cartesian directions. In (a) the optical bench below the main chamber is shown, where beams are distributed between the various levels labelled. In (b) we see beams in the $x - z$ plane, including all beams passing vertically through the main chamber. In (c) we see all beams passing horizontally (in the $y - z$ plane) through the main chamber. Electronics labelled BPD and CCD are the balanced photodiode and camera respectively.

Original System and Upgrades

The experiment has been altered from the original laser system in place at the beginning of my PhD. Details of the old system are provided as much of the spectroscopy data was taken using this set-up. Initially six ECDLs were used: three from Toptica Photonics and three home-built lasers. The Toptica lasers are still present in the experiment, but the home-built lasers have been removed and one further Toptica laser added. The cooler and repump lasers are unchanged, and the detection laser was already present but has moved position and purpose. The layout of the original $D1$ -laser system is shown in Figure 5.6a, where two lasers were used to generate the $F = 1$ and 2 detection components separately. The use of an EOM to generate both frequencies from a single laser has the advantage of providing common-mode suppression, as detailed in Section 4.2.3. The laser which originally produced the $F = 1$ detection beam is now providing simultaneous detection of both states. In the original case, the two detection beams were combined together using a Wollaston prism (Figure 5.6b) before entering the main chamber. Although overlapped in their path through the atom cloud, the beams were not both pulsed at the same time unlike in the current system.

Due to instabilities in the frequency of all the home-built lasers, which contained diodes approaching the end of their usable lifespan, these were all removed. In addition to the removal of the $F = 2$ detection laser, the optical pumping laser was replaced with a Toptica DL-Pro. The stability of the optical pumping laser is key to the functionality of the experiment, as it provides the reference for the beat signal locking the detection laser. Replacing the home-built ECDL, which is more susceptible to thermal drifts and mode-hopping, has improved the robustness of all three frequencies of light on the $D1$ -line. The imaging and state cleaning was originally produced by a separate home-built laser, but this has also been removed, and instead a small fraction of light from the cooler beam is picked off and used for this purpose. This is the only difference in the set-up of $D2$ -lasers compared to in Figure 5.4. Polarising beam splitters and waveplates allow for complete control over the power fraction in each of the beams.

The decreased maintenance needs of the experiment with fewer, more robust lasers, allows both for additional time the experiment is fully operational, as well as improving the quality of the data by reducing the amount of times a laser will come unlocked during an experimental run. The need to stop data taking, lock the lasers and delete any points with incorrect locking, introduces irregular time delays between data points. Due to drifts in atom number over the course of a day, the detected signals require normalisation by a fit to the total atom number. Any discontinuities in the smooth fit, due

(a) Optical Bench (*D1*-Lasers)

(b) Through Chamber

Figure 5.6: The beam paths for the laser system with two separate detection lasers are shown in the figure. The optical bench configuration for the *D1*-lasers is shown in (a). The method of combining these two beams at the vacuum chamber using a Wollaston prism is shown in (b), with other beams though this level the same as in Figure 5.5c. AOMs display their modulation frequency $\omega_{\text{AOM}}/(2\pi)$ in MHz.

to increased time between measurements, will lead to additional noise in the processed data. Some experimental runs take many hours, and therefore the lasers may come unlocked several times during one data set, so such irregularities are unavoidable. However, more robust locking reduces this effect. A further advantage is that the commercial lasers provide inbuilt optical isolation and beam shaping, as well as a different grating configuration, allowing

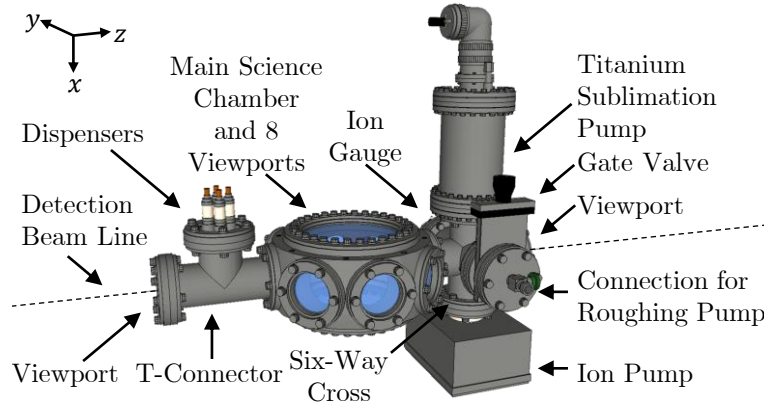


Figure 5.7: The figure shows a schematic of the vacuum system used in the experiment. Optical access to the chamber is possible through 10 viewports, and Rb dispensers and pumps are attached via a T and an 8-way connector to the main chamber respectively. Due to perspective, axes are only indicative.

for wavelength adjustment without changing the angle of the output beam.

5.2 Other Apparatus

In this section, we go through the various physical equipment and electronics necessary to run this experiment. We begin with the vacuum chamber set-up (Section 5.2.1), then detail the equipment used for generating the static and AC-magnetic fields (Section 5.2.2). The majority of this equipment was in place at the start of my PhD, see [97]. The new circuitry used to enable the generation of multiple MW-dressings is detailed in Section 5.2.3.

5.2.1 Vacuum Equipment and Dispensers

In order to be able to perform ultra-cold atom experiments, an ultra-high vacuum (UHV) system is a requirement. Typically UHV is classed as roughly $< 10^{-9}$ Torr, in the region of free molecular flow, where collisions with the chamber edges are much more common than collisions between atoms. As the lifetime of atoms in a MOT is inversely proportional to the vacuum pressure [17], the lower the pressure the better. Our vacuum system has a pressure of $\sim 5 \times 10^{-10}$ Torr, which gives a lifetime of the order of tens of seconds, which is adequate for our ~ 3 s sequences.

A schematic of the vacuum system is shown in Figure 5.7. The main chamber is where the atom cloud is trapped and manipulation of the internal state of the atom occurs. The spherical octagon chamber design, with eight small side ports and large ports at the top and bottom, has viewports fitted directly

to eight of the connectors. In order to attach all the necessary components for maintaining the vacuum in the chamber without removing optical access to the remaining two small chamber ports, connectors are required. On one side of the main chamber a T-connector horizontally attaches the main chamber to a viewport, as well as holding the vertically mounted Rb dispensers. The port on other side of the chamber connects to a six-way cross, which also contains a viewport, allowing optical access along the dashed line marked in the figure. Together with our main chamber viewports, this allows for significant optical access to the centre of the chamber.

The other components connected to the six-way cross are used to form and maintain the vacuum. The gate valve and connection for roughing pump allow for the initial pump down into a pressure range where the ion pump can take over. Before this stage a bakeout must be performed, where the chamber is wrapped in heating tape for several days to remove any contamination from inside the chamber which could lead to outgassing. At this stage the gate valve can be closed and the turbo pump safely removed, allowing the ion pump to maintain vacuum using a metal getter material which absorbs or otherwise reacts with particles in the chamber. The ion pump continuously sputters getter material in order to refresh the top layer. A titanium sublimation pump is also connected, which similarly releases a getter material, although this requires active heating of the titanium filament to refresh the getter. The titanium sublimation pump is used for removing active gases such as oxygen and carbon dioxide, whereas the ion pump removes inactive materials such as hydrogen and the noble gasses. For more details on vacuum systems see [184]. An ion gauge is also connected in order to monitor the vacuum pressure.

In addition to sufficiently high vacuum, we also require the presence of ^{87}Rb atoms in the chamber. For this we use dispensers which release atoms when heated by an applied current. Typically these dispensers take ~ 30 minutes to heat up to the requisite temperature for our desired atom number whilst at high current, and this can then be dropped over the course of the day to try maintain a relatively stable atom number. The maximum MOT number will be limited by the vapour pressure of ^{87}Rb in the chamber, and we find for a typical dispenser current this power is sufficient to trap $\approx 10^7$ atoms with a 2 s MOT time, which is adequate for our purposes. We keep our MOT times short as atom number has not been a key constraint with relatively new dispensers, whereas maximising the number of data points which can be taken in one day is important. Taking a single experimental run over multiple days is inadvisable due to atom number drifts which will lead to discontinuities in amplitude when piecing together data sets, and these cannot reliably be normalised out.

We do however normalise for atom number drifts over the course of a

long (\sim hours) experimental run, as smooth thermal drifts can be removed by a simple division by a polynomial fit to the total atom number (adding together the $F = 1$ and $F = 2$ signals, accounting for relative detection strength). Dispenser currents can be increased to reduce MOT times further, but due to the finite amount of ^{87}Rb available it is best not to run dispensers at maximum current continuously, as well as to turn these off overnight, in order to only need to break the vacuum and replace the dispensers once every few years. The system also had two sets of dispensers inbuilt, so when the first set failed a back-up was instantly available.

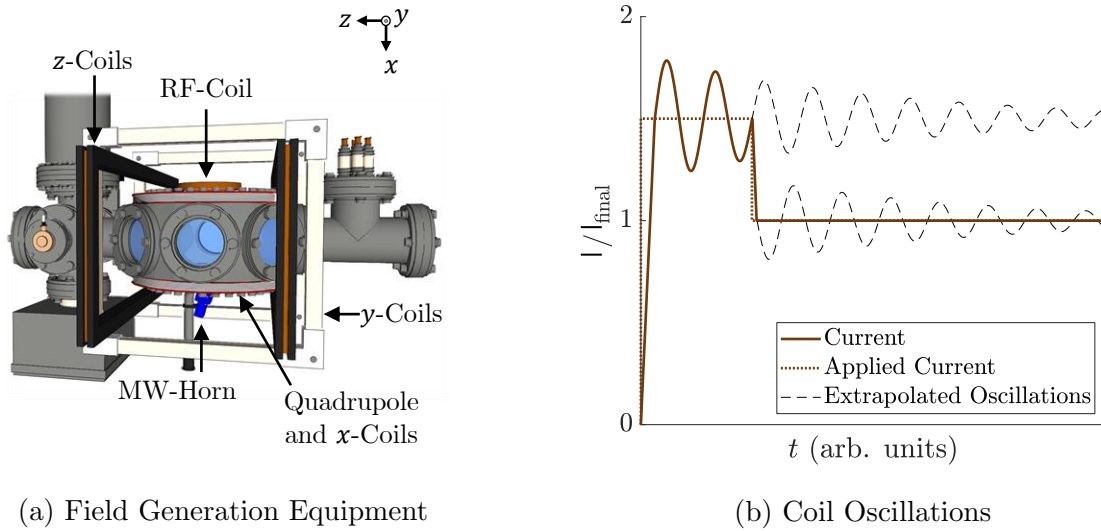
5.2.2 Magnetic Field Generation

A number of static and AC-magnetic fields are required in this experiment. Uniform magnetic fields can be generated with a pair of Helmholtz coils, which generate an approximately spatially invariant static magnetic field in the central region between the two coils. In Figure 5.8a the three pairs of coils around the the main chamber are shown; all pairs of coils must be oriented such that current flows in the plane perpendicular to the axis of the desired static field, and be centred on the main chamber. Due to residual static fields in the laboratory, both from geomagnetism and laboratory equipment, current compensation is provided in all three pairs of coils. The required compensation voltages are given in Table 5.3. These voltages are continuously applied, and are the zero offset for any voltages used to generate static fields. When altering static fields, in order to achieve fast switching the current is jumped to higher than required for ~ 1 ms, then jumped down to the required value in order to cancel oscillatory effects, as illustrated in Figure 5.8b. The current oscillations are of the form

$$I = I_{\text{final}} e^{-t/\tau} \sin(\omega_{\text{osc}} t), \quad (5.1)$$

Field	Compensation (V)	\mathbf{a} (V/G)
B_x	0.58	-
B_y	0.81	0.48 ± 0.02
B_z	-0.51	-7.0 ± 0.2

Table 5.3: Three pairs of mutually perpendicular Helmholtz coils are used to cancel residual static fields in the main chamber. The compensation voltage applied to each of coils is given in the table, and the calibration factors \mathbf{a} , the voltage per unit static field at the region of the atomic cloud, is also given. B_x is for compensation only.



(a) Field Generation Equipment

(b) Coil Oscillations

Figure 5.8: A schematic of the equipment used for generation of all static and AC-magnetic fields is shown in (a). Three pairs of coils are used for the static fields, and an RF-coil above and a MW-horn below the main chamber provide the required AC-fields. Due to perspective, axes are only indicative. In (b) the effects of jumping the current through a coil is shown. The set current is shown (dashed brown) in comparison to the actual current through the coil (solid brown). Oscillations which would occur with only a single current jump are shown in dashed black, as given by Eq. 5.1.

where I_{final} is the desired current, τ is the time constant of the damping and ω_{osc} is the current oscillation angular frequency, which is dependent on the coil inductance [26]. The duration and magnitude of the first current change needs to be calibrated such that the initial oscillation cancels the oscillation caused by the second jump.

The MOT quadrupole coils are wound on top of the x -coils, with one of the currents counter-propagating. We recall from Eq. 3.2 that the trapping force provided by the MOT is proportional to the spatial gradient of the static field, therefore the tightness of a quadrupole trap will increase with the current passed through the coils. For tight traps however, the capture volume for the atoms decreases. Our quadrupole current is slightly below the optimal for maximum atom capture, but sufficiently close for this not to be significant. The maximum input current is limited by our field-effect-transistors, used to reduce quasi-static field fluctuations after fast switching of the coil currents.

The resonant static magnetic field is known to be 257 mG due to the frequency of the applied RF-dressing at 180 kHz (Eq. 2.32). We calibrate

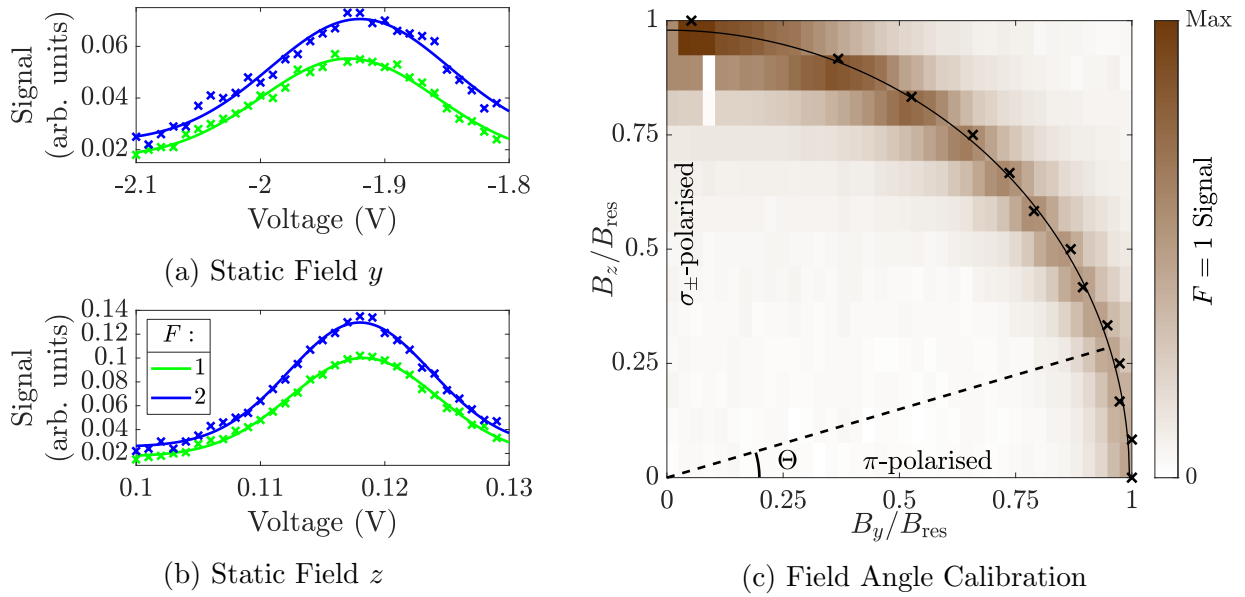


Figure 5.9: A graph of the measured atomic signal in both F -states is shown in (a) and (b) as a function of the voltage applied to the y and z -coils, giving the resonance voltages (-1.925 ± 0.003) V and (0.1182 ± 0.0002) V respectively. A colour-map of the detected signal from a pure $|1, -1\rangle$ state is shown in (c) for possible combinations of fields in the y and z -directions. A fit to the peak signal values shows a simple trigonometric relationship between the field angle and the coil voltages, after appropriate calibration factors are included.

the coils by preparing a 50 – 50 superposition of $F = 1$ and 2, and then use our detection method to measure the signal from each state as a function of voltage. The point at which the signal is maximal is the resonant static field. From Figures 5.9a and 5.9b for the y and z -coils respectively, we see that the resonances occur at (-1.925 ± 0.003) V and (0.1182 ± 0.0002) V. These values are averages of the two F -level resonances, which will differ slightly due to g_F -factor differences. To a good approximation, applied coil voltage is proportional static field, and as such we can use this data to obtain the static magnetic field generated by a given pair of coils as a function of voltage, giving the calibration values a in Table 5.3.

The orientation of the static field can be changed using a combination of currents in the y and z -coils. In Figure 5.9c, atoms are prepared in a dressed $|1, -1\rangle$ state. Scanning the magnitudes of the voltages in both the y and z -directions, we measure the final detected signal, which should be maximal at resonance. A Gaussian fit to the signal strength as a function of V_z for each set value of V_y gives the peak voltage, as marked with crosses. A circular fit

to the peak signal shows that the field angle Θ from the y -direction can be set by a combination of voltages (in Volts) V_y and V_z in the two respective coils, as given by

$$V_y = \mathbf{a}_y B_{\text{DC}} \sin(\Theta), \quad V_z = \mathbf{a}_z B_{\text{DC}} \cos(\Theta), \quad (5.2)$$

where B_{DC} is the desired static field (in Gauss) and \mathbf{a} are the appropriate calibration factors. This experimentally confirms that the field angle alters with voltage as expected from simple trigonometric rules.

The RF-fields are provided using a simple coil above the main chamber, connected to a generator. In order to protect against 50 Hz mains noise, we trigger our experimental sequence after the MOT stage by introducing a hold time to ensure the RF is phase locked to the AC-line trigger. The MW is generated using a wave-guide horn placed underneath the main chamber, which is optimised for the wavelengths required by our experiment. Both the RF-coil and MW-horn are labelled in Figure 5.8a. The flare of the horn is optimised for transmission of a given wavelength $\lambda = w^2/\sqrt{3}l$, where w is the width of the horn in the direction of the B -field and l is the length of the horn in this direction [8]. A Rohde and Schwarz MW-generator is used for spectroscopy. The power of the RF and MW at the location of the atoms cannot be directly measured, and we rely on measurements of the atomic signal to obtain this, as will be described in Sections 6.3.1 and 6.3.2 respectively.

5.2.3 Microwave-Dressing Generator

The generator used for MW-dressing (Section 7.2) consists of a different frequency sources, mixed in such a way as to be able to simultaneously provide multiple MW-dressings at various amplitudes and frequencies. This generator consists of two crystal-oscillators, at 6 GHz and 100 MHz. In order to generate the required frequencies in the region of 6.835 GHz, these signals are combined in the manner shown in Figure 5.10. After mixing the 6 GHz and 1 GHz signals (gained by frequency multiplying the 100 MHz frequency by a factor of ten) we have an output signal at a combination of 5 and 7 GHz (as mixers give out the sum and the difference of the two input signals). A four-slot programmable RF-generator card produces 165 MHz, which after mixing with a 7 GHz signal gives out 6.835 GHz. The frequency the RF-card can be tuned more finely to give the desired final frequency, accurate to < 1 kHz. Further combiners can be added to provide higher order dressings by connecting to other outputs of the RF-generator.

After mixing, a variety of other frequencies will be present, so a cavity tuned to (6.8 ± 0.1) GHz is used for filtering. A combiner is then used to put this signal into the same cable as the MW-probe from our separate generator, and both signals are then sent to the MW-horn. The output power of the

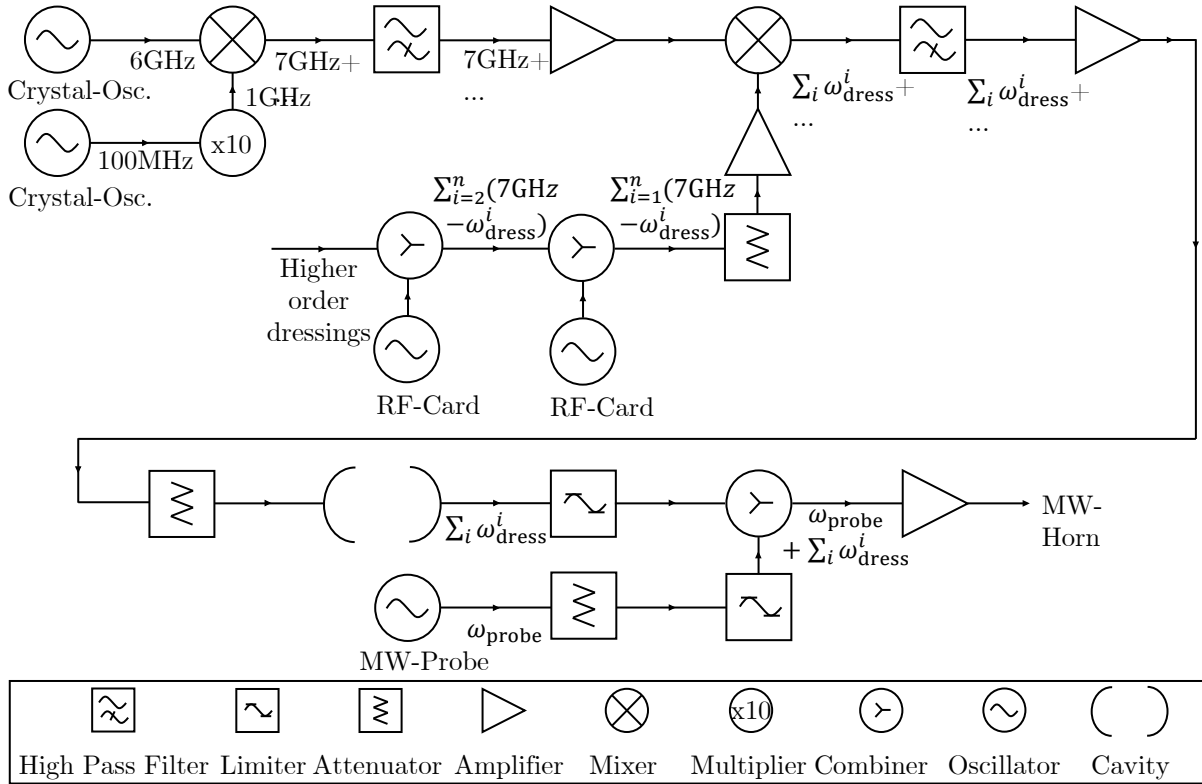


Figure 5.10: The figure shows the electrical diagram of the microwave dressing generator. Frequencies are labelled underneath the electrical connections. Note that high pass filters remove some but not all incorrect frequencies.

programmable RF-card is adjustable as well as the frequency, allowing for complete control over the individual dressings. Due to breakable components, a number of limiters and attenuators are in place in the set-up. Various filters remove any frequencies which, after mixing, may generate an undesired component within the permissible region of the band-pass cavity. Combinations of amplifiers and attenuators are used to get the required output power with the available components. All components are protected such that the maximum output power from the oscillators will not be outside the permissible range of later circuit components.

Chapter 6

Microwave Spectroscopy

In this chapter we make use of microwave fields to study the structure of and control the internal state of radio-frequency dressed ^{87}Rb atoms. In Section 6.1 we formulate theoretically the effect of applying MW-couplings between the ground state F -levels in alkali atoms, finding the coupling strengths of the transitions and their dependence on static magnetic field. As previously, more specific details are given for the case of ^{87}Rb . We then show experimental measurements of these transitions, with a focus on transition frequencies, strengths and linewidths (Section 6.2). The couplings between energy levels are also considered, both at the field resonance and as a function of static field (Section 6.3). The field dependence of transition frequencies is measured, and we then demonstrate the use of a particular transition for interferometry.

6.1 Theoretical Formulation

In this section we study the effect of applying MW-fields to the RF-dressed atom in order to facilitate transitions between F -manifolds. We begin by considering the possible transitions which arise due to the RF-dressed quasi-energies, and the MW-polarisations and frequencies required to address these (Section 6.1.1). We then use the rotating wave approximation to gain the strengths of the couplings between these levels (Section 6.1.2). This section contains theory developed with our collaborators at the University of Sussex and the Institute of Electronic Structure and Laser, Foundation for Research and Technology-Hellas, as detailed in our paper [167]. The bare coupling coefficients are also discussed (Section 6.1.3).

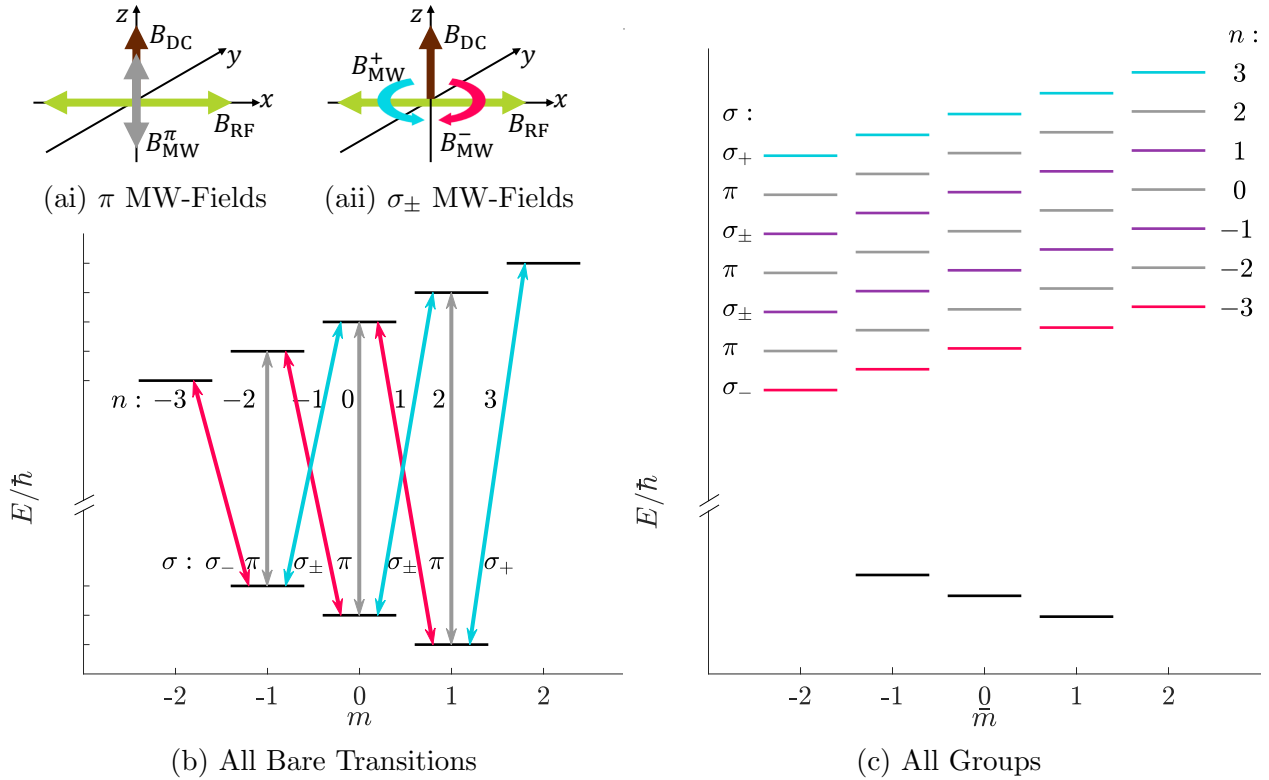


Figure 6.1: The figure shows RF-dressed groups of transitions and the corresponding MW-polarisations they can be addressed with. The π -polarised case (ai) has the MW parallel to the static magnetic field and perpendicular to the RF, and the σ_\pm -polarised case (aia) has all fields orthogonal. Note that the axis definitions in (ai) differ from those of physical space. The MW-field orientation is shown in red, grey and blue for σ_- , π and σ_+ respectively, with the DC-field shown in brown and the RF in lime (superposition of the green and yellow σ_\pm RF-couplings from Figure 2.3a). The required MW-polarisation to drive transitions in each group is labelled on the bare transitions in (b), in the same colours as in (a). The polarisation and group number is labelled to the left of each transition, with the exception of the degenerate cases. Each group forms a set of quasi-energy levels in the dressed case shown in (c), with the $F = 2$ levels shown in the colour corresponding to their appropriate bare transition polarisation (the superposition σ_\pm states are shown in purple). This is equivalent to displaying the groups as having a fixed set of $F = 2$ level energies and showing $F = 1$ as a set of quasi-energy levels. Note that the frequency spacing between the groups of levels is not to scale. Adapted from [97] and our paper [167].

6.1.1 Dressed Microwave Transitions

Working from the complete picture of the ground state energies of the RF-dressed levels in the weak field regime established in Chapter 2, we can consider the effects of adding couplings between magnetic sublevels in the two F -manifolds. These couplings will be of MW-frequency due to the energy splitting between the two manifolds of $E_{\text{HFS}} = \hbar\omega_{\text{HFS}} = h \times 6.8347$ GHz for ^{87}Rb [171]. As both the levels $|F, 0\rangle$ and $|F + 1, 0\rangle$ have no static field dependence, the transition between these levels is fixed at E_{HFS} . For the bare atom in the presence of a static field, m -levels in each manifold are spaced by $\hbar\omega_{\text{bare}} = \mu_B g_F B_{\text{DC}}$ (Eq. 2.13). Therefore transitions between F -manifolds will occur at

$$\omega_{\text{bare}, F, \bar{m} \rightarrow F+1, \bar{m}'} = \omega_{\text{HFS}} + \omega_{\text{bare}} m' - \omega_{\text{bare}} m \quad (6.1)$$

for all possible combinations of m and m' , given by $|m| \leq F$, $|m'| \leq F + 1$, $|m - m'| \leq 1$. Applying the RF-dressing $\omega_{\text{RF}} = \omega_{\text{bare}}$ causes the frequency of transitions between the \bar{m} levels in different F -manifolds to become

$$E_{F, \bar{m} \rightarrow F+1, \bar{m}'}^n = E_{\text{HFS}} + n\hbar\omega_{\text{RF}} + E_{F+1, \bar{m}'} - E_{F, \bar{m}}, \quad (6.2)$$

for transitions $|F, \bar{m}\rangle \rightarrow |F + 1, \bar{m}'\rangle$, where $E_{F, \bar{m}}$ is given by Eq. 2.43. n is the group number, which corresponds to the bare state transition being addressed. Using Eq. 2.42 we see that in the case of $B_{\text{DC}} = B_{\text{res}}$ then

$$\omega_{F, \bar{m} \rightarrow F+1, \bar{m}'}^n = \omega_{\text{HFS}} + n\omega_{\text{RF}} + \Omega_{\text{RF}}^+ \bar{m}' - \Omega_{\text{RF}}^- \bar{m}, \quad (6.3)$$

which is more helpful for the categorising of transitions, as we shall see in Section 6.2 when we study the full dressed spectrum.

We now consider the emergence and nature of the groups n , which are strongly dependent on the polarisation of the MW-probe. For the π -polarised MW case, the MW is parallel to the static field (Figure 6.1ai), and in the σ_{\pm} cases the MW rotates in the plane perpendicular to the static field with the appropriate helicity (Figure 6.1aii). Note that here we define the static field to be always in the z -direction, which for the π -polarised case requires a rotation by 90° in the $y - z$ plane with respect to the coordinate system defined for the laboratory, such as that shown in Figure 5.5. This is due to our experiment having a fixed MW-field direction, due to the single stationary MW-horn, and altering the polarisation experienced by the atoms by controlling the static field orientation. Photons of polarisation $\sigma = \sigma_{\pm}, \pi$ have angular momentum $\varsigma = \pm 1, 0$ respectively. The group number $|n| \leq 2F + 1$ (where the value F is that of the lower of the two levels), and the number of transitions which can be addressed with each polarisation of MW is given by $2F + 1$. In ^{87}Rb we have $|n| \leq 3$, so three bare transitions are possible to address with each polarisation, giving a total of 9 possible transitions. The polarisation σ_-

forms the groups $n = -3, -1, 1$, π forms the groups $n = -2, 0, 2$ and σ_+ forms groups $n = -1, 1, 3$. These transitions are labelled in Figure 6.1b, where we see that the groups $n = \pm 1$ can be addressed by two polarisations σ_{\pm} . In the general case, a total of $6F + 3$ bare transitions are allowed by the standard selection rules, $2F$ of which will be degenerate.

For our purposes, because our MW is linearly-polarised and we therefore cannot generate the σ_{\pm} -polarisations separately, we treat our dressed ^{87}Rb atom as having a set of 7 groups. Each of these forms a set of quasi-energy levels at multiples of the RF-dressing frequency, as shown in Figure 6.1c. The RF-dressing field in our experiment is relatively weak, with an RF Rabi frequency more than 10 times smaller than the dressing frequency, with $\omega_{\text{RF}}/(2\pi) = 180$ kHz and $\Omega_{\text{RF}}^{\pm}/(2\pi) \approx 12$ kHz, meaning that there is no overlap in frequency between transitions in different groups at around the resonant static field. The purpose of the application of a MW-field is to spectroscopically probe the transitions, and for the preparation of atoms in any chosen state. In full Floquet theory, these quasi-energy levels are a consequence of the periodic boundary conditions of the system [105], meaning that energy levels in groups $|n| \geq 2F + 2$ also exist, but are much suppressed and therefore we discount these from our model.

In our experiment, spectroscopy is performed by preparing a pure $|F, \bar{m}\rangle$ state and then applying a MW-pulse of some frequency ω_{MW} . If population is transferred between F -levels by the application of the MW, this frequency is close to that of a transition. The experimental implementation of this method in the bare case was described in Section 3.2.1. To theoretically model this in the dressed case, first we must formulate the effects of the addition of a new magnetic field. This will add a new term to Eq. 2.19, causing the total field to become

$$\hat{\mathbf{B}}(t) = \hat{\mathbf{B}}_{\text{DC}} + \hat{\mathbf{B}}_{\text{RF}}(\omega_{\text{RF}}t) + \hat{\mathbf{B}}_{\text{MW}}(\omega_{\text{MW}}t). \quad (6.4)$$

The MW is of a form similar to that of the RF from Eq. 2.21:

$$\begin{aligned} \hat{\mathbf{B}}_{\text{MW}}(\omega t) &= \hat{\mathbf{B}}_{\text{MW}} e^{-i\omega_{\text{MW}}t} + \hat{\mathbf{B}}_{\text{MW}}^* e^{i\omega_{\text{MW}}t}, \\ \hat{\mathbf{B}}_{\text{MW}} &= B_{\text{MW}}^+ \hat{\mathbf{e}}_+ + B_{\text{MW}}^- \hat{\mathbf{e}}_- + B_{\text{MW}}^{\pi} \hat{\mathbf{e}}_{\pi}. \end{aligned} \quad (6.5)$$

We then require an additional component in the total Hamiltonian to account for the MW-field

$$\hat{H}_{\text{tot}} = \hat{H}_0^F + \hat{H}_{\text{DC}} + \hat{H}_{\text{RF}} + \hat{H}_{\text{MW}}. \quad (6.6)$$

It is now necessary to transfer to a rotating frame by a method similar to the RF-case in Sec. 2.2.2.

6.1.2 Rotating Wave Approximation

This derivation follows the formalism detailed in our paper [167]. Using the same form as Eq.s 2.12 and 2.38, we have the Hamiltonian

$$\hat{H}_{\text{MW}} = \mu_B g_J \hat{\mathbf{B}}_{\text{MW}} \cdot \hat{\mathbf{J}}, \quad (6.7)$$

where we are now using $\hat{\mathbf{J}}$ instead of $\hat{\mathbf{F}}$ as the MW is coupling between F -manifolds, and it is therefore no longer valid to treat the vectors with respect to a single value $\hat{\mathbf{F}}$. We are once again using spherical polar coordinates as defined in Eq. 2.20, and the angular momentum relations from Appendix A.1. Accounting for all polarisations we obtain

$$\hat{H}_{\text{MW}} = \sum_{\sigma \in \{-, \pi, +\}} \eta_\sigma \mu_B g_J (B_{\text{MW}}^\sigma e^{-i\omega t} \hat{\mathcal{J}}_\sigma + B_{\text{MW}}^{\sigma*} e^{i\omega t} \hat{\mathcal{J}}_{-\sigma}), \quad (6.8)$$

similarly to the RF case in Eq. 2.24, with η_σ given by Eq. 2.25. The components of angular momentum $\mathcal{J}_{\pm, \pi}$ should not be confused with the ladder operators, which they relate to by

$$\hat{\mathcal{J}}_+ = -\frac{1}{\sqrt{2}} \hat{J}_+, \quad \mathcal{J}_\pi = \hat{J}_z, \quad \hat{\mathcal{J}}_- = \frac{1}{\sqrt{2}} \hat{J}_-. \quad (6.9)$$

We note that $\mathcal{J}_\pi \equiv \mathcal{J}_0$ found elsewhere in literature [60].

We recall that $\sigma = \sigma_\pm, \pi$ for $\varsigma = \pm 1, 0$. As previously, for subscripts we are using the notational simplification $\sigma_- = -\sigma_+$ and $\pi = -\pi$, which states that different values σ relate in the same way as their associated angular momenta ς . Because \hat{B}^* must be counter rotating with respect to \hat{B} , and will therefore couple to a different spin component of \hat{J} in the case of σ_\pm -polarisation, we introduce the MW-field components

$$\begin{aligned} \mathbf{B}_{\text{MW}}^\sigma = & (1 - \delta_{\sigma, \pi}) (B_{\text{MW}}^\sigma + B_{\text{MW}}^{-\sigma*}) e^{i\varsigma \omega_{\text{MW}} t} \\ & + \delta_{\sigma, \pi} (B_{\text{MW}}^\pi e^{i\omega_{\text{MW}} t} + B_{\text{MW}}^{\pi*} e^{-i\omega_{\text{MW}} t}) \end{aligned} \quad (6.10)$$

in order to simply the Hamiltonian as a sum of spin components

$$\hat{H}_{\text{MW}} = \mu_B g_J \sum_{\sigma \in \{-, \pi, +\}} \eta_\sigma \mathbf{B}_{\text{MW}}^\sigma \hat{\mathcal{J}}_\sigma. \quad (6.11)$$

Using the same method we applied to \hat{F} in Eq. 2.51, we now require two rotations. We begin with the rotation around the RF-field using the same $\hat{U}_\pm = e^{\pm i\omega_{\text{RF}} t F_z}$ from Eq. 2.27 (setting $\varphi = 0$). Our second rotation is around θ_F , as defined in Eq. 2.47. This operator is labelled $\hat{U}_y(\theta_{F+1}, \theta_F)$, and accounts for rotations in the two different manifolds. It is related to the single manifold rotation operator $\hat{U}_y(\theta_F)$ from Eq. 2.49.

Applying these rotations to $\hat{\mathbf{J}}$ gives

$$\hat{\mathbf{J}} = \hat{U}_y^\dagger(\theta_{F+1}, \theta_F) \hat{U}_\pm^\dagger(\omega_{\text{RF}}t) \hat{\mathbf{J}} \hat{U}_\pm(\omega_{\text{RF}}t) \hat{U}_y(\theta_{F+1}, \theta_F), \quad (6.12)$$

which allows the transformation of the Hamiltonian into the rotating frame given by

$$\hat{H}_{\text{MW}}^{\text{rot}} = \mu_B g_J \sum_{\sigma \in -, \pi, +} \eta_\sigma \mathbf{B}_{\text{MW}}^\sigma \hat{\mathcal{J}}_\sigma. \quad (6.13)$$

To formulate the coupling of states $|F, \bar{m}\rangle \leftrightarrow |F+1, \bar{m}'\rangle$ we require the element $\langle F+1, \bar{m}' | \hat{\mathcal{J}}_\sigma | F, \bar{m} \rangle$. Note that although in our system we only have values $F = 1, 2$ as we are interested in ^{87}Rb , this treatment is valid for any RF-dressed alkali atom in the ground state and the weak field regime. As such the formulation is left general with regards to the F -value. We make use of the identity in a single manifold

$$\mathbb{1} = \sum_{m=-F}^F |F, m\rangle \langle F, m|, \quad (6.14)$$

and Eq. 6.12 to gain the expression

$$\begin{aligned} \langle F+1, \bar{m}' | \hat{\mathcal{J}}_\sigma | F, \bar{m} \rangle &= \sum_{m'=-F+1}^{F+1} \sum_{m=-F}^F \langle F+1, \bar{m}' | \hat{U}_\pm^\dagger(\omega_{\text{RF}}t) \hat{U}_y^\dagger(\theta_{F+1}) | F+1, m' \rangle \\ &\times \langle F+1, m' | \hat{\mathcal{J}}_\sigma | F, m \rangle \langle F, m | \hat{U}_y(\theta_F) \hat{U}_\pm(\omega_{\text{RF}}t) | F, \bar{m} \rangle. \end{aligned} \quad (6.15)$$

As the identity commutes with F_z , and therefore \hat{U}_\pm :

$$\begin{aligned} \langle F+1, \bar{m}' | \hat{\mathcal{J}}_\sigma | F, \bar{m} \rangle &= \sum_{m'=-F+1}^{F+1} \sum_{m=-F}^F \langle F+1, \bar{m}' | \hat{U}_y^\dagger(\theta_{F+1}) | F+1, m' \rangle e^{im'\omega_{\text{RF}}t} \\ &\times \langle F+1, m' | \hat{\mathcal{J}}_\sigma | F, m \rangle e^{im\omega_{\text{RF}}t} \langle F, m | \hat{U}_y(\theta_F) | F, \bar{m} \rangle, \end{aligned} \quad (6.16)$$

where we have substituted in for $\hat{U}_\pm(\omega_{\text{RF}}t)$ and used the fact that the rotation operator is diagonal in this basis to simplify.

Although rotation in a single manifold may be gained simply from Eq. 2.55, transitions between F -manifolds require a more complex treatment using Wigner d -matrices. The Wigner d -matrix is given by

$$d_{\bar{m}', \bar{m}}^F(\theta_F) = \langle F, \bar{m}' | \hat{U}_y(\theta_F) | F, \bar{m} \rangle, \quad (6.17)$$

which is simply the rotated form of $\hat{U}_y(\theta_F)$. These matrices allow the formulation of states which are a superposition of different $|F, \bar{m}\rangle$ states, including for different values of F . For more details on Wigner d -matrices, see Appendix A.4, where the matrices for $F = 1, 2$ are given in full by Eq. A.34 and

Eq. A.35 respectively. If we now substitute this into Eq. 6.16, we obtain

$$\begin{aligned} \langle F+1, \bar{m}' | \hat{\mathcal{J}}_\sigma | F, \bar{m} \rangle &= \sum_{m'=-F+1}^{F+1} \sum_{m=-F}^F d_{\bar{m}', m'}^{F+1}(-\theta_{F+1}) e^{i(m'+m)\omega_{\text{RF}}t} \\ &\times d_{m, \bar{m}}^F(\theta_F) \langle F+1, m' | \hat{\mathcal{J}}_\sigma | F, m \rangle. \end{aligned} \quad (6.18)$$

We see from this that the dressed transition $|F, \bar{m}\rangle \leftrightarrow |F+1, \bar{m}'\rangle$ is simply a rotated version of the undressed transition $|F, m\rangle \leftrightarrow |F+1, m'\rangle$. We now require use of the the Wigner-Eckart Theorem, which states that for some tensor $T_{m_j}^j$ the m_j dependence can be extracted, giving

$$\langle j_1, m_1 | T_{m_2}^{j_2} | j_3, m_3 \rangle = (-1)^{j_1-m_1} \begin{pmatrix} j_1 & j_2 & j_3 \\ -m_1 & m_2 & m_3 \end{pmatrix} \langle j_1 || T^{j_2} || j_3 \rangle, \quad (6.19)$$

where the 3×2 matrix is the Wigner $3j$ -symbol discussed in Appendix A.3 [60]. The values of these matrices can be calculated using the Racah equation, Eq. A.26 [144].

We can calculate the irreducible tensor operator $\langle F+1 || \mathcal{J}^1 || F \rangle$ by choosing the simplest matrix element to obtain from product space analysis $\langle F+1, 0 | \mathcal{J}_0^1 | F, 0 \rangle = 1/2$, and rearranging to see that

$$\langle F+1 || \mathcal{J}^1 || F \rangle = (-1)^{-F-1} \langle F+1, 0 | \mathcal{J}_0^1 | F, 0 \rangle / \begin{pmatrix} F+1 & 1 & F \\ 0 & 0 & 0 \end{pmatrix}. \quad (6.20)$$

Substituting in for the $3j$ -matrix result from Eq. A.30 therefore finds

$$\langle F+1 || \mathcal{J}^1 || F \rangle = \sqrt{\frac{2I(I+1)}{2I+1}}, \quad (6.21)$$

which we can then substitute back into Eq. 6.19 to obtain the result

$$\langle F+1, m' | \hat{\mathcal{J}}_\sigma | F, m \rangle = (-1)^{F+1-m'} \sqrt{\frac{2I(I+1)}{2I+1}} \begin{pmatrix} F+1 & 1 & F \\ -m' & \varsigma & m \end{pmatrix}. \quad (6.22)$$

We now recall the conservation of momentum requirement $m' = m + \varsigma$, which allows us to simplify our equation to no longer sum over forbidden values of m' for a given m (which would result in a Wigner $3j$ term equal to zero). Plugging Eq. 6.22 into Eq. 6.18 and making this simplification gives

$$\begin{aligned} \langle F+1, \bar{m}' | \hat{\mathcal{J}}_\sigma | F, \bar{m} \rangle &= (-1)^{F+1-m-\varsigma} \sqrt{\frac{2I(I+1)}{2I+1}} \sum_{m=-F}^F d_{\bar{m}', m+\varsigma}^{F+1}(-\theta_{F+1}) \\ &\times d_{m, \bar{m}}^F(\theta_F) e^{i(2m+\varsigma)\omega_{\text{RF}}t} \begin{pmatrix} F+1 & 1 & F \\ -m-\varsigma & \varsigma & m \end{pmatrix}. \end{aligned} \quad (6.23)$$

If we then put this into Eq. 6.13 we obtain our rotating frame Hamiltonian

$$\begin{aligned} \langle F+1, \bar{m}' | \hat{H}_{\text{MW}} | F, \bar{m} \rangle &= \mu_B g_J (-1)^{F+1-m-\varsigma} \sqrt{\frac{2I(I+1)}{2I+1}} \\ &\times \sum_{\varsigma=-1}^1 \sum_{m=-F}^F \eta_\sigma \mathbf{B}_{\text{MW}}^\sigma d_{\bar{m}', m+\varsigma}^{F+1}(-\theta_{F+1}) d_{m, \bar{m}}^F(\theta_F) \\ &\times e^{i(2m+\varsigma)\omega_{\text{RF}}t} \begin{pmatrix} F+1 & 1 & F \\ -m-\varsigma & \varsigma & m \end{pmatrix}, \end{aligned} \quad (6.24)$$

where as previously $\sigma = \sigma(\varsigma)$. Decomposing the Hamiltonian into the polarisation constituents

$$\hat{H}_{\text{MW}}^\sigma = \sum_n \left(\hat{H}_{\text{MW}}^{\sigma, n} e^{-i(\omega_{\text{MW}} + n\omega_{\text{RF}})t} + \hat{H}_{\text{MW}}^{\sigma, n*} e^{i(\omega_{\text{MW}} + n\omega_{\text{RF}})t} \right) \quad (6.25)$$

allows the removal of the time dependence, as well as the simplification of the \mathbf{B}_{MW} term, giving us the final result

$$\begin{aligned} \langle F+1, \bar{m}' | \hat{H}_{\text{MW}}^{\sigma, n=2m+\varsigma} | F, \bar{m} \rangle &= \mu_B g_J \text{sign}(1-2\varsigma) (-1)^{F+1-m-\varsigma} \left(\frac{1}{\sqrt{2}}\right)^\varsigma \sqrt{\frac{2I(I+1)}{2I+1}} \\ &\times B_{\text{MW}}^\sigma d_{\bar{m}', m+\varsigma}^{F+1}(-\theta_{F+1}) d_{m, \bar{m}}^F(\theta_F) \begin{pmatrix} F+1 & 1 & F \\ -m-\varsigma & \varsigma & m \end{pmatrix}, \end{aligned} \quad (6.26)$$

where we have substituted in for η_σ from Eq. 2.25. We should also explicitly note that

$$\langle F+1, \bar{m}' | \hat{H}_{\text{MW}}^{\sigma, n \neq 2m+\varsigma} | F, \bar{m} \rangle = 0, \quad (6.27)$$

due to the angular momentum selection rules. The relationship between the σ_\pm -polarisation components of the Hamiltonian will be given by

$$\langle F+1, \bar{m}' | \hat{H}_{\text{MW}}^{\sigma, n} | F, \bar{m} \rangle = \frac{B_{\text{MW}}^\sigma}{B_{\text{MW}}^{-\sigma}} (-1)^{\varsigma + \bar{m}' + \bar{m} - 1} \langle F+1, \bar{m}' | \hat{H}_{\text{MW}}^{-\sigma, -n} | F, -\bar{m} \rangle. \quad (6.28)$$

It is convenient to normalise the full Hamiltonians by a factor

$$\Omega_{\text{norm}}^\sigma = \frac{1}{16} \sqrt{\frac{3}{2}} \mu_B g_J B_{\text{MW}}^\sigma \quad (6.29)$$

in order to simplify the expression when using this for ^{87}Rb ($I = 3/2$). The complete set of tables and plots for all normalised non-zero Hamiltonians are given in Appendix B.1. As we are using linearly-polarised MW, and therefore cannot apply a MW-field in B_{MW}^+ without also applying B_{MW}^- and visa versa, it is also required to consider the combination of the two fields $\frac{1}{\sqrt{2}}(B_{\text{MW}}^+ + B_{\text{MW}}^-)$, for which the equations and plots are shown in Appendix B.2. All plots in

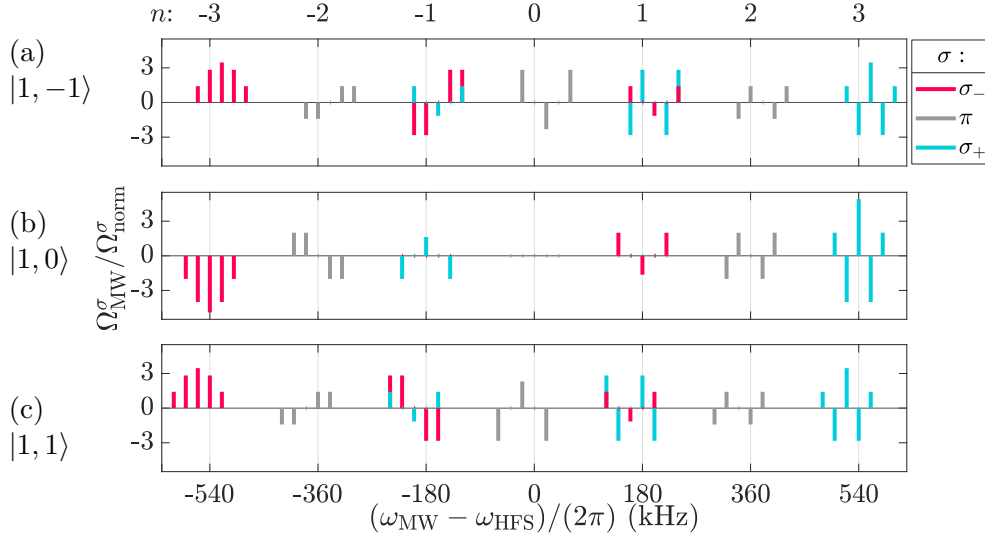


Figure 6.2: Relative magnitudes of coupling strength for each transition in the approximation $g_2 = -g_1 = 0.5$ at the static field resonance. Numerical values for all couplings are given in Table 6.1. Adapted from our paper [167] ($\Omega_{\text{norm}}^\sigma$ differs by η_σ).

transition	n	$\hat{H}_{\text{MW,res}}^- / \Omega_{\text{norm}}^-$			$\hat{H}_{\text{MW,res}}^\pi / \Omega_{\text{norm}}^\pi$			$\hat{H}_{\text{MW,res}}^+ / \Omega_{\text{norm}}^+$			$\Delta\bar{m}$
		-3	-1	1	-2	0	2	-1	1	3	
$ 1, -1\rangle \leftrightarrow 2, -2\rangle$		$\sqrt{2}$	$-2\sqrt{2}$	$\sqrt{2}$	$-\sqrt{2}$	$2\sqrt{2}$	$-\sqrt{2}$	$\sqrt{2}$	$-2\sqrt{2}$	$\sqrt{2}$	-1
$ 1, -1\rangle \leftrightarrow 2, -1\rangle$		$2\sqrt{2}$	$-2\sqrt{2}$	0	$-\sqrt{2}$	0	$\sqrt{2}$	0	$2\sqrt{2}$	$-2\sqrt{2}$	0
$ 1, -1\rangle \leftrightarrow 2, 0\rangle$		$2\sqrt{3}$	0	$-\frac{2}{\sqrt{3}}$	0	$-\frac{4}{\sqrt{3}}$	0	$-\frac{2}{\sqrt{3}}$	0	$2\sqrt{3}$	1
$ 1, -1\rangle \leftrightarrow 2, 1\rangle$		$2\sqrt{2}$	$2\sqrt{2}$	0	$\sqrt{2}$	0	$-\sqrt{2}$	0	$-2\sqrt{2}$	$-2\sqrt{2}$	2
$ 1, -1\rangle \leftrightarrow 2, 2\rangle$		$\sqrt{2}$	$2\sqrt{2}$	$\sqrt{2}$	$\sqrt{2}$	$2\sqrt{2}$	$\sqrt{2}$	$\sqrt{2}$	$2\sqrt{2}$	$\sqrt{2}$	3
$ 1, 0\rangle \leftrightarrow 2, -2\rangle$		-2	0	2	2	0	-2	-2	0	2	-2
$ 1, 0\rangle \leftrightarrow 2, -1\rangle$		-4	0	0	2	0	2	0	0	-4	-1
$ 1, 0\rangle \leftrightarrow 2, 0\rangle$		$-2\sqrt{6}$	0	$-2\sqrt{\frac{2}{3}}$	0	0	0	$2\sqrt{\frac{2}{3}}$	0	$2\sqrt{6}$	0
$ 1, 0\rangle \leftrightarrow 2, 1\rangle$		-4	0	0	-2	0	-2	0	0	-4	1
$ 1, 0\rangle \leftrightarrow 2, 2\rangle$		-2	0	2	-2	0	2	-2	0	2	2
$ 1, 1\rangle \leftrightarrow 2, -2\rangle$		$\sqrt{2}$	$2\sqrt{2}$	$\sqrt{2}$	$-\sqrt{2}$	$-2\sqrt{2}$	$-\sqrt{2}$	$\sqrt{2}$	$2\sqrt{2}$	$\sqrt{2}$	-3
$ 1, 1\rangle \leftrightarrow 2, -1\rangle$		$2\sqrt{2}$	$2\sqrt{2}$	0	$-\sqrt{2}$	0	$\sqrt{2}$	0	$-2\sqrt{2}$	$-2\sqrt{2}$	-2
$ 1, 1\rangle \leftrightarrow 2, 0\rangle$		$2\sqrt{3}$	0	$-\frac{2}{\sqrt{3}}$	0	$\frac{4}{\sqrt{3}}$	0	$-\frac{2}{\sqrt{3}}$	0	$2\sqrt{3}$	-1
$ 1, 1\rangle \leftrightarrow 2, 1\rangle$		$2\sqrt{2}$	$-2\sqrt{2}$	0	$\sqrt{2}$	0	$\sqrt{2}$	0	$2\sqrt{2}$	$-2\sqrt{2}$	0
$ 1, 1\rangle \leftrightarrow 2, 2\rangle$		$\sqrt{2}$	$-2\sqrt{2}$	$\sqrt{2}$	$\sqrt{2}$	$-2\sqrt{2}$	$\sqrt{2}$	$\sqrt{2}$	$-2\sqrt{2}$	$\sqrt{2}$	1

Table 6.1: Relative magnitudes of coupling strength for each transition in the approximation $g_2 = -g_1 = 0.5$ at the static field resonance, calculated using Eq. 6.26. Cell colours correspond to the data sets in Figure 6.2.

Appendix B are as a function of static magnetic field, as θ_F (Eq. 2.47) in the Wigner rotation matrices is a function of B_{DC} .

If we make the approximation $g_2 = -g_1 = 0.5$, the coupling coefficients at the static field resonance ($\theta_1 = \theta_2 = \pi/2$) are as shown in Figure 6.2. The figure shows the coupling coefficients of all transitions from $|1, \bar{m}\rangle$ for $\bar{m} = -1, 0, 1$ in panels (a-c) respectively. Transition frequencies are given by Eq. 6.3, with $\omega_{\text{RF}}/(2\pi) = 180$ kHz and $\Omega_{\text{RF}}^{\pm}/(2\pi) = 20$ kHz. The chosen RF-field strength in the plot is roughly a factor of 2 greater than that used in our experiment, in order to clearly separate all transitions in the figure. We recall that each polarisation can only drive one bare state transition per $|1, m\rangle$ level, which accounts for the three groups of transitions per polarisation. The corresponding group n for each set of transitions is also labelled, with dashed lines indicating the group centre frequencies. The corresponding values of the coupling coefficients for each transition are given in Table 6.1. We also recall that each group will contain 5 transitions to $|2, \bar{m}'\rangle$ for each possible value of \bar{m} . It can be seen in the figure that some of these transitions are missing, for instance in Figure 6.2b the entire set of transitions $|1, 0\rangle \leftrightarrow |2, \bar{m}'\rangle$ cannot be seen. This is because in the given approximation all of these couplings have a strength of zero. We call these suppressed transitions, because they cannot easily be driven on resonance (note that in the real case, using the non-approximated values of g_F , there is a negligible non-zero coupling).

In the following sections we will see that suppressed transitions do not appear strongly when using the MW-spectroscopy technique to scan the spectrum. We will also make measurements of the predicted coupling strengths using the Rabi frequencies of the transitions, where the Rabi frequencies are given by

$$\left| \hat{H}_{\text{MW}}^{\sigma, n} \right| = \hbar \Omega_{\text{MW}}^{\sigma, n}. \quad (6.30)$$

In Chapter 7 we will be using these coupling strength predictions to choose frequencies and field strengths for the application of MW-dressings which may change the static field dependence of the transitions. Firstly however, we will briefly consider the couplings in the case of no RF-dressing.

6.1.3 Bare Microwave Couplings

For a complete characterisation of the atomic system, we also require an understanding of the coupling coefficients between energy levels in the undressed case ($B_{\text{RF}} = 0$). To this end, we consider the product space of angular momenta, starting from our known values $L = 0$, $S = 1/2$, $I = 3/2$ for the ground state of ^{87}Rb . The equivalent values for other alkali atoms can be similarly calculated using their corresponding product space. The individual

m	m'	-2	-1	0	1	2
-1		$\frac{\sqrt{3}}{2}i$	$-\frac{\sqrt{3}}{2}$	$\frac{\sqrt{2}}{4}i$	0	0
0		0	$\frac{1}{2}\sqrt{\frac{3}{2}}i$	-1	$\frac{1}{2}\sqrt{\frac{3}{2}}i$	0
1		0	0	$\frac{\sqrt{2}}{4}i$	$-\frac{\sqrt{3}}{2}$	$\frac{\sqrt{3}}{2}i$

Table 6.2: The table gives the required coupling coefficients $\Omega_{\text{MW}}/\Omega_{\text{norm}}^\sigma$ when MW-dressing on the bare transition $|1, m\rangle \leftrightarrow |2, m'\rangle$.

Cartesian components of these spins can be calculated from Eq.s A.5, A.17 and A.18 (recalling that the $|F, m_F\rangle$ relations also apply to the constituent angular momentum components). As $L = 0$ this does not contribute to the product space, but the 2×2 matrices $S_{x,y,z}$ and 4×4 matrices $I_{x,y,z}$ require consideration. In order to account for all 8 possible combinations of m_S and m_I , we use outer products

$$\hat{\mathbf{F}}_{x,y,z}^{SI} = \hat{\mathbf{S}}_{x,y,z} \otimes \mathbf{1}_8 + \mathbf{1}_8 \otimes \hat{\mathbf{I}}_{x,y,z}, \quad (6.31)$$

where $\mathbf{1}_8$ is the 8×8 identity matrix, and F is formed in the SI -basis. As F and SI have a basis in common, we can then use the eigenvectors of F to convert this to the F -basis:

$$\hat{\mathbf{F}}_{x,y,z} = \hat{\mathbf{V}}^\dagger \hat{\mathbf{F}}_{x,y,z}^{SI} \hat{\mathbf{V}}, \quad (6.32)$$

where $\hat{\mathbf{V}}$ is a matrix of the eigenvalues of F . Using the resulting $\hat{\mathbf{F}}$ matrix, extracting the elements $|F, \bar{m}\rangle \langle F+1, \bar{m}'|$ provides the angular momentum couplings given in Table 6.2, once the polarisation normalisation factors η_σ from Eq. 2.25 are included. The normalisation factor

$$\Omega_{\text{norm}}^\sigma = \frac{1}{2}(g_S - g_I)\mu_B B_{\text{MW}}^\sigma = (g_{F=2} - g_{F=1})\mu_B B_{\text{MW}}^\sigma, \quad (6.33)$$

is stated separately for conciseness, and is equivalent to the dressed normalisation factor Eq. 6.29. The conversion between Landé g -Factors uses Eq. 2.14.

6.2 Microwave Frequency Spectra

In this section, data is presented showing the full spectrum of possible transitions between RF-dressed F -manifolds in ^{87}Rb . Firstly we consider how to process two state detection data to account for atom number fluctuations and state dependent differences in detection strength (Section 6.2.1). Spectroscopic data on the full set of quasi-energy level transitions is then shown (Section 6.2.2), giving measurements of the transition frequencies and RF-field strength. Certain groups are studied in more detail. Next, we consider

the linewidths of the transitions, including distortion due to power and other broadening effects (Section 6.2.3). Finally, in Section 6.2.4 we look at the effects of Rabi oscillations on the lineshape of single transition peaks. Specifically, this chapter focuses on comprehensively analysing groups $n = 3$ and 1, i.e. one group which is dependent purely on a single MW-polarisation component (σ_+) and one which depends on a superposition of both σ_{\pm} .

6.2.1 Signal Normalisation

In order to measure the transition frequencies in the dressed ^{87}Rb ground state, we begin with atoms prepared in a pure $|1, \bar{m}\rangle$ state using the method described in Section 3.2. In this section, we are interested in the resonant static field case only; the effects of different static magnetic field strengths will be discussed in Section 6.3.1. We therefore set the static field to the resonant magnitude, in the y -direction for π -polarisation, the z -direction for σ_{\pm} polarisation, or some other angle for a combination of the two (see Figure 5.9c). As discussed in Section 5.2.1, the first issue that we encounter is that the number of atoms in the MOT will vary over the course of the day, subject to dispenser heating times and slow thermal drifts.

As we are only interested in the population fraction in a given state, we can normalise against atom number fluctuations by comparing the $F = 1$ and 2 data sets. In Figure 6.3, signals from the two states are shown for an initially pure RF-dressed $|1, 0\rangle$ state probed with a MW, and the measured signal strength is plotted as a function of probe frequency. The features of this spectroscopy data will be discussed in Section 6.2.2; for now we consider only the change in total atom number over time. The populations in the two states were measured consecutively from the same atom cloud, with each pair of data points taken using the full experimental sequence (Figures 3.8 and 4.3), measured in order from low to high MW-frequencies. The $F = 1$ signal is clearly increasing over time, whilst the $F = 2$ signal is fixed at zero, excluding the five large peaks. This shows that the change in signal amplitude is not due to population transfer: aside from at the peaks, the internal state of each atom has not changed, merely the total number of atoms is rising over the course of the (~ 30 minute) run. In order to fit this increase in atom number, the regions near transitions need to be excluded. By finding points in the $F = 2$ data set which are more than 4 standard deviations from the root mean squared noise level, we can exclude the corresponding $F = 1$ points. The omitted points are marked in red in Figure 6.3a, with all other points marked in green. The fit to the allowed data shown in the figure is quadratic, although for much longer length runs (\sim hours) we may require a higher order polynomial. The data sets for both F -levels can then be

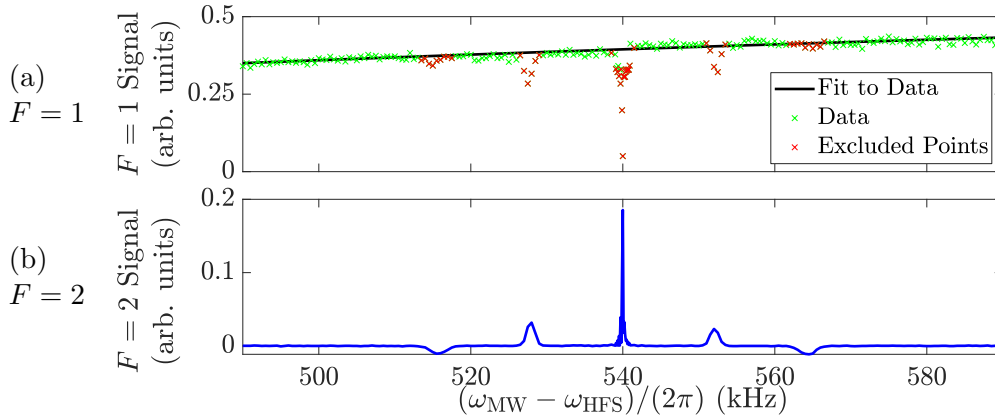


Figure 6.3: The figure shows the method of normalising the atomic signal against changes in atom number. Atoms are prepared in the initial RF-dressed state $|1, 0\rangle$ and then probed for 5 ms by the MW. The $F = 1$ and 2 signals are plotted in (a) and (b) as a function of MW-probe frequency in the group $n = 3$. When far from a transition, the $F = 1$ data is proportional only to the atom number and the detection strength of the state $|1, 0\rangle$. We can therefore fit the $F = 1$ data, excluding peaks, and use this to normalise against atom number changes for both states. Adapted from our paper [167].

divided by the magnitude of this fit to account for the atom number variation. Such a method can also be used to account for changes in detection strength, for instance due to external static field drifts, assuming they happen on a timescale much longer than the ~ 3 s sequence time.

Another consideration is the reduction in measured atomic signal as a function of drop time. After the MOT stage, the entire experimental sequence takes place whilst the atoms are in free-fall. Collisions between atoms in the cloud or background gases are likely a negligible effect, as in our UHV system the lifetime should be at least tens of seconds [160]. A more pertinent consideration is the issue of the free-falling atomic cloud passing away from the central region of the Gaussian detection beam. As the atoms are interrogated with a smaller fraction of the light further from the centre of the beam, a smaller change in polarisation is measured. We can see this effect in Figure 6.4a, where Rabi cycles on the dressed transition $|1, 0\rangle \leftrightarrow |2, 0\rangle$ are shown, with the amplitude of the oscillation in both states decreasing by 35% over the course of 5 ms. We can process the two signals (after accounting for different state detection strengths) to obtain the total atomic signal shown in black. Such a method establishes the form of the envelope of the two sine waves, which is required in the fit used to extract the Rabi frequency. Note that in all data sets, each pair of measurements of the states $F = 1$ and 2 is

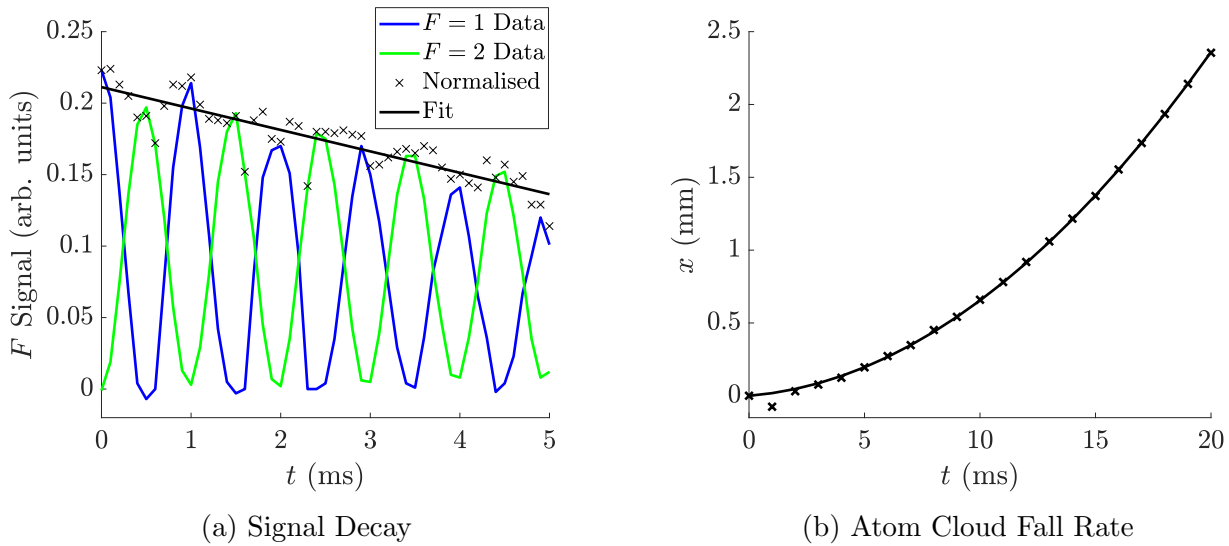


Figure 6.4: An example Rabi oscillation between the two F -levels is shown in (a). The decay in total signal strength over time can be measured by summing the two signals. In (b) the position of the atom cloud over time in free fall is plotted, using the same absorption image data used to generate Figure 3.4b. The position is fit as a function of time, measuring the cloud acceleration to be $(10.5 \pm 0.4) \text{ ms}^{-2}$, as discussed in the main text. It is this cloud motion through the detection beam region which causes the reduction in signal strength over time shown in (a).

taken using a separate experimental run.

The detection beam is aligned just below the MOT location using fluorescence imaging [164]. We see that the reduction in signal strength is approximately linear over time, due to the detection beam being centred slightly above the cloud at $t = 0 \text{ ms}$ as defined in Figure 6.4a. This is intentional, as it allows for sufficient detection light whilst also making the measured signal be less strongly dependent on drop time. In a standard sequence, the detection of the atomic state occurs $\sim 35 \text{ ms}$ after the end of the CMOT phase. An estimate of the free-fall distance expected during this time can be obtained from measuring the rate at which the atoms fall using absorption imaging. This can be performed in the same manner as the MOT expansion over time was measured in Figure 3.4b; reanalysing the same absorption imaging data, but now fitting the vertical cloud position x as a function of drop time gives the graph in Figure 6.4b, which also shows a fit to the equation of motion. The acceleration of the cloud is measured to be $(10.5 \pm 0.4) \text{ ms}^{-2}$, faster than if simply due to gravity, so static field spikes during the CMOT stage due to

fast switching of the quadrupole coils could be increasing this. An error of 7 % on the magnification of the imaging system would also wholly account for the discrepancy. After 35 ms the cloud will have fallen by (6.5 – 6.9) mm, accounting for either explanation or some combination of the two. This is of course simply measuring the cloud after the CMOT phase with none of the following parts of the sequence, including various field ramps and laser pulses, which may somewhat alter the acceleration. The errors on these values are therefore likely higher than stated. We also note that changes in cloud location due to MOT realignment, which is performed every few months, will also cause variation in detection strength between some measurements.

It is also important to recall that the signal strength depends on the particular $|F, \bar{m}\rangle$ state the atoms are in, by an amount given in Table 4.1. This is harder to account for if the atoms are in a superposition of \bar{m} states for a fixed value F , but due to our state cleaning procedure this can usually be discounted. In the case of spectra such as Figure 6.3b, the change in the sign of the signal allows state labelling: the outer two peaks indicate transitions to $|2, \pm 2\rangle$. All peak heights could be individually scaled if required. The effect of the signal strengths of the $|1, \bar{m}\rangle$ state which the $F = 2$ signals are normalised against will also need to be accounted for. However, at this stage we make the choice to leave in all effects related to state detection strength, such that the spectra presented in the following section are representative of both the physical effects and the experimental method used. Disentangling these two components will be addressed in Section 6.3.2.

6.2.2 Transition Frequencies

In order to experimentally confirm the predicted transition frequencies from Eq. 6.3, we must spectroscopically measure this. Atoms are prepared in each of the three possible states $|1, \bar{m}\rangle$, and a MW-probe is applied for 0.4 ms, with points taken at frequencies around ω_{HFS} , and then the population in both F -levels is measured. Population transfer occurs only at or near transitions, and therefore the peaks in the $F = 2$ spectrum mark these locations in Figure 6.5, where each panel corresponds to a different initial state. Some transitions are not visible, due either to being suppressed as the coupling strength is approximately zero on resonance, or due to the effects of driving multiple Rabi oscillations, which we will consider in Section 6.2.4. Note that due to high MW-driving power ($B_{\text{MW}} = 2.9$ mG), even suppressed lines may be driven. The seven groups n of transitions are labelled in the figure, with the location of the corresponding bare transition frequencies (as given by Eq. 6.1) marked as grid lines.

The atom number has been normalised as described in the previous section,

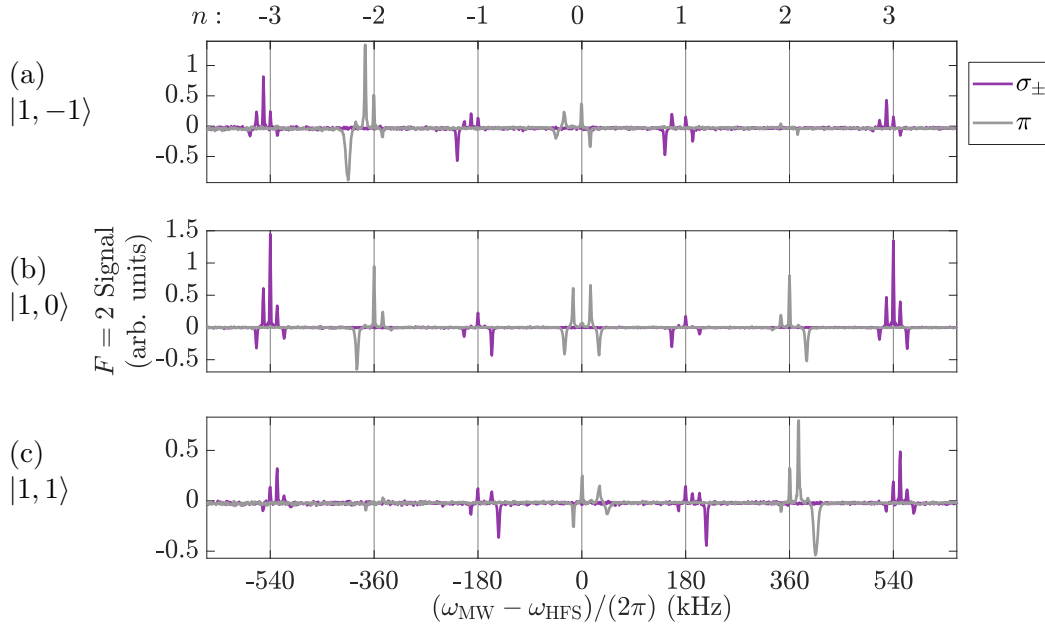


Figure 6.5: Data showing the full spectrum of transitions from $F = 1$ in the RF-dressed ground state of ^{87}Rb . The three panels correspond to different initial state preparations. The state was probed for 0.4 ms with relatively high MW-probe strength ($B_{\text{MW}} = 2.9$ mG). Adapted from our paper [167].

so we recall that there will be scaling differences between panels. The data sets for σ_{\pm} and π -polarisation were taken on two separate days, with points taken for each of $\bar{m} = -1, 0, 1$ taken consecutively for a set MW-frequency, in order to ensure peak heights within an given group are subject to the same thermal drifts in atom number. Normalisation is especially important over such an experimental run lasting many hours, as over this time the atom number changes by a factor of ~ 2 . Points were taken every 1 kHz, and a rough fit to transition frequencies gives $\Omega_{\text{RF}}^{\pm}/(2\pi) = (12 \pm 0.5)$ kHz, which using Eq. 2.42 gives $B_{\text{RF}}^{\pm} = (24 \pm 1)$ mG. This method is imperfect, however, as it assumes circularly polarised RF, whereas in practice there is likely some small ellipticity due to practical constraints. The reason for the uncertainty in RF-field strength is that we cannot measure the RF-power at the region of the atoms directly in the vacuum chamber.

We can make a rough estimate of the RF-power from the coil properties and input power, but the error on the distance to the atoms makes this a less reliable method of power determination. As the atoms are in free-fall, the length of the experimental run will also alter the strength of the RF-field seen by the atoms. A rough approximation of the location of the atoms in the chamber, the typical length of a single experimental sequence, and a $1/r^2$

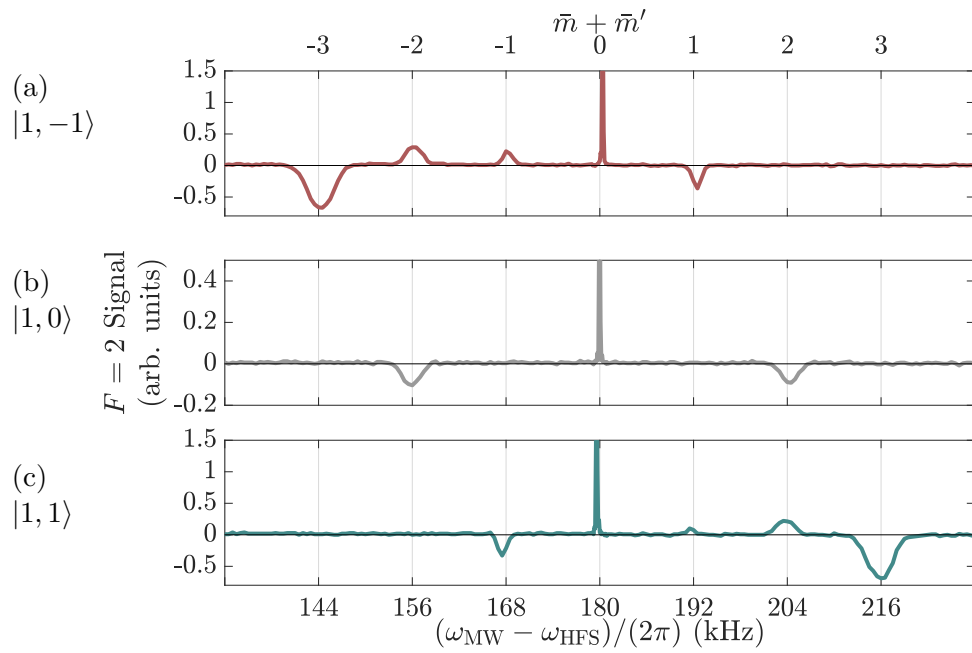


Figure 6.6: Group 1 low MW-probe power ($B_{\text{MW}} = 0.4$ mG) transition data. Adapted from our paper [103].

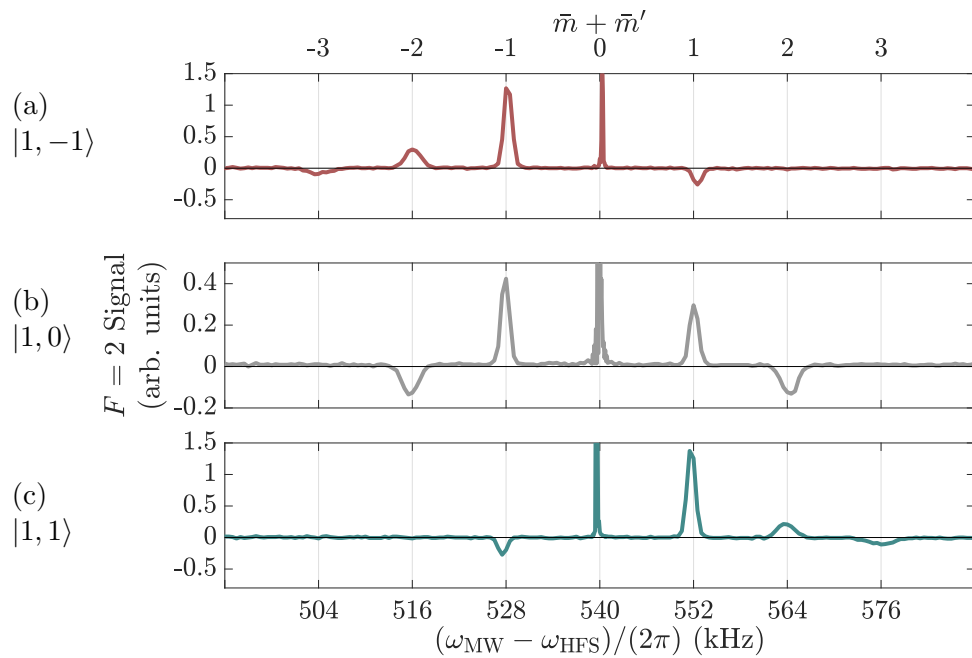


Figure 6.7: Group 3 low MW-probe power ($B_{\text{MW}} = 0.4$ mG) transition data. Adapted from our paper [167].

drop off in coil power indicates that a change in sequence length of 1 ms gives a change in RF-power of $(3 \pm 1)\%$. Data-sets taken either side of a realignment of the MOT could vary in RF-field strength by as much as 20% due to potential changes in vertical position by ~ 1 cm. Thus variation in RF-power measurements between data-sets need not be a cause for concern.

The main drawback of using a high power MW-probe, in this case 2.9 mG, is that the peaks are highly power broadened, as we will discuss in Section 6.2.3. In order to gain more detailed information on the dressed spectrum, a fine scan of groups $n = 1$ and 3 are shown in Figures 6.6 and 6.7 respectively. Once again, the three panels per group correspond to the three possible initial states $|1, \bar{m}\rangle$, and the data was taken and normalised in the same way as for Figure 6.5, only purely using σ_{\pm} -polarisation, a 5 ms spectroscopy pulse and 18 dB lower MW-probe power. The data in each of the panels will again be subject to different scalings. Data points were taken every 0.5 kHz, aside from in the region $(\omega_{\text{MW}} - \omega_{\text{HFS}})/2\pi = (180n \pm 1)$ kHz, where the points are every 0.1 kHz so the sharpness of the peaks can be resolved. The data in Figure 6.7b was previously used as a normalisation example in Figure 6.3b. The transition frequencies are as given by Eq. 6.3, with the grid lines marking the predicted frequencies for $\Omega_{\text{RF}}^{\pm}/(2\pi) = 12$ kHz, which the data shows to be true to within ± 0.5 kHz.

Each of the transitions $|1, \bar{m}\rangle \leftrightarrow |2, \bar{m}'\rangle$ have their respective values $\bar{m} + \bar{m}'$ marked on the figure. Only two of the peaks cannot be seen, the $|1, 0\rangle \leftrightarrow |2, \pm 1\rangle$ peaks in group $n = 1$ (Figure 6.7b); this agrees with the predicted coupling strengths shown in Figure 6.2b. It is clear that in all panels the peak with $\bar{m} + \bar{m}' = 0$ is considerably narrower than the others. We call these the clock transitions due to their increased robustness against static magnetic field variations, for reasons considered in Section 6.3.1. The full height of these peaks has been cropped in this figure, as we will analyse these in more detail in Section 6.2.4, along with other effects on peak widths in Section 6.2.3.

6.2.3 Broadening Effects

In this section the factors which alter the linewidths in our spectroscopy measurements are considered. In the simplest model, a transition between two energy levels is a delta function centred on the transition frequency; total absorption occurs at resonance, and zero elsewhere. This is of course unphysical, as other effects need to be taken into account, such as the natural linewidth of a transition which depends on the spontaneous decay rate. Another factor is collisional broadening, where interactions between atoms in the cloud due to thermal motion will widen the possible range of frequencies the probe light (in this case MW) can be absorbed at. As the CMOT was measured to be $23 \mu\text{K}$

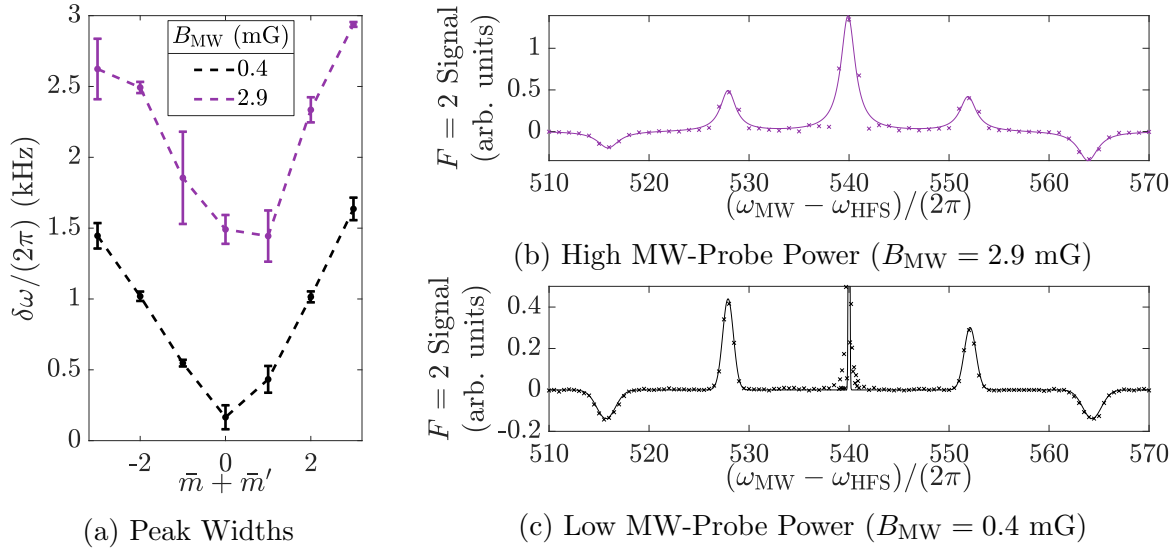


Figure 6.8: In (a) the average widths of the transition peaks $\delta\omega$ are plotted in groups $n = 1$ and 3 for two different probe powers. Example fits to these spectra are given in (b) and (c) for the high and low power spectra respectively, where the difference in power between the two probes is 18 dB. In (b) the fit is Lorentzian, Eq. 6.34, and in (c) it is Gaussian, Eq. 6.35, with $w = \delta\omega$ plotted from both equations. Adapted from our paper [167].

this is unlikely to be a substantial effect however, as the collision rate will be < 0.1 Hz. The linewidth of the transition will also be increased by power broadening, which occurs when the probe power is sufficiently above the saturation intensity of the transition that absorption on resonance is suppressed, but at small detunings transitions may still be driven [181].

The effect of power broadening on the measured amplitude A is given by a Lorentzian lineshape

$$A \propto \frac{1}{\pi} \frac{\frac{1}{2}w}{(\omega - \omega_0)^2 + (\frac{1}{2}w)^2}, \quad (6.34)$$

where ω is the probe frequency, ω_0 is the transition frequency and the proportionately sign accounts for the amplitude dependence on detection strength. The width w depends on the probe intensity [69]. Further broadening can be caused by external fields, as the AC-Stark and AC-Zeeman effects can cause a change in linewidth for electric or magnetic fields respectively. There two different types of effect this can have on the linewidth: homogeneous and inhomogeneous broadening. Thus far the effects we have considered have only been of a form which affect all atoms in the cloud equally. Such homogeneous

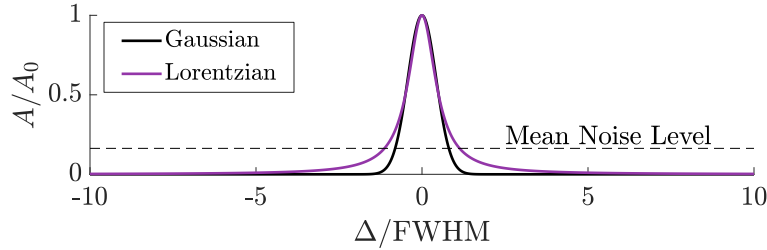


Figure 6.9: Gaussian and Lorentzian peaks of the same full width half maximum are plotted in the figure, normalised to 1 at $\Delta = 0$. The mean noise level of 16% in Figure 6.5 is also marked, showing the difficulty in distinguishing between the two lineshapes in the data.

effects typically cause a Lorentzian change in lineshape [46], as we calculated for power broadening. Assuming uniform field fluctuations across the cloud, light-shifts are a homogeneous effect. Some effects on the linewidth do not affect all atoms equally however, for example Doppler broadening in room temperature vapours (shown in Figure 5.2), and these are known as inhomogeneous effects.

In the case of magnetic fields, a pair of Helmholtz coils will not form a perfectly even magnetic field across the whole region of the cloud. As such, we have inhomogeneous broadening, which is not Lorentzian in nature. Due to statistical variation in the AC-Zeeman shift across the cloud, we expect a Gaussian

$$A \propto w\sqrt{2\pi}e^{-\frac{(\omega-\omega_0)^2}{2w^2}} \quad (6.35)$$

linewidth, where w is dependent on the magnetic field variation. The proportionality sign is once again required to account for the detection strength. Some transitions $|1, \bar{m}\rangle \leftrightarrow |2, \bar{m}'\rangle$ will experience such a broadening to a higher extent than others, depending on the value $\bar{m} + \bar{m}'$. In the approximation $-g_1 = g_2$, transitions with $\bar{m} + \bar{m}' = 0$ are between two levels with a matching dependence on the trapping potential, and as such are impervious to field fluctuations, as we see from Eq. 2.43. At low powers ($B_{\text{MW}} \lesssim 0.4$ mG), this appears to be the dominant effect. In Figure 6.8 the linewidths of transitions in the groups $n = 1$ and 3 are plotted. These are taken in the low power case from fits to Figures 6.6 and 6.7, and in the high power case ($B_{\text{MW}} = 2.9$ mG) from fits to Figure 6.5. An example fit to both the high and low power spectra are shown in Figures 6.8b and 6.8c respectively, for the case of $n = 3$, $|1, 0\rangle \rightarrow |2, \bar{m}'\rangle$.

The Gaussian fit to lineshape in the low power case is good, aside from for the clock transition, which will be considered in detail in Section 6.2.4.

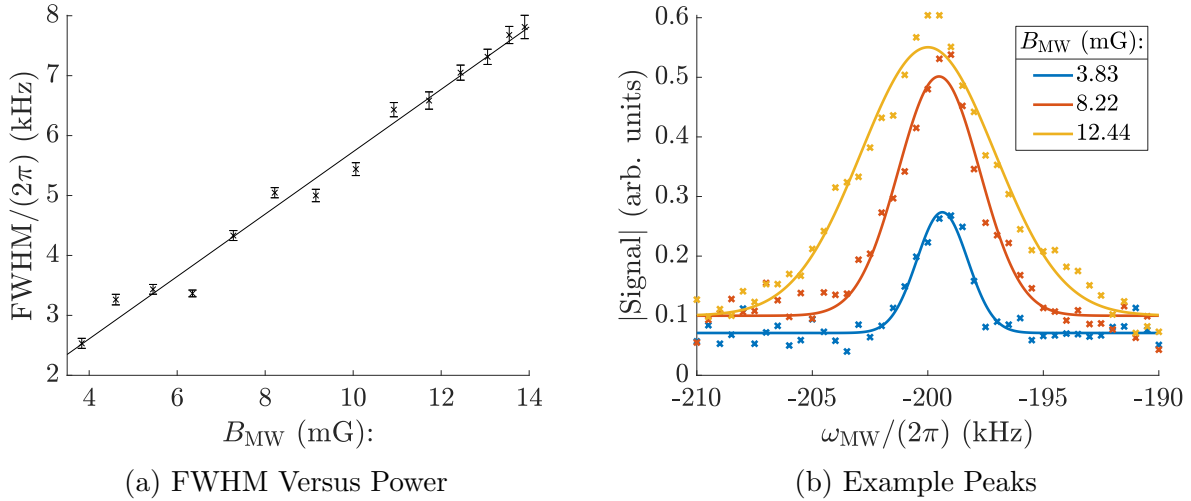


Figure 6.10: The width of the transition peak $|1, 0\rangle \rightarrow |2, -2\rangle$ as a function of MW-probe power is plotted in (a), as an average of three repeat measurements. Three sample peaks of different MW-powers are shown in (b) with Gaussian fits also plotted. The shift in transition frequency of < 1 kHz between peaks is likely due to the back action of the MW on the RF-dressing power. The fit to the highest power peak is less good as the lineshape contains a larger Lorentzian component due to power broadening.

The linewidth can be seen in Figure 6.8a to be dominated by magnetic field inhomogeneities, as there is a pronounced dependence on $\delta\bar{m}$ (we will consider this further in Section 6.3.1). As the linewidth is still finite at $\delta\bar{m} = 0$, there is a small contribution from power and/or collisional broadening and the natural linewidth. In the high power case, the fit to lineshape is Lorentzian as power broadening is a significant effect. Note the difference in scale between the two example spectra: the additional power is substantially changing the peak shapes. As the power broadening is consistent across all peaks, this is effectively offsetting the peak widths from the low power case.

Note that as two different lineshapes have been fit, the two sets of widths w are not directly comparable. Strictly speaking, the fit to the spectral peaks in both data sets should be to a convolution of the two lineshapes, but for the sake of simplicity the fit is performed only to the dominant of the two effects. The difficulty in fitting a combination of a Gaussian and a Lorentzian linewidth to our data is illustrated in Figure 6.9, where the amplitude A of the two lineshapes is plotted with the same full width half maximum (FWHM), normalised in height by $A_0 = A(\Delta = 0)$. As the noise level is $\sim 16\%$ of the average peak height in the full data set, this causes the issue that region where the two peak shapes are most distinct, $|\Delta/\text{FWMH}| > 1$, is not able to

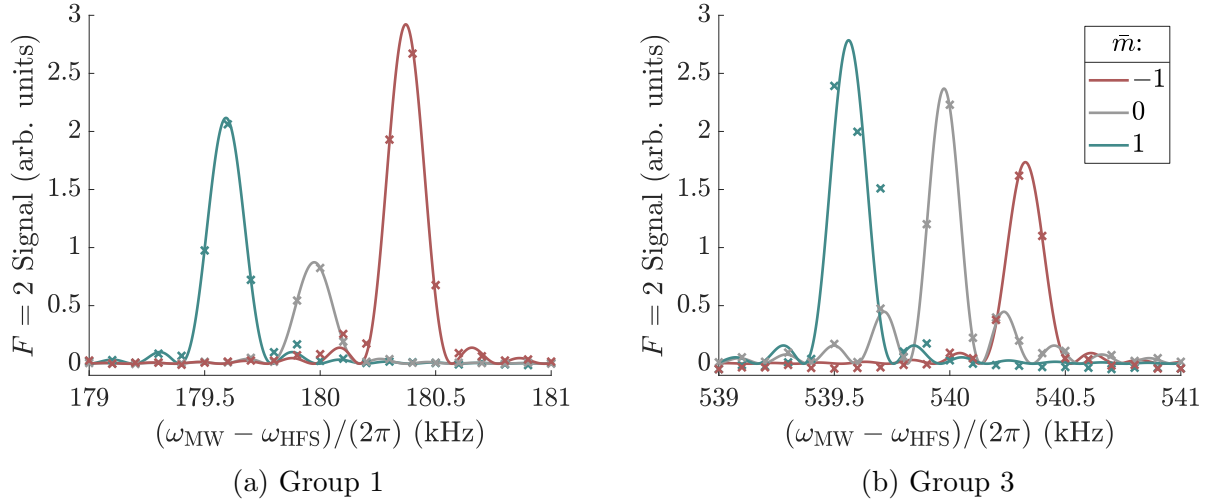


Figure 6.11: The clock transitions $|1, \bar{m}\rangle \rightarrow |2, -\bar{m}\rangle$ in groups $n = 1$ and 3 are plotted in (a) and (b) respectively, as extracted from the data in Figures 6.6 and 6.7. $B_{\text{MW}} = 0.4$ mG. These can be fit to Eq. 6.36, which accounts for the effects of multiple Rabi cycles. Adapted from our paper [167].

be fit. The relevance of the peak shape below the noise level will be explained in Section 7.1.2 when considering minimum detunings to avoid population transfer.

In Figure 6.10a, the width of a spectroscopy peak is plotted as a function of MW-probe power. The chosen peak is on the transition $|1, 0\rangle \leftrightarrow |2, -2\rangle$, which exhibits large inhomogeneous broadening, and was also selected because the state $|1, 0\rangle$ gives detection signals which are twice as strong as the $|1, \pm 1\rangle$ states. Gaussian fits were used, although as we see from sample peaks in Figure 6.10b, this is not a good fit to the lineshape at high probe powers. In spite of this, fitting a Gaussian to a partially Lorentzian lineshape is permissible as either model should give a similar measure of the FWHM. We see that at high MW-probe powers where homogeneous broadening is dominant, the linewidth rises linearly with power. Accounting for the vertical intercept determined by the inhomogeneous broadening, this plot can be used to extrapolate the fractional increase in linewidth of an arbitrary transition as a function of MW-power ($0.52 B_{\text{MW}}$ kHz/mG) which will be considered in more detail in Section 7.1.2. Note that the data in Figure 6.10 was taken using a different MW-generator which can achieve higher powers, and will be discussed in Section 7.2.1.

6.2.4 Rabi Cycle Distortion

One further linewidth consideration is the effect of driving multiple Rabi cycles. For instance, if measuring the transition peak in $F = 2$, starting from zero population before driving, at times before $t = \pi/\Omega$ the signal strength will increase with t . For instance in Figure 6.4a the $F = 2$ signal increased up until ~ 0.5 ms. After this point with total population in the upper state, further MW-driving will reduce the measured signal. If we consider the variation of the coupling strength as a function of detuning, this allows different parts of the same peak to undergo different numbers of Rabi cycles for the same input MW-probe power and duration, which will distort the shape of the peak. In order to get a representative idea of transition magnitudes, it is important to not drive more than one full Rabi cycle.

The lineshapes of peaks experiencing such distortion can still be useful to study however. The amplitude is given by

$$A \propto \frac{\Omega_{\text{MW}}^2}{\Omega_{\text{MW}}^2 + \Delta_{\text{MW}}^2} \sin^2 \left(\frac{\sqrt{\Omega_{\text{MW}}^2 + \Delta_{\text{MW}}^2} t}{2} \right) \quad (6.36)$$

as a function of MW-pulse duration t , where Ω_{MW} is the Rabi frequency and Δ_{MW} is the detuning [69]. Such a fit is performed for the clock transitions $n = 1$ and 3 in Figures 6.11a and 6.11b respectively. These are a zoom into the central frequency region of the Figures 6.6 and 6.7 previously discussed. We now see why the Gaussian fit in Figure 6.8c was so inaccurate: the lineshapes are much distorted in the case of these sharp transitions.

The fraction of power in the peak sidebands is small for such a low MW-probe power, but increasing this power can cause peaks to be completely suppressed at the central frequency. As the transition $|1, 0\rangle \leftrightarrow |2, 0\rangle$ in $n = 3$ shows the highest level of distortion of all given MW-peaks, this provides an interesting case to study when the maximum MW-power is limited by experimental equipment. We see in Figure 6.2b that this transition has the highest of all predicted coupling strengths (joint with the corresponding transition in $n = -3$), and therefore its strong dependence on MW-power is as expected. Note that only the absolute value of coupling strength is relevant here. A fine scan of the peak shape, with points every 50 Hz, is shown in Figure 6.12, with fits to Eq. 6.36. The transition peak on resonance is clearly much reduced in the case of high power. The data for the corresponding clock transition in $n = 1$ is also shown, to allow comparison with a lower coupling strength case. Fits to the data allow for extraction of the Rabi frequency, and hence coupling strength as a function of MW-probe power; this will be studied further in Section 6.3.2.

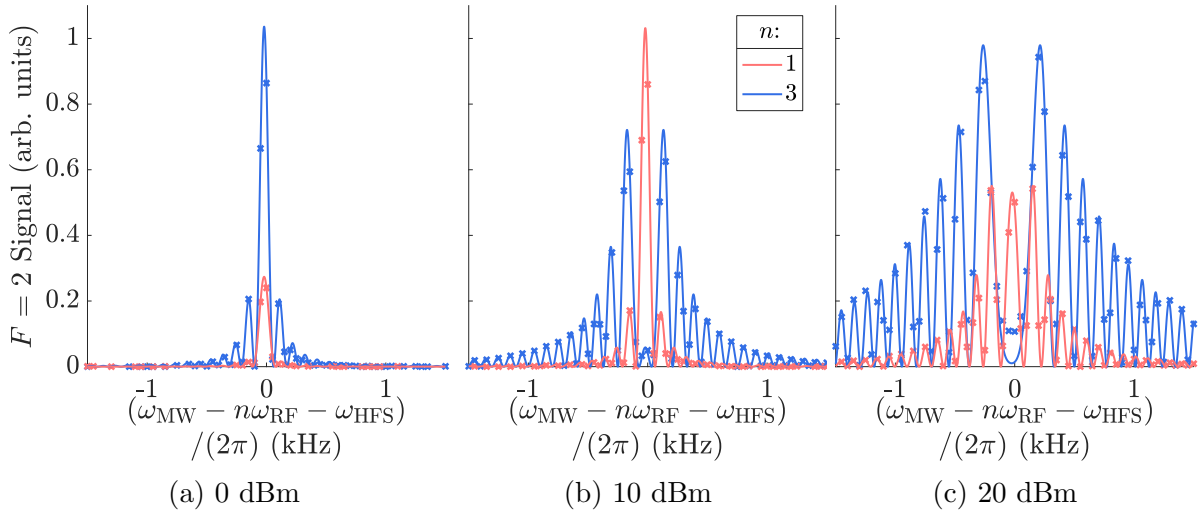


Figure 6.12: Fine scan (points spaced by 50 Hz) of the clock transition $|1, 0\rangle \leftrightarrow |2, 0\rangle$, in groups $n = 1$ and 3 at three different MW-driving powers, with fit to Eq 6.36. In (a-c) the 0, 10 and 20 dBm probe powers are shown, later calibrated as $B_{\text{MW}} = 0.4, 1.2$ and 3.7 mG respectively.

6.3 Coupling and Field Dependence Data

In this section, we experimentally study the properties RF-dressed transitions, starting with the frequency dependence on static magnetic field (Section 6.3.1). We then measure the strength of the couplings between sublevels, and how these depend on static field (Section 6.3.2), as well as comparing a number of methods of measuring the static field strength of resonant transitions. Finally in Section 6.3.3 we demonstrate the ability of multi-photon transitions to perform Ramsey interferometry. As in the previous section, the data shown focuses on the groups $n = 1$ and 3 .

6.3.1 Static Field Dependence

We recall from Figure 6.8a that the widths of the transition peaks in an RF-dressed spectroscopy measurement depend strongly on the value $\bar{m} + \bar{m}'$. As there are no differences between the $|F, \bar{m}\rangle$ levels with regards to spatial separation or magnetic trapping, as the atoms are in free fall, we know that this effect is inherent to the energy levels. The dependence on sublevel number can be explained using Eq. 2.43, which states that the energy dependence of a given level is proportional to $g_F \bar{m}$. In the approximation $-g_1 = g_2$ and $B_{\text{RF}}^+ = B_{\text{RF}}^-$, transitions between a pair of levels with $\bar{m} + \bar{m}' = 0$ will have zero static field dependence.

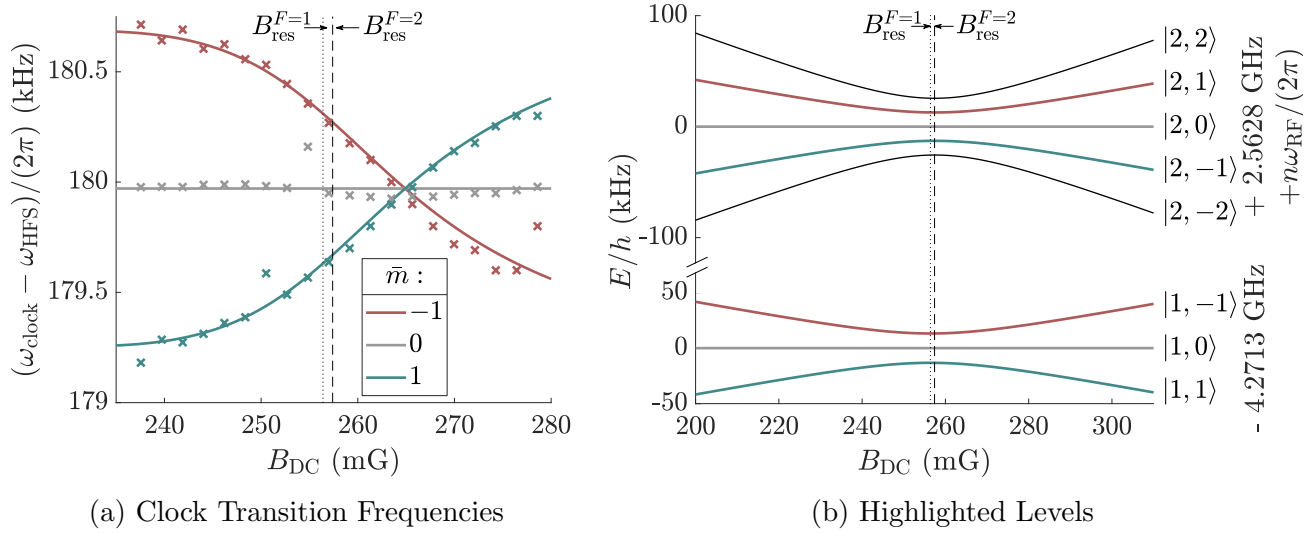


Figure 6.13: The frequency dependence of the clock transitions $|1, \bar{m}\rangle \leftrightarrow |2, -\bar{m}\rangle$ in group $n = 1$ are shown in (a), with fits to Eq. 6.2 giving $B_{\text{RF}}^{\pm} = (26 \pm 1)$ mG. The dotted and dashed lines mark the $F = 1$ and 2 resonances respectively. The theoretical energy levels are plotted in (b) in an arbitrary group n , with the pairs of clock levels highlighted in colours corresponding to the transitions in (a). Adapted from our papers [103] and [167] respectively.

The measured transition frequencies for such clock transitions $|1, \bar{m}\rangle \leftrightarrow |2, -\bar{m}\rangle$ in $n = 1$ are plotted in Figure 6.13a, along with a fit to Eq. 6.2 which yields $B_{\text{RF}}^{\pm} = (25 \pm 1)$ mG. The frequency was measured by taking spectroscopy data in the same manner as for Figure 6.11, only now for numerous values of static magnetic field. The peak atomic signal was then fit as a Gaussian in order to extract the transition frequency, which is now plotted as function of static field. The $|1, 0\rangle \leftrightarrow |2, 0\rangle$ clock transition has a (5 ± 1) Hz/mG dependence of transition frequency on static field at resonance, attributable to intermediate field effects. The other clock transitions $|1, \mp 1\rangle \leftrightarrow |2, \pm 1\rangle$ have a more pronounced dependence of $(-40 \pm 2, 38 \pm 2)$ Hz/mG at this point respectively, due to the imbalance in the g_F -factor magnitudes. The corresponding energy levels are shown in Figure 6.13b, with the pairs of clock states highlighted in colours corresponding to the transitions in Figure 6.13a. As the highlighted pairs of energy levels have a near equal dependence on static field, these transitions are the most robust against fluctuations. The two resonance points B_{res}^F are marked in the both figures. Considering how small the (1 mG) difference between the two resonances is, we see that it is valid to treat this as a single resonance point for our current purposes.

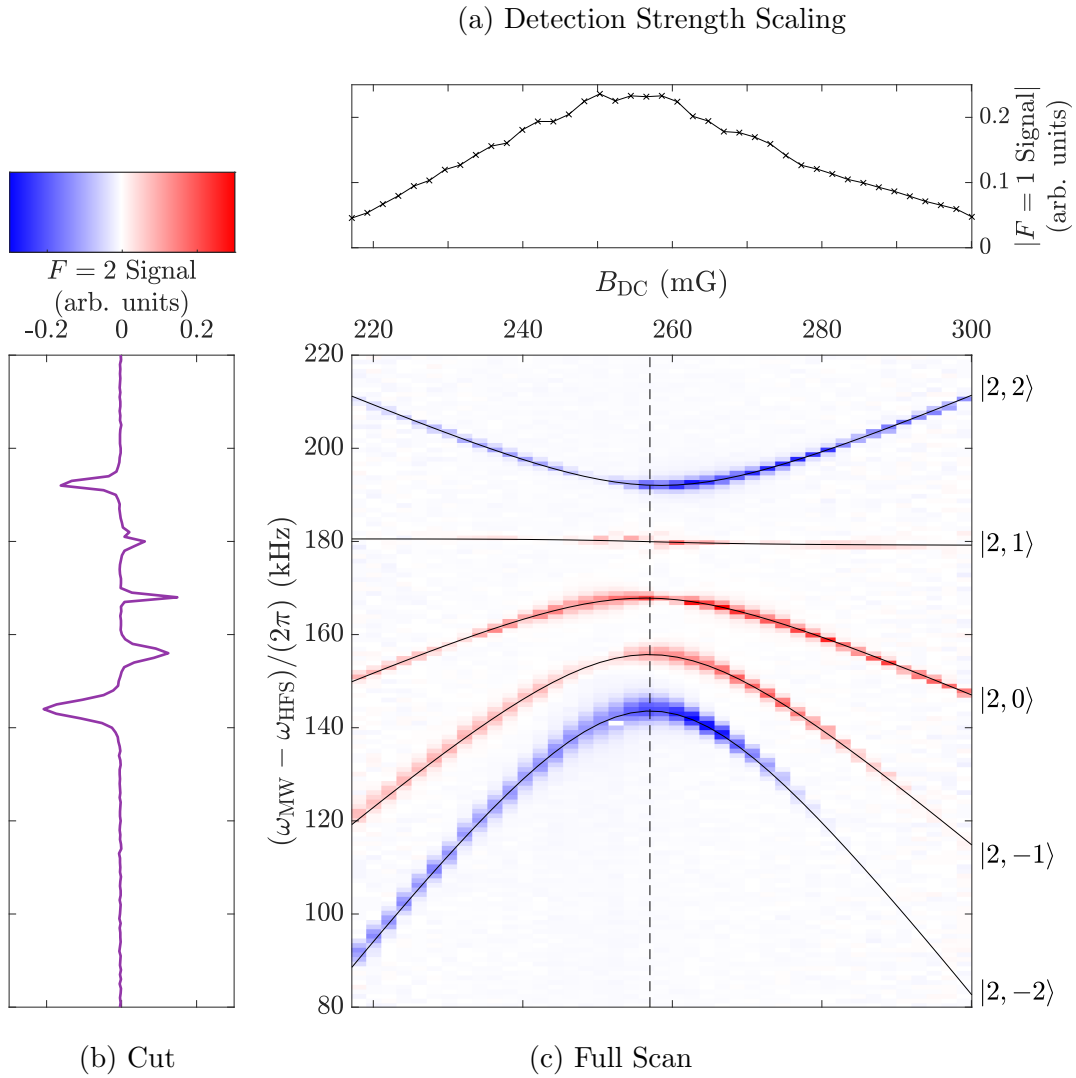


Figure 6.14: A colour map of the population in $F = 2$, plotting static field as a function of MW-probe frequency, is shown in (c) after applying a MW-pulse to a pure $|1, -1\rangle$ state. The resonant static field is marked with a dashed line, and a cut of the data at this point is plotted in (b). The solid lines in (c) are fits to the transition frequencies, as given by Eq. 6.2, yielding $B_{\text{RF}}^{\pm} = (24.5 \pm 0.5)$ mG ($B_{\text{MW}} = 2.0$ mG). Adapted from our paper [71]. The $F = 1$ signal as a function of static field is shown in (a), when probed with a MW far from resonance with any transition. This was used to normalise changes in atom number and signal strength in the $F = 2$ data.

Cancelling the effects due to $-g_1 \neq g_2$ is the subject of Chapter 7.

A full scan of all transitions from $|1, -1\rangle$ in group 1 is shown in Figure 6.14c. In the same manner as for previous spectroscopy measurements, the atoms are prepared in a pure $|1, -1\rangle$ state and then probed for 4 ms with a MW-pulse, where the frequency and static field are scanned. The final population fraction in $F = 2$ is plotted as a colour-map, where positive signals are shown in red, negative in blue and zero in white. We see that the clock transition $|1, -1\rangle \leftrightarrow |2, 1\rangle$ is the flattest as expected. Due to the necessity of a large step size in both static field (2 mG) and probe frequency (1 kHz), in order to make taking the data in one day possible, the peak shapes are not fully representative. The transition frequencies can be extracted from a rough Gaussian fit to the atomic signal as a function of probe frequency for each static field, in the same manner as performed in Figure 6.8c. The peak locations as a function of static field for all transitions are then simultaneously fit to Eq. 6.2, obtaining the RF-field strength $B_{\text{RF}} = (24.5 \pm 0.5)$ mG. Thus far we have assumed that the static field strength is always linearly proportional to the current in the relevant coils. This calibration is likely imperfect, however, as the fit also requires the static field scaling to be changed by 4 % about the resonance point. A cut of the spectroscopy data at the resonant static field is plotted in Figure 6.14b, which corresponds to the data at the dashed line in Figure 6.14c. All data was normalised against the mean $F = 1$ signal measured far from resonance with any transitions, shown in Figure 6.14a, accounting for variation in detection strength as a function of static field, as well as atom number drifts over time.

6.3.2 Coupling Coefficient Measurements

The coupling strengths for all possible transitions between quasi-energy levels $|1, \bar{m}\rangle \leftrightarrow |2, \bar{m}'\rangle$ were given by Eq. 6.26, with the resonant strengths given in Table 6.1. In this section we will consider a number of different ways of measuring coupling strength, and compare each of these results with the predicted values for the corresponding $n = 1$ and $n = 3$ transitions. Using the simplest data analysis method, the full set of all resonant transition strengths in these groups will also be measured. Finally, the dependence of coupling strength on static magnetic field will be experimentally demonstrated for the clock transitions.

Our measurements rely on the fact that Rabi frequency is directly proportional to coupling strength (see Eq. 6.30). The MW-probe power is also a factor in the coupling strength, and in order to separate the two effects it is necessary to measure the Rabi frequency at a number of different MW-probe powers. We already know from Eq. 6.36 that we can measure the Rabi

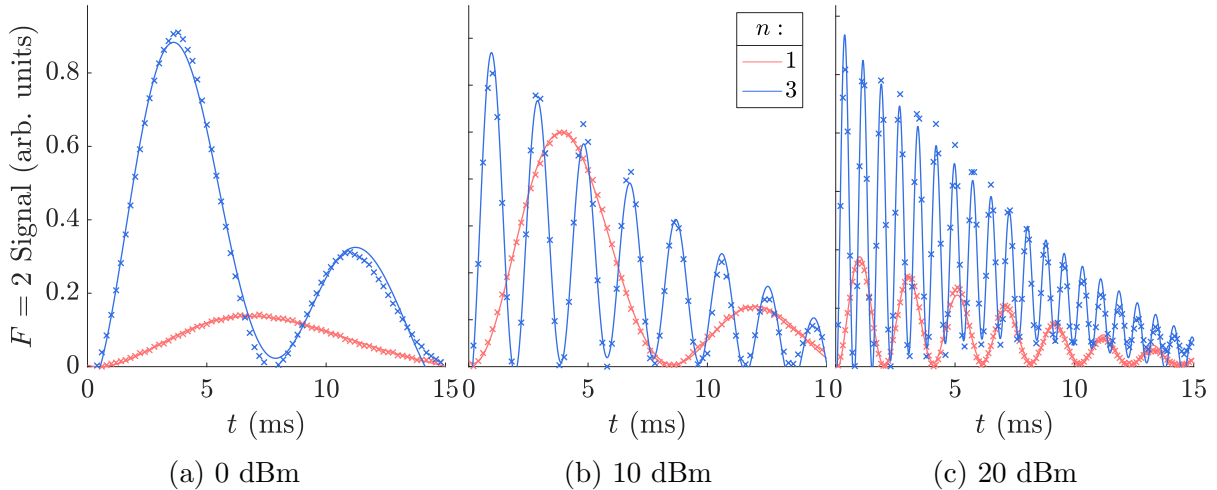


Figure 6.15: Rabi oscillations on the RF-dressed transition $|1, 0\rangle \leftrightarrow |2, 0\rangle$ in groups $n = 1$ and 3 are shown for relative MW-probe powers of $(0, 10, 20)$ dBm in (a-c), later calibrated as $B_{\text{MW}} = (0.4, 1.2, 3.7)$ mG respectively. The fits are to a sine wave decaying in amplitude as a function of the MW-pulse duration t .

frequency from fits to the power distorted peak shapes in spectral data. Alternatively we can use the more direct approach of simply preparing a pure $|1, \bar{m}\rangle$ state and driving Rabi cycles to $|2, \bar{m}'\rangle$, measuring the population transfer as a function of pulse duration. We have already seen in Figure 6.4a that such measurements suffer from signal strength reduction over time. For short (~ 5 ms) pulse times this loss was roughly linear, but for longer pulse times this is a more complex function. Fits to Rabi frequencies, with an arbitrary non-periodic envelope, are shown in Figure 6.15 for the same MW-powers and frequencies used for taking the spectral data in Figure 6.12.

As the resonant coupling strength of the $|1, 0\rangle \leftrightarrow |2, 0\rangle$ clock transition in $n = 1$ is one third the strength of the corresponding transition in $n = 3$, it is unsurprising that there is a marked difference in their measured Rabi frequencies. Rabi frequency as a function of MW-power is plotted in Figures 6.18a and 6.18b for the spectral and temporal measurements respectively, with errorbars scaled to the goodness of the fits. We see from this that the fits to spectral lineshapes give a more precise measure of Rabi frequency. This may be because the MW-pulse duration, and hence the signal detection strength, are fixed for all points, and therefore there is no error introduced by an envelope fit. Fitting the gradient of the Rabi frequency versus the MW-amplitude extracts the values given in Table 6.3 for both models, in comparison with the theoretical result. The values are given for analysis of all clock transitions

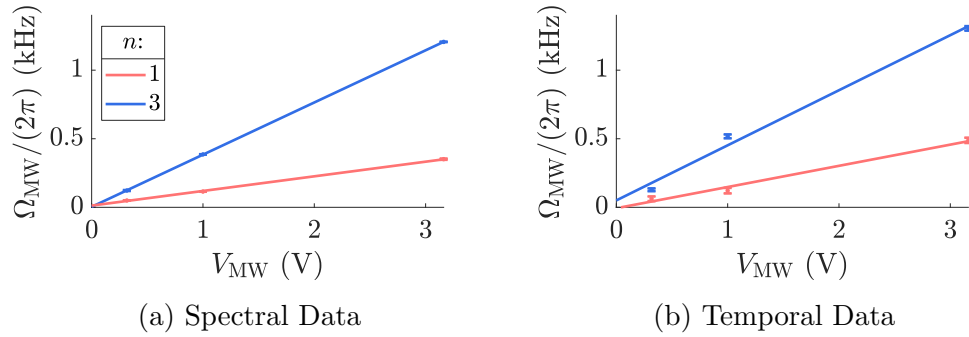


Figure 6.16: The figure shows the Rabi frequency as a function of MW-probe peak voltage, as extracted from a spectral scan (a) and a temporal scan (b), using data from Figures 6.12 and 6.15 respectively. Transitions were driven on $|1, 0\rangle \leftrightarrow |2, 0\rangle$ in groups $n = 1$ and 3. The gradient of the input voltage versus Rabi frequency is a measure of the coupling strength, as given in Table 6.3. V_{MW} is the voltage output from the MW-generator, which will be proportional to amplitude of the MW at the atom cloud.

in the chosen two groups. As the amplitude of the MW at the atom cloud is not directly measurable, the plots are as a function of the amplitude output by the MW-generator. However, use of the coupling strengths from Eq. 6.26 along with our Rabi frequency data from Figure 6.16 allows the calculation of the field B_{MW} at the region of the atom cloud:

$$B_{\text{MW}} = 10^{P_{\text{dBm}}/20} \times (0.367 \pm 0.034) \text{ mG}, \quad (6.37)$$

where P_{dBm} is the power output from the MW-generator in dBm. The error on the calibration factor is likely larger than stated, as the MW-power experienced by the atomic cloud is dependent on its location, which may vary due to both MOT alignment and time of flight (as discussed in Section 6.2.2). For conversion from V_{MW} (in Volts) to static field, we substitute in $10^{P_{\text{dBm}}/20} = V_{\text{MW}}/(5\sqrt{2})$, as the generator has an output resistance of 50Ω .

For comparison, we can also calculate this same calibration factor from the bare MW Rabi frequencies. From the data in Figure 3.6b, we can measure the Rabi frequencies of the bare π -polarised transitions $|1, m\rangle \leftrightarrow |2, m\rangle$, which gave $\omega_{\text{Rabi}}/(2\pi) = (7.3 \pm 0.1, 8.3 \pm 0.1, 7.4 \pm 0.1)$ kHz for $m = -1, 0, 1$ respectively. The theoretical coupling coefficients for the three transitions have the strength ratio $\sqrt{3}/2 : 1 : \sqrt{3}/2$ (≈ 0.87) which compares favourably with the measured ratio of $0.88 \pm 0.2 : 1 : 0.89 \pm 0.2$, where the $m = 0$ coupling is used as the reference. Having established that the couplings do appear to be of the predicted form, the relationship between the Rabi frequencies and the static field can now be obtained using Eq. 6.33, along with the bare coupling coeffi-

cients from Table 6.2. As this data was taken with a MW-power of 23.7 dBm, we calculate that

$$B_{\text{MW}} = 10^{P_{\text{dBm}}/20} \times (0.393 \pm 0.006) \text{ mG}, \quad (6.38)$$

which is in good agreement with the dressed prediction.

One further way of extracting coupling strengths is from the amplitudes of the transition peaks, using spectroscopy data such as from Figures 6.8b and 6.8c for comparatively high and low MW-probe powers respectively. Due to the various reasons discussed in Section 6.2.1, such as imperfect atom number normalisation and detection strength variation, this is not a reliable method, but is good for giving a rough indication. Using fits to the Lorentzian or Gaussian peak shape, in the same manner as we fit the peak widths in Figure 6.8a, the amplitudes are extracted, as given by the constant of proportionality in Eq.s 6.34 and 6.35 respectively. The mean height of all measured transition peaks is compared with the mean predicted coupling strength, in order to provide a scale factor which accounts for the arbitrary units of the detected signal. This is performed as a single factor for each initial state preparation $|1, \bar{m}\rangle$, after the appropriate detection strength scalings from Table 4.1 are accounted for.

The appropriately scaled measurements of coupling strength are shown in comparison with the theory in Figure 6.17, for both low and high MW-probe power. As expected, the values are subject to a high level of error, particularly for the clock transitions where Rabi-peak distortion makes the simple fits unreliable, but the approximate values are a decent match with the theory. For the clock transitions, the predictions of coupling strength from the measured Rabi-frequency are also shown, providing a much more reliable match with the theory. The Rabi peak distortion method provides the best match, but this can only be reliably measured for peaks with low inhomogeneous broadening; for non-clock transitions, this does not provide a reliable fit. Direct measurement of the Rabi frequency is data and time intensive, and therefore

$\frac{ H_{\text{MW}} }{\Omega_{\text{norm}}}$	n m	$n = 1$			$n = 3$		
		-1	0	1	-1	0	1
Theory		2.83	1.63	2.83	2.83	4.90	2.83
Spectral		3.07 ± 0.37	1.35 ± 0.03	2.88 ± 0.43	2.90 ± 0.37	4.83 ± 0.03	2.82 ± 0.43
Temporal		2.75 ± 0.59	1.96 ± 0.40	2.54 ± 0.83	2.66 ± 0.20	5.10 ± 0.29	2.85 ± 0.21

Table 6.3: The couplings strengths of the $n = 1$ and 3 clock transitions $|1, \bar{m}\rangle \leftrightarrow |2, -\bar{m}\rangle$ are given in the table, measured using two different types of fits to Rabi frequency as a function of power. Example fits are shown in Figure 6.16.

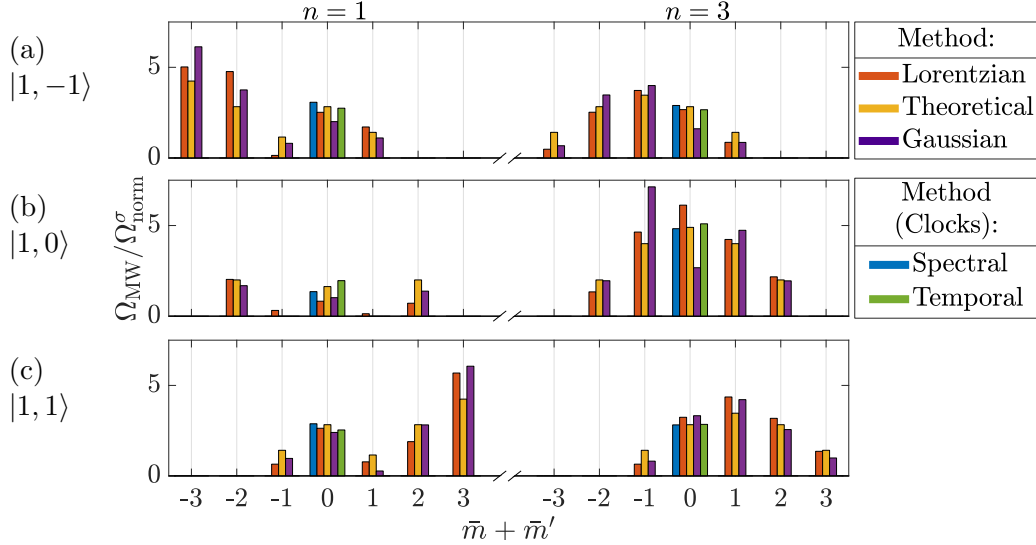


Figure 6.17: The figure shows the measured and predicted coupling strengths of all transitions in groups $n = 1$ and 3 . The high (2.9 mG) and low (0.4 mG) MW-power peak heights were measured using fits such as those in Figure 6.8. These measurements have been scaled by a single factor in each panel which accounts for the MW-probe power. The spectral and temporal Rabi frequency measurements were only performed for the clock transitions ($\bar{m} + \bar{m}' = 0$), and use fits such as those in Figure 6.16.

was only performed for the clock transitions of particular interest in Chapter 7. Such a method would be the most accurate way of determining any arbitrary coupling strength.

Thus far, only the resonant coupling strengths have been investigated. It is also possible to measure the Rabi frequencies, and hence the coupling strengths, as a function of static magnetic field, as was theoretically predicted by Eq. 6.26. We can use the same method of measuring the Rabi frequency as in Figure 6.15, but fix the MW-probe power and instead scan the static magnetic field and the MW-pulse duration. In this case we need to ensure that the MW-probe is always resonant with the transition. For group $n = 1$, the MW-transition frequency as a function of static field was shown in Figure 6.13a, and corresponding data was taken for $n = 3$. Although it should be sufficient to use the predicted transition frequency dependence on static field from Eq. 6.2, which the data shows good agreement with, the decision was made to directly measure the transition frequencies before measuring the Rabi frequencies, in order to be confident there is no miscalibration of the static field. Using the measured transition frequency for each static field strength, the Rabi frequency was measured for all clock transitions in groups $n = 1$

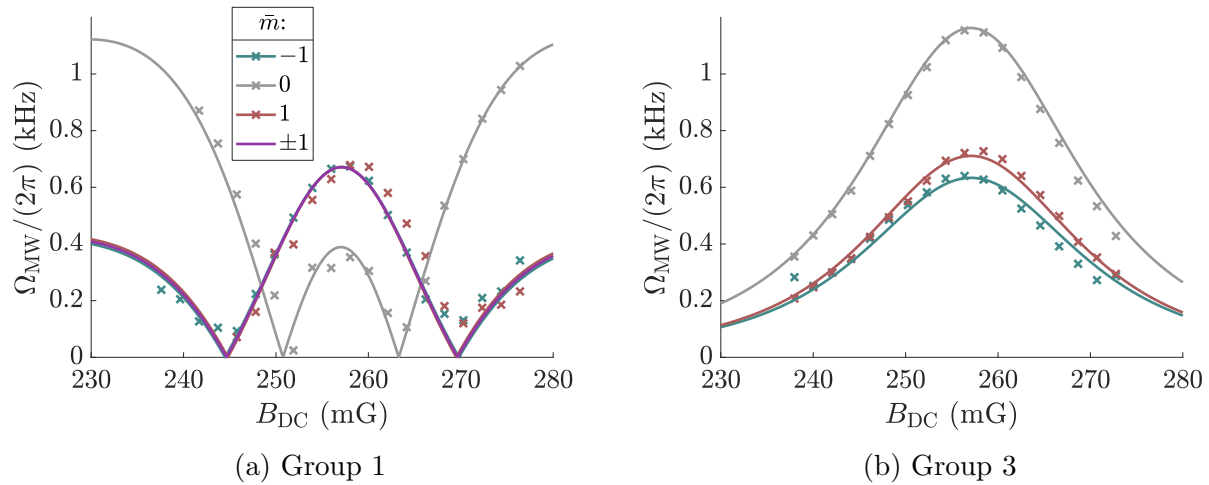


Figure 6.18: Measurements of Rabi frequency as a function of static field for all clock transitions $|1, \bar{m}\rangle \rightarrow |2, -\bar{m}\rangle$ in groups $n = 1$ and 3 are shown in (a) and (b) respectively ($B_{\text{MW}} = 2.9$ mG). Predicted Rabi frequencies from Eq. 6.26 are plotted, using the measured RF-field strengths from Figure 6.14, and a fit to the overall amplitude scale factor accounting for the MW-probe strength.

and 3 , as plotted in Figures 6.18a and 6.18b respectively. The corresponding theoretical predictions are also plotted, using the measured RF-field strengths from Figure 6.14; the amplitude is scaled by a factor to account for the MW-probe power and other constants. The match between data and theory is good, including the zero coupling points in the $n = 1$ case expected from the change in sign of the coupling strength.

A less accurate but much simpler method of coupling strength estimation uses fits to the spectroscopy peaks such as those in Figure 6.8c, only now as a function of static field. For this, we reanalyse the data from Figure 6.14c, fitting the peak locations for each value of static field (e.g. Figure 6.14b). As previously, this does not give good results for the clock transition ($|1, -1\rangle \leftrightarrow |2, 1\rangle$), particularly in this case as the linewidth is of the same magnitude as the frequency step size. For the other transitions from $|1, -1\rangle$ in $n = -1$, the peak height as a function of static field is plotted in Figure 6.19, along with the corresponding theoretical predictions. The data has been scaled by the appropriate detection strengths, as well as a single factor accounting for the arbitrary units of the detected signal. Despite the imprecision of this method, the approximate locations of the minima and maxima roughly correspond. The two transitions with $|\bar{m} + \bar{m}'| = 1$ show better agreement with the data, likely due to reduced susceptibility to static field noise. As the clock transition

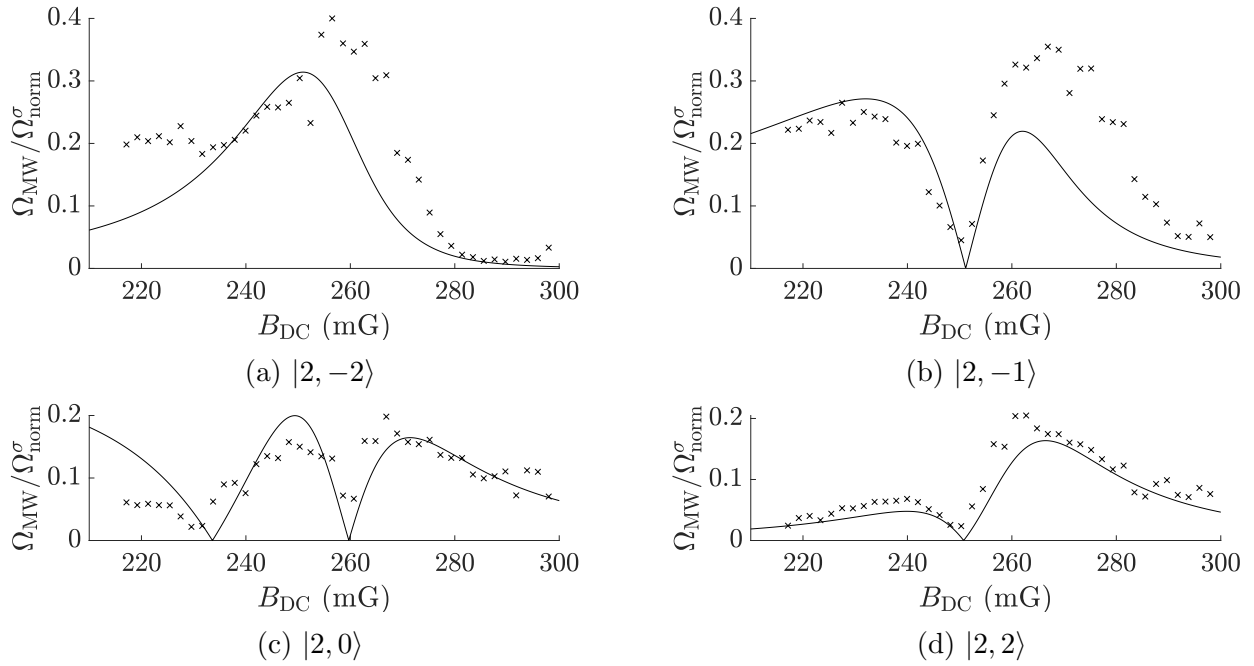


Figure 6.19: Estimates of the $n = 1$ coupling strengths of the transitions $|1, -1\rangle \leftrightarrow |2, \bar{m}'\rangle$ as a function of static field are gained from fits to the signal amplitudes at the transition frequencies in Figure 6.14. These are plotted for all non-clock transitions, along with corresponding theoretical predictions. Overall features of the theory and data are consistent, although as this is a crude method of measuring the coupling coefficients the correlation is imperfect. Adapted from our paper [71].

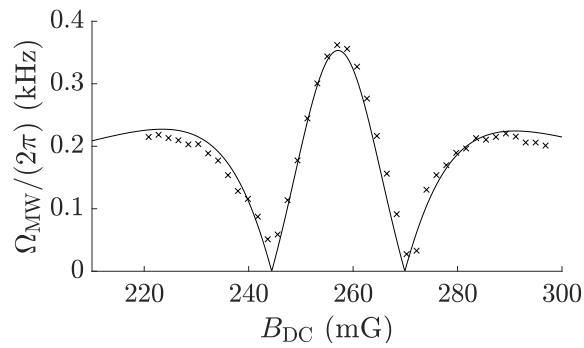


Figure 6.20: Data and corresponding theoretical prediction of Rabi frequency for the transition $|1, -1\rangle \leftrightarrow |2, 1\rangle$ in group $n = 1$. The scale of the figure matches that used in Figure 6.19. Adapted from our paper [71].

$|1, -1\rangle \rightarrow |2, 1\rangle$ is of particular interest in this work, the Rabi frequency as a function of static field was measured again, using the same method as in Figure 6.18a, only with a smaller step size and wider static field range. This is plotted in Figure 6.20, along with the theoretical prediction as before. This transition will be used for interferometry purposes in Section 6.3.3 as well as coherence control data in Chapter 7.

6.3.3 Ramsey Interferometry

In this section, experimental and theoretical results on interferometry using dressed states are shown. This work was performed with Dr Fabio Gentile and also appears in his thesis [75], as well as our paper [103]. Interferometry is the method of combining two waves and studying their interference pattern in order to make a measurement. In the case of atoms, the Ramsey interferometric technique is used [145], which requires splitting a cloud in two and recombining after some delay time. Assuming there is a difference between the paths experienced by the two parts of the cloud, this can have some effect on the final phase. We can therefore extract information on a measurable parameter using our interferometric phase.

A basic two-pulse-Ramsey sequence in a two-level system begins with atoms in a pure $|1\rangle$ state. In order to split the cloud, a $\pi/2$ MW-pulse is used to put the atoms into a superposition of states, e.g. $(|1\rangle + |2\rangle)/\sqrt{2}$, and then after some hold time a further $\pi/2$ -pulse puts all population into $|2\rangle$ if the two parts of the atom cloud experience the same effects and the MW is resonant with the transition. If the two pulses are of duration t_p and the delay between pulses is t_{gap} , the final population fraction in state $|2\rangle$ will be given by [69]

$$N_2/N_{\text{tot}} = \Omega_{\text{MW}}^2 \frac{\sin^2(\Delta_{\text{MW}} t_p / 2)}{\Delta_{\text{MW}}} \cos^2\left(\frac{\Delta_{\text{MW}} t_{\text{gap}}}{2}\right), \quad (6.39)$$

where Ω_{MW} and Δ_{MW} are the Rabi frequency and the detuning of the MW-driving field respectively. This is similar in form to the interference seen when performing an optical two-slit diffraction experiment [89]. Performing this experiment using the RF-dressed states $|1\rangle = |1, -1\rangle$ and $|2\rangle = |2, 1\rangle$ gives the data shown in Figure 6.21a, with the corresponding theoretical prediction shown in Figure 6.21b. The sequence was taken with $t_p = 0.416$ ms and $t_{\text{gap}} = 2$ ms, and the theory is purely the plot of Eq. 6.39 with these values, rather than a fit to the data. The theory and data show good agreement in their general shape, even if they do not match perfectly due to the simplifications required to generate the theoretical model, e.g. no free phase evolution, and the approximation as a two-level-system. For instance, the fact that the population fraction never reaches zero in the central set of peaks is

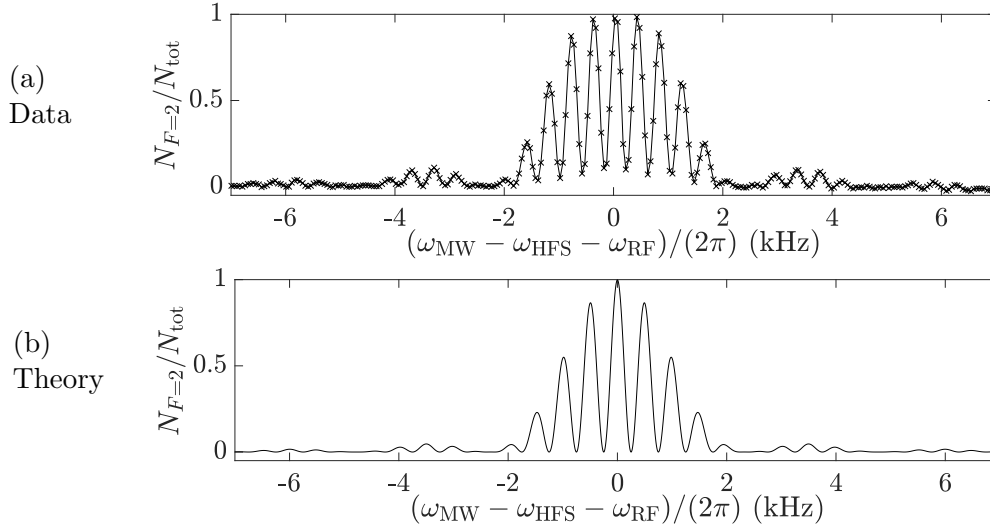


Figure 6.21: An initial state $|1, -1\rangle$ is subjected to the full two-pulse-Ramsey sequence, with a MW-probe detuned from resonance with the transition to $|2, 1\rangle$ (in $n = 1$) by $\Delta_{\text{MW}} = \omega_{\text{MW}} - \omega_{\text{HFS}} - \omega_{\text{RF}}$. The data, for a 2 ms pulse separation and a 0.416 ms pulse time, is shown in (a), with the corresponding theoretical prediction in (b) as given by Eq. 6.39.

a characteristic feature [14] not predicted by the simple model.

The primary drawback of the basic two-pulse Ramsey sequence is that a dynamical phase may accumulate between the two parts of the cloud, increasing the noise level in the final reading. This undesired phase evolution over time is likely to take place even in the presence of no driving. It is therefore advantageous to instead use the full three-pulse-Ramsey sequence, which adds a central π -pulse to fully flip the state $(|1\rangle + |2\rangle)/\sqrt{2} \rightarrow (|1\rangle - |2\rangle)/\sqrt{2}$, in order to reverse the direction of the phase evolution in the second part of the sequence, and hence remove the dynamical phase. The final pulse therefore puts the atoms back into state $|1\rangle$ in the case of resonant MW and no external influences. How pure a final state $|1\rangle$ is regained is a necessary measurable from which the externally induced phase is extracted. Such a sequence of MW-pulses is shown in Figure 6.22, with the spacing between the centre of the two $\pi/2$ -pulses given by t_{seq} .

The three-pulse sequence requires a more complex treatment, using the Hamiltonian of a two level system driven with an AC-field

$$H = \frac{\hbar}{2} \begin{pmatrix} \Delta & \Omega \\ \Omega^* & -\Delta \end{pmatrix}, \quad (6.40)$$

as originally derived for RF-coupling in Eq. 2.41. In deriving this for the

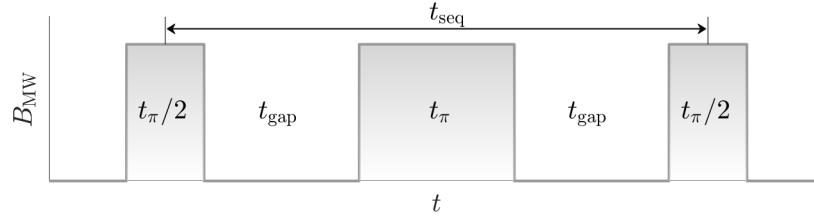


Figure 6.22: The figure shows the MW-probe strength during a three-pulse Ramsey sequence. t_{π} is the Ramsey π -pulse duration for a fixed MW-power, and the separation between pulses is t_{gap} . This sequence was used to generate the data in Figure 6.23a, where a phase φ is applied to the final pulse, with the other pulses defined as having zero phase.

RF case, where the phase was a fixed value, we incorporated the phase of the dressing into the Rabi frequency term. For the MW-field, we require a variable phase, and therefore need a slight change in the definition of the Rabi-frequency, which is no longer inclusive of the phase dependent factor. Our Hamiltonian is now

$$\begin{aligned} H_{\text{MW}}^{\varphi} &= \frac{\hbar}{2} \begin{pmatrix} \Delta_{\text{MW}} & \Omega_{\text{MW}} e^{i\varphi} \\ \Omega_{\text{MW}}^* e^{-i\varphi} & -\Delta_{\text{MW}} \end{pmatrix} \\ &= \Omega_{\text{MW}} (\cos(\varphi) \begin{pmatrix} 0 & 1 \\ 1 & 0 \end{pmatrix} + i \sin(\varphi) \begin{pmatrix} 0 & -i \\ i & 0 \end{pmatrix}) - \Delta_{\text{MW}} \begin{pmatrix} 1 & 0 \\ 0 & -1 \end{pmatrix}, \end{aligned} \quad (6.41)$$

and we require the use of an evolution operator, given by

$$U^{\varphi} = e^{-iH_{\text{MW}}^{\varphi}t/\hbar}, \quad (6.42)$$

in order to calculate the change in population between our two levels over the course of the sequence. In the case of free evolution, the Hamiltonian is as before, only with $\Omega_{\text{MW}} = 0$ as there is no MW-driving. We then need to find the total evolution caused by the different stages of the sequence, from the wavefunction

$$|\Psi\rangle = U_{\pi/2}^{\varphi} U(t_{\text{gap}}) U_{\pi}^0 U(t_{\text{gap}}) U_{\pi/2}^0. \quad (6.43)$$

This can be solved numerically with the use of a quantum mechanics toolbox in Python [102].

In order to test interferometry using dressed states in our experiment, an arbitrary phase needs to be applied in order to simulate some measurable change. I-Q modulated signals consist of in-phase ‘I’ and quadrature ‘Q’ components. This allows the generation of a signal of arbitrary phase φ by the combination of two signals at both zero and $\pi/2$ phase. The I-Q modulated

amplitudes are given by

$$\begin{aligned} A_I &= A_{\text{tot}} \cos(\varphi) \sin(\omega_{\text{MW}} t), \\ A_Q &= A_{\text{tot}} \sin(\varphi) \cos(\omega_{\text{MW}} t), \end{aligned} \quad (6.44)$$

which can be combined together to make the signal

$$A = A_I + A_Q = A_{\text{tot}} \sin(\omega t + \varphi). \quad (6.45)$$

It is only the relative phase which is measurable, and as such we only change the phase of the final $\pi/2$ -pulse.

We can now scan the parameter space of all possible values φ , as well as the detuning of the MW from resonance with a transition (normalised by the Rabi frequency, so as to not be dependent on the MW-power). Performing the full Ramsey sequence on the transition $|1, -1\rangle \leftrightarrow |2, 1\rangle$ in group $n = 1$ gives the colourmap data in Figure 6.23a, which shows the final population fraction in $F = 2$. The input duration of the π -pulse was calibrated using the same technique as in Figure 3.6b, which provided the input parameter $t_\pi = (0.74 \pm 0.05)$ ms, and the spacing between pulses was set to be $t_{\text{gap}} = 1$ ms. The theoretical model of the same data is shown in Figure 6.23b, which shows good agreement with the data, particularly considering that this is a pure theoretical prediction with no fit parameters. The measured Ramsey fringes are not as smooth as in the predicted case due to slight fluctuations in experimental parameters (e.g. atom number, external static fields) over the course of the ~ 2 hour experimental run.

One notable discrepancy with the theoretical prediction is an offset in phase; this is more easily visible in a cut through the data at a fixed frequency. In Figure 6.24a, the phase scan for a resonant MW-probe frequency, we see that in the case of applied phase $\varphi = 0$, there is still a residual phase of 0.38 rad. This is likely due to some external variation, such as static field inhomogeneity. As the atoms are in free-fall, they will experience some small change in static field over the course of the sequence as Helmholtz coils do not provide a perfectly uniform static field. MW-probe strength will also have a small spatial variation. In Figure 6.24b two further cuts through the data are shown, this time for variable detuning and fixed phase. Both the $\varphi = 0$ and π rad cases are shown, as well as the corresponding theoretical predictions, offset by 0.38 rad to account for measured phase. The agreement with the data is good, although imperfect atom number normalisation leads to some discrepancies, particularly around zero phase. Overall, we have shown that interferometry using dressed states is achievable and can be used to measure changes in some external parameter. In this case we have measured an artificially applied phase, but this method can be logically extended to measure more physical parameters.

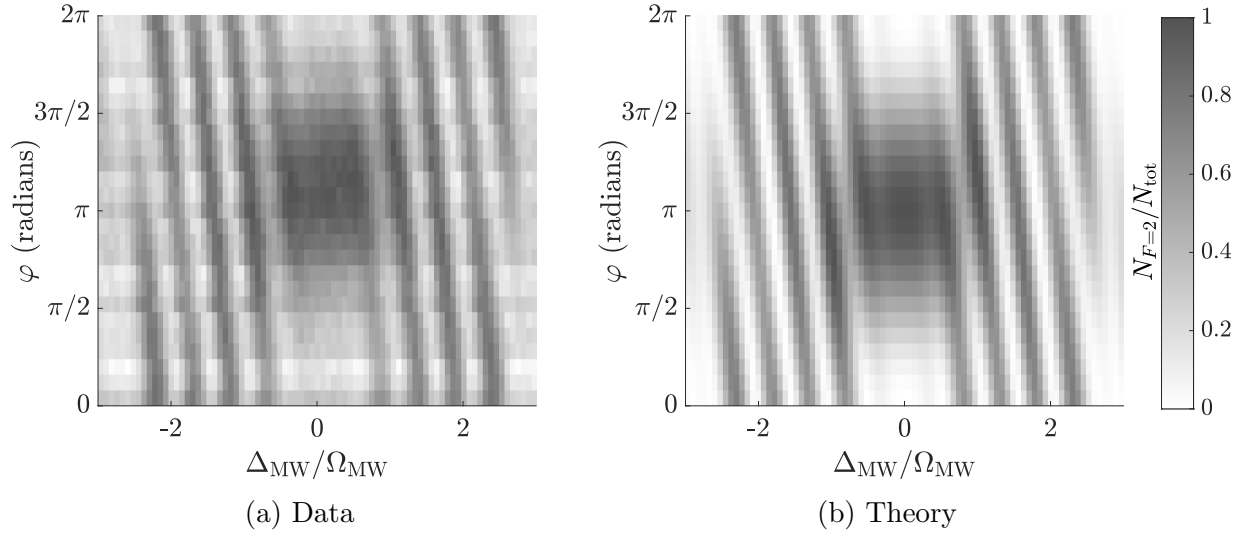


Figure 6.23: Performing the full three-pulse-Ramsey sequence, scanning both the detuning of the MW-probe and the phase of the final pulse, gives the colourmap in (a) of the population fraction in $F = 2$ at the end of the sequence. In (b) the theoretical prediction of the same sequence is shown. Adapted from our paper [103].

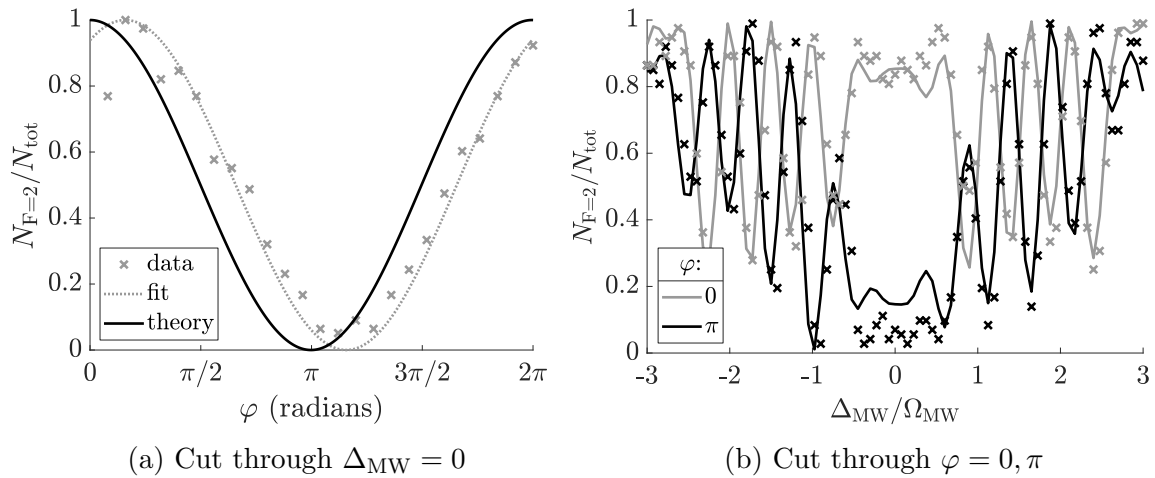


Figure 6.24: Ramsey interferometry data plotting the final population fraction in $F = 2$ is shown in (a) as a function of the applied phase at the resonant static field, along with the corresponding theoretical prediction. We see from this that there is a mismatch of $\delta\varphi = 0.38$ rad between the applied and measured phases at the end of the the sequence. In (b) the applied phase is fixed at $\varphi = 0$ or π rad, and the theoretical prediction is plotted for $\varphi - \delta\varphi$, to account for the phase mismatch. Adapted from our paper [103].

Chapter 7

Coherence Control

In order to maintain the coherence of an atomic superposition state, all populated energy levels must react in the same way to external variables. A significant factor in the case of magnetically trapped atoms is magnetic field gradients and fluctuations. The ability to engineer the magnetic field dependence of atomic energy levels by use of the AC-Zeeman effect will be demonstrated in this chapter, in order to increase the robustness of the atomic state by reducing decoherence due to static magnetic field gradients. We begin with theoretical methods of modelling this effect (Section 7.1) before showing data and analysis of such methods in action (Section 7.2).

7.1 Theoretical Model

In this section the general theory of using the AC-Zeeman effect to manipulate the static field dependence of energy levels is set out. We begin with the basics of quantum coherence and how this may be influenced by the AC-Zeeman effect (Section 7.1.1), before moving on to consider appropriate frequencies for dressing in order to cancel field dependence (Section 7.1.2). We then consider two different ways of modelling the effect of such a MW-dressing, firstly in the case of treating the dressed levels (Section 7.1.3) and then in analysis of the bare system (Section 7.1.4).

7.1.1 Coherence and the AC-Zeeman Effect

Quantum coherence is a property of an isolated system in a linear superposition of states, which we describe using a density matrix. A state Ψ composed of a superposition of levels 1 and 2 has a density matrix given by

$$|\Psi\rangle\langle\Psi| = \begin{pmatrix} |c_1|^2 & c_1c_2^* \\ c_2c_1^* & |c_2|^2 \end{pmatrix} = \begin{pmatrix} \rho_{11} & \rho_{12} \\ \rho_{21} & \rho_{22} \end{pmatrix}, \quad (7.1)$$

where c_1 and c_2 are the quantum amplitudes of the two states. ρ_{11} and ρ_{22} are the populations in each state, and the off-diagonal elements ρ_{12} and ρ_{21} are the coherences between the two states [69]. Decoherence occurs when the system interacts with external parameters; interactions with the environment turn a pure superposition state into an incoherent mixed state by introducing external couplings which cannot be fully modelled [79]. As we can control the internal state of the atom using magnetic fields (Section 3.2) a coherent process can be reversed, but decoherent changes are irreversible as we do not have full control of the environment. In order to perform interferometry, where the superposition state of the atom is used to make a measurement, coherence is a key requirement. Any decoherence from interactions with the environment will manifest as noise on the measurement, or destroy the measurement altogether. As the interaction with the environment is equivalent to making a measurement of the state, decoherent quantum systems will begin to behave more like a classical system where the state of the system is defined by a sum of probabilities, rather than a probability density [195]. One possible cause of decoherence is magnetic field variations or gradients; control of the magnetic field dependence of a system can be used to alter its coherence.

In this work, our interest is in improving the coherence of an RF-dressed atomic superposition state. If there is no variation in transition frequency with static field, this decouples a superposition state between the two energy levels from the effects of the static field, making the system robust against field fluctuations or gradients, and removing static-field related decoherence effects. This is necessary in cases where magnetically trapped atoms are used, as we cannot simply remove static field gradients, which are a requirement of many trapping geometries. In cases where static fields are not required, such a technique could be used in place of magnetic shielding, which can be bulky and inconvenient.

Thus far we have considered both the effects of a static magnetic field on the magnetic sublevels of RF-dressed ^{87}Rb and of a resonant MW-field which drives population transfer between manifolds. The next step in the manipulation of the internal state of the atom is to introduce detuned MW-fields to alter energy levels without transferring population. The AC-Zeeman effect is the shifting of energy levels in the presence of a detuned AC-field. In the simple case of a two-level system with a non-zero coupling coefficient, the application of a red-detuned ($\Delta < 0$) dressing causes the levels to shift further apart in energy, and in the case of a blue-detuned ($\Delta > 0$) dressing this shifts the lines closer together, as illustrated in Figure 7.1a.

In the laboratory frame, we can treat the shift as a simple perturbation w of the two level system with energies 0 and $\hbar\omega_0$ for the ground and excited state respectively. The Hamiltonian and corresponding eigenvalues will therefore

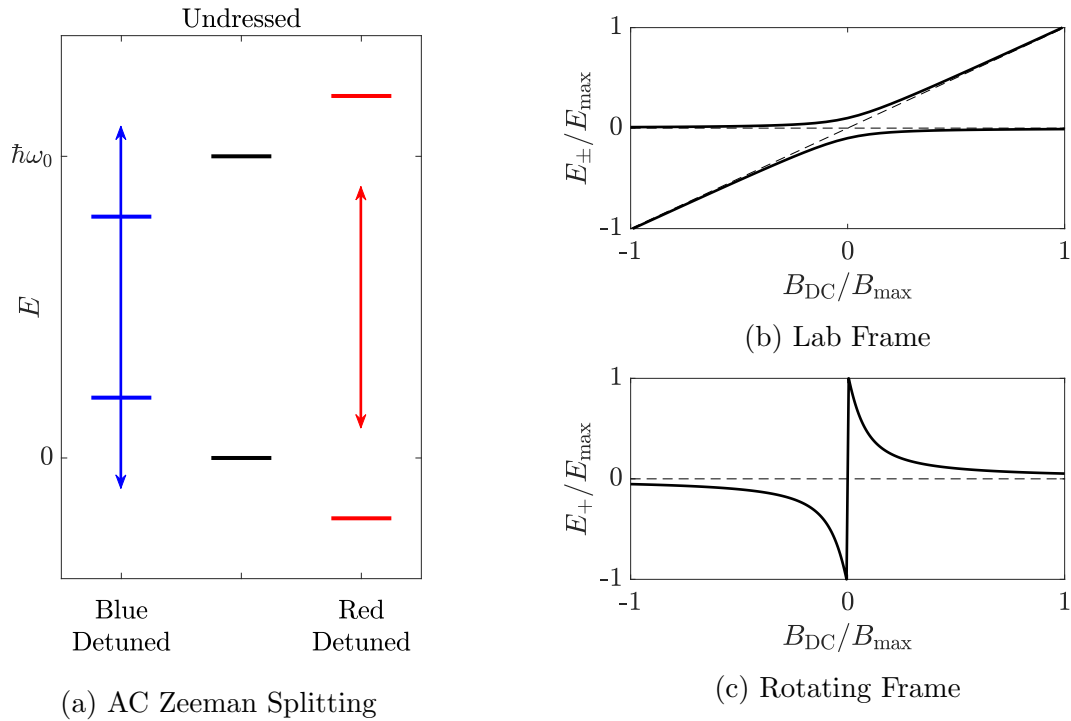


Figure 7.1: The splitting of a two level system in the presence of a detuned AC-magnetic field is shown in the figure. In the schematic (a) the effects of a blue and red-detuned dressing on a two level system are shown. Adapted from [27]. The avoided crossing between two energy levels when a dressing field is applied (Eq. 7.2) is shown in (b), and the energy dependence of a single one of these levels in the rotating frame (Eq. 7.4) is shown in (c). Dashed lines indicate the undressed case.

be

$$H = \hbar \begin{pmatrix} 0 & \mathbf{w}^* \\ \mathbf{w} & \omega_0 \end{pmatrix}, \quad E_{\pm} = \frac{\hbar}{2} \left(\omega_0 \pm \sqrt{\omega_0^2 + 4\mathbf{w}^2} \right). \quad (7.2)$$

For an arbitrary choice of perturbation strength, in the case where the energy level splitting is a function of static field, this is plotted in Figure 7.1b, with the undressed case indicated with dashed lines. We see from this that the AC-coupling causes the emergence of an avoided crossing, derived in more detail in [186].

We now consider the same effect in the rotating frame of the dressing frequency. Applying a MW-dressing of the form $B_{\text{MW}} = \Omega_{\text{MW}} \cos(\omega_{\text{MW}} t) / 2$

gives the Hamiltonian

$$H = \frac{\hbar}{2} \begin{pmatrix} 0 & \Omega_{\text{MW}}^* \cos(\omega_{\text{MW}} t) \\ \Omega_{\text{MW}} \cos(\omega_{\text{MW}} t) & 2\omega_0 \end{pmatrix}, \quad (7.3)$$

which we can move to the rotating frame, using the same method as in Section 2.2.2 and Eq. 2.29,

$$i\hbar\dot{\phi} = i\hbar\hat{U}\dot{\hat{U}}^\dagger\phi + \hat{U}\hat{H}\hat{U}^\dagger\phi, \quad \hat{U} = \begin{pmatrix} 1 & 0 \\ 0 & e^{i\omega_{\text{MW}} t} \end{pmatrix}. \quad (7.4)$$

After performing this transformation and dropping the fast oscillating terms, this gives the new Hamiltonian and eigenvalues

$$H_{\text{rot}} = \frac{\hbar}{2} \begin{pmatrix} 0 & \Omega^* \\ \Omega & -2\Delta \end{pmatrix}, \quad E_{\text{rot}} = \frac{\hbar}{2} \left(-\Delta \pm \sqrt{\Omega^2 + \Delta^2} \right), \quad (7.5)$$

where $\Delta = \omega_0 - \omega$, and we have removed the MW subscripts for ease of reading. Which of the eigenvalues is the lowest energy in the laboratory frame will flip at resonance, i.e.

$$\delta E = \frac{\hbar}{2} \left(-\Delta + \text{sign}(\Delta) \sqrt{\Omega^2 + \Delta^2} \right) \approx \hbar \frac{\Omega^2}{\Delta}, \quad (7.6)$$

where the approximation is a good model at sufficiently large detuning. The full equation is plotted in Figure 7.1c as a function of static field, which in this simple case will be proportional to detuning. The approximation is invalid at close to zero detuning as it tends to infinity at this point.

In order to build up a picture of the effects of a single off-resonant MW-dressing in a multi-level atom, we first consider that only the transition closest to resonance with the dressing field will be shifted by the dressing. To cancel the difference in static field dependence between two energy levels, we therefore require a dressing on a transition which has a Rabi-frequency of the appropriate form

$$\Omega_{\text{dress}}^2 \propto E_{F+1, \bar{m}'} - E_{F, \bar{m}} + \hbar\omega_{\text{offs}}, \quad (7.7)$$

where $E_{F, \bar{m}}$ is as defined in Eq. 2.43, and ω_{offs} is an arbitrary offset. This offset is included to account for static field independent energy contributions, such as the hyperfine splitting, as well as any field independent shifts in the transition energy caused by the dressing. Using the approximation as a three-level-system, Figure 7.2 shows the dressed energy level shifts, where the dressing is on a level with magnetic sublevel number \bar{m}_d . If the choice is made to dress the lower energy level on $|F, \bar{m}\rangle \leftrightarrow |F+1, \bar{m}_d\rangle$, this generates a shift $\delta E_{F, \bar{m}}$, or in an equivalent system the upper energy level is dressed via $|F, \bar{m}_d\rangle \leftrightarrow |F+1, \bar{m}'\rangle$, and the resultant shift is $\delta E_{F+1, \bar{m}'}$. The figure shows red and blue detuning in (a) and (b) respectively. The sign of the shift on the chosen

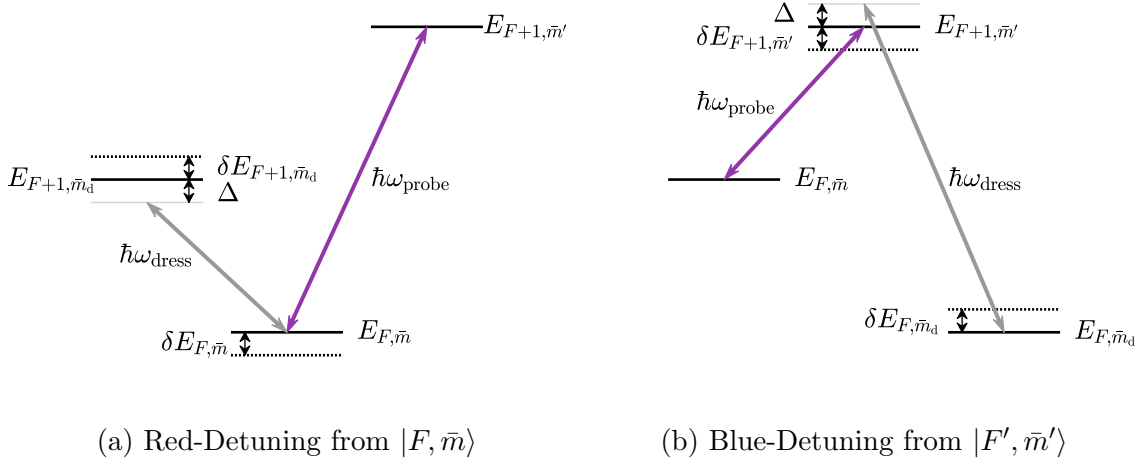


Figure 7.2: In the figure we consider a three-level-system, probed on the transition $|F, \bar{m}\rangle \rightarrow |F + 1, \bar{m}'\rangle$ and dressed using a third state with magnetic sub-level number m_d . In (a) the dressing is on the transition $|F, \bar{m}\rangle \leftrightarrow |F + 1, \bar{m}_d\rangle$, which causes a shift of $\delta E_{F, \bar{m}}$ in the energy of the probed transition, and in (b) the dressing is on the transition $|F, \bar{m}_d\rangle \leftrightarrow |F + 1, \bar{m}'\rangle$, which causes a shift of $\delta E_{F+1, \bar{m}'}$. Undressed energy levels are marked with solid lines, shifted levels with dashed lines and detuned frequencies in grey. Red and blue-detuning are shown in (a) and (b) respectively, although the sign of detuning is not constrained.

energy level will depend on the detuning by

$$\text{sign}(\delta E_F) = (-1)^{F-I+1/2} \text{sign}(\Delta) \quad (7.8)$$

in order to ensure the shift decreases the transition frequency between the two F -levels for blue detuning and increases it for red.

7.1.2 Choice of Dressing Frequency

From here on, we fix our probe on the RF-dressed transition $|1, -1\rangle \leftrightarrow |2, 1\rangle$, although the same method can of course be used to adjust the field dependence of any arbitrary transition. Explicitly the field dependence to be cancelled is

$$E_{2,1} - E_{1,-2} = \mu_B g_2 \sqrt{\frac{|B_{\text{RF}}^+|^2}{2} + (B_{\text{DC}} - B_{\text{res},2})^2} + \mu_B g_1 \sqrt{\frac{|B_{\text{RF}}^-|^2}{2} + (B_{\text{DC}} - B_{\text{res},1})^2} \quad (7.9)$$

from Eq. 2.43, as was plotted in Figure 6.13a for the experimental values of $B_{\text{RF}}^\pm = (26 \pm 1)$ mG and $B_{\text{res},1,2} = (256.4, 257.4)$ mG respectively. This is true

for all values n , as we have discounted field independent terms, which only contribute to the linear offset $\omega_{\text{offs}}(B_{\text{MW}}^{\text{dress}} = 0) = \omega_{\text{HFS}} + n\omega_{\text{RF}}$.

We now need to make a choice of energy levels on which to dress our clock states, using Eq.s 7.7 and 7.9 to find an appropriate transition. Firstly, we need to consider detuning restrictions, as one of the requirements of our MW-dressing field is that it is not sufficiently close to an allowed transition from any populated state to actively drive population transfer. It is clear that we cannot maintain a coherent superposition between two states in a system where atoms are being driven to a third state. A simple way to estimate the minimum required detuning from resonance with a transition to ensure robustness against population transfer is to look at the linewidth of the transition when probed. From our analysis of linewidths in Section 6.2.3, we can estimate the required detuning.

Figure 6.10a showed that at high powers the linewidth of a transition increases linearly as a function of MW-probe power. Also, as we saw from Figure 6.8, despite the differences in heights of transition peaks due to variations in coupling strength, the increase in linewidth due to power broadening is uniform across peaks. From a linear fit to peak width versus $|\bar{m} + \bar{m}'|$ from the low power data in this figure, we obtain the inhomogeneous linewidth contribution. The increase in linewidth as a function of MW-power can be obtained from Figure 6.10a. A rough approximation of any linewidth is therefore given by

$$\text{FWHM}/(2\pi) \approx |\bar{m} + \bar{m}'| \times 1.10 \text{ kHz} + 0.52 B_{\text{MW}} \text{ kHz/mG}, \quad (7.10)$$

where B_{MW} is in milligauss. We are working using the FWHM as this is comparable in both Gaussian and Lorentzian lineshapes, unlike the defined width w (see Figure 6.9). The total population fraction transferred will depend on the coupling strength of the transition, so instead we standardise by choosing the point where the population has dropped by some fraction. Using the Gaussian lineshape, the population transfer has dropped to 1 % of its resonant value at 1.29 FWHM from resonance, or for 0.1 % this is 1.58 FWHM. We make the choice to dress at $\Delta/(2\pi) = 10 \text{ kHz}$, where for $B_{\text{MW}} = 8 \text{ mG}$ the population transfer drops to $< 0.1 \%$ of its maximum value before MW-dressing. However, we are still safe to dress at higher MW-powers than this, as the transition frequency is shifted by an amount $\propto B_{\text{MW}}^2$ away from the dressing frequency, whereas the linewidth of the transition increases roughly $\propto B_{\text{MW}}$. Treating the lineshape as Lorentzian, the $< 0.1 \%$ population transfer point is a factor of 10 further detuned. With the outermost transitions in two neighbouring groups separated by less than this frequency, this is not practical to achieve. The transition peak is also well below the noise level at our chosen detuning, so this should be sufficient.

In the above discussion we are of course only choosing a best case scenario for our limited experimental parameters. A final atom loss of 0.1 % is likely due to a higher fraction of the atoms having some interaction with the third state, particularly over long interrogation times. Measurement of atom loss to a third state would therefore be beneficial, and could potentially be achieved using a state cleaning procedure to remove atoms in the clock states after dressing. This would allow measurement of the residual population fraction in the third state. Potentially also Rabi cycles on the dressing transition may be measurable, although these would be subject to a significant level of noise. A number of experimental improvements to increase both atom number and detection strength would be required in order to make the measurement of such a small atom fraction achievable. Future upgrades to the experiment (Section 8.2.2) should enable these measurements, as this area warrants further study. Population transfer is not a concern in the unconstrained case, however. For interferometry, the use of considerably higher RF-dressing frequency and strength make higher detunings easily achievable, allowing for an arbitrarily low atom fraction loss. A detuning of $\Delta/(2\pi) = 310$ kHz from all populated states is used in [157] for a MW-dressing on the bare ^{87}Rb atom to have a negligible probability of undesired population transfer. Increasing each of the radio frequency, RF-power and static field strength by a factor of ten in our experiment would facilitate such a MW-dressing of the RF-dressed atom.

As the MW-probe will be on the trappable clock transition, the only two levels which will be populated are $|1, -1\rangle$ and $|2, 1\rangle$. We are therefore unconcerned by any couplings near-resonant with transitions solely between unpopulated states. The lowest frequency transition in any group is $|1, -1\rangle \leftrightarrow |2, -2\rangle$, and the highest frequency transition from a populated state is $|1, 1\rangle \leftrightarrow |2, 1\rangle$. In order to meet the requirements on MW-dressing detuning, we require the frequency to be either red-detuned from the former or blue-detuned from the latter of these two transitions. Opposite signs of detuning would lead to population transfer on $|1, -1\rangle \leftrightarrow |2, -1\rangle$ or $|1, 0\rangle \leftrightarrow |2, 1\rangle$ respectively. The chosen transitions are 120 kHz detuned from the nearest transition from a populated state in another group, or 300 kHz if the MW is purely either π or σ_{\pm} polarised and therefore some groups are forbidden.

We now consider which of these couplings are of an appropriate form to cancel the field dependence as given by Eq. 7.7 and plotted in Figure 6.13a. The values Ω^2 for all transitions $|1, -1\rangle \rightarrow |2, -2\rangle$ and $|1, 1\rangle \rightarrow |2, 1\rangle$ are shown in Figures 7.3a and 7.3b respectively. Due to our requirements on detuning, for dressings primarily on $|1, -1\rangle$ we require Ω^2 have the opposite static field dependence of that to be cancelled, whereas for dressings on $|2, 1\rangle$ we require Ω^2 to match this dependence. Explicitly, as we saw in Figure 7.2,

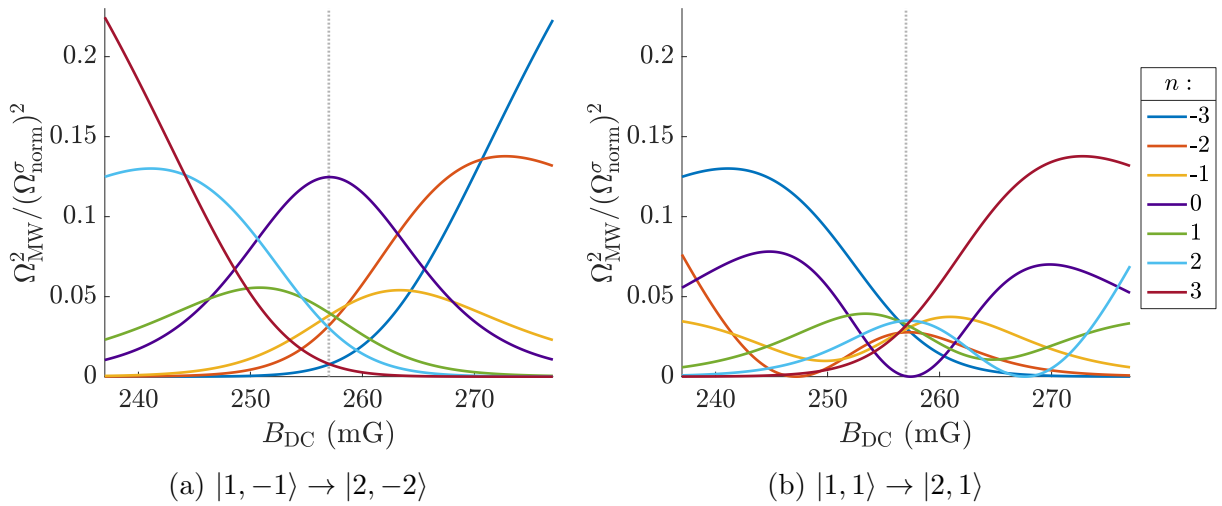


Figure 7.3: The values Ω_{MW}^2 are shown as a function of static field for dressings on the outermost transitions from our chosen clock states, in all groups n . Dashed lines indicate the resonant static field. For plots of coupling strengths of all possible transitions, see Appendix B.1.

both a red-detuned dressing on the lower energy level and a blue-detuned dressing on the upper level negatively shift the dressed energy of the level in question. As only one of the clock levels is shifted, dressing on the lower level thus increases the separation between the two clock levels, whereas dressing on the upper level reduces it.

As the clock transition is decreasing in frequency as a function of static field at the resonance point (Eq. 7.9), the first order cancellation requires a dressing either using a transition where a value Ω^2 shown in (a) has a positive gradient at resonance, or one in (b) that has a negative gradient at

Δ	Transition	n	-3	-2	-1	0	1	2	3
red	$ 1, -1\rangle \leftrightarrow 2, -2\rangle$		-ve	-ve	-ve	min	+ve	+ve	+ve
blue	$ 1, 1\rangle \leftrightarrow 2, 1\rangle$		-ve	max	+ve	min	-ve	max	+ve

Table 7.1: When intending to reduce the static field dependence about resonance for an arbitrary transition, we begin by establishing the slope of the transition frequency versus static field at this point. We then select a group with the ability to cancel this dependence, marked as positive or negative gradient, or minimum or maximum point in the table. Note that the table is not directly giving the slope of Ω^2 as shown in Figure 7.3, but that of the dependence to be cancelled when accounting for the sign of the detuning.

resonance. Transitions which fit this requirement are $|1, -1\rangle \rightarrow |2, -2\rangle$ for $n = -3, -2, -1$ and $|1, 1\rangle \rightarrow |2, 1\rangle$ for $n = -3, -1$, as marked in Table 7.1. The table gives the sign of the field dependence of a transition at resonance which can be reduced using the stated dressings, as well as minima and maxima in order to cancel second order dependencies. In the general case with no restrictions on detuning, a similar table can be drawn up for all transitions using the slopes of Ω^2 at resonance from Appendix B in the case of blue detuning, or for red detuning $-ve \leftrightarrow +ve$ and $min \leftrightarrow max$. Note that although the strength of the (approximately circularly polarised) RF-dressing does determine the gradient at resonance, it will not alter the overall sign. It is also important to recall that, due to the differences in the magnitudes of the g_F -factors of the two clock states, there is not a single resonance point, and by ‘at resonance’ we mean in the region $B_{\text{res}}^{F=1} \leq B_{\text{DC}} \leq B_{\text{res}}^{F=2}$. Making the choice to have our first order dressing predominantly shift $|1, -1\rangle$ and adding the chosen detuning, we obtain the first order MW-dressing frequencies $(\omega_{\text{MW}}^{\text{d}} - \omega_{\text{HFS}})/(2\pi) = (-598, -415, -236)$ kHz when dressing on the identified groups $n = -3, -2, -1$ respectively.

7.1.3 Treatment of Quasi-Energy Levels

The theory thus far has worked in the simplified case where only a single one of the two clock levels is shifted by the dressing, with only the transition closest to resonance causing a shift. In simple level schemes where the required detuning is much smaller than the separation between transitions, this model is sufficient. However, we recall that in our experiment the minimum detuning and the level separation are both of the order of 10 kHz, and that the full level scheme allows 105 RF-dressed transitions of different frequencies. One method of approximating the effect of dressing on a many level system is by summing over multiple detuning and level dependent shifts. This model has successfully been used by Prof. József Fortágh’s group at the Universität Tübingen, in the case of the ^{87}Rb atom [157]. We are using the same method, only with our more complex level scheme which emerges when RF-dressing couples magnetic sublevels. Another difference is that we are working with the full definition of the AC Zeeman shift on each level, rather than the approximation $\delta E \approx \Omega^2/\Delta$, which has purely been used as an aid to determining appropriate MW-dressing frequencies in this thesis. The choice to use the full theory was made because our MW-dressing detunings are two orders of magnitude lower than in the case of the aforesaid paper, and as such the approximated δE , which tends to infinity at zero detuning, is not appropriate.

In a two-level system, the shift on an energy level by a dressing detuned by Δ from a transition with coupling coefficient Ω is given by Eq. 7.6. However,

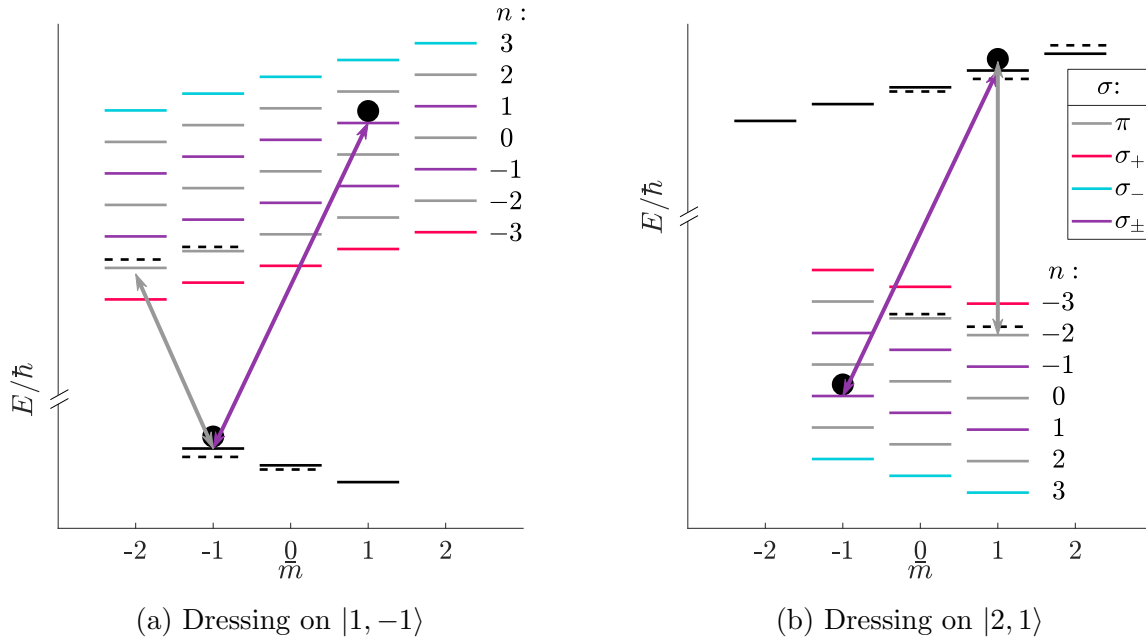


Figure 7.4: In the full set of quasi-energy levels, a dressing is shown on the transitions $|1, -1\rangle \leftrightarrow |2, -2\rangle$ and $|1, 1\rangle \leftrightarrow |2, 1\rangle$ in (a) and (b) respectively. Correspondingly, the quasi-energies are drawn in $F = 2$ and 1. The purple arrow indicates a clock transition $|1, -1\rangle \leftrightarrow |2, 1\rangle$, and the grey arrow indicates the MW-dressing. Black dashed lines indicate the shift on the energy of the neighbouring dressed levels, although all other levels are also shifted by decreasing amounts with increased detuning. Note that the frequency spacing of the levels is not to scale.

as shown in Figure 7.4, when considering the full level system the number of possible transitions from $|1, -1\rangle$ is 35, and from $|2, 1\rangle$ is 21. The energy levels are depicted with the frequency of the $F = 1$ and 2 groups set as constant in (a) and (b) respectively, with the groups of quasi-energy levels shown for the other F -manifold in the same manner as in Figure 6.1c. Note that the energy level spacings between groups are not to scale. In both cases the probe frequency is fixed on $|1, -1\rangle \leftrightarrow |2, 1\rangle$ in group $n = 1$, and the dressing is red or blue-detuned from all populated transitions in group $n = -2$ in (a) and (b) respectively. Shifts on the energy levels directly involved in the dressing are marked as in the three level system (Figure 7.2), and smaller additional shifts are marked on neighbouring energy levels. Although only a small number of shifts are indicated in the picture, all energy levels in the system will in fact be similarly shifted, although by decreasing amounts as the detuning increases.

In order to model the total shift on a single energy level, it is therefore re-

quired to take into account the shifts from all possible transitions by summing over all transitions \mathbf{k} from that level,

$$\delta E_{F,\bar{m}} = (-1)^{F-I+1/2} \sum_{\mathbf{k}} \frac{\hbar}{2} \left(-\Delta_{\mathbf{k}} + \text{sign}(\Delta_{\mathbf{k}}) \sqrt{\Omega_{\mathbf{k}}^2 + \Delta_{\mathbf{k}}^2} \right), \quad (7.11)$$

where $\Omega_{\mathbf{k}}$ is the Rabi frequency of the transition and $\Delta_{\mathbf{k}}$ is the corresponding detuning. Note that $|F, \bar{m}\rangle$ is the level on which the shift is being considered, and \mathbf{k} is all transitions from this level to magnetic sublevels in the other ground state F -manifold, including for all components of MW-polarisation and all groups n . The sign of the shift is fixed by the inclusion of the prefactor from Eq. 7.8, ensuring the lower and upper levels shift in opposite directions. As Ω is a function of B_{MW}^σ , this allows groups of transitions to be suppressed by the choice of MW-polarisation. We can likewise account for mixed combinations of σ_\pm and π -polarisation using $B_{\text{MW}}^\sigma = B_{\text{MW}} \cos(\Theta)$ and $B_{\text{MW}}^\pm = B_{\text{MW}} \sin(\Theta)$, where Θ is the angle of the static field relative to B_x , as marked in Figure 5.9c. Accounting for the shifts on both clock levels $|F, \bar{m}\rangle$ and $|F+1, \bar{m}'\rangle$, the total transition energy will be given by

$$E_{\text{tot}} = \hbar\omega_{\text{HFS}} + \hbar n\omega_{\text{RF}} + (E_{F+1,\bar{m}'} + \delta E_{F+1,\bar{m}'}) - (E_{F,\bar{m}} + \delta E_{F,\bar{m}}), \quad (7.12)$$

where $E_{F,\bar{m}}$ is as defined in Eq. 2.43. As the RF-dressed transition frequencies are a function of B_{DC} , the MW-detuning must account for this. The detuning from any arbitrary transition will be given by

$$\Delta_{F,\bar{m} \rightarrow F+1,\bar{m}'}^n = \omega_{\text{HFS}} + n\omega_{\text{RF}} + (E_{F+1,\bar{m}'} - E_{F,\bar{m}})/\hbar - \omega_{\text{MW}}, \quad (7.13)$$

where ω_{MW} is the MW-dressing frequency. As we have fixed the sign of the detuning relative to the transition rather than relative to a certain energy level, $\Delta_{F,\bar{m} \rightarrow F+1,\bar{m}'}^n \equiv \Delta_{F+1,\bar{m}' \rightarrow F,\bar{m}}^n$.

Advantages of this theory are that it is simple to extend to account for an arbitrary number of dressing frequencies, and it deals well with the effects of multiple groups of RF-dressed transitions. One limitation is that the model does not account for the interdependence between energy levels, i.e. that non-clock transitions that are involved in generating shifts will themselves also be shifted by other couplings. As the maximum energy shifts we measure are of the order of 100 Hz, and the minimum detuning is 10 kHz, this is not a substantial effect. This does however mean that the accuracy of the model will decrease with increasing MW-dressing power, unless the detuning is likewise increased. A further consideration is that, due to the model treating degenerate energy levels as singularities, we also face issues when extrapolating the potentials to static fields further from resonance. An alternative method, treating the bare levels directly, has different advantages and limitations, as follows.

7.1.4 Treatment of Bare Energy Levels

Thus far we have focused solely on the dressed couplings, but in this model we turn our attention to the MW-couplings between the bare energy levels in different F -manifolds $|1, m\rangle \leftrightarrow |2, m'\rangle$. Although this method lacks the ability to properly account for the effects of quasi-energy levels, it has the advantage that in the rotating wave approximation it gives complete information on all energy levels and their inter-dependencies, avoiding the complications associated with singularities in the other model. The bare treatment also should be able to better account for the back action of the MW-dressing on the RF-dressing power.

Using the bare coupling coefficients, as were given in Table 6.2, we can begin to construct the complete laboratory frame Hamiltonian. As we are only considering the energy levels with $L = 0$, there is no spin-orbit coupling (g_S and g_J differ by a factor 6×10^{-6} [171]), and the hyperfine splitting from Eq. 2.4 can be simplified to $\hat{H}_{\text{HFS}} = \mathcal{A}_{\text{HFS}} \hat{\mathbf{S}} \cdot \hat{\mathbf{I}}$. Also included in the Hamiltonian are the effects of static magnetic field from Eq. 2.13, as well as the RF-coupling between sublevels of the form $\hat{H}_{\text{RF}} = \hat{F}_x B_{\text{RF}} \cos(\omega_{\text{RF}} t)$. We also require a MW-coupling term in the matrix cells representing $|1, m\rangle \leftrightarrow |2, m + \varsigma\rangle$ (where $\varsigma = \pm 1, 0$ for MW-polarisations σ_{\pm}, π respectively), recalling that $n = 2m + \varsigma$. These terms are summed to give the total Hamiltonian

$$\begin{aligned} \hat{H}_{\text{tot}}^{n,\sigma} = & \frac{\mathcal{A}_{\text{HFS}}}{\hbar^2} \hat{\mathbf{S}} \cdot \hat{\mathbf{I}} + \frac{\mu_B}{\hbar} \hat{g}_F \left(\hat{F}_z B_z + \hat{F}_x B_{\text{RF}} \cos(\omega_{\text{RF}} t) \right) \\ & + \sum_{\sigma} \Omega_{\text{MW}}^{n,\sigma} \cos(\omega_{\text{MW}} t) (|F, m\rangle \langle F+1, m+\varsigma| + \text{h.c.}), \end{aligned} \quad (7.14)$$

where $\sigma = \sigma_-, \pi, \sigma_+$ or σ_{\pm} as determined by the group number. The sum over σ in the MW-coupling term is only necessary in the case of $n = \pm 1$, as all other groups may only be addressed with a single polarisation component.

Using the rotation operator $\hat{U} = \hat{U}_{\text{RF}} \hat{U}_{\text{MW}}$, with

$$\hat{U}_{\text{RF}} = \begin{pmatrix} e^{in\omega_{\text{RF}} t \hat{\mathbf{F}}_z^{F=2}/\hbar} & \mathbf{0} \\ \mathbf{0} & e^{-in\omega_{\text{RF}} t \hat{\mathbf{F}}_z^{F=1}/\hbar} \end{pmatrix}, \quad \hat{U}_{\text{MW}} = \begin{pmatrix} e^{i(\omega_{\text{MW}} - n\omega_{\text{RF}})t} \mathbb{1}_5 & \mathbf{0} \\ \mathbf{0} & \mathbb{1}_3 \end{pmatrix}, \quad (7.15)$$

and Eq. 7.4 will take us into the rotating frame of both the RF and the MW-dressing relative to the centre frequency of group n . We have now generated the final Hamiltonian

$$\hat{H}_{\text{rot}}^{n,\sigma} = \begin{pmatrix} H_{\text{tot},F=2} + \hbar(\omega_{\text{HFS}} + n\hbar\omega_{\text{RF}} - \omega_{\text{MW}}) \mathbb{1}_5 & \hat{M}_{n,\sigma}^\dagger \\ \hat{M}_{n,\sigma} & H_{\text{tot},F=1} \end{pmatrix}, \quad (7.16)$$

where $H_{\text{tot},F}$ are from Eqs 2.44 and 2.45, and $\hat{M}_{n,\sigma}$ is the matrix of the

couplings between F -manifolds given by

$$\hat{M}_{n,\sigma} = \frac{\hbar\Omega_{\text{norm}}^\sigma}{2} \begin{pmatrix} \frac{\sqrt{3}}{2}i\delta_{n,-3} & -\frac{\sqrt{3}}{2}\delta_{n,-2} & \frac{\sqrt{2}}{4}i\delta_{n,-1} & 0 & 0 \\ 0 & \frac{1}{2}\sqrt{\frac{3}{2}}i\delta_{n,-1} & -\delta_{n,0} & \frac{1}{2}\sqrt{\frac{3}{2}}i\delta_{n,1} & 0 \\ 0 & 0 & \frac{\sqrt{2}}{4}i\delta_{n,1} & -\frac{\sqrt{3}}{2}\delta_{n,2} & \frac{\sqrt{3}}{2}i\delta_{n,3} \end{pmatrix}. \quad (7.17)$$

$\Omega_{\text{norm}}^\sigma$ is given by Eq. 6.33 and δ is the Kronecker delta. The eigenvalues of this Hamiltonian will give the full set of energies of all 8 magnetic sublevels. The value n is chosen to be the group whose centre frequency is the least detuned from the MW-dressing frequency. One problem with the model is that only a single dressing frequency may properly be accounted for, due to the limited applicability of the rotating wave approximation. Adding multiple couplings $F \leftrightarrow F+1$ means that we cannot simply discount terms oscillating at twice the rotation frequency, as the model will not simplify properly. We can however approximate a second MW-dressing, now on the transition $|1, m_2\rangle \rightarrow |2, m_2 + \varsigma_2\rangle$ (group $n_2 = 2m_2 + \varsigma_2$), by including an extra shift on the bare levels

$$\hat{H}_{\text{rot}}^{n,\sigma,n_2,\sigma_2} = \hat{H}_{\text{rot}}^{n,\sigma} + \mathbf{a} |F, m_2\rangle \langle F, m_2| - \mathbf{a} |F+1, m_2 + \varsigma_2\rangle \langle F+1, m_2 + \varsigma_2|, \quad (7.18)$$

by an amount $\mathbf{a} \propto (B_{\text{MW}}^{n_2,\sigma_2})^2$. This hybrid of the Hamiltonian and dressed level models can be used to obtain a rough estimate of the second order potentials only. The first order dressing should be defined as the strongest of the two, and the model becomes more reliable as the first order dressing increases in power relative to the second dressing. Third and higher order MW-dressings should not be estimated using this method.

A further drawback is that the model only handles transitions occurring via photons of σ_- -polarised RF in $F = 1$ and σ_+ -polarised RF in $F = 2$, which resonantly couple neighbouring $|F, m\rangle$ sublevels. In fact, both components of the RF-field interact equally with both sets of sublevels. All single-photon RF-interactions with the magnetic sublevels are marked in Figure 7.5a, with solid arrows marking transitions handled by the model and other interactions indicated by dashed arrows. As dashed arrows do not correspond to a transition between energy levels, these have previously been discounted. However, these become relevant when we add in a MW-field, for instance a σ_\pm -polarised field on the bare transition $|1, -1\rangle \leftrightarrow |2, -2\rangle$ (Figure 7.5b), or a π -polarised field on $|1, -1\rangle \leftrightarrow |2, -1\rangle$ (Figure 7.5c), which correspond to the centre frequency of the dressed groups $n = -3$ and -2 respectively. For simplicity the MW-field is marked as resonant with a transition, although in practice the detuning is not constrained. We see in the figures that in addition to single photon transitions, there are several two-photon transitions which now

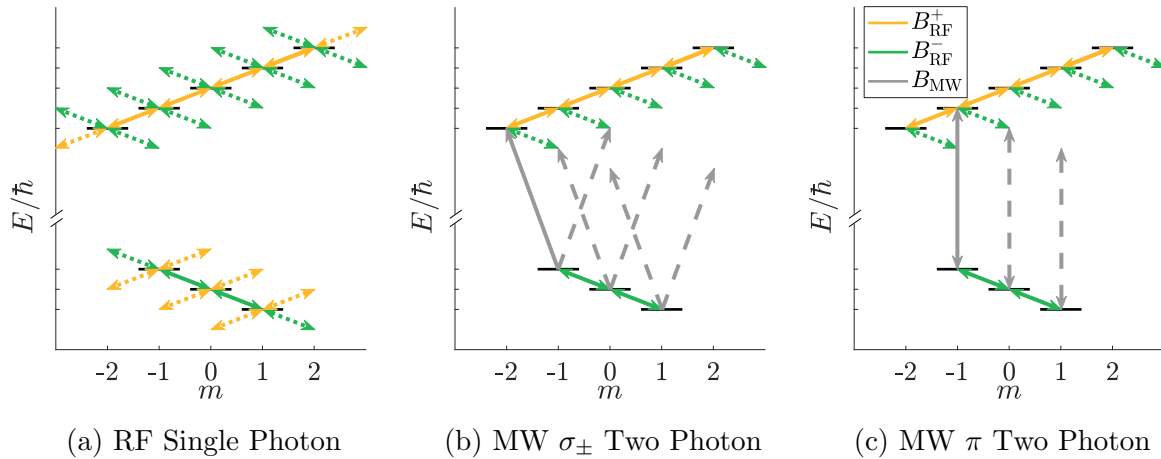


Figure 7.5: The arrows show some of the possible energy changes due to the RF and MW-fields in the laboratory frame picture, in solid lines if on possible single photon transitions, and dashed otherwise. In (a) all direct interactions between a single resonant RF-photon and an energy level are shown. A MW-field at the $n = -3$ and -2 centre frequencies are shown respectively for σ_{\pm} and π -polarisation in (b) and (c). Example two-photon transitions using the MW-field and a σ_{-} polarised RF-photon are also shown, with equivalent transitions using σ_{+} omitted for readability.

emerge. Only interactions using a single σ_{-} -polarised RF-photon and the MW are marked, although equivalent transitions using σ_{+} -polarised RF are also enabled. The number of possible paths between F -levels will increase significantly with higher order transitions, with increasing numbers of RF-photons forming ever more complex chains of couplings. These multi-photon paths correspond to the effect of other groups of transitions on the energy levels.

Although higher order transitions have a decreasing effect on the system, the fact that only couplings via the solid arrows marked in the figures can be handled by this model is the main drawback compared to the quasi-energy level method. The greater the detuning from the centre of the nearest group, the less accurate the model will be, due to the single group modelled having less of an effect compared to that of other groups. Via the treatment as quasi-single-photon transitions, the quasi-energy level model fully accounts for all multi-photon couplings. The Hamiltonian model should however be better at handling the back-action of the MW-dressing on the RF. We will therefore need to see how the models compare with experimental data before coming to a conclusion as to which is more appropriate for our purposes.

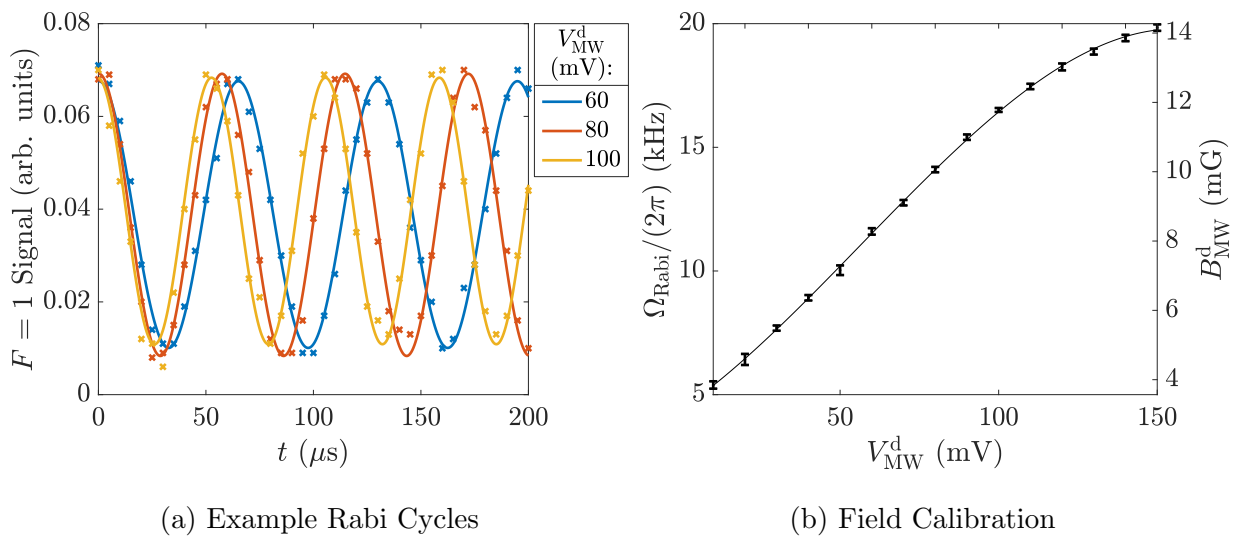


Figure 7.6: The MW-dressing field strength is calibrated using the Rabi-frequency data extracted from temporal measurements such as those shown in (a). Plot (b) shows the voltage input into the MW-dressing generator versus the Rabi frequency of the bare $|1,0\rangle \leftrightarrow |2,0\rangle$ transition, as well as the associated static field, calibrated using the same method as for Eq. 6.38.

7.2 Coherence Data

Now that we have an understanding of the theory behind our method of coherence control, we can begin to experimentally investigate. In this section we begin by detailing the method used for measuring the effectiveness of our coherence control (Section 7.2.1), before providing data showing the effect of a single MW-dressing for three different frequencies which can all reduce the first order static field dependence at resonance (Section 7.2.2). After comparing the fit of our theoretical models to this data, we move on to suppression of the field dependence to second order (Section 7.2.3).

7.2.1 Measurement Method

Before we can begin making measurements using our MW-dressing generator, we first require a calibration of the field strength generated at the region of the atoms. The home-built MW-dressing generator described in Section 5.2.3 is used to generate the fields. Previous data was taken with only the MW-probe generator (Figure 5.10) enabled, with the RF-card inputs for the MW-dressing switched off. We now turn on the RF-card, and set the power of the MW-dressing by adjusting the peak to peak voltage. After frequency mixing and

amplification, we obtain the final output power which requires calibration. The simplest way to measure the MW-field at the atoms is by measuring the Rabi frequency using the same method as in Figure 3.6b. Rabi cycles were measured on the bare $|1, 0\rangle \leftrightarrow |2, 0\rangle$ transition, a few examples of which are shown in Figure 7.6a. Extracting the Rabi frequencies from fits to such data allows the plotting of the Rabi-frequency as a function of voltage, as shown in 7.6b, where the errorbars are given by the 95 % certainty bounds on the frequency fit. Using the bare Rabi-frequency predictions from Table 6.2, we gain the conversion to static field also marked on the figure. The coefficients of the third order polynomial

$$B_{\text{MW}} \approx (-3.11V^3 \times 10^{-6} + 5.18V^2 \times 10^{-4} + 0.0656V + 3.09) \times 1 \text{ mG} \quad (7.19)$$

were determined from a fit to the data, where V is the input RF peak to peak voltage in volts. The fit has a root mean squared error of 0.06 mG in the measured range $10 \text{ mV} \leq V \leq 150 \text{ mV}$. After mixing the RF with a 7 GHz MW, the signal goes through 4 different amplifiers to reach the MW-horn, as well as numerous other non-linear electrical components. It is therefore unsurprising that the voltage versus Rabi frequency data is non-linear, and we see the effects of non-linear compression. The specifics of the compression profile are not of particular interest in this work, and are sufficiently well approximated by the above equation, but for more details of such effects see [13]. One unexplained curiosity is the 3.1 mG vertical intercept. We would, of course, expect the fit to extrapolate to zero MW-power at zero input voltage; the cause of this discrepancy is unknown, but one possibility is that there is an inaccuracy in the way the RF peak to peak voltage is controlled in the low voltage regime. As undressed data is taken with the RF-output triggered off, rather than simply having the amplitude set to zero, this does not have an effect on the undressed data.

In order to measure the coherence increase due our dressing, we require a minimum of two different MW-frequencies and strengths. From here on the different MW-fields will be denoted B_{MW}^{p} and B_{MW}^{d} for the probe and dressing respectively. Our transition of interest is the RF-dressed trappable clock $|1, -1\rangle \leftrightarrow |2, 1\rangle$. Using the state preparation method described in Section 3.2, a pure dressed $|1, -1\rangle$ state is produced. The only difference from the sequence used for spectroscopy (Figure 4.3) is that an additional MW-dressing field is switched on 0.2 ms before the MW-probe is applied. We are initially considering only the first order dressing, red-detuned from the transition $|1, -1\rangle \rightarrow |2, -2\rangle$, in the three different groups $n = -3, -2, -1$. The measurement of the clock transition is taken in group $n = 1$, which introduces an additional complication for the $n = -2$ dressing.

Due to the constraint of having a single horn outputting the MW for both

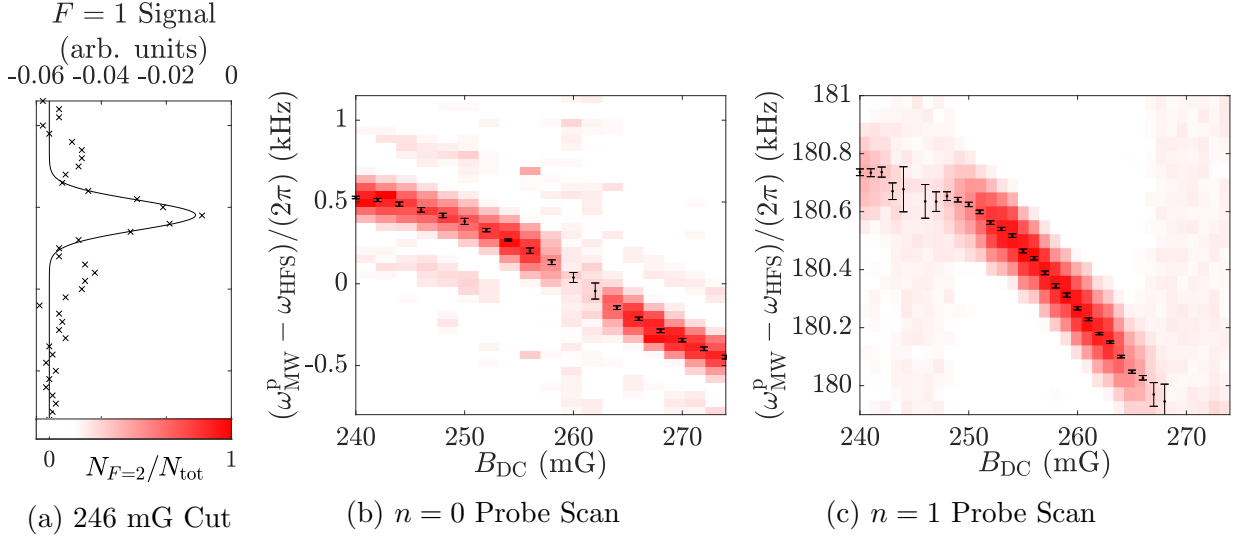


Figure 7.7: Coloumaps of the $|1, -1\rangle \leftrightarrow |2, 1\rangle$ transition in groups $n = 0$ and 1 are shown in (b) and (c) respectively as a function of both static field and MW-probe frequency ($B_{\text{MW}}^{\text{d}} = 0$), taken using the same method as in Figure 6.14. A cut through (b) of fixed $B_{\text{DC}} = 246$ mG is shown in (a). A Gaussian fit, rather than the full fit to Eq. 6.36 is used, in order for the fitted centre frequency of the main peak to not be compromised by other fit parameters.

the probing and the dressing, these must be of the same polarisation. This is not an issue in the case of dressing on σ_{\pm} -polarised groups, as a measurement of the clock transition in all four odd numbered groups is possible for the region $|B_{\text{DC}} - B_{\text{res}}| \leq 12$ mG, as was experimentally and theoretically shown in Figure 6.18 for groups $n = 1$ and 3. For the same transition in $n = \pm 2, 0$ the zero coupling point is closer to resonance, and as such measurement of the transition across a sufficiently large static field range is not possible. We therefore require measurement of the transition using σ_{\pm} -polarisation, and hence need the MW to contain a mixture of σ_{\pm} and π -polarisation if dressing on $n = -2$. Quick tests found that the $n = 1$ clock transition could be measured with sufficient resolution to locate the transition peak over the desired static field region at 15° from purely π -polarised. Due to the limits on the maximum power output of the MW-generator, this angle was minimised to allow for the maximum component B_{MW}^{π} , and therefore enable the measurement of a larger MW-dressing power range.

The problems associated with detection of the static field dependence of the clock state in groups which have zero-coupling points can be seen in Figure 7.7. The resonant point $B_{\text{DC}} = 257$ mG is roughly at the zero coupling

point in the group $n = 0$ (in the approximation $g_1 = -g_2$ this is exactly true) and as such this is a bad choice for measuring the change in static field dependence at resonance. Group $n = 1$, on the other hand, is at a local maximum in the coupling at the resonance point, and therefore provides the better measurement. Interestingly the minima do not appear when using a 15° field angle from pure π -polarisation, and detecting on $n = 1$. As our model of the coupling coefficients only gives either pure σ_\pm or pure π -polarised couplings, this is not a fault in the model, but does reveal an unforeseen limitation when combining MW-polarisations.

Figure 7.7 was taken using the same method as for Figure 6.14, only now displaying the $F = 1$ population rather than $F = 2$, due to a breakage of the $F = 2$ laser at the time this data was taken. As the state is prepared in $F = 1$, detection on $F = 2$ has the advantage that the noise level of the spectroscopy measurements far from any transition is much lower, as a fluctuation in atom number does not have any effect on this region. Due to time constraints, this and some of the later data (Section 7.2.2) has not been retaken since the upgrade to the common-mode suppressed detection system. Figure 7.7a shows a single scan of the MW-probe frequency at $B_{DC} = 246$ mG, with the signal strength at which there is zero population in $F = 2$ approximated from the mean signal strength far from the transition. Some of the additional noise in the measurement is not seen in the full colourmaps due to the choice of colour scale.

Transition frequencies as a function of static field are still clearly discernible when detecting on $F = 1$, as the transition peaks are much larger than the noise level at all static fields sufficiently far from a coupling minimum. As we are primarily interested in the frequencies, rather than the coupling strength of the clock transition, the additional signal noise is not the limiting factor in our first order dressing data (Section 7.2.2). The MW-probe step size, and hence the overall number of data points per set, limited by practical experimental run times, is a bigger constraint. For second order data (Section 7.2.3) the upgraded detection system allowed the direct measurement of population in $F = 2$.

The transition frequency is measured using a Gaussian fit to the peak for each value B_{DC} , with the errors given by the 95 % confidence bounds. We recall that for high MW-probe powers, the peak shape becomes distorted (Eq. 6.36), but so long as the power is kept sufficiently low that the centre of the transition peak is not reduced by multiple Rabi-cycles, a simple Gaussian fit to the central peak provides a more accurate frequency measurement than fitting a distorted peak shape. This is because fitting the full model to ‘sideband’ peaks, which are in some cases barely above the noise level, gives a larger error on the transition frequency. The interdependence of the height

and width of the peaks in this model also makes it less robust to fit programmatically. As such, the Gaussian model (with amplitude as a fit parameter) is used for this and all future such plots, with the zero population in $F = 2$ point fixed as the centre of the noise far from resonance with a transition, and the point with all population in $F = 2$ set at where the $F = 1$ signal is zero.

Analysis of the field dependence of the clock transition as a function of static field for different strengths and frequencies of MW-dressing will be made using purely the transition frequencies and their associated errors gathered from fitting in this manner. For simplicity, fits to RF and MW-dressing field strengths will not be made using the full colourmap data, due to long computation times, and the fact that the linewidth of the transition is purely dictated by the MW-probe power. Using a lower MW-probe power would increase the accuracy of the transition frequency measurement, but would also require a much finer scan of MW-probe frequency in order to be detectable. For reasons previously stated (Section 6.2.1) relating to thermal drifts in atom number and practical constraints on experimental run times, we are restricted in the number of points it is reasonable to take in a single data set. As such, a probe strength of $B_{\text{MW}}^{\text{p}} = 0.46$ mG was chosen in order to give a linewidth of ≈ 200 Hz, which allows us to clearly measure the transition frequency when using a MW-probe step size of 50 Hz. Using 1 mG steps in static field over a range of $B_{\text{res}} \pm 12$ mG allows scanning the full range of possible transition frequencies in roughly an hour. The transition frequency varies by < 1.5 kHz in this static field region using MW-dressing strengths achievable in our experiment. The probe strength is increased to $B_{\text{MW}}^{\text{p}} = 0.92$ mG when using a 15° field angle, giving a similar linewidth.

7.2.2 First Order Dressing

We now experimentally explore dressing using the MW-frequencies chosen in Section 7.1.2. In the case of dressing on a σ_{\pm} -polarised MW group, we begin by applying a MW-dressing at $(\omega_{\text{MW}}^{\text{d}} - \omega_{\text{HFS}})/(2\pi) = (-598, \text{ or } -236)$ kHz, i.e. red-detuned from the $n = -3$ or -1 group, and measuring the transition frequency as a function of MW-dressing power by detecting on the clock transition in $n = 1$, with pure σ_{\pm} polarisation for both dressing and detection. For the comparable case for dressing on a π -polarised group, the MW-dressing is at $(\omega_{\text{MW}}^{\text{d}} - \omega_{\text{HFS}})/(2\pi) = -415$ kHz, red-detuned from the $n = -2$ group and detecting on the $n = 1$ clock transition, with all MW 15° from pure π -polarisation. All three dressing frequencies are marked in Figure 7.8, relative to the spectroscopy data from Figure 6.5a. The data shows the frequencies of the transitions from $|1, -1\rangle$ to all possible states $|2, \bar{m}'\rangle$, and gives an idea of the associated detunings.

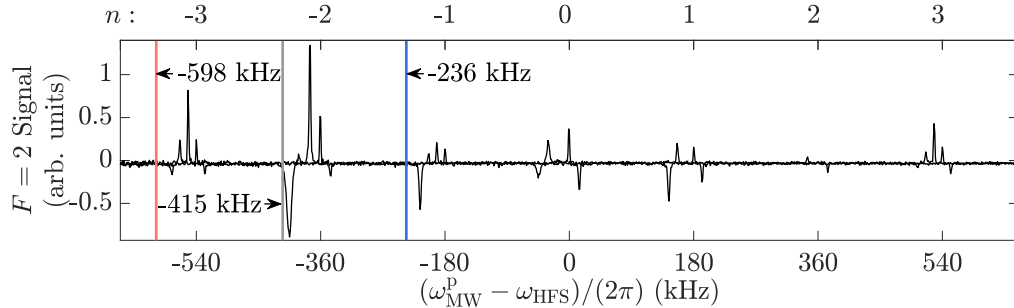


Figure 7.8: The MW spectroscopy data from Figure 6.5a, taken using an initially pure $|1, -1\rangle$ state, is shown in the figure, with all chosen first order MW-dressing frequencies marked. The red, grey and blue lines shown MW-dressings primarily on $n = -3, -2, -1$ respectively.

Using these frequencies, Figure 7.9 shows colourmaps of static field versus probe MW-frequency, with dressings on $n = -3, -2$ and -1 shown in (a-c) respectively. In all figures, (i) shows the case with no MW-dressing, and two increasing dressing strengths are shown in (ii) and (iii). In the case of $n = -3$ and -1 these dressings were formed by $V_{\text{MW}}^{\text{d}} = (80 \text{ and } 140) \text{ mV}$ input to the MW-dressing generator, corresponding to $B_{\text{MW}}^{\text{d}} = (10.1 \text{ and } 13.9) \text{ mG}$. For $n = -2$, the corresponding values are $V_{\text{MW}}^{\text{d}} = (70, 120) \text{ mV}$ and $B_{\text{MW}}^{\text{d}} = (9.1, 12.4) \text{ mG}$. The particular examples in (ii) were chosen to show a dressing strength where the static field dependence is somewhat reduced, but the gradient of static field versus transition frequency is still clearly negative. In (aiii) and (biii) the examples chosen show a small positive gradient, and in (ciii) the gradient remains negative but is close to zero, limited by the power output of our dressing generator. Note that (ai) and (ci) show the same data (over different ranges), as the two undressed cases with the MW-probe purely σ_{\pm} -polarised are identical. The range of the scanned static field varies slightly due to datasets for dressings on different groups being taken at different times, and not originally intended to be collated. Regions below the red lines in (cii) and (ciii) do not have available data.

All MW-dressings shown cause the transition frequency to increase somewhat across the whole static field range, due to red-detuned dressings always increasing the separation between two levels. All have a lesser effect on the transition frequency at static fields below the resonance point, as predicted by the coupling coefficients (Figure 7.3). In all cases, this causes the gradient $d\omega_{\text{MW}}^{\text{d}}(B_{\text{res}})/dB_{\text{DC}}$ at the resonance point to increase from $\sim -40 \times 2\pi \text{ Hz/mG}$ towards zero with increasing MW-dressing power. This is shown in Figure 7.10a, where the gradient at resonance for a range of dressing strengths is plotted. In order to not have the extracted gradient be dependent on the

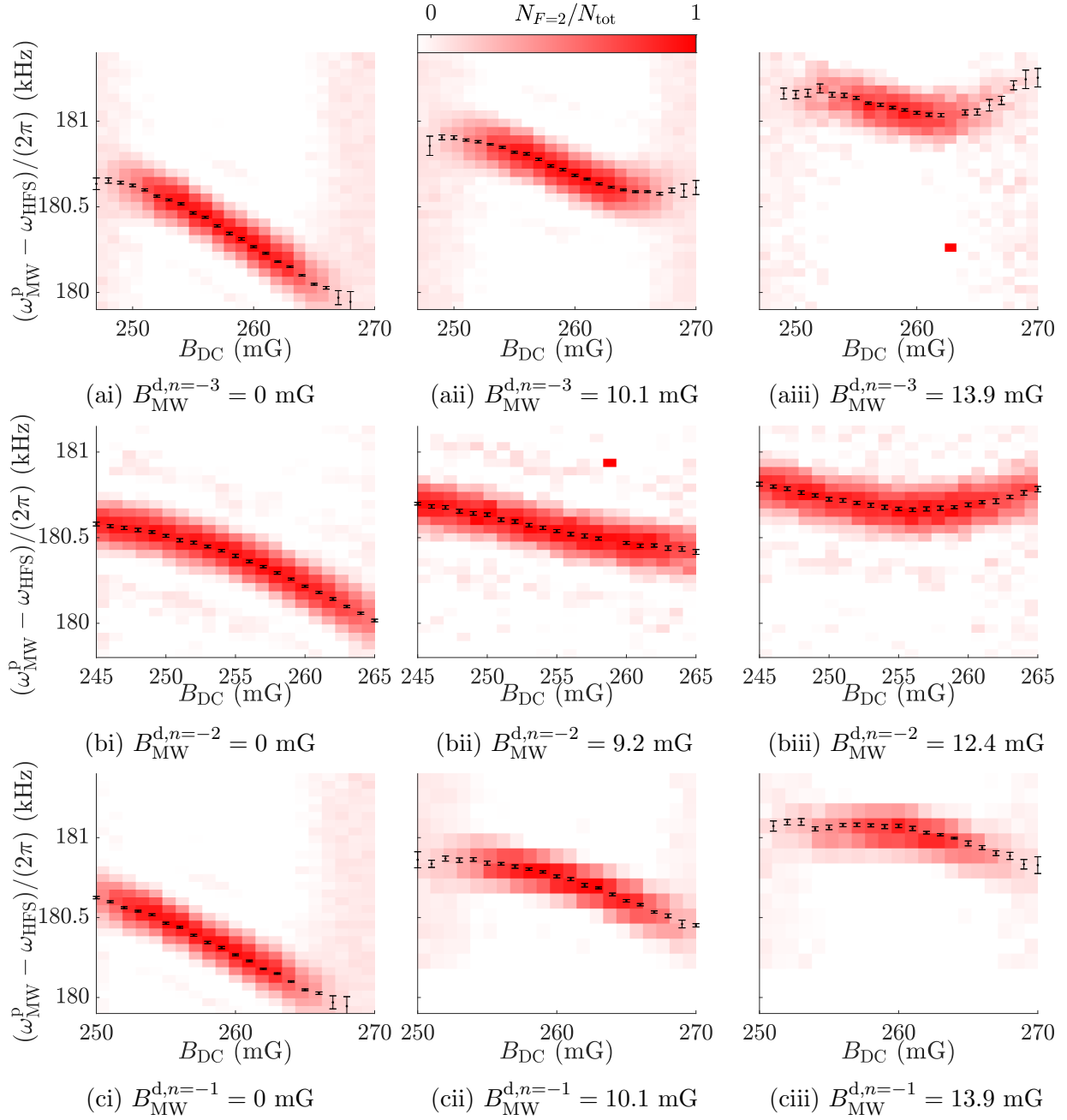


Figure 7.9: With a MW-dressing frequency of $(\omega_{\text{MW}}^{\text{d}} - \omega_{\text{HFS}})/(2\pi) = (-598, -415$ and $-236)$ kHz in (a-c) respectively, the field dependence of the transition frequency is shown for the undressed case and two different dressing strengths $B_{\text{MW}}^{\text{d},n}$ in each case.

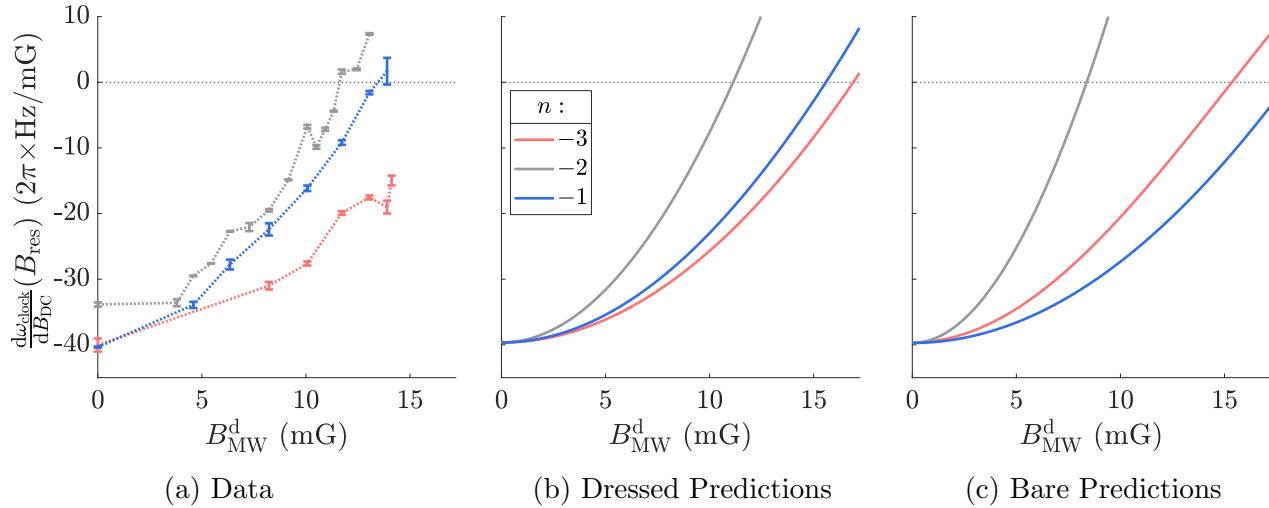


Figure 7.10: The measured change in the derivative of the clock transition frequency $d\omega_{\text{clock}}/dB_{\text{DC}}$ at resonance due to a change in the MW-dressing strength is shown in (a). The theoretical predictions based on the treatment of both the dressed and the bare level system are shown in (b) and (c) respectively. Note that the errors on the data points are the error on the measurement of the gradient for a single dressing power. Fluctuations in relevant fields between data-sets may account for the lack of a smooth trend. These predictions are with the RF-power as a fixed input value. The line colours correspond to those of the marked dressing frequencies in Figure 7.8.

theoretical model chosen, this was measured from a fit to the data using a quartic function, which provides a good fit across all data-points, although this is of course completely unreliable outside of the measured static field range. The errors on the measured gradients are propagated from the errors on the transition frequencies. It would appear that day-to-day fluctuations in RF and MW-field strengths also add to the measurement error, as we can see that the measured gradient is not the smooth continuous change we would otherwise expect.

The theoretical predictions of this gradient are shown in Figure 7.10b for the dressed treatment and Figure 7.10c for the bare treatment. The shape of the gradient's dependence on dressing power is similar in both cases, although neither accurately fits the experimental data. As the gradient predictions have the measured values B_{RF}^{\pm} as a fixed input, the back-action of the MW on the RF-power is not accounted for in (b), and (c) is inaccurate due to its only modelling a single group of transitions. We see from the data that in the $n = -3$ and -2 cases the resonant gradient has passed zero, i.e. there is a

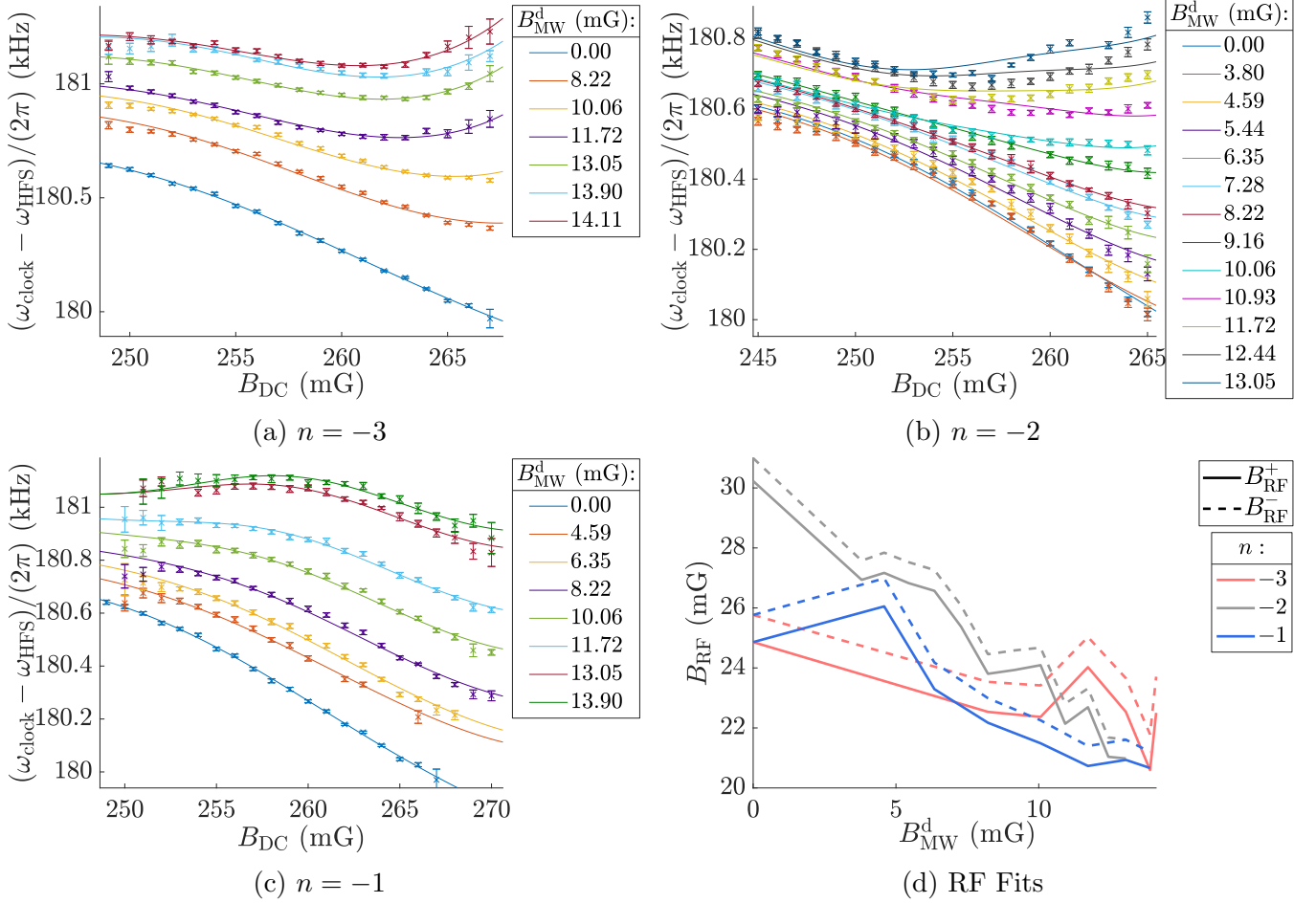


Figure 7.11: Shown in (a-c) are the extracted clock transition frequencies as a function of MW-dressing power for three different dressing frequencies, $(\omega_{\text{MW}}^{\text{d}} - \omega_{\text{HFS}})/(2\pi) = (-598, -415 \text{ and } -236) \text{ kHz}$ respectively. Fits are to Eq. 7.12, with B_{RF}^{\pm} as the fit parameters. The output RF strengths from all fits are plotted in (d).

dressing strength at which the first order field dependence is fully cancelled. In the case of dressing on $n = 1$, the data indicates that the gradient will fall to zero at a higher MW-dressing power than we can currently produce.

We can now consider the predictions of both models relative to the data. In Figure 7.11, the measured transition frequency as a function of static field is shown for all three dressing frequencies $(\omega_{\text{MW}}^{\text{d}} - \omega_{\text{HFS}})/(2\pi) = (-598, -415 \text{ and } -236) \text{ kHz}$ in (a-c) respectively, for a range of MW-dressing strengths. Available data has dictated which MW-powers are shown, but a larger number different of MW-powers were taken for the 15° case, as this reaches zero first-

order field dependence at resonance at the lowest MW-power, and is therefore the best candidate for second order dressing given our power limitations. The fits to the data are from Eq. 7.12, with the RF-power of both σ_{\pm} components as a fit parameter. As this model does not otherwise account for the back-action of the MW-dressing on the RF, we expect the fitted RF-power to decrease with increasing MW-power. As we see in Figure 7.11d, this is broadly true, although with some fluctuations, potentially due to variations in RF-power, MW-power, or location of the atoms due to static field fluctuations which can alter the effective power of both the RF and the MW seen by the atoms. The input MW-power is calculated using Eq. 7.19, only with the zero dressing case forced to $B_{\text{MW}}^{\text{d}} = 0$, as the equation does not provide accurate predictions when the MW-dressing is triggered off. We see that the fit quality across the whole range is good, although some of the highest MW-power data in the $n = -2$ case does not fit so well. We see that for $n = -3$ and -2 dressings, the point where the gradient of transition frequency versus static field is zero will be a local minimum, whereas for $n = -1$ this will be a local maximum. The shape of this residual field dependence will be important as the starting point for applying higher order dressings.

In Figure 7.12 the root mean squared error (RMSE) on the fit to all data points in each set is shown for various fit types. For the fits previously discussed, the $\text{RMSE}/(2\pi) = (14, 17 \text{ and } 17)$ Hz for $n = -3, -2$ and -1 respectively. Another possibility for fitting the data is to fit independent clock transition frequency offsets for each of the different B_{MW} values. This would account for any inaccuracies in the probe frequency due to thermal drifts causing miscalibrations in the generator. Although we see from the figure that this does cause an increase in the quality of the fit, this may be simply because any increase in the number of fit parameters will improve matters. Fitting both the RF and the offset together improves the RMSE somewhat compared to fits to RF-power alone, but the 14 % improvement in fit quality may be insufficient evidence that MW-frequency fluctuations are really a contributory factor. In order to investigate this effect, a GPS device to use as a stable reference for the generator is to be installed, which will completely remove any mechanical effects of device temperature on output frequency. Once this has been added, we will be able to conclusively say whether probe frequency drifts are a significant factor, which we cannot be certain of at this time.

We can however conclude that the RF-field requires fitting as a function of MW-dressing strength, due to a combination of the effect of the back-action of the MW on the RF, and day-to-day fluctuations in the RF-power experienced by the atoms, as shown by both Figure 7.11d and the substantial (88%) reduction in RMSE this fit parameter causes. The ellipticity of the RF is also fit, indicating a $(3.4 \pm 0.4)\%$ higher B_{RF}^{-} component. Although

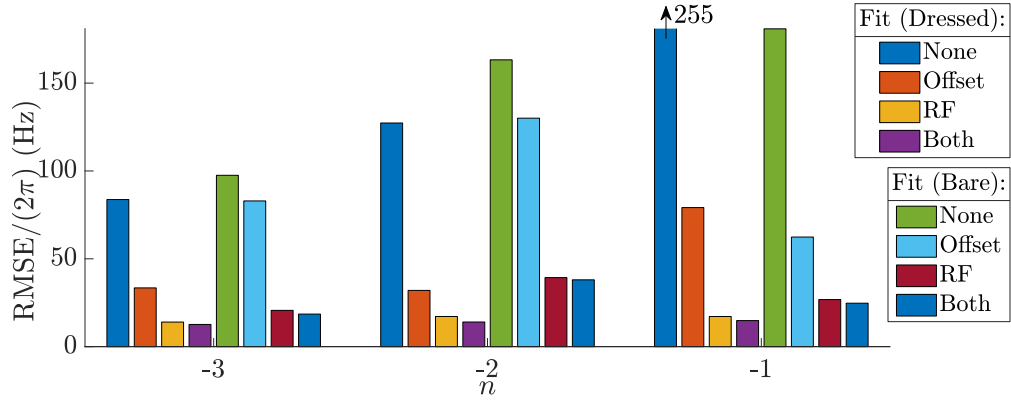


Figure 7.12: The root mean squared error on fits to the data in Figure 7.11 are shown using different fit parameters: the RF-field strength, the MW-probe frequency offset, both or neither, for both the treatments of the dressed and of the bare levels.

there is little variation in fit quality between the three different dressings, as expected the $n = -3$ dressing fits the best, as this is the simplest case with a single (σ_-) polarisation contributing to the dressing. The data for dressing on $n = -2$ fits the least well, particularly at high MW-dressing powers, due to the fact that our model for predicting coupling coefficients does not fully account for mixed π - σ_{\pm} dressings. The σ_{\pm} -polarised $n = -1$ dressing can be fully modelled however, and provides a robust fit.

We can also consider the alternative method, modelling the bare levels using the eigenvalues of Eq. 7.16. The RMSEs of such a fit are also shown in Figure 7.12. Note that as the bare model does not consider the transition frequency offsets due to the RF-dressed groups, even in the case where the fit parameters are stated to be ‘none’ an offset frequency is required as an input. This was set to fix the zero dressing case at the correct frequency, but was not fit separately for each individual value of B_{MW}^{d} in the unfit case shown by the green bars. Fitting each MW-probe frequency offset separately for each MW-dressing power improves the fit somewhat. Interestingly, fitting the RF-powers improves the fit substantially, although as this model is intended to account for the back-action of the MW-dressing on the RF-power, this is unexpected. Either the RF-power fluctuation is a much larger effect than the back-action, or simply this improvement in fit is a result of an increase in number of fit parameters. As with the previous model, fitting individual MW-probe frequency offsets improves the fit quality somewhat (by 8%), but again this may simply be due to the increase in number of fit parameters. The RMSE of the fit to RF-power is 42% lower in the dressed treatment than the

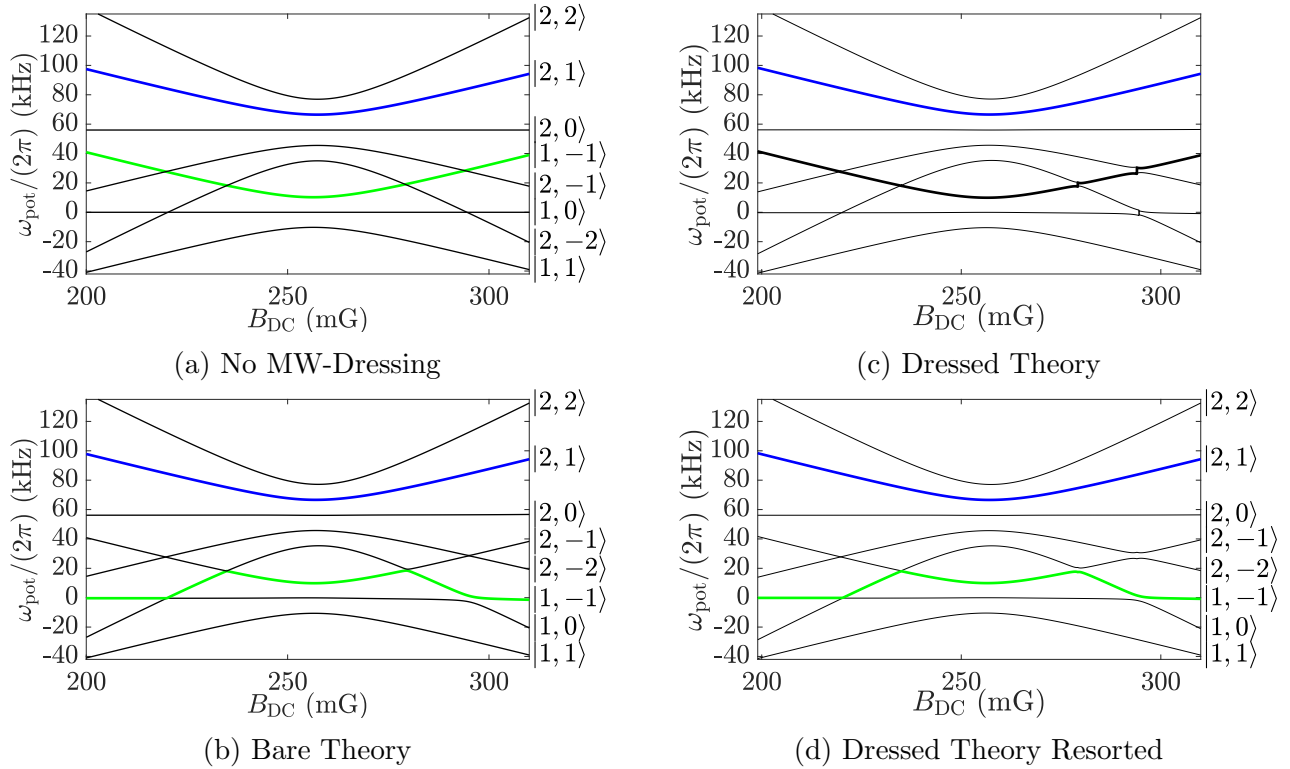


Figure 7.13: In (a) all energy levels are shown with no MW-dressing power, but in the rotating frame of a $\omega_{\text{HFS}}/(2\pi) - 236$ kHz MW-Dressing. Other figures show the level scheme with a MW-dressing of strength $B_{\text{MW}}^{\text{d}2} = 13.9$ mG at this dressing frequency. In (b) prediction using the treatment of the bare energy levels is shown. Both (c) and (d) show the predictions from the quasi-energy level model, which in the case of (d) has the level scheme reorganised to account for degeneracies. Levels $|1, -1\rangle$ and $|2, 1\rangle$ are highlighted in green and blue respectively.

corresponding bare treatment. We therefore choose to work primarily with the quasi-energy level model, as not only does it provide the better fit, but also because the main advantage of the bare level treatment, in accounting for the back action of the MW on the RF, does not appear to be sufficient in practice.

We now consider the full energy level structure of the $n = 1$ group. In the rotating frame of both the RF-dressing and a MW-dressing at $\omega_{\text{HFS}}/(2\pi) - 236$ kHz, the potential energies of all $|F, \bar{m}\rangle$ levels are plotted in Figure 7.13a in the limit $B_{\text{MW}}^{\text{d}} = 0$ mG. Both theoretical models give the same predicted potentials in the case of zero MW-dressing power. The clock levels are highlighted in green and blue for $|1, -1\rangle$ and $|2, 1\rangle$ respectively. One area where

the treatment of bare levels has a practical advantage is in the calculation of potential energies. As there are no singularities in the model, the eigenvalues of the Hamiltonian directly give the potential energies of all $|F, \bar{m}\rangle$ levels. The predicted levels using this model are plotted in Figure 7.13b for $B_{\text{MW}}^{\text{d}} = 13.9$ mG, i.e. using the parameters in Figure 7.11c which gave the minimum gradient $d\omega_{\text{clock}}/dB_{\text{DC}}$ at the static field resonance. We see that the shift on the energy level $|1, -1\rangle$ is primarily due to avoided crossings with $|2, -2\rangle$. Increasing the MW-dressing power will increase the number of avoided crossings, as well as increasing the magnitude of the distortion caused by any given avoided crossing.

It is also possible to predict the potential energies using the quasi-energy level model, if we account for the emergence of singularities. In Figure 7.13c the predicted potentials using this model are plotted, for the same dressing strength and frequency as previously. The blue potential $|2, 1\rangle$ and three other potentials are accurately described by the model; these are the levels which are never degenerate in energy with any other level within the static field range shown. The energy level highlighted with a thicker black line is $|1, -1\rangle$ at $235 \text{ mG} \lesssim B_{\text{DC}} \lesssim 280 \text{ mG}$, but at the points where $\Delta_{1,-1 \leftrightarrow 2,-2} = 0$ ($\Delta_{F, \bar{m} \leftrightarrow F', \bar{m}'}$) we get a discontinuity in the potential energy. This sign change is a result of the potentials $|1, -1\rangle$ and $|2, -2\rangle$ switching which is the lowest energy level in the laboratory frame. In order to obtain a more physical prediction of the potential energies, we require a redefinition of the states. We therefore we relabel the levels whenever they experience a sudden jump in frequency, which we define to be at static field B_{degen} , obtaining the potential energy scheme shown in Figure 7.13d. To do this, we flip the labels of the two states $|F, \bar{m}\rangle \leftrightarrow |F + 1, \bar{m}'\rangle$ which exhibit a jump in transition frequency at the same static field. Note that there can be multiple static fields at which this is true. If $B_{\text{res}} < B_{\text{degen}}$, the energy levels are flipped for all values $B_{\text{DC}} > B_{\text{degen}}$, or if $B_{\text{res}} > B_{\text{degen}}$ the energy levels are flipped for all values $B_{\text{DC}} < B_{\text{degen}}$. This ensures that the definition of the states at the static field resonance remains unaltered. This method gives a similar prediction to the alternative treatment from Figure 7.13b. Note that the potential energies in Figure 7.13c experience small offset discontinuities, (300 – 500) Hz, at energy level degeneracies, which have been removed in the resorted level prediction. The reasons for the jumps are unclear, although as the region of interest is around the static field resonance this should not cause an issue in our transition frequency predictions. We also note that, depending on the strength of the dressing, not all degenerate levels will form avoided crossings. The shape of the potential energy levels are shown purely as an illustration of the practical consequences of the dressed couplings.

Both the shape and depth of the potentials are important to understand,

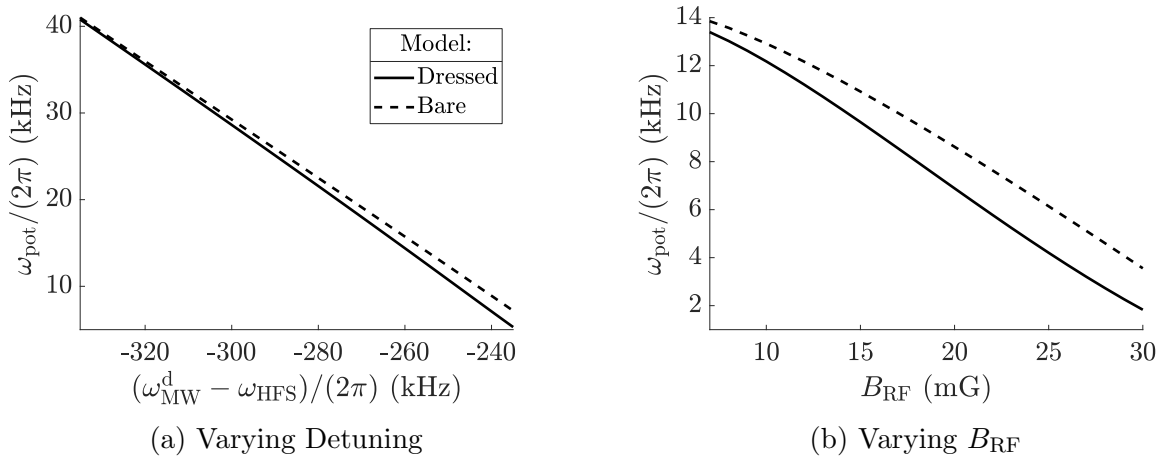


Figure 7.14: The effects on the trap depth of holding B_{RF} constant and varying the MW-dressing detuning are shown in (a), and the corresponding effect for fixing detuning and varying B_{RF} is shown in (b). Both dressed and bare treatments are shown.

as when magnetically trapping this will dictate the maximum temperature of atoms which may be trapped. With $B_{\text{MW}} = 13.9$ mG, using the approximation $\hbar\omega_{\text{pot}} = k_{\text{B}}T$, the predicted trap depth of $|1, -1\rangle$ using the dressed (bare) treatment is 7.53 (8.48) kHz, giving a temperature of 361 (407) nK. Due to the relative detuning, the depth of the $|2, 1\rangle$ potential is 19 times deeper: our interest is therefore in increasing the depth of the $|1, -1\rangle$ potential. In our experiment, due to limitations on our MW-dressing power, this number cannot be significantly improved. In future experiments not subject to the same constraints however, a substantially increased trap depth should be achievable whilst still providing first order coherence control. Theoretical models indicate that both increasing the magnitude of the detuning from the transition (within the restrictions on detuning) and decreasing the RF-power increase the trap depth, but likewise require higher MW-dressing power to achieve first order coherence. The required dressing strength for optimal coherence control can be established by calculating the derivative at resonance as a function of MW-dressing power, as in Figure 7.10, and extracting the zero crossing point in the gradient. The trap depth is then measured as the difference in trap frequency between the potential minimum close to the resonance point and at the first turning point. This was performed for a range of MW-dressing frequencies, with B_{RF} fixed at its measured value, see Figure 7.14a. Alternatively, the MW-dressing frequency can be fixed at $(\omega_{\text{MW}}^{\text{d}} - \omega_{\text{HFS}})/(2\pi) = -236$ kHz, and the RF-dressing strength varied, as shown in Figure 7.14b, assuming circular

RF-polarisation. In both cases the dressing is primarily on $n = -1$, and we note that lower dressing frequencies have a higher magnitude of detuning. We therefore see that both theoretical models of potentials predict that both increasing the detuning and reducing the RF-power increases the trap depth, as these parameters control the static field at which avoided crossings occur. Note that the exact values of trap depth predicted are not robust, as the back action of the MW-dressing on the RF cannot be accounted for in the dressed treatment, and the bare treatment is less reliable due to not modelling the effects of other groups of transitions. However, both models are sufficient to indicate the overall trend.

7.2.3 Second Order Dressing

In order to achieve higher order coherence control, multiple MW-dressings of different frequencies can be simultaneously applied to the RF-dressed atom. Data in this section was taken using the common-mode suppressed detection system, and measurements are of the final population fraction in $F = 2$ after MW-probing. There are two logical ways of numbering the MW-dressing orders: by MW-power, or by which order of static field dependence they are chosen to cancel. For convenience, this section discusses the dressings in terms of the latter definition, with the superscripts d1 and d2 denoting the dressings cancelling the first and second order static field dependencies respectively. However, for all data shown here either definition would result in the same numbering. This is because it is likely (but not always guaranteed) that higher order field dependencies will require lower MW-dressing powers in order to be cancelled.

We begin by choosing an appropriate first order dressing as a basis on which to build higher order coherence. It transpires that there are no single σ_{\pm} -polarised dressing frequencies which can flatten a field dependence which is at a minimum or maximum at the static field resonance (see Table 7.1). The choice is therefore made to focus on flattening the field dependence of the transition after a first order π -polarised dressing with $(\omega_{\text{MW}}^{\text{d1}} - \omega_{\text{HFS}})/(2\pi) = -415$ kHz. It is of course possible to have a first order dressing using σ_{\pm} and a second dressing of π -polarisation. However, due to our system being limited in the maximum dressing power which can be produced, as well as having a single MW-horn so all MW-fields must be of the same polarisation, we can achieve higher MW-dressing powers for both orders if they are of the same polarisation. As previously, we choose a static field which orients the atoms at 15° from experiencing pure π -polarised MW, in order to still have sufficient σ_{\pm} -polarised MW to probe the atoms in group $n = 1$.

Table 7.1 shows that dressing either red or blue-detuned from the $n =$

0 group has the effect of flattening a field minimum. We now investigate the effects of an additional dressing at $(\omega_{\text{MW}}^{\text{d2}} - \omega_{\text{HFS}})/(2\pi) = 43$ kHz, i.e. blue detuned by 19 kHz from the $|1, 0\rangle \leftrightarrow |2, 1\rangle$ transition, so predominantly shifting the upper clock state $|2, 1\rangle$. As the two different dressing orders manipulate different states, it will later be easier to disentangle the effects of the two dressings on the full set of potential energies. From Eq. 6.26, we know that the coupling coefficient of $|1, 0\rangle \leftrightarrow |2, 1\rangle$ in $n = 0$ is

$$\hbar\Omega_{\text{MW}} = |\sqrt{3}(1 + \cos\theta_1) \sin(2\theta_2)\Omega_{\text{norm}}^\pi|, \quad (7.20)$$

as plotted in Figure 7.3b. In the approximation $g_2 = -g_1 = 0.5$, then $\theta_1 = \theta_2$ (Eq. 2.47). As $\theta_F = 0$ at B_{res} , this means that the coupling coefficient is zero at the static field resonance. Therefore in order to cancel the second order field dependence at this point, we simply start from a first order dressing at $(\omega_{\text{MW}}^{\text{d1}} - \omega_{\text{HFS}})/(2\pi) = -415$ kHz, of strength $B_{\text{MW}}^{\text{d1}} = 12.4$ mG, which completely removes the static field dependence of the transition frequency at the resonant static field. We then apply our second order dressing frequency, which has zero coupling at the field resonance, but flattens the second order dependence symmetrically about this point.

Two complications arise when using this method, one of which is inherent to the model and the other of which is a technical constraint particular to our experiment. Firstly, we recall that $\theta_1 \neq \theta_2$, meaning that the coupling minimum is not exactly at B_{res} (which we defined as the mean of the two state dependent resonances B_{res}^F). This is simple enough to account for, as a slight change in the strength of $B_{\text{MW}}^{\text{d1}}$ can shift the zero gradient point after first order dressing to coincide with that of the coupling minimum in the second dressing. The second issue we encounter is that we do not have a proper characterisation of the 1 dB compression profile of our MW-dressing generator. This was not problematic when setting the power of the first order MW-dressing, as we could simply measure the dressing power using Rabi-frequency data, as in Figure 7.6. In the case of two simultaneous dressings of different frequencies we cannot easily measure the ensuing power reduction. For the time being, we therefore simply use trial and error to find the appropriate generator input voltages for the two dressings to maximally reduce the second order field dependence within the constraints of the dressing powers achievable with our system. In the future, the installation of a MW-antenna near the main chamber to directly measure the power of different spectral components of the dressing would remove the uncertainty on dressing power.

In Figure 7.15 the measured singly dressed clock transition frequency with $B_{\text{MW}}^{\text{d1}} = 12.4$ mG is plotted, alongside three different doubly dressed cases. In all cases $V_{\text{MW}}^{\text{d1}} = 110$ mV, although with increasing second dressing power the first order MW-dressing power experienced by the atoms will reduce. The

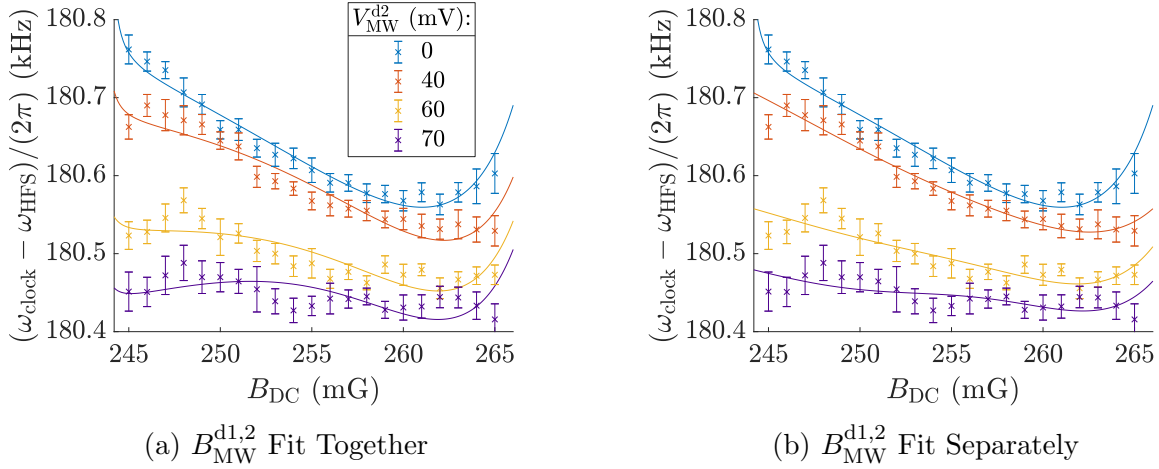


Figure 7.15: The clock transition frequency as a function of static field is shown for a single first order MW-dressing at $(\omega_{\text{MW}}^{\text{d1}} - \omega_{\text{HFS}})/(2\pi) = -415$ kHz, and three double dressings with an additional frequency of $(\omega_{\text{MW}}^{\text{d2}} - \omega_{\text{HFS}})/(2\pi) = 43$ kHz. In both figures the RF-power is a fit parameter, but in (a) the fit forces both MW-frequency components to be reduced by the same amount due to the limits of the generator, and in (b) the two fractions are fit separately.

input peak to peak voltages for each of these data sets were $V_{\text{MW}}^{\text{d2}} = (0, 40, 60$ and $70)$ mV. In Figure 7.15a the parameters of the fit were B_{RF} and the overall scale factor on both $B_{\text{MW}}^{\text{d1}}$ and $B_{\text{MW}}^{\text{d2}}$, which the fit predicts to be a reduction in power $(36 \pm 2)\%$ compared to the MW-dressing powers calculated from Eq. 7.19. However, fitting the two MW-dressing powers as separate parameters allows for decent quality fits with a wide range of ratios between the two. The fits in Figure 7.15b predict that $B_{\text{MW}}^{\text{d1}}$ is attenuated by 17 %, but $B_{\text{MW}}^{\text{d2}}$ is attenuated by 45 %. This does not seem likely, as the higher power components should be similarly or more largely attenuated; however the RMSE is reduced by a factor of two compared to the previous fit. This shows that we cannot accurately obtain the field strength of the two MW-dressings from this data. The data does however show that with the combination of two different dressing we can fully flatten the clock transition frequency to less than the resolution-limited linewidth over the measured range.

Figure 7.16 shows colourmaps of three different dressing scenarios. Figure 7.16ai shows the undressed clock transition, and Figure 7.16bi shows the transition with a single dressing of $(\omega_{\text{MW}}^{\text{d1}} - \omega_{\text{HFS}})/(2\pi) = -415$ kHz and strength $B_{\text{MW}}^{\text{d1}} = 12.4$ mG. In Figure 7.16ci, this same dressing ($V_{\text{MW}}^{\text{d1}} = 110$ mV) is again applied, but with an additional second order dressing at

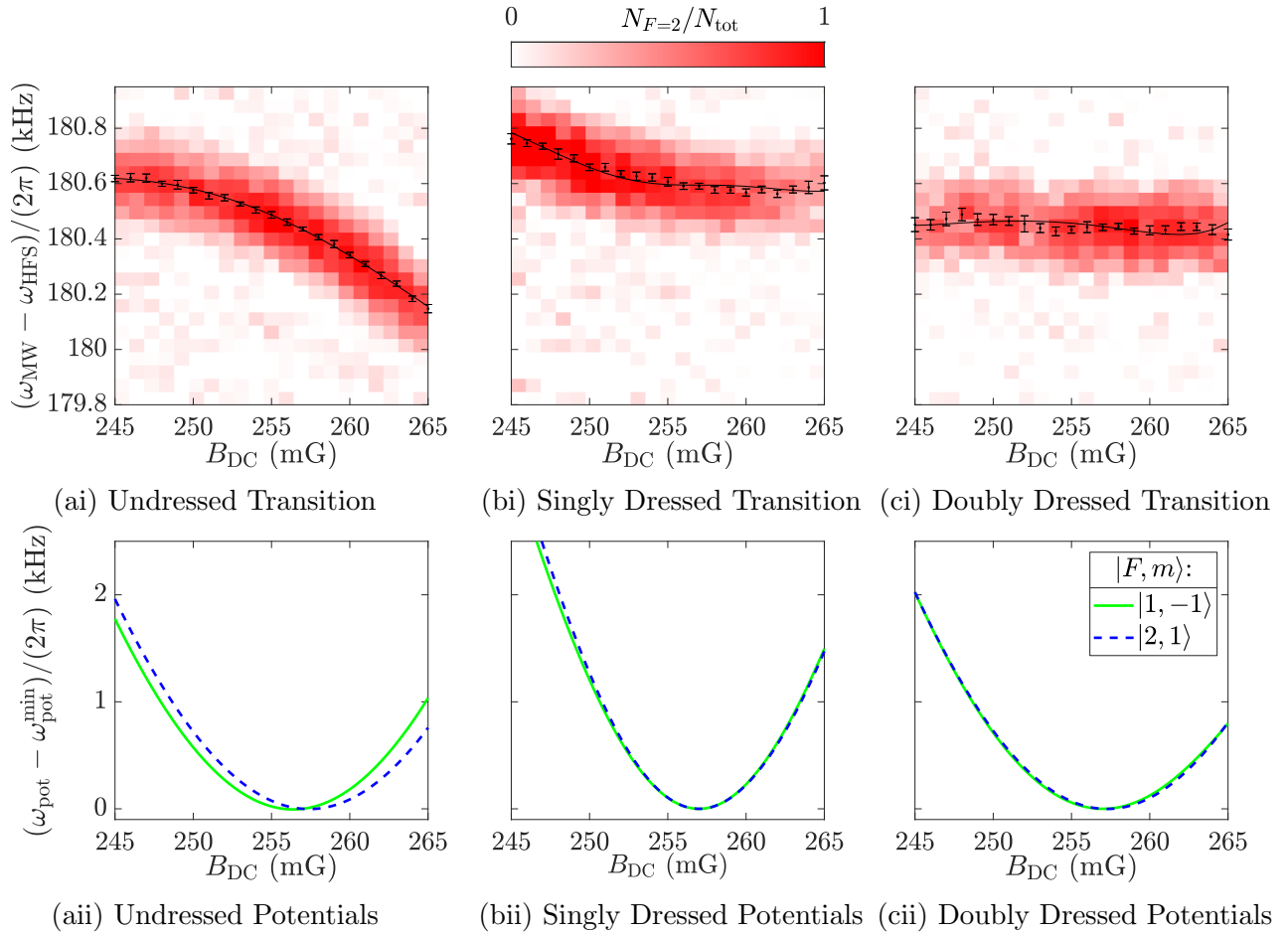


Figure 7.16: The colormaps show the MW-probe frequency versus static field, with the clock transition frequencies marked. In (a) we see the case with no MW-dressing, in (b) a single dressing at $(\omega_{MW}^{d1} - \omega_{HFS})/(2\pi) = -415$ kHz of strength $B_{MW}^{d1} = 10.92$ mG is shown, and in (c) the doubly dressed transition is shown, with the additional dressing at $(\omega_{MW}^{d2} - \omega_{HFS})/(2\pi) = 43$ kHz. We see that in the doubly dressed case we achieve a clock frequency dependence on static field of less than the resolution-limited linewidth. Theoretical predictions of the clock state potentials are also plotted in the corresponding figures (ii). Adapted from our paper [71]

$(\omega_{\text{MW}}^{\text{d2}} - \omega_{\text{HFS}})/(2\pi) = 43$ kHz with an input voltage of $V_{\text{MW}}^{\text{d2}} = 70$ mV. In the case of first order dressing, this voltage input to the generator would form a dressing of strength $B_{\text{MW}}^{\text{d2}} = 9.1$ mG; however as both the first and second order dressings are passing through the same set of amplifiers simultaneously, the previous calibration of MW-dressing field strength as a function input peak-to-peak voltage no longer applies. In the fit to the dressed model, a reduction in both dressing strengths by $(36 \pm 2)\%$ is required. As there is some interdependence in how these two values can alter the fit, if the two frequencies are not attenuated equally the errors on these values will be larger.

In the corresponding figures (ii), the predicted potentials of the clock states are plotted. We see in Figure 7.16a(ii) that the undressed potentials differ in minimum static field by 1 mG, as predicted by Eq. 2.32. The purpose of the first order dressing is to overlap these two potentials, in this case by shifting the lower clock state $|1, -1\rangle$ to the same potential minimum as that of $|2, 1\rangle$ (Figure 7.16b(ii)). The purpose of the second dressing is to alter the curvature of the $|2, 1\rangle$ potential about the static field resonance to match that of $|1, -1\rangle$, which we see in Figure 7.16c(ii). If we look at the full set of potential energy levels we can consider the mechanism by which this is achieved. We recall from Figure 7.13d that it is an avoided crossing with $|1, -1\rangle \leftrightarrow |2, -2\rangle$ which causes the shift in the potential minimum due to the first order dressing. This was when dressing on a different group of transitions, but we see from Figure 7.17b that a dressing on $n = -2$ has a similar effect. One difference in the $n = -2$ dressing case is that state $|1, 1\rangle$ at close to 200 mG shows an avoided crossing which does not correspond to a degeneracy with an energy level in this group. Instead we see that this turning point must be a result of the interaction with another group of transitions, in this case $n = -3$. Due to the small σ_{\pm} -polarisation component of the primarily π -polarised dressing, interactions with the $n = -3$ group are permitted, the centre of which is a 124 kHz detuned from the centre of the $n = -2$ group in the rotating frame of the dressing. Similar effects are not seen for a dressing using pure σ_{\pm} -polarisation on $n = -1$ (Figure 7.13d) as both neighbouring groups may only be addressed with π -polarisation, and therefore the centre of the nearest non-forbidden group is 236 kHz detuned, and hence has a negligible effect on the energy levels within the static field range shown. Note that the MW and RF-dressing strengths used are as extracted from the fit to Figure 7.15a.

In Figure 7.17a we see that the second dressing shifts the potential of $|2, 1\rangle$ via an avoided crossing with $|2, 2\rangle$. However, how we choose to define our MW-dressed states in this case matters. In the rotating frame of the MW-dressing, in the limit of zero MW-dressing power, the states $|1, 1\rangle$ and $|2, 1\rangle$ are degenerate at (233 and 281) mG. It is these two degeneracies which are primarily responsible for the change in the shape of the potential. However,

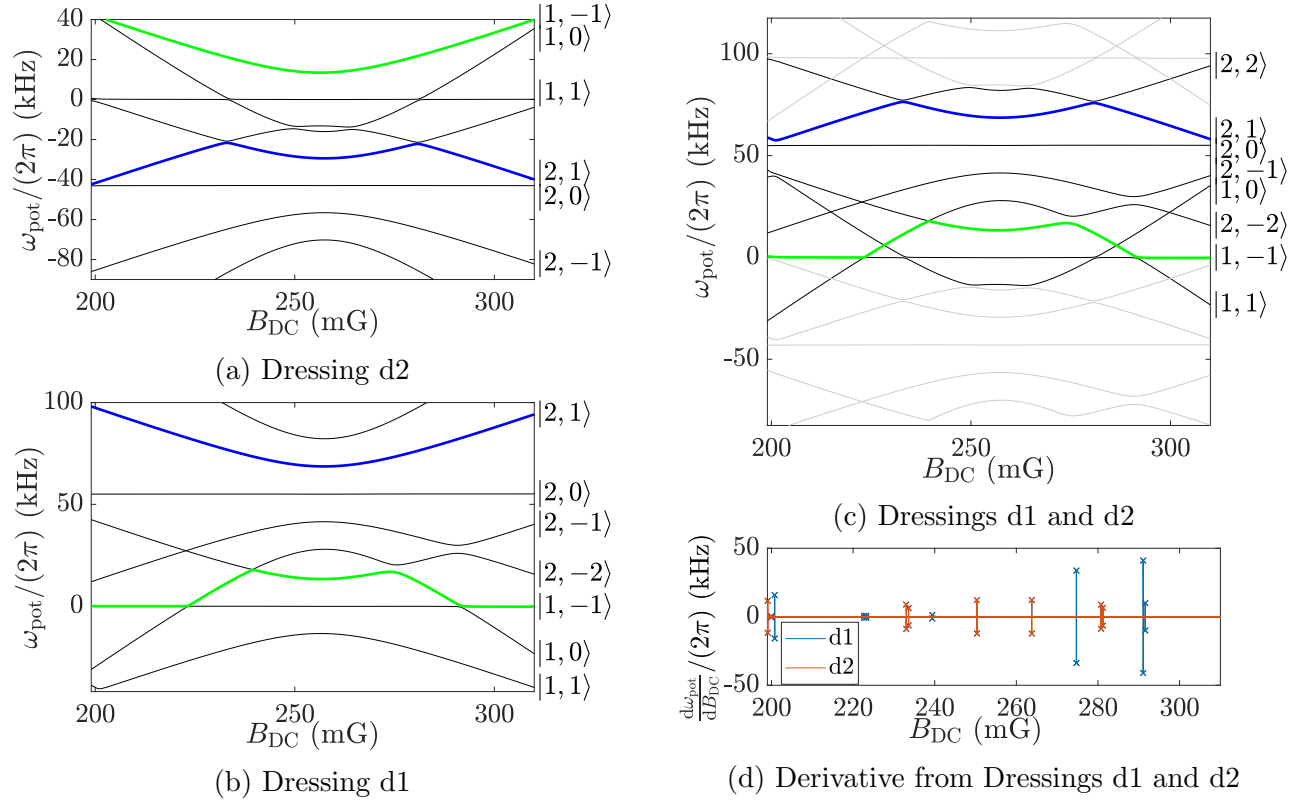


Figure 7.17: The MW-dressed potentials for all MW-dressed energy levels are shown for different dressing possibilities. In (a) a dressing at $(\omega_{\text{MW}}^{\text{d2}} - \omega_{\text{HFS}})/(2\pi) = 43$ kHz is shown, and (b) shows a dressing at $(\omega_{\text{MW}}^{\text{d1}} - \omega_{\text{HFS}})/(2\pi) = -415$ kHz. The effects of combining both dressings is shown in (c). The clock states $|1, -1\rangle$ and $|2, 1\rangle$ are highlighted in green and blue respectively, and in (c) other groups of quasi-energy levels are shown in grey. In (d) the derivative of the potentials as a function of static field is shown, before resorting the energy levels, with the derivatives of the shifts caused by both the first and second order dressings plotted separately, which simply sum to make the derivative of the doubly dressed potentials. This plot marks the locations of flips in the definition of states with crosses.

due to our choice to fix the state labels at B_{res} , when resorting the potentials to account for flips in the definition of states, these states become redefined. We are however primarily interested in the potential minima of our clock states, which are close to the resonant static field. Therefore defining our MW-dressed states relative to this point gives the most intuitive method of labelling potentials.

In Figure 7.17c, the effect of applying both orders of MW-dressing to the full set of potentials is shown. As previously, a set of 8 quasi-energies is shown in black (aside from the highlighted clock states), but unlike previously we now require a representation of the shift from two different dressings on different groups of quasi-energy levels. The 8 main energy levels are shown in the rotating frame of the (stronger) first order dressing, with another group of quasi-energies marked in grey representing the second order dressing. We see that, because the two dressings primarily manipulate different clock states, there is little interaction between the two dressings, and as such the two effects may be considered separately. We know from Figure 7.13c that before accounting for flips in the definition of MW-dressed states, we see sudden jumps in the potential energies corresponding to avoided crossing locations. If we take the derivative of these potentials as a function of static field, whenever there is a state flip we see a spike in the derivative. Performing this analysis for all potentials in the case of the dressing shown in Figure 7.17c before state reorganisation gives the derivative as a function of static field shown in Figure 7.17d. Crosses mark the location of state flips, where our analysis redefines the energy levels in order to extract smooth potentials. This analysis gives an identical plot to the derivative of both dressings d1 and d2 taken separately and then added together on the scale shown (i.e. a sufficiently broad vertical axis scale that only derivative spikes are visible). We are therefore effectively adding the avoided crossings caused by dressing one to the avoided crossings caused by dressing two to create the final set of potentials. This is not necessarily true in the case of two dressings primarily manipulating the same state, but does give an idea of how multiple dressings interact.

In order to demonstrate the improved coherence of a superposition of clock states due to the MW-dressings, we could use the simple interferometric sequence demonstrated in Section 6.3.3. Simulating arbitrary field fluctuations, the resulting phase change of the test interferometer both with and without MW-dressing could be compared. The coherence of MW-dressed superposition states in the presence of static field gradients could also be measured with the use of asymmetric currents in pairs of compensation coils. Quick tests indicate that we require an improved atom number, achievable after replacing the ^{87}Rb dispensers in the chamber, before such measurements can be reliably obtained. This, along with measurement atom losses to a third state

as a function of MW-dressing detuning, are areas for future study.

Overall, in this section we have shown the potential for multi-order control of clock transitions, experimentally showing that we can remove the field dependence of the transition to at least second order. With the help of improvements to the system to be able to detect transition frequencies to a higher level of precision, this technique could be used to generate and measure improvements in coherence control to higher orders. Increased interrogation time, for example by measuring trapped atoms, removing the measurement time limitations which are a consequence of working in free fall, would allow for such advancement. We have however achieved our goal of providing a generalised method of selecting and optimising MW-dressings to achieve coherence control of clock transitions, which is applicable in the ground state of all alkali atoms with a σ_{\pm} RF-dressing, and experimentally shown the effectiveness of this for ^{87}Rb atoms to second order.

Chapter 8

Conclusion and Outlook

In this chapter, we first summarise the results of work to date on the measurement of the spectrum of radio-frequency dressed ^{87}Rb , and on the coherence control of its trappable clock states (Section 8.1). We then consider the broader applications of these results, in quantum sensing in general and trapped rotation sensors in particular, as well as how the experiment can be improved in the future (Section 8.2).

8.1 Conclusion

The first major aim of this work was to use birefringent detection to measure the internal state of the radio-frequency dressed ^{87}Rb atom. Using this method, the energy level structure and couplings between levels have been studied (Section 8.1.1). This knowledge has then been used to facilitate the development of a technique to engineer robust clock transitions which have a reduced transition frequency dependence on static magnetic field (Section 8.1.2).

8.1.1 Microwave Spectroscopy

Microwave spectroscopy is a useful tool for characterising the energy level structure of the ^{87}Rb atom when dressed with a radio-frequency field chosen to couple between the hyperfine magnetic sublevels. Such a dressing allows multi-photon transitions between F -manifolds, which enables transitions which are forbidden in the bare case by the standard angular momentum selection rules. Our state preparation sequence utilises a ‘shelving’ method consisting of microwave and laser pulses to prepare atoms purely in a single magnetic sublevel. Using a birefringent detection method, we can determine the population fraction in each of the two F -levels. The introduction of

common-mode suppression, using a single laser to probe both states, has made this detection system robust against the effects of laser power fluctuations.

Starting from an initially pure atomic state, a MW-probe can be used to transfer population between F -manifolds. Probe frequencies at which population transfer can occur correspond to one of the 105 (non-degenerate) transitions between manifolds in the atomic ground state. This full spectrum has been measured at the resonant static field, and a sample group of transition frequencies has been measured as a function of static magnetic field, in both cases confirming the predicted energy level structure of the RF-dressed atom. Utilising the full spectral data, the resonant coupling coefficients in sample groups have been analysed. For specific transitions, these coefficients have been measured more accurately using Rabi-frequency data. Both at the static field resonance, and as a function of static magnetic field, these coupling coefficient measurements verify our theoretical predictions.

8.1.2 Coherence Control

Pairs of clock states have a reduced transition frequency dependence on external parameters. Utilising our knowledge of the internal state of the atom gained from spectroscopic data, we can manipulate the static field dependence of an energy level. This method utilises the AC-Zeeman effect, the shifting of pairs of energy levels in the presence of a detuned AC magnetic field. The transition frequency dependence of the coupling coefficients on static field allows for a MW-dressing which alters the field dependence of one or both of the two states. This allows for the matching of the field dependencies of the two clock states in the desired static field range. If both states have a matching response to variations in the trapping potential, static field gradients and field noise will affect both states equally, and as such will not lead to the decoherence of a superposition of the two states.

This work presents data on manipulating the field dependence of $|1, -1\rangle \leftrightarrow |2, 1\rangle$, a pair of RF-dressed weak-field seeking states of interest in trapped interferometry experiments. From these, we engineer pairs of trappable clock states which have no first order dependence of transition frequency versus static magnetic field at the field resonance. Data is included which shows that at resonance the gradient of static field versus transition frequency turns from negative, with no MW-dressing, to positive with increasing dressing power for two different dressing frequencies. We also demonstrate that further dressing at a different frequency can be combined with this first order dressing to reduce the field dependence of the transition to less than the resolution-limited linewidth. Predictions of the potentials of the clock states are also included for both orders of dressing, to demonstrate that these remain trappable states.

Appropriately chosen third and higher order MW-dressings are predicted to be able to reduce this dependence still further. The general method for choosing appropriate dressing frequencies in order to reduce the decoherence of an arbitrary superposition state in the ground state of any RF-dressed atom is also described.

8.2 Outlook

In this work, we have gained an increased understanding of the energy structure of ^{87}Rb and how this may be manipulated. Broadly this is intended to be used as a tool for the development of RF-dressed alkali atom systems, providing the full theoretical couplings which form the basis necessary for manipulation of the field dependence of atomic states. Although the experimental focus has been on ^{87}Rb , the equations and methodology provided should allow for easy extrapolation to other alkali atom species. A rotation sensing experiment is intending to implement this technique in the near future (Section 8.2.1). With regards to the experimental apparatus itself, a number of upgrades are planned to further improve its detection capabilities (Section 8.2.2).

8.2.1 Interferometric Sensing

The initial driver behind developing a coherence control method for trappable clock states came from an experiment being developed by my colleagues at the University of Nottingham, working towards a Sagnac rotation sensor using state dependent trapping of ^{87}Rb atoms. The Sagnac effect occurs when a beam is split into two parts which propagate around the same path in opposite directions. When the two parts of the beam meet and interfere, if the paths taken by the beams are identical, constructive interference will occur. However, if the device is rotating the effective paths taken by the beams will differ in length, and this will manifest as a phase change between the two components. Originally, such interferometers used a beam of light, but the use of atoms has the advantage that the mass energy of the atom is $\sim 10^{10}$ higher than the equivalent mass energy of a visible photon; this should similarly increase the sensitivity of the device. Ramsey interferometry enables the splitting and recombining of atoms as required.

An atomic cloud is prepared in a state $|1\rangle$, at location \textcircled{A} in the laboratory frame (Figure 8.1a), and then split into into a superposition of states, $(|1\rangle + |2\rangle)/\sqrt{2}$ using a $\pi/2$ -pulse (Figure 8.1b). State dependent trapping allows the transport of the two halves of the cloud in opposite directions around the ring. With the device rotating at angular frequency ω_S , in order for the

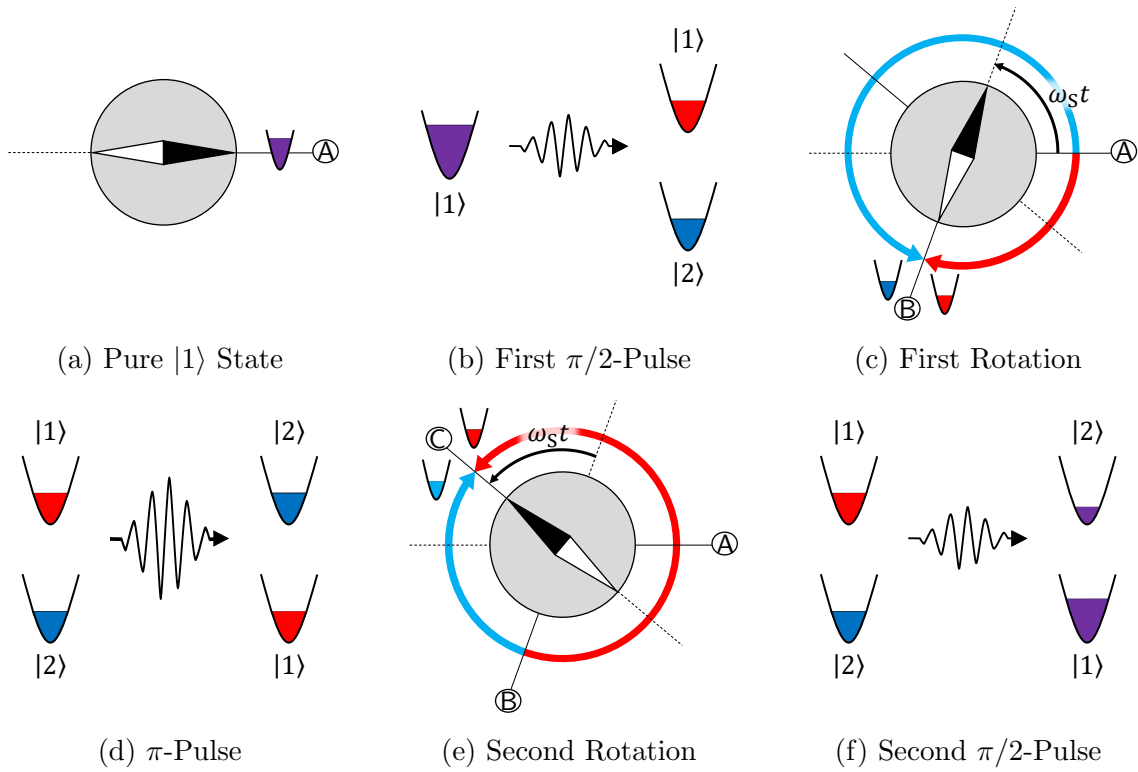


Figure 8.1: Schematic of the phases of a Sagnac interferometric sequence. Adapted from our paper [103] and others [75, 172].

atoms to travel half way around the ring in the device's inertial frame, one of the two states has to travel ω_{st} further than the other (Figure 8.1c). As the two states will evolve over time, a π -pulse is used to flip the superposition by π radians into $(|1\rangle - |2\rangle)/\sqrt{2}$ at this point, so that this evolution occurs in the opposite direction in the next stage and therefore cancels (Figure 8.1d). The atoms then travel from this location \textcircled{B} another half rotation around the device to location \textcircled{C} , with the total path lengths of the two states differing by $2\omega_{st}$ (Figure 8.1e). Finally a $\pi/2$ -pulse is applied to recombine the two states (Figure 8.1f). The atom fraction in state $|2\rangle$ can then be used to extract the Sagnac phase and determine the rotation rate of the device.

The ability of the trapping and state-dependent guiding to transport the two states along identical paths around the edge of the device, and to perfectly spatially overlap the atoms at the correct locations, is vital to the reliability of the device. Using a toroidal ring trap, the location of the atoms is determined wholly by the magnetic field. However, Landé g_F -factor differences mean that pair trappable of states do not have a matching response to the trapping

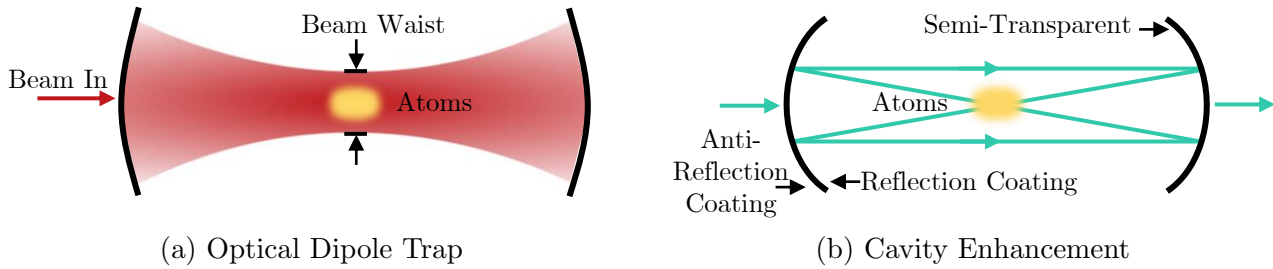


Figure 8.2: Increasing the interaction time of detection light with atoms can improve measurement precision. Trapping atoms in a optical dipole trap, as illustrated in (a), would remove the constraint of free-fall times. The addition of another cavity for the detection light (b) around the region of the cloud could also improve the measured signal by enabling each detection photon to pass through the interaction region many times, enhancing the signal.

potential. This is where the coherence control technique developed in this thesis will be applied. Engineering the field dependence of the two states to have a matching response to the trapping potential using the methods developed in this work will enable further development of this device. For more information see [75, 103].

8.2.2 Experimental Improvements

There are a number of planned experiment improvements which will be advantageous in taking increased sensitivity data on the spectrum of radio-frequency dressed ^{87}Rb and the effects of microwave dressings. Data showing double MW-dressing of the clock transition reducing the transition frequency dependence on static field to less than the linewidth is near the limit of the current measurable flatness. This could be improved by increased interrogation time, and improved state detection. Also, issues with measurements of atoms in free fall experiencing gradients in AC-field strength can cause errors on temporal measurements.

These issues could be avoided if the atoms were spatially confined. As a significant part of this work requires the investigation of atoms in a range of different static fields, magnetic trapping is not viable. We therefore consider electrical trapping, namely using an optical dipole trap. When an atom is placed in a light beam, the electric field of the beam introduces an oscillating dipole moment in the atom. The interaction potential of this dipole moment is proportional to the intensity of the light beam, and this therefore has the effect of pushing the atom towards regions of greater light power. In order to spatially confine atoms, an intensity maximum is created by focusing the

beam. In Figure 8.2a the beam shaping of an optical dipole trap is shown, with the atoms trapped at the focal point.

Current interrogation times, the length of time we can apply a MW-probe to the atoms, are limited to < 15 ms due to the atoms falling out of the detectable region. However, trapped atoms can be interrogated for of the order of seconds. We could therefore use much lower MW-probe powers, lowering the linewidth of transitions, whilst still having clearly measurable population change between energy levels. Also, as the length of the beam is much larger than its waist, atoms are trapped in an elongated shape. This means that if detecting along the same axis as the dipole laser, overlapped using dichroic mirrors which reflect the detection beam whilst permitting through the trapping light in order to only receive the correct light at the detector, this would allow a long, dense column of atoms for the detection laser to pass through. As the detected signal strength is proportional to the number of atoms in the beam path, this would give clearer signals. For more details on optical dipole traps see [83].

A further improvement to the system would be adding in an optical cavity around the atoms to increase the interaction time of the detection beam. Passing light into a cavity which has a focal point at the centre of the beam at which the atoms are located allows each photon to make multiple journeys through the atom cloud, enhancing the detection strength proportionally to the average number of passes through the cloud. A semi-transparent mirror would then allow the light to travel to the detector after many passes through the atom cloud, see Figure 8.2b. The method of introducing a cavity to increase interrogation times has been effective in other experiments [77, 176]. A combination of both the optical dipole trap, and the cavity enhanced detection would enable stronger detection of the internal state of the atom, allowing for investigation of the effects of higher order MW-dressings, as well as improved spectroscopic data.

Further minor improvements include adding in a MW pick-up antenna near the main chamber to directly measure the power in multiple different MW-dressing orders. This would bypass the issue of the uncertainty in output power from the multi-order MW-generator. Changing from referencing the frequency of the MW-generator using a quartz oscillator to referencing directly from GPS would also remove possible MW-probe frequency drifts over time. Increasing the maximum output power from our home-built MW-dressing generator would also allow for the investigation of the effects of higher power dressings. Replacing the ^{87}Rb dispensers in the main chamber is also a priority, in order to improve the signal to noise ratio of all measurements of the atomic cloud. This would also enable proper study of the benefits of the common mode suppressed state detection method.

Appendix A

Angular Momentum

A.1 Magnitudes and Commutation

This section contains a summary of the relationships between different components of angular momentum, which are used as tools in many calculations throughout this thesis. The relations and matrices given here are for the total angular momentum (F) case, but the same relations will apply to the individual components (S, L, I, J) of angular momenta. For further details see [127]. The relationship between angular momentum $\hat{\mathbf{F}}$ and its associated azimuthal and magnetic quantum numbers F and m_F is given by

$$\begin{aligned}\hat{\mathbf{F}}^2 |F, m\rangle &= \hbar^2 F(F+1) |F, m\rangle, \\ \hat{F}_z |F, m\rangle &= \hbar m_F |F, m\rangle,\end{aligned}\tag{A.1}$$

where F_z is the projection of $\hat{\mathbf{F}}$ onto the z -axis. By definition, the commutation relations

$$[F_x, F_y] = iF_z, \quad [F_z, F_x] = iF_y, \quad [F_y, F_z] = iF_x,\tag{A.2}$$

are true. The angular momentum must also commute with its square

$$\hat{\mathbf{F}}^2 = F_x^2 + F_y^2 + F_z^2,\tag{A.3}$$

i.e.

$$[\hat{\mathbf{F}}, \hat{\mathbf{F}}^2] = 0.\tag{A.4}$$

We can now define the raising and lowering operators as

$$F_+ = F_x + iF_y, \quad F_- = F_x - iF_y\tag{A.5}$$

respectively. Using Eq. A.2 we can then derive the commutation relations for F_{\pm} :

$$[F_z, F_+] = iF_+, \quad [F_z, F_-] = -iF_+,\tag{A.6}$$

and

$$[F_+, F_-] = 2F_z. \quad (\text{A.7})$$

The final commutation relations required, which can be seen from A.4, are

$$[\hat{\mathbf{F}}^2, F_\pm] = [\hat{\mathbf{F}}^2, F_z] = 0. \quad (\text{A.8})$$

Substituting the raising and lowering operators into $\hat{\mathbf{F}}^2$ gives

$$\hat{\mathbf{F}}^2 = \hbar^2 \left(\frac{1}{2}(F_+F_- + F_-F_+) + F_z^2 \right), \quad (\text{A.9})$$

which using Eq. A.7 provides the result

$$F_\pm F_\mp = (\hat{\mathbf{F}}^2 - F_z(F_z \mp 1)). \quad (\text{A.10})$$

Using Eq. A.1 gives

$$\langle F, m | F_\pm F_\mp | F, m \rangle = F(F+1) + m(m \pm 1). \quad (\text{A.11})$$

We can now use Eq. A.6 to obtain the relation

$$F_z F_\pm | F, m \rangle = F_\pm (F_z \pm 1) | F, m \rangle = \hbar F_\pm (m \pm 1) | F, m \rangle. \quad (\text{A.12})$$

Comparing this with

$$F_z | F, m \pm 1 \rangle = \hbar (m \pm 1) | F, m \pm 1 \rangle \quad (\text{A.13})$$

indicates that $F_\pm | F, m \rangle$ is proportional to $| F, m \pm 1 \rangle$, i.e.

$$F_\pm | F, m \rangle = \mathbf{a}_\pm | F, m \pm 1 \rangle. \quad (\text{A.14})$$

To find the constant \mathbf{a} , we use Eq. A.10 and $F_\pm^\dagger = F_\mp$ to obtain

$$\langle F, m | F_\pm^\dagger F_\pm | F, m \rangle = \langle F, m | F_\mp F_\pm | F, m \rangle = \mathbf{a}_\pm^2, \quad (\text{A.15})$$

where we have also used the fact that F_\pm are a Hermite conjugate pair. Recalling Eq. A.11, this gives the raising and lowering constants

$$F_\pm | F, m \rangle = \sqrt{F(F+1) - m(m \pm 1)} | F, m \pm 1 \rangle. \quad (\text{A.16})$$

From this we can gain the couplings between two levels $| F, m \rangle$ and $| F', m' \rangle$

$$\langle F', m' | F_\pm | F, m \rangle = \sqrt{F(F+1) - mm'} \delta_{m, m' \pm 1} \delta_{F, F'}, \quad (\text{A.17})$$

where δ is the Kronecker delta function. We should also note the equivalent equation for F_z derived from Eq. A.1:

$$\langle F', m' | F_z | F, m \rangle = m \delta_{m, m'} \delta_{F, F'}. \quad (\text{A.18})$$

We can then use the F_{\pm} matrices and Eq. A.5 to give F_x and F_y

$$F_x = \hbar \begin{pmatrix} 0 & 1 & 0 & 0 & 0 & 0 & 0 & 0 \\ 1 & 0 & \sqrt{\frac{3}{2}} & 0 & 0 & 0 & 0 & 0 \\ 0 & \sqrt{\frac{3}{2}} & 0 & \sqrt{\frac{3}{2}} & 0 & 0 & 0 & 0 \\ 0 & 0 & \sqrt{\frac{3}{2}} & 0 & 1 & 0 & 0 & 0 \\ 0 & 0 & 0 & 1 & 0 & 0 & 0 & 0 \\ 0 & 0 & 0 & 0 & 0 & 0 & \frac{1}{\sqrt{2}} & 0 \\ 0 & 0 & 0 & 0 & 0 & \frac{1}{\sqrt{2}} & 0 & \frac{1}{\sqrt{2}} \\ 0 & 0 & 0 & 0 & 0 & 0 & \frac{1}{\sqrt{2}} & 0 \end{pmatrix}, \quad (\text{A.22})$$

$$F_y = \hbar \begin{pmatrix} 0 & i & 0 & 0 & 0 & 0 & 0 & 0 \\ -i & 0 & i\sqrt{\frac{3}{2}} & 0 & 0 & 0 & 0 & 0 \\ 0 & -i\sqrt{\frac{3}{2}} & 0 & i\sqrt{\frac{3}{2}} & 0 & 0 & 0 & 0 \\ 0 & 0 & -i\sqrt{\frac{3}{2}} & 0 & i & 0 & 0 & 0 \\ 0 & 0 & 0 & -i & 0 & 0 & 0 & 0 \\ 0 & 0 & 0 & 0 & 0 & 0 & \frac{i}{\sqrt{2}} & 0 \\ 0 & 0 & 0 & 0 & 0 & -\frac{i}{\sqrt{2}} & 0 & \frac{i}{\sqrt{2}} \\ 0 & 0 & 0 & 0 & 0 & 0 & -\frac{i}{\sqrt{2}} & 0 \end{pmatrix}. \quad (\text{A.23})$$

Also of interest for our purposes are the 2×2 reduced F -matrices,

$$F_x = \frac{\hbar}{2} \begin{pmatrix} 0 & 1 \\ 1 & 0 \end{pmatrix}, F_y = \frac{\hbar}{2} \begin{pmatrix} 0 & -i \\ i & 0 \end{pmatrix}, F_z = \frac{\hbar}{2} \begin{pmatrix} 1 & 0 \\ 0 & -1 \end{pmatrix}, \quad (\text{A.24})$$

which can be gained from the Pauli matrices, and have associated ladder matrices

$$F_+ = \hbar \begin{pmatrix} 0 & 1 \\ 0 & 0 \end{pmatrix}, F_- = \hbar \begin{pmatrix} 0 & 0 \\ 1 & 0 \end{pmatrix}. \quad (\text{A.25})$$

These are useful when working with reduced Hamiltonians where individual m levels are not analysed.

A.3 Wigner $3j$ -Symbols

Wigner $3j$ -symbols are used when calculating couplings between angular momenta. In our case we are considering the angular momentum of the final energy level j_1 accessed by adding a photon of angular momentum j_2 to an initial energy level of angular momentum j_3 , all of which have corresponding magnetic sublevels m_j . We can explicitly calculate these terms using

the Racah formula, derived in [144]. This formula states that the Wigner 3j-symbols are given by

$$\begin{aligned} \begin{pmatrix} j_1 & j_2 & j_3 \\ m_1 & m_2 & m_3 \end{pmatrix} &= (-1)^{j_1-j_2-j_3} \sqrt{\Delta_{\text{co}}(j_1, j_2, j_3)} \sum_{\mathbf{k}} \frac{(-1)^{\mathbf{k}}}{K} \\ &\times \sqrt{(j_1 + m_1)!(j_2 + m_2)!(j_3 + m_3)!} \\ &\times \sqrt{(j_1 - m_1)!(j_2 - m_2)!(j_3 - m_3)!} \end{aligned} \quad (\text{A.26})$$

where

$$\begin{aligned} K &= \mathbf{k}!(j_3 - j_2 + \mathbf{k} + m_1)!(j_3 - j_1 + t - m_2)!(j_1 + j_2 - j_3 - \mathbf{k})! \\ &\times (j_1 - \mathbf{k} - m_1)!(j_2 - \mathbf{k} - m_2)! \end{aligned} \quad (\text{A.27})$$

and Δ_{co} is the triangle coefficient

$$\Delta_{\text{co}}(j_1, j_2, j_3) = \frac{(j_1 + j_2 - j_3)!(j_1 - j_2 + j_3)!(-j_1 + j_2 + j_3)!}{(j_1 + j_2 + j_3 + 1)!}. \quad (\text{A.28})$$

The sum over \mathbf{k} is for all integers which make all factorial coefficients non-negative. Explicitly this means that all of $(j \pm m_j)$, $(j_1 + j_2 - j_3)$, $(j_2 + j_3 - j_1)$ and $(j_3 + j_1 - j_2)$ must be positive, and the number of terms is given by one plus the lowest of these values. We are subject to the constraint $m_1 + m_2 + m_3 = 0$ due to conservation of angular momentum, and also require that $j_{\text{tot}} = j_1 + j_2 + j_3$ is an integer.

Setting all values $m_j = 0$ and simplifying obtains

$$\begin{aligned} \begin{pmatrix} j_1 & j_2 & j_3 \\ 0 & 0 & 0 \end{pmatrix} &= (-1)^{J/2} \sqrt{\frac{(j_{\text{tot}} - 2j_1)!(j_{\text{tot}} - 2j_2)!(j_{\text{tot}} - 2j_3)!}{(j_{\text{tot}} + 1)!}} \\ &\times \frac{(j_{\text{tot}}/2)!}{(j_{\text{tot}}/2 - j_1)!(j_{\text{tot}}/2 - j_2)!(j_{\text{tot}}/2 - j_3)!}. \end{aligned} \quad (\text{A.29})$$

As we require being in the ground state we have $L = 0$, $S = \pm 1/2$, and $F = I \pm 1/2$. We are therefore interested in $j_1 = I + 1/2$, $j_2 = 1$ and $j_3 = I - 1/2$ (as we are applying a photon (angular momentum 1) to change between energy levels). In the case all values of $m = 0$ the Wigner 3j symbol evaluates as

$$\begin{aligned} \begin{pmatrix} I + 1/2 & 1 & I - 1/2 \\ 0 & 0 & 0 \end{pmatrix} &= (-1)^{I+1/2} \frac{(I + 1/2)!}{(I - 1/2)!} \sqrt{\frac{2(2I - 1)!}{(2I + 2)!}} \\ &= (-1)^{I+1/2} \sqrt{\frac{2I + 1}{8I(I + 1)}}. \end{aligned} \quad (\text{A.30})$$

A.4 Wigner d -Matrices

In this section we define and provide the full Wigner d -matrices for the $F = 1, 2$ levels of interest in this thesis, as given in [130, 151]. From combining Eq. 6.17 and Eq. 2.49 we see that these matrices are defined as

$$d_{\bar{m}', \bar{m}}^F(\theta_F) = \langle F, \bar{m}' | e^{-i\theta_F \hat{F}_y} | F, \bar{m} \rangle, \quad (\text{A.31})$$

which is the rotated form of our rotation operator $\hat{U}_y(\theta_F)$. As given in Eq. 2.47, θ_F is the rotation angle within one F -manifold. Explicitly the rotation matrix is given by

$$d_{\bar{m}', \bar{m}}^F(\theta_F) = \sum_{\mathbf{k}} \frac{(-1)^{\mathbf{k}} \sqrt{(F + \bar{m})!(F - \bar{m})!(F + \bar{m}')!(F - \bar{m}')!}}{\mathbf{k}!(F - \mathbf{k} - \bar{m}')!(F + \bar{m} - \mathbf{k})!(\bar{m}' + \mathbf{k} - \bar{m})!} \times \left(\cos \frac{\theta_F}{2} \right)^{2F + \bar{m} - \bar{m}' - 2\mathbf{k}} \times \left(-\sin \frac{\theta_F}{2} \right)^{\bar{m}' - \bar{m} + 2\mathbf{k}}, \quad (\text{A.32})$$

where the sum is over all integers \mathbf{k} where the argument of the factorials is non-negative. Explicitly this requires that $\bar{m}' - \bar{m}$, $F + \bar{m}$ and $F - \bar{m}'$ are all greater than or equal to $2F$. Assuming these conditions are met, we can then define \mathbf{k} as all integers

$$\min(0, \bar{m} - \bar{m}') \leq \mathbf{k} \leq \max(0, j + m, j - m). \quad (\text{A.33})$$

This then provides matrices of size $(2F + 1) \times (2F + 1)$ where the columns each correspond to a possible value \bar{m}' and the rows to a possible value \bar{m} . In full these are given by

$$d_{\bar{m}', \bar{m}}^1(\theta_1) = \frac{1}{2} \begin{pmatrix} (1 + \cos \theta_1) & -\sqrt{2} \sin \theta_1 & (1 - \cos \theta_1) \\ \sqrt{2} \sin \theta_1 & 2 \cos \theta_1 & -\sqrt{2} \sin \theta_1 \\ (1 - \cos \theta_1) & \sqrt{2} \sin \theta_1 & (1 + \cos \theta_1) \end{pmatrix}, \quad (\text{A.34})$$

$$d_{\bar{m}', \bar{m}}^2(\theta_2) = \frac{1}{2} \begin{pmatrix} \frac{1}{2}(1 + \cos \theta_2)^2 & (1 + \cos \theta_2) \sin \theta_2 & \sqrt{\frac{3}{2}} \sin^2 \theta_2 & (1 - \cos \theta_2) \sin \theta_2 & \frac{1}{2}(1 - \cos \theta_2)^2 \\ -(1 + \cos \theta_2) \sin \theta_2 & -(1 - \cos \theta_2 - 2 \cos^2 \theta_2) & \sqrt{\frac{3}{2}} \sin(2\theta_2) & (1 + \cos \theta_2 - 2 \cos^2 \theta_2) & (1 - \cos \theta_2) \sin \theta_2 \\ \sqrt{\frac{3}{2}} \sin^2 \theta_2 & -\sqrt{\frac{3}{2}} \sin(2\theta_2) & -(1 - 3 \cos^2 \theta_2) & \sqrt{\frac{3}{2}} \sin(2\theta_2) & \sqrt{\frac{3}{2}} \sin^2 \theta_2 \\ -(1 - \cos \theta_2) \sin \theta_2 & -(1 + \cos \theta_2 - 2 \sin^2 \theta_2) & -\sqrt{\frac{3}{2}} \sin(2\theta_2) & -(1 - \cos \theta_2 - 2 \sin^2 \theta_2) & (1 + \cos \theta_2) \sin \theta_2 \\ \frac{1}{2}(1 - \cos \theta_2)^2 & -(1 - \cos \theta_2) \sin \theta_2 & \sqrt{\frac{3}{2}} \sin^2 \theta_2 & -(1 + \cos \theta_2) \sin \theta_2 & \frac{1}{2}(1 + \cos \theta_2)^2 \end{pmatrix}, \quad (\text{A.35})$$

for $F = 1, 2$. We note that $d_{\bar{m}', \bar{m}}^F(\theta_F) = d_{\bar{m}, \bar{m}'}^F(-\theta_F)$.

Appendix B

Coupling Coefficients

B.1 Individual Coupling Coefficients

In this section we provide the complete set of coupling equations for transitions $|F, \bar{m}\rangle \leftrightarrow |F', \bar{m}'\rangle$ in the ground state of ^{87}Rb . We give the couplings for σ_{\pm} separately, ignoring the polarisation degeneracy in groups $n = \pm 1$, which will be addressed in Section B.2. The tables and level diagrams in this section are adapted from those in our paper [167]. θ_F is as defined in Eq. 2.47. In Tables B.1, B.2 and B.3 we give the full equations for all couplings for MW-polarisations $\sigma_{-}, \pi, \sigma_{+}$ respectively, as given by the Rabi frequency, normalised by $\Omega_{\text{norm}}^{\sigma}$ (Eq. 6.29). The absolute values of the couplings are plotted, as a sign change in the Rabi frequency merely indicates a phase change, whereas we are only interested in coupling strength.

Figures B.2, B.4 and B.6 show the plots of each of these transitions as a function of B_{DC} for each of the corresponding tables. All plots have the same vertical axis scaling to enable a direct comparison of relative coupling strengths. Figures B.1, B.3 and B.5 show the bare state transitions and their corresponding dressed transitions, and also indicate which transitions are suppressed. In all figures red, grey and blue lines indicate the lowest frequency, central and highest frequency groups in each set, with the corresponding coupling equation table headers in the same colours. Coupling plots are shown for the values used in our experiment, $\omega_{\text{RF}}/(2\pi) = 180$ kHz, $B_{\text{RF}}^{\pm} = 25$ mG and $B_{\text{res}} = 257$ mG, although as $\omega_{\text{RF}} \propto B_{\text{res}}$ (Eq. 2.32) the dependence about the static field resonance will be of the same shape for other RF-dressing frequencies. From the data given in this section we can easily see which transitions are appropriate for use in the MW coherence control of a given RF dressed transition, as described in Chapter 7. The full formula for deriving all couplings given in this chapter is Eq. 6.26, and the relationship between the σ_{\pm} -components is given by Eq. 6.28.

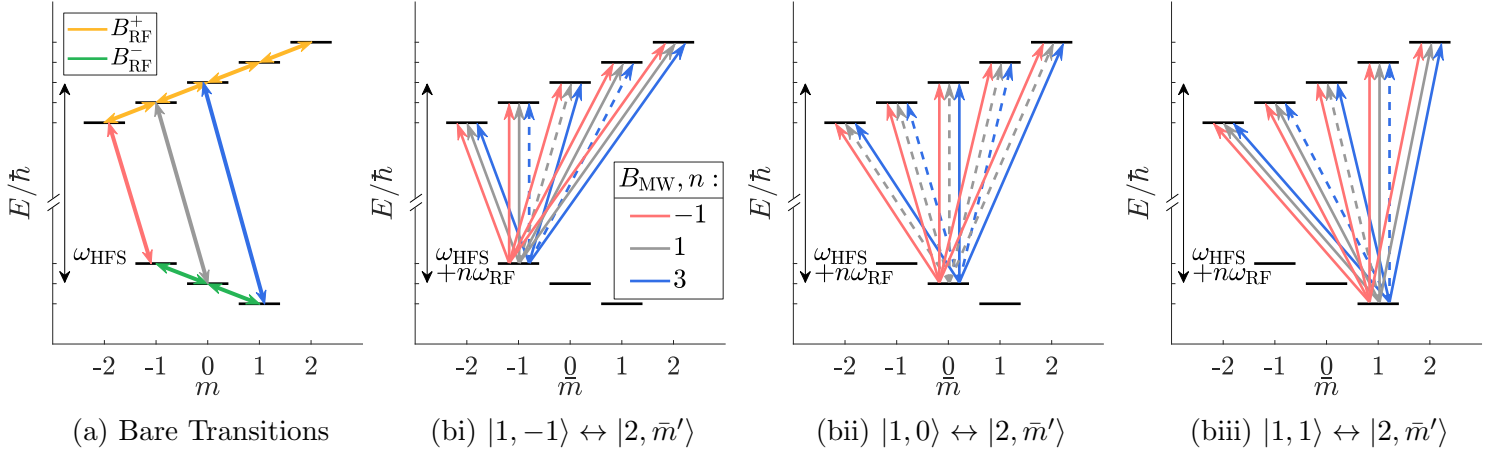


Figure B.1: The figure shows all σ_- -polarised bare (a) and associated dressed (b) MW-transitions. Associated coupling equations are given in Table B.1 and plotted in Figure B.2 with the same colour code of red, blue and grey for $n = -3, -1, 1$. Dashed lines indicate suppressed transitions (see Table 6.1).

transition	$\hat{H}_{\text{MW}}^{-, n=-3} / \Omega_{\text{norm}}^-$	$\hat{H}_{\text{MW}}^{-, n=-1} / \Omega_{\text{norm}}^-$	$\hat{H}_{\text{MW}}^{-, n=1} / \Omega_{\text{norm}}^-$
$ 1, -1\rangle \leftrightarrow 2, -2\rangle$	$\frac{1}{\sqrt{2}}(1 + \cos \theta_1)(1 + \cos \theta_2)^2$	$-\sqrt{2} \sin \theta_1(1 + \cos \theta_2) \sin \theta_2$	$\frac{1}{\sqrt{2}}(1 - \cos \theta_1) \sin^2 \theta_2$
$ 1, -1\rangle \leftrightarrow 2, -1\rangle$	$\frac{1}{\sqrt{2}}(1 + \cos \theta_1)(1 + \cos \theta_2) \sin \theta_2$	$-\sqrt{2} \sin \theta_1(1 - \cos \theta_2 - 2 \cos^2 \theta_2)$	$-\frac{1}{\sqrt{2}}(1 - \cos \theta_1) \sin(2\theta_2)$
$ 1, -1\rangle \leftrightarrow 2, 0\rangle$	$\sqrt{3}(1 + \cos \theta_1) \sin^2 \theta_2$	$\sqrt{3} \sin \theta_1 \sin(2\theta_2)$	$-\frac{1}{\sqrt{3}}(1 - \cos \theta_1)(1 - 3 \cos^2 \theta_2)$
$ 1, -1\rangle \leftrightarrow 2, 1\rangle$	$\sqrt{2}(1 + \cos \theta_1)(1 - \cos \theta_2) \sin \theta_2$	$\sqrt{2} \sin \theta_1(1 + \cos \theta_2 - 2 \cos^2 \theta_2)$	$\frac{1}{\sqrt{2}}(1 - \cos \theta_1) \sin(2\theta_2)$
$ 1, -1\rangle \leftrightarrow 2, 2\rangle$	$\frac{1}{\sqrt{2}}(1 + \cos \theta_1)(1 - \cos \theta_2)^2$	$\sqrt{2} \sin \theta_1(1 - \cos \theta_2) \sin \theta_2$	$\frac{1}{\sqrt{2}}(1 - \cos \theta_1) \sin^2 \theta_2$
$ 1, 0\rangle \leftrightarrow 2, -2\rangle$	$-\sin \theta_1(1 + \cos \theta_2)^2$	$-2 \cos \theta_1(1 + \cos \theta_2) \sin \theta_2$	$\sin \theta_1 \sin^2 \theta_2$
$ 1, 0\rangle \leftrightarrow 2, -1\rangle$	$-2 \sin \theta_1(1 + \cos \theta_2) \sin \theta_2$	$-2 \cos \theta_1(1 - \cos \theta_2 - 2 \cos^2 \theta_2)$	$-\sin \theta_1 \sin(2\theta_2)$
$ 1, 0\rangle \leftrightarrow 2, 0\rangle$	$-\sqrt{6} \sin \theta_1 \sin^2 \theta_2$	$\sqrt{6} \cos \theta_1 \sin(2\theta_2)$	$-\sqrt{\frac{2}{3}} \sin \theta_1(1 - 3 \cos^2 \theta_2)$
$ 1, 0\rangle \leftrightarrow 2, 1\rangle$	$-2 \sin \theta_1(1 - \cos \theta_2) \sin \theta_2$	$2 \cos \theta_1(1 + \cos \theta_2 - 2 \cos^2 \theta_2)$	$\sin \theta_1 \sin(2\theta_2)$
$ 1, 0\rangle \leftrightarrow 2, 2\rangle$	$-\sin \theta_1(1 - \cos \theta_2)^2$	$2 \cos \theta_1(1 - \cos \theta_2) \sin \theta_2$	$\sin \theta_1 \sin^2 \theta_2$
$ 1, 1\rangle \leftrightarrow 2, -2\rangle$	$\frac{1}{\sqrt{2}}(1 - \cos \theta_1)(1 + \cos \theta_2)^2$	$\sqrt{2} \sin \theta_1(1 + \cos \theta_2) \sin \theta_2$	$\frac{1}{\sqrt{2}}(1 + \cos \theta_1) \sin^2 \theta_2$
$ 1, 1\rangle \leftrightarrow 2, -1\rangle$	$\sqrt{2}(1 - \cos \theta_1)(1 + \cos \theta_2) \sin \theta_2$	$\sqrt{2} \sin \theta_1(1 - \cos \theta_2 - 2 \cos^2 \theta_2)$	$-\frac{1}{\sqrt{2}}(1 + \cos \theta_1) \sin(2\theta_2)$
$ 1, 1\rangle \leftrightarrow 2, 0\rangle$	$\sqrt{3}(1 - \cos \theta_1) \sin^2 \theta_2$	$-\sqrt{3} \sin \theta_1 \sin(2\theta_2)$	$-\frac{1}{\sqrt{3}}(1 + \cos \theta_1)(1 - 3 \cos^2 \theta_2)$
$ 1, 1\rangle \leftrightarrow 2, 1\rangle$	$\sqrt{2}(1 - \cos \theta_1)(1 - \cos \theta_2) \sin \theta_2$	$-\sqrt{2} \sin \theta_1(1 + \cos \theta_2 - 2 \cos^2 \theta_2)$	$\frac{1}{\sqrt{2}}(1 + \cos \theta_1) \sin(2\theta_2)$
$ 1, 1\rangle \leftrightarrow 2, 2\rangle$	$\frac{1}{\sqrt{2}}(1 - \cos \theta_1)(1 - \cos \theta_2)^2$	$-\sqrt{2} \sin \theta_1(1 - \cos \theta_2) \sin \theta_2$	$\frac{1}{\sqrt{2}}(1 + \cos \theta_1) \sin^2 \theta_2$

Table B.1: The table gives all σ_- -polarised MW-coupling strength equations. These are in groups $n = -3, -1, 1$ (red, grey and blue), with all transitions shown in Figure B.1 and plotted in Figure B.2 in the colours of the table headers.

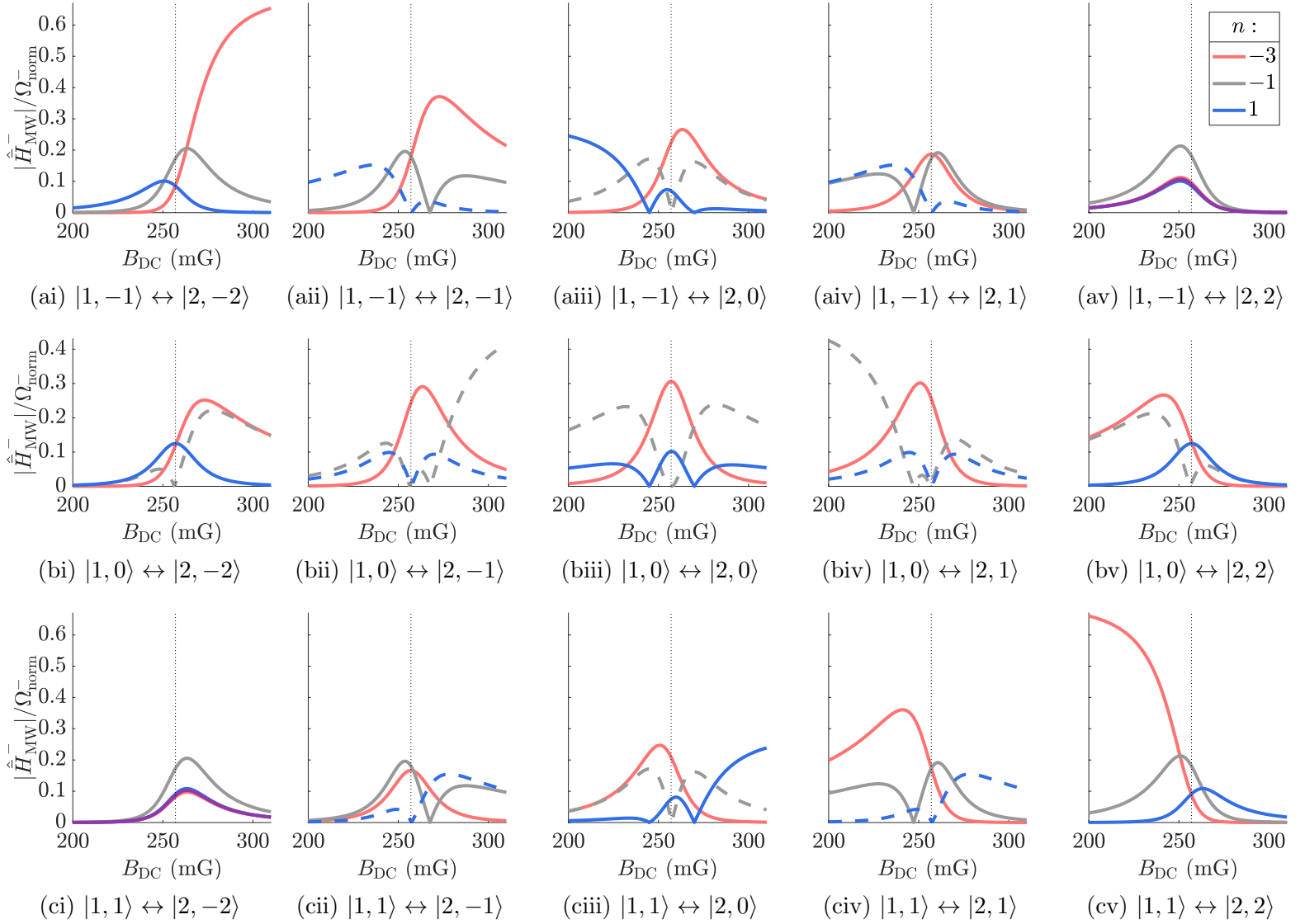


Figure B.2: The figure shows plot of all σ_- -polarised coupling coefficients as a function of static magnetic field, as given in Table B.1. The transitions and the colours of the groups correspond to the those shown in Figure B.1. Groups $n = -3, -1, 1$ are shown in red, grey and blue respectively, and dashed lines indicate suppressed couplings (see Table 6.1). The resonant static field is indicated by the dotted line and purple indicates near equal $n = -3, 1$ couplings.

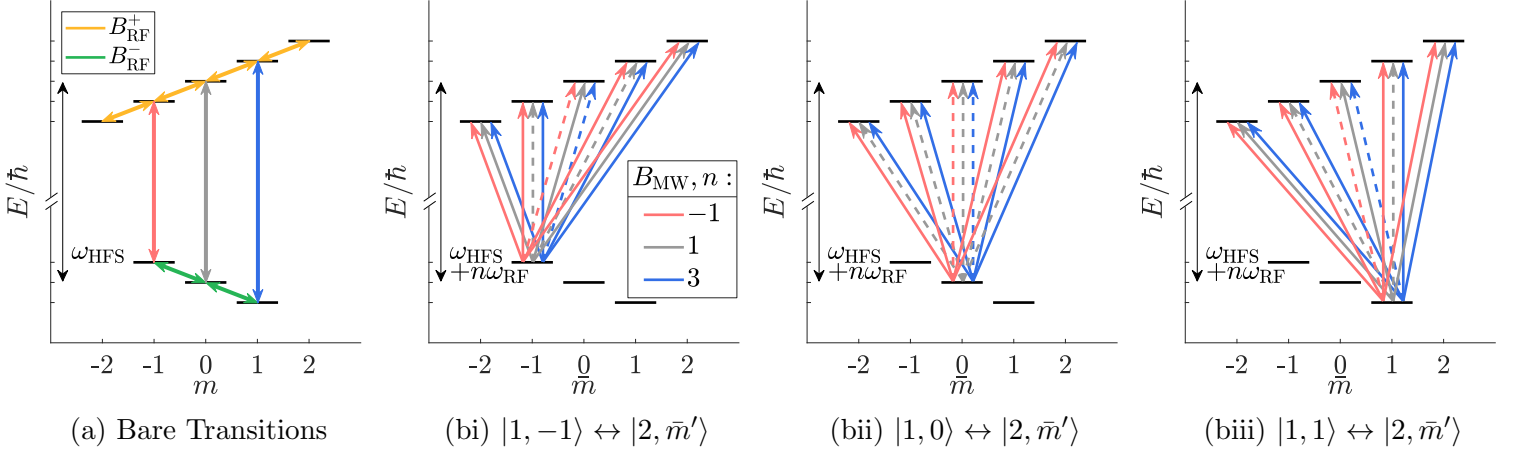


Figure B.3: The figure shows all π -polarised bare (a) and associated dressed (b) MW-transitions. Associated coupling equations are given in Table B.2 and plotted in Figure B.4 with the same colour code of red, blue and grey for $n = -2, 0, 2$. Dashed lines indicate suppressed transitions (see Table 6.1).

transition	$\hat{H}_{MW}^{\pi, n=-2} / \Omega_{\text{norm}}^{\pi}$	$\hat{H}_{MW}^{\pi, n=0} / \Omega_{\text{norm}}^{\pi}$	$\hat{H}_{MW}^{\pi, n=2} / \Omega_{\text{norm}}^{\pi}$
$ 1, -1\rangle \leftrightarrow 2, -2\rangle$	$-\sqrt{2}(1 + \cos \theta_1)(1 + \cos \theta_2) \sin \theta_2$	$2\sqrt{2} \sin \theta_1 \sin^2 \theta_2$	$-\sqrt{2}(1 - \cos \theta_1)(1 - \cos \theta_2) \sin \theta_2$
$ 1, -1\rangle \leftrightarrow 2, -1\rangle$	$-\sqrt{2}(1 + \cos \theta_1)(1 - \cos \theta_2 - 2 \cos^2 \theta_2)$	$-2\sqrt{2} \sin \theta_1 \sin(2\theta_2)$	$\sqrt{2}(1 - \cos \theta_1)(1 + \cos \theta_2 - 2 \cos^2 \theta_2)$
$ 1, -1\rangle \leftrightarrow 2, 0\rangle$	$\sqrt{3}(1 + \cos \theta_1) \sin(2\theta_2)$	$-\frac{4}{\sqrt{3}} \sin \theta_1 (1 - 3 \cos^2 \theta_2)$	$-\sqrt{3}(1 - \cos \theta_1) \sin(2\theta_2)$
$ 1, -1\rangle \leftrightarrow 2, 1\rangle$	$\sqrt{2}(1 + \cos \theta_1)(1 + \cos \theta_2 - 2 \cos^2 \theta_2)$	$2\sqrt{2} \sin \theta_1 \sin(2\theta_2)$	$-\sqrt{2}(1 - \cos \theta_1)(1 - \cos \theta_2 - 2 \cos^2 \theta_2)$
$ 1, -1\rangle \leftrightarrow 2, 2\rangle$	$\sqrt{2}(1 + \cos \theta_1)(1 - \cos \theta_2) \sin \theta_2$	$2\sqrt{2} \sin \theta_1 \sin^2 \theta_2$	$\sqrt{2}(1 - \cos \theta_1)(1 + \cos \theta_2) \sin \theta_2$
$ 1, 0\rangle \leftrightarrow 2, -2\rangle$	$2 \sin \theta_1 (1 + \cos \theta_2) \sin \theta_2$	$4 \cos \theta_1 \sin^2 \theta_2$	$-2 \sin \theta_1 (1 - \cos \theta_2) \sin \theta_2$
$ 1, 0\rangle \leftrightarrow 2, -1\rangle$	$2 \sin \theta_1 (1 - \cos \theta_2 - 2 \cos^2 \theta_2)$	$-4 \cos \theta_1 \sin(2\theta_2)$	$2 \sin \theta_1 (1 + \cos \theta_2 - 2 \cos^2 \theta_2)$
$ 1, 0\rangle \leftrightarrow 2, 0\rangle$	$-\sqrt{6} \sin \theta_1 \sin(2\theta_2)$	$-4\sqrt{\frac{2}{3}} \cos \theta_1 (1 - 3 \cos^2 \theta_2)$	$-\sqrt{6} \sin \theta_1 \sin(2\theta_2)$
$ 1, 0\rangle \leftrightarrow 2, 1\rangle$	$-2 \sin \theta_1 (1 + \cos \theta_2 - 2 \cos^2 \theta_2)$	$4 \cos \theta_1 \sin(2\theta_2)$	$-2 \sin \theta_1 (1 - \cos \theta_2 - 2 \cos^2 \theta_2)$
$ 1, 0\rangle \leftrightarrow 2, 2\rangle$	$-2 \sin \theta_1 (1 - \cos \theta_2) \sin \theta_2$	$4 \cos \theta_1 \sin^2 \theta_2$	$2 \sin \theta_1 (1 + \cos \theta_2) \sin \theta_2$
$ 1, 1\rangle \leftrightarrow 2, -2\rangle$	$-\sqrt{2}(1 - \cos \theta_1)(1 + \cos \theta_2) \cos \theta_2$	$-2\sqrt{2} \sin \theta_1 \sin^2 \theta_2$	$-\sqrt{2}(1 + \cos \theta_1)(1 - \cos \theta_2) \sin \theta_2$
$ 1, 1\rangle \leftrightarrow 2, -1\rangle$	$-\sqrt{2}(1 - \cos \theta_1)(1 - \cos \theta_2 - 2 \cos^2 \theta_2)$	$2\sqrt{2} \sin \theta_1 \sin(2\theta_2)$	$\sqrt{2}(1 + \cos \theta_1)(1 + \cos \theta_2 - 2 \cos^2 \theta_2)$
$ 1, 1\rangle \leftrightarrow 2, 0\rangle$	$\sqrt{3}(1 - \cos \theta_1) \sin(2\theta_2)$	$\frac{4}{\sqrt{3}} \sin \theta_1 (1 - 3 \cos^2 \theta_2)$	$-\sqrt{3}(1 + \cos \theta_1) \sin(2\theta_2)$
$ 1, 1\rangle \leftrightarrow 2, 1\rangle$	$\sqrt{2}(1 - \cos \theta_1)(1 + \cos \theta_2 - 2 \cos^2 \theta_2)$	$-2\sqrt{2} \sin \theta_1 \sin(2\theta_2)$	$-\sqrt{2}(1 + \cos \theta_1)(1 - \cos \theta_2 - 2 \cos^2 \theta_2)$
$ 1, 1\rangle \leftrightarrow 2, 2\rangle$	$\sqrt{2}(1 - \cos \theta_1)(1 - \cos \theta_2) \sin \theta_2$	$-2\sqrt{2} \sin \theta_1 \sin^2 \theta_2$	$\sqrt{2}(1 + \cos \theta_1)(1 + \cos \theta_2) \sin \theta_2$

Table B.2: The table gives all π -polarised MW-coupling strength equations. These are in groups $n = -2, 0, 2$ (red, grey and blue), with all transitions shown in Figure B.3 and plotted in Figure B.4 in the colours of the table headers.

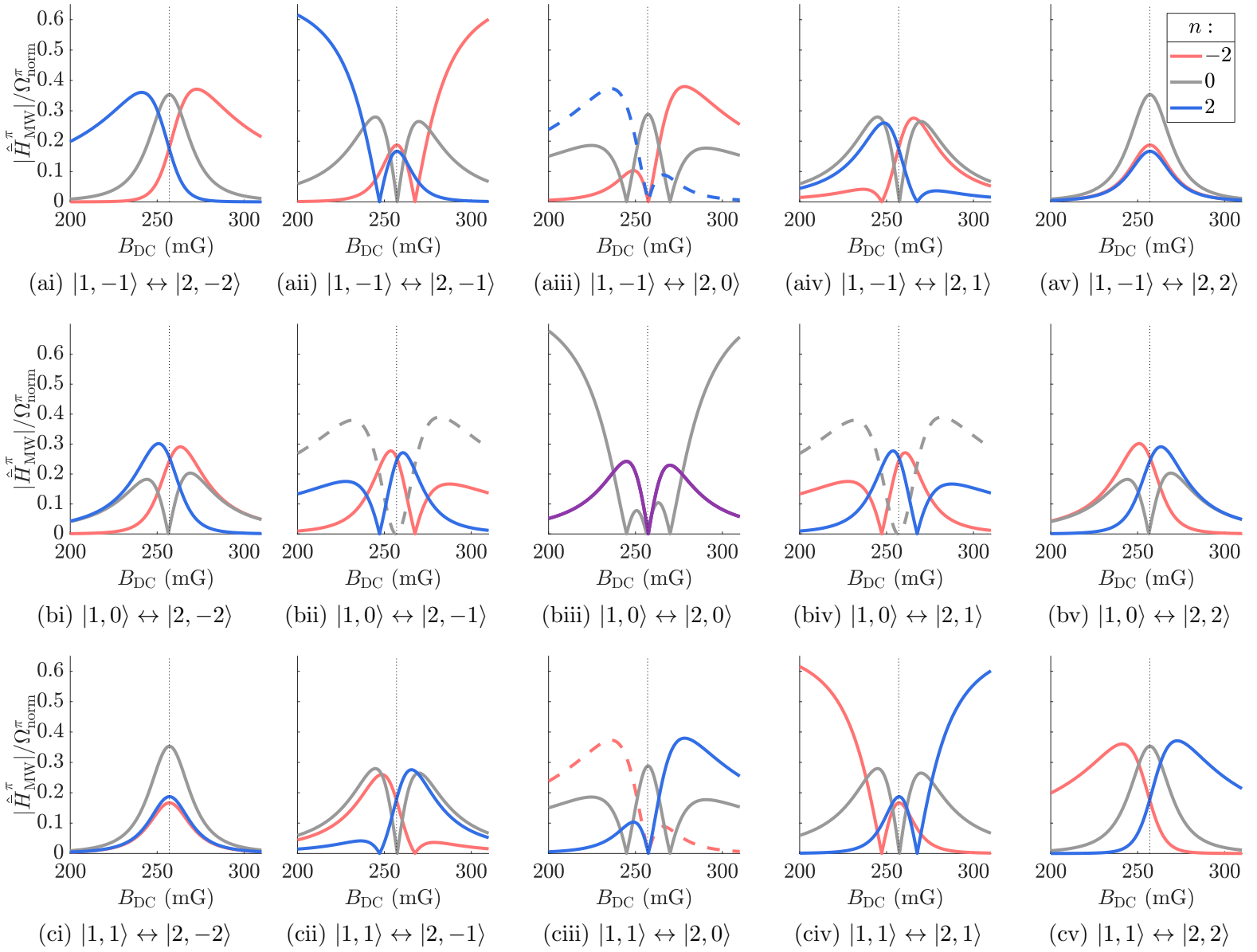


Figure B.4: The figure shows plots of all π -polarised coupling coefficients as a function of static magnetic field, as given in Table B.2. The transitions and the colours of the groups correspond to the those shown in Figure B.3. Groups $n = -2, 0, 2$ are shown in red, grey and blue respectively, and dashed lines indicate suppressed couplings (see Table 6.1). The resonant static field is indicated by the dotted line and purple indicates near equal $n = \pm 2$ couplings.

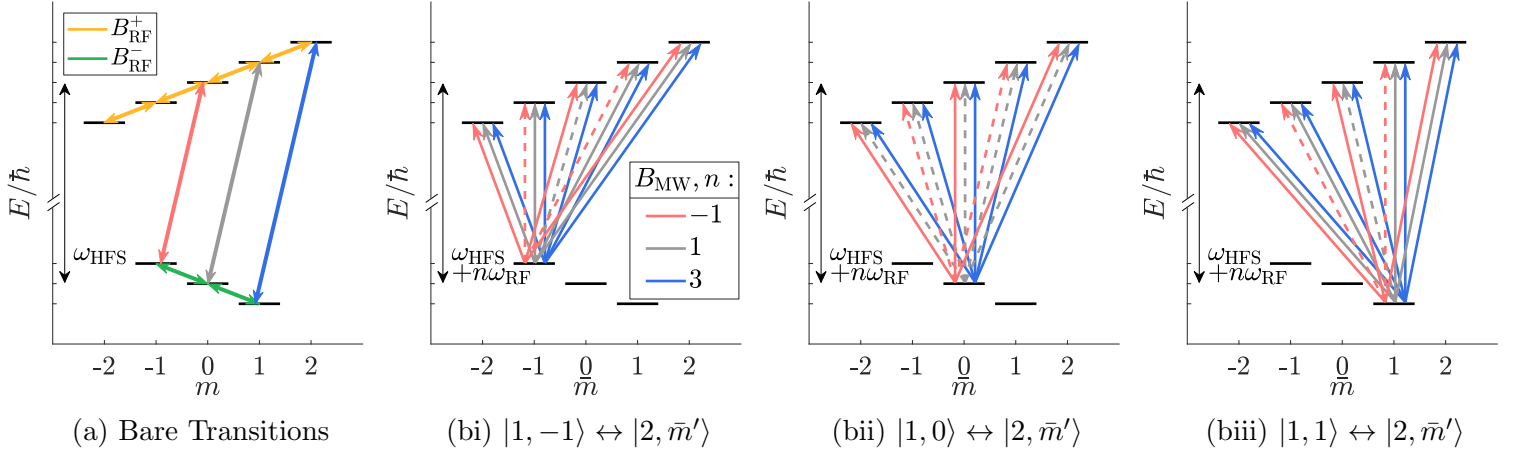


Figure B.5: The figure shows all σ_+ -polarised bare (a) and associated dressed (b) MW-transitions. Associated coupling equations are given in Table B.3 and plotted in Figure B.6 with the same colour code of red, blue and grey for $n = -1, 1, 3$. Dashed lines indicate suppressed transitions (see Table 6.1).

transition	$\hat{H}_{\text{MW}}^{+,n=-1}/\Omega_{\text{norm}}^+$	$\hat{H}_{\text{MW}}^{+,n=1}/\Omega_{\text{norm}}^+$	$\hat{H}_{\text{MW}}^{+,n=3}/\Omega_{\text{norm}}^+$
$ 1, -1\rangle \leftrightarrow 2, -2\rangle$	$-\frac{1}{\sqrt{2}}(1 + \cos \theta_1) \sin^2 \theta_2$	$\sqrt{2} \sin \theta_1 (1 - \cos \theta_2) \sin \theta_2$	$-\frac{1}{\sqrt{2}}(1 - \cos \theta_1)(1 - \cos \theta_2)^2$
$ 1, -1\rangle \leftrightarrow 2, -1\rangle$	$\frac{1}{\sqrt{2}}(1 + \cos \theta_1) \sin (2\theta_2)$	$-\sqrt{2} \sin \theta_1 (1 + \cos \theta_2 - 2 \cos^2 \theta_2)$	$\sqrt{2}(1 - \cos \theta_1)(1 - \cos \theta_2) \sin \theta_2$
$ 1, -1\rangle \leftrightarrow 2, 0\rangle$	$\frac{1}{\sqrt{3}}(1 + \cos \theta_1)(1 - 3 \cos^2 \theta_2)$	$\sqrt{3} \sin \theta_1 \sin (2\theta_2)$	$-\sqrt{3}(1 - \cos \theta_1) \sin^2 \theta_2$
$ 1, -1\rangle \leftrightarrow 2, 1\rangle$	$-\frac{1}{\sqrt{2}}(1 + \cos \theta_1) \sin (2\theta_2)$	$\sqrt{2} \sin \theta_1 (1 - \cos \theta_2 - 2 \cos^2 \theta_2)$	$\sqrt{2}(1 - \cos \theta_1)(1 + \cos \theta_2) \sin \theta_2$
$ 1, -1\rangle \leftrightarrow 2, 2\rangle$	$-\frac{1}{\sqrt{2}}(1 + \cos \theta_1) \sin^2 \theta_2$	$-\sqrt{2} \sin \theta_1 (1 + \cos \theta_2) \sin \theta_2$	$-\frac{1}{\sqrt{2}}(1 - \cos \theta_1)(1 + \cos \theta_2)^2$
$ 1, 0\rangle \leftrightarrow 2, -2\rangle$	$\sin \theta_1 \sin^2 \theta_2$	$2 \cos \theta_1 (1 - \cos \theta_2) \sin \theta_2$	$-\sin \theta_1 (1 - \cos \theta_2)^2$
$ 1, 0\rangle \leftrightarrow 2, -1\rangle$	$-\sin \theta_1 \sin (2\theta_2)$	$-2 \cos \theta_1 (1 + \cos \theta_2 - 2 \cos^2 \theta_2)$	$2 \sin \theta_1 (1 - \cos \theta_2) \sin \theta_2$
$ 1, 0\rangle \leftrightarrow 2, 0\rangle$	$-\sqrt{\frac{2}{3}} \sin \theta_1 (1 - 3 \cos^2 \theta_2)$	$\sqrt{6} \cos \theta_1 \sin (2\theta_2)$	$-\sqrt{6} \sin \theta_1 \sin^2 \theta_2$
$ 1, 0\rangle \leftrightarrow 2, 1\rangle$	$\sin \theta_1 \sin (2\theta_2)$	$2 \cos \theta_1 (1 - \cos \theta_2 - 2 \cos^2 \theta_2)$	$2 \sin \theta_1 (1 + \cos \theta_2) \sin \theta_2$
$ 1, 0\rangle \leftrightarrow 2, 2\rangle$	$\sin \theta_1 \sin^2 \theta_2$	$-2 \cos \theta_1 (1 + \cos \theta_2) \sin \theta_2$	$-\sin \theta_1 (1 + \cos \theta_2)^2$
$ 1, 1\rangle \leftrightarrow 2, -2\rangle$	$-\frac{1}{\sqrt{2}}(1 - \cos \theta_1) \sin^2 \theta_2$	$-\sqrt{2} \sin \theta_1 (1 - \cos \theta_2) \sin \theta_2$	$-\frac{1}{\sqrt{2}}(1 + \cos \theta_1)(1 - \cos \theta_2)^2$
$ 1, 1\rangle \leftrightarrow 2, -1\rangle$	$\frac{1}{\sqrt{2}}(1 - \cos \theta_1) \sin (2\theta_2)$	$\sqrt{2} \sin \theta_1 (1 + \cos \theta_2 - 2 \cos^2 \theta_2)$	$\sqrt{2}(1 + \cos \theta_1)(1 - \cos \theta_2) \sin \theta_2$
$ 1, 1\rangle \leftrightarrow 2, 0\rangle$	$\frac{1}{\sqrt{3}}(1 - \cos \theta_1)(1 - 3 \cos^2 \theta_2)$	$-\sqrt{3} \sin \theta_1 \sin (2\theta_2)$	$-\sqrt{3}(1 + \cos \theta_1) \sin^2 \theta_2$
$ 1, 1\rangle \leftrightarrow 2, 1\rangle$	$-\frac{1}{\sqrt{2}}(1 - \cos \theta_1) \sin (2\theta_2)$	$-\sqrt{2} \sin \theta_1 (1 - \cos \theta_2 - 2 \cos^2 \theta_2)$	$\frac{1}{\sqrt{2}}(1 + \cos \theta_1)(1 + \cos \theta_2) \sin \theta_2$
$ 1, 1\rangle \leftrightarrow 2, 2\rangle$	$-\frac{1}{\sqrt{2}}(1 - \cos \theta_1) \sin^2 \theta_2$	$\sqrt{2} \sin \theta_1 (1 + \cos \theta_2) \sin \theta_2$	$-\frac{1}{\sqrt{2}}(1 + \cos \theta_1)(1 + \cos \theta_2)^2$

Table B.3: The table gives all σ_+ -polarised MW-coupling strength equations. These are in groups $n = -3, -1, 1$ (red, grey and blue), with all transitions shown in Figure B.5 and plotted in Figure B.6 in the colours of the table headers.

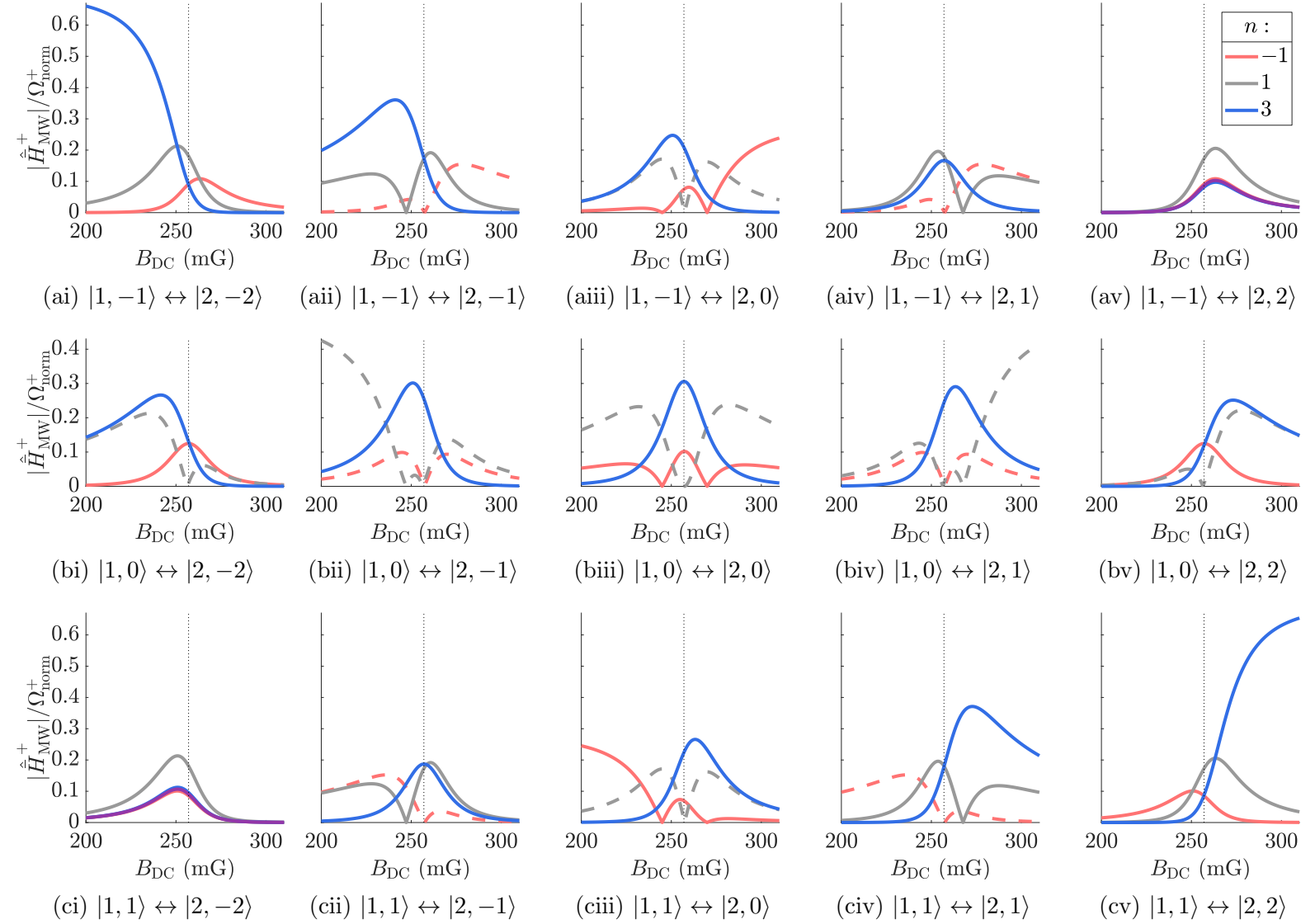


Figure B.6: The figure shows plots of all σ_+ -polarised coupling coefficients as a function of static magnetic field, as given in Table B.3. The transitions and the colours of the groups correspond to the those shown in Figure B.5. Groups $n = -1, 1, 3$ are shown in red, grey and blue respectively, and dashed lines indicate suppressed couplings (see Table 6.1). The resonant static field is indicated by the dotted line and purple indicates near equal $n = -1, 3$ couplings.

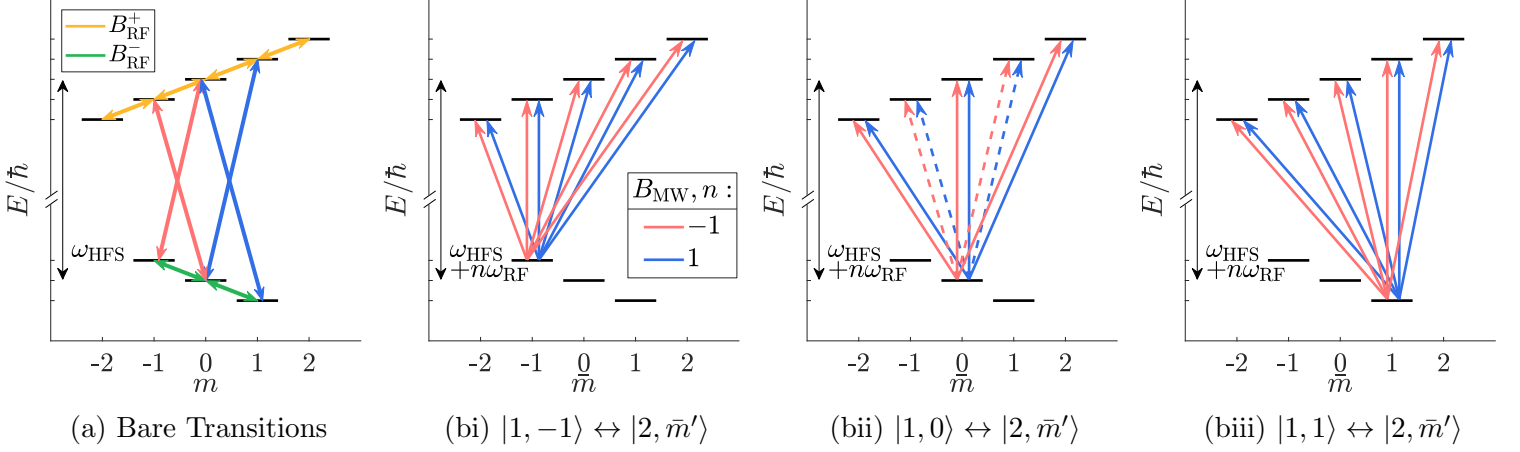


Figure B.7: The figure shows all σ_{\pm} -polarised bare (a) and associated degenerate dressed (b) MW-transitions. Associated coupling equations are given by Eq. B.1 and plotted in Figure B.8 with the same colour code of red, blue and grey for $n = -1, 1$. Dashed lines indicate suppressed transitions (see Table B.4).

B.2 Coefficients of Degenerate Groups

The majority of groups of transitions can only be addressed by a single polarisation of MW, the exceptions being groups $n = \pm 1$ which have possible transitions due to both σ_{\pm} . This is because the bare transitions $|1, -1\rangle \leftrightarrow |2, 0\rangle$ and $|1, 0\rangle \leftrightarrow |2, -1\rangle$ are of the same frequency assuming circularly polarised RF, in the approximation $-g_1 = g_2$. This is likewise true for the transitions $|1, 0\rangle \leftrightarrow |2, 1\rangle$ and $|1, 1\rangle \leftrightarrow |2, 0\rangle$. The degenerate coupling coefficients are given by

$$\frac{\hat{H}_{\text{MW}}^{\pm, n}}{\Omega_{\text{norm}}^{\pm}} = \frac{\hat{H}_{\text{MW}}^{+, n}}{\Omega_{\text{norm}}^{+}} + \frac{\hat{H}_{\text{MW}}^{-, n}}{\Omega_{\text{norm}}^{-}} = \frac{\hat{H}_{\text{MW}}^{+, n} + \mathbf{k} \hat{H}_{\text{MW}}^{-, n}}{\Omega_{\text{norm}}^{\pm}} \quad (\text{B.1})$$

for $n = \pm 1$, where $\hat{H}_{\text{MW}}^{-, n}$ and $\hat{H}_{\text{MW}}^{+, n}$ are given in Table B.1 and B.3 respectively, calculated using Eq. 6.26. The normalisation factors are given by Eq. 6.29 and $\mathbf{k} = \Omega_{\text{norm}}^{+}/\Omega_{\text{norm}}^{-}$. Resonant transition couplings in the approximation $g_2 = -g_1 = 0.5$ are given in Table B.4, in the equivalent manner as were given in Table 6.1 for separate polarisation components. This new table is correct for the case of circularly polarised \hat{B}_{MW} ($\mathbf{k} = 1$). We know from Table 6.1 that for certain other values of \mathbf{k} different transitions can be suppressed. These transitions are $|1, -1\rangle \leftrightarrow |2, -2\rangle$ and $|1, 1\rangle \leftrightarrow |2, 2\rangle$ in both groups $n = \pm 1$, and can be suppressed for some choice of \mathbf{k} as the individual polarisation components have coupling coefficients of opposite sign.

$\begin{array}{c} \bar{m} \\ \bar{m}' \end{array}$	-1					0					1				
	-2	-1	0	1	2	-2	-1	0	1	2	-2	-1	0	1	2
$ \hat{H}_{\text{MW}}^{\pm, n=-1}/\Omega_{\text{norm}}^{\pm} $	$-3\sqrt{2}$	$-2\sqrt{2}$	$\frac{2}{\sqrt{3}}$	$2\sqrt{2}$	$\sqrt{2}$	2	0	$-2\sqrt{\frac{2}{3}}$	0	2	$\sqrt{2}$	$2\sqrt{2}$	$\frac{2}{\sqrt{3}}$	$-2\sqrt{2}$	$-3\sqrt{2}$
$ \hat{H}_{\text{MW}}^{\pm, n=1}/\Omega_{\text{norm}}^{\pm} $	$3\sqrt{2}$	$-2\sqrt{2}$	$-\frac{2}{\sqrt{3}}$	$2\sqrt{2}$	$-\sqrt{2}$	2	0	$-2\sqrt{\frac{2}{3}}$	0	2	$-\sqrt{2}$	$2\sqrt{2}$	$-\frac{2}{\sqrt{3}}$	$-2\sqrt{2}$	$3\sqrt{2}$

Table B.4: The table gives the relative magnitudes of coupling strength for each transition $|1, \bar{m}\rangle \leftrightarrow |2, \bar{m}'\rangle$ in degenerate groups in the approximation $g_2 = -g_1 = 0.5$ at the magnetic field resonance as shown in Figure B.7. These are calculated using Eq. B.1 with $k = 1$.

The bare transitions as well as their associated dressed transitions are shown in Figure B.7, where red and blue lines indicate $n = \pm 1$ respectively. Dashed lines indicate the suppressed groups, of which there are significantly fewer than for the individual polarisations shown in Figures B.1 and B.5. This is due to the increased number of possible pathways. The plots of the degenerate groups as a function of static magnetic field are given in Figure B.8. These are plotted for $k = 1$, which is approximately true in our experiment. These graphs are more informative than the separate polarisation plots of the same groups shown in Figures B.1 and B.5, as our MW is circularly polarised and as such we cannot measure or alter transitions using the individual components of σ_{\pm} separately.

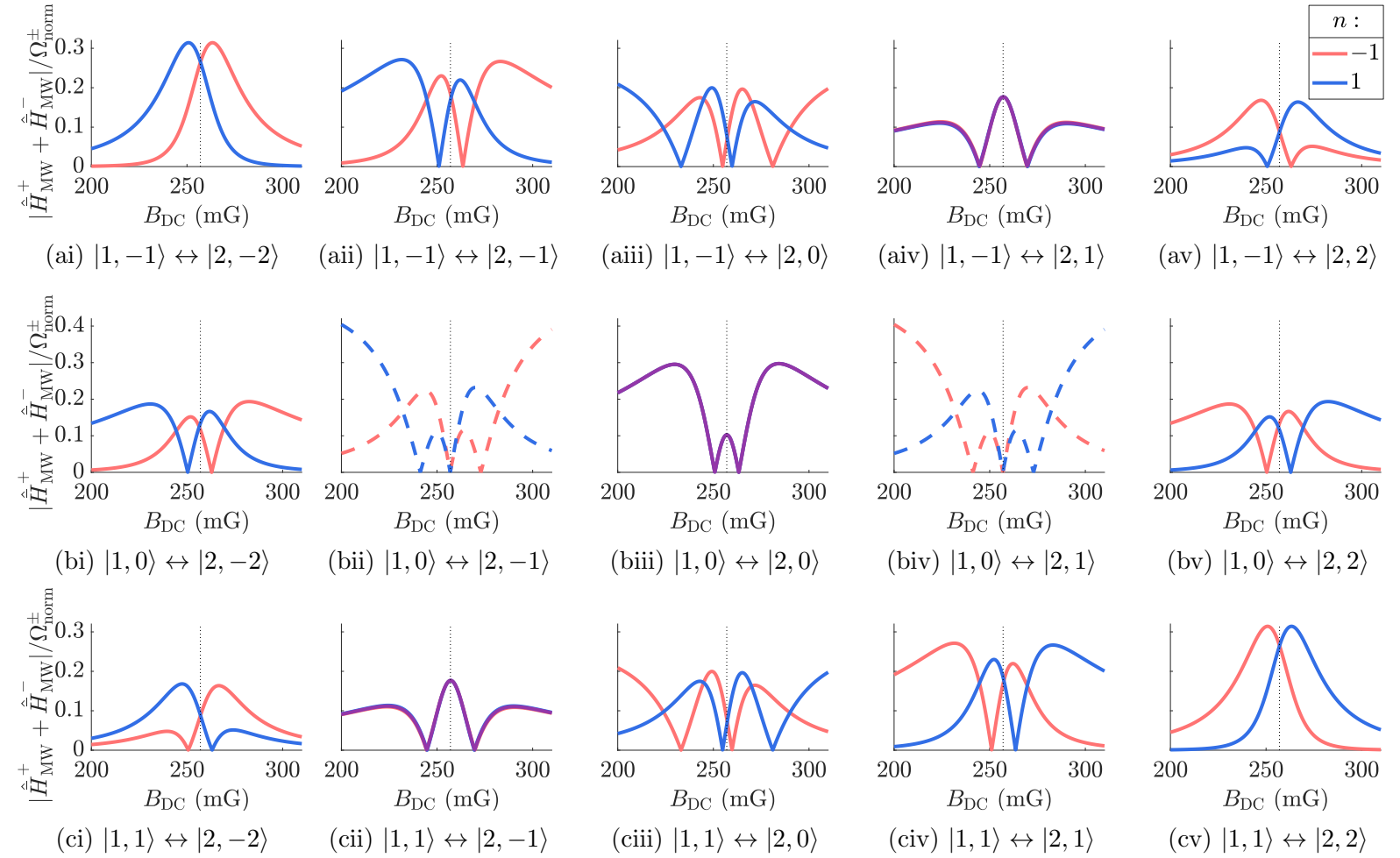


Figure B.8: The figures shows plots of all combined σ_{\pm} -polarised coupling coefficients as a function of static magnetic field as given in Eq. B.1, with $k = 1$. The transitions and the colours of the groups correspond to the those shown in Figure B.7. Groups $n = -1, 1$ are shown in red and blue respectively, and dashed lines indicate suppressed couplings (see Table B.4). The resonant static field is indicated by the dotted line and purple indicates near equal $n = \pm 1$ couplings.

Bibliography

- [1] R. Achilles and A. Bonfiglioli. The early proofs of the theorem of Campbell, Baker, Hausdorff, and Dynkin. *Archive for History of Exact Sciences*, 66(3):295–358, 2012.
- [2] J. Aldegunde, H. Ran, and J.M. Hutson. Manipulating ultracold polar molecules with microwave radiation: The influence of hyperfine structure. *Physical Review A*, 80:043410, 2009.
- [3] D.W. Allan. Statistics of atomic frequency standards. *Proceedings of the IEEE*, 54:221–230, 1966.
- [4] M.C. Amann. Semiconductor light sources. In G. Martinez, editor, *Optical Properties of Semiconductors*, pages 291–320. Springer, Dordrecht, 1993.
- [5] M.H. Anderson, J.R. Ensher, M.R. Matthews, C.E. Wieman, and E.A. Cornell. Observation of Bose-Einstein condensation in a dilute atomic vapor. *Science*, 269(5221):198–201, 1995.
- [6] J. Appel, A. MacRae, and A.I. Lvovsky. A versatile digital GHz phase lock for external cavity diode lasers. *Measurement Science and Technology*, 20:055302, 2009.
- [7] S.L. Bajaj, R. Ranaweera and D.P. Agrawal. GPS: location-tracking technology. *Computer*, 35(4):92–94, 2002.
- [8] K.A. Bakshi, A.V. Bakshi, and U.A. Bakshi. *Antennas And Wave Propagation*. Technical Publications, Pune, 2009.
- [9] P.A. Barton, C.J.S. Donald, D.M. Lucas, D.A. Stevens, A.M. Steane, and D.N. Stacey. Measurement of the lifetime of the $3d^2D_{5/2}$ state in $^{40}\text{Ca}^+$. *Physical Review A*, 62:032503, 2000.

- [10] B. Battelier, B. Barrett, L. Fouché, L. Chichet, L. Antoni-Micollier, H. Porte, F. Napolitano, J. Lautier, A. Landragin, and P. Bouyer. Development of compact cold-atom sensors for inertial navigation. *Proceedings of SPIE, Quantum Optics*, page 990004, 2016.
- [11] H. Becquerel. Sur les radiations invisibles émises par les corps phosphorescents [On invisible radiation emitted by phosphorescent bodies]. *Comptes-Rendus de l'Académie des Sciences*, 122:501–503, 1896.
- [12] P. Benioff. The computer as a physical system: A microscopic quantum mechanical Hamiltonian model of computers as represented by Turing machines. *Journal of Statistical Physics*, 22(5):563, 1980.
- [13] A. Bensky. *Short-range Wireless Communication*. Newnes, London, 2019.
- [14] P. Berthoud, A. Joyet, G. Dudley, N. Sagna, and P. Thomann. A continuous beam of slow, cold cesium atoms magnetically extracted from a 2D magneto-optical trap. *Europhysics Letters*, 41:141–146, 1998.
- [15] N. Beverini, A. Di Virgilio, J. Belfi, A. Ortolan, K.U. Schreiber, A. Gebauer, and T. Klügel. High-accuracy ring laser gyroscopes: Earth rotation rate and relativistic effects. *Journal of Physics: Conference Series*, 723:012061, 2016.
- [16] S. Bize, M.S. Sortais, Y. Santos, C. Mandache, A. Clairon, and C. Salomon. High-accuracy measurement of the ^{87}Rb ground-state hyperfine splitting in an atomic fountain. *Europhysics Letters*, 45(5):558–564, 1999.
- [17] J.E. Bjorkholm. Collision-limited lifetimes of atom traps. *Physical Review A*, 38:1599, 1988.
- [18] I. Bloch and P. Zoller. Ultracold atoms and molecules in optical lattices. In K. Levin, A.L. Fetter, and D.M. Stamper-Kurn, editors, *Contemporary Concepts of Condensed Matter Science*, volume 5, pages 121–156. Elsevier, Oxford, 2012.
- [19] N. Bohr. On the constitution of atoms and molecules. *The London, Edinburgh, and Dublin Philosophical Magazine and Journal of Science*, 26(151):1–24, 1913.

- [20] V. Bolpasi, J. Grucker, M.J. Morrissey, and W. von Klitzing. A gradient and offset compensated Ioffe-Pritchard trap for Bose-Einstein condensation experiments. *Journal of Physics B: Atomic, Molecular and Optical Physics*, 45(23):235301, 2012.
- [21] K. Bongs, M. Holynski, and Y. Singh. ψ in the sky. *Nature Physics*, 11(8):615–617, 2015.
- [22] M. Born. Zur quantenmechanik der stoßvorgänge [Quantum mechanics of collision processes]. *Zeitschrift für Physik*, 37:853–867, 1926.
- [23] S.N. Bose. Plancks gesetz und lichtquantenhypothese [Planck’s law and light quantum hypothesis]. *Zeitschrift für Physik*, 26:178–181, 1924.
- [24] E. Boto, N. Holmes, J. Leggett, G. Roberts, V. Shah, S.S. Meyer, L. Duque Muñoz, K.J. Mullinger, T.M. Tierney, S. Bestmann, G.R. Barnes, R. Bowtell, and M.J. Brookes. Matter-wave interferometers using TAAP rings. *New Journal of Physics*, 18:075014, 2016.
- [25] G. Breit and I.I. Rabi. Measurement of nuclear spin. *Physical Review*, 38:2082, 1931.
- [26] I.N. Bronshtein, K.A. Semendyayev, G. Musiol, and H. Mühlig. *Handbook of Mathematics*. Springer Science and Business Media, Berlin, 2013.
- [27] P.H. Bucksbaum, R.R. Freeman, M. Bashkansky, and T.J. McIlrath. Role of the ponderomotive potential in above-threshold ionization. *Journal of the Optical Society of America B*, 4(5):760–764, 1987.
- [28] D. Budker and M. Romalis. Optical magnetometry. *Nature Physics*, 3:227–234, 2007.
- [29] C. Burrage, E.J. Copeland, and E.A. Hinds. Probing dark energy with atom interferometry. *Journal of Cosmology and Astroparticle Physics*, 2015(03):42, 2015.
- [30] O. Carnal and J. Mlynek. Young’s double-slit experiment with atoms: A simple atom interferometer. *Physical Review Letters*, 66:2689–2692, 1991.
- [31] E. Caurier, G. Martínez-Pinedo, F. Nowacki, A. Poves, and A.P. Zuker. The shell model as unified view of nuclear structure. *Review of Modern Physics*, 77:427–488, 2005.

- [32] D. Chen, Z. Fang, Z. Cai, and R. Qu. Polarization characteristics of an external cavity diode laser with Littman–Metcalf configuration. *IEEE Photonics Technology Letters*, 21(14):984 – 986, 2009.
- [33] J.-B. Chen, F.-Z. Wang, D.-H. Yang, and Y.-Q. Wang. Alternating current Zeeman and Stark interference effect in Ramsey separated oscillating fields. *Chinese Physics Letters*, 18(2):202–204, 2001.
- [34] S. Chu, L. Hollberg, J.E. Bjorkholm, A. Cable, and A. Ashkin. Three-dimensional viscous confinement and cooling. *Physical Review Letters*, 55(1):48–51, 1985.
- [35] J.I. Cirac, P. Zoller, H.J. Kimble, and H. Mabuchi. Quantum state transfer and entanglement distribution among distant nodes in a quantum network. *Physical Review Letters*, 78:3221–3224, 1997.
- [36] D. Clément, N. Fabbri, L. Fallani, C. Fort, and M. Inguscio. Exploring correlated 1D Bose gases from the superfluid to the Mott-insulator state by inelastic light scattering. *Physical Review Letters*, 102:155301, 2009.
- [37] J. Clerk Maxwell. A dynamical theory of the electromagnetic field. *Philosophical Transactions*, 155, 1865.
- [38] E.R. Cohen and J.W.M. DuMond. Our knowledge of the fundamental constants of physics and chemistry in 1965. *Review of Modern Physics*, 37:537–594, 1965.
- [39] C. Cohen-Tannoudji, J. Dupont-Roc, and G. Grynberg. *Photons and Atoms: Introduction to Quantum Electrodynamics*. John Wiley and Sons, New Jersey, 1989.
- [40] E. Colombe, Y. and Knyazchyan, O. Morizot, B. Mercier, V. Lorent, and H. Perrin. Ultracold atoms confined in rf-induced two-dimensional trapping potentials. *Europhysics Letters*, 67(4):593–599, 2004.
- [41] L. Coraggio, A. Covello, A. Gargano, N. Itaco, and T.T.S. Kuo. Shell-model calculations and realistic effective interactions. *Progress in Particle and Nuclear Physics*, 62:135–182, 2009.
- [42] D.R. Crick, S. Donnellan, D.M. Segal, and R.C. Thompson. Magnetically induced electron shelving in a trapped Ca^+ ion. *Physical Review A*, 81:052503, 2010.

- [43] P. Curie and M. Skłodowska Curie. Sur une substance nouvelle radioactive, contenue dans la pechblende [On a new radioactive substance, contained in pitchblende]. *Comptes-Rendus de l'Académie des Sciences*, 127:175–178, 1898.
- [44] J. Dalton. On the absorption of gases by water and other liquids. *Memoirs and Proceedings of the Manchester Literary and Philosophical Society*, 6, 1803.
- [45] G. Dattoli, A. Torre, S. Lorenzutta, G. Maino, and C. Chiccoli. Theory of generalized Bessel functions II. *Il Nuovo Cimento B*, 106:21–51, 1991.
- [46] C.C. Davis. *Lasers and Electro-optics: Fundamentals and Engineering*. Cambridge University Press, Cambridge, 1996.
- [47] K.B. Davis, M.O. Mewes, M.A. Joffe, M.R. Andrews, and W. Ketterle. Evaporative cooling of sodium atoms. *Physical Review Letters*, 74:5202–5205, 1995.
- [48] C.J. Davisson and L.H. Germer. Reflection of electrons by a crystal of nickel. *Proceedings of the National Academy of Sciences*, 14(4):317–322, 1928.
- [49] G.W. Day and A.H. Rose. Faraday effect sensors: The state of the art. In R.P. DePaula and E. Udd, editors, *Fiber Optic and Laser Sensors VI*, volume 0985, pages 138–150. International Society for Optics and Photonics, SPIE, 1989.
- [50] M. de Angelis, M.C. Angonin, Q. Beauvils, C. Becker, A. Bertoldi, K. Bongs, T. Bourdel, P. Bouyer, V. Boyer, S. Dörscher, H. Duncker, W. Ertmer, T. Fernholz, T.M. Fromhold, W. Herr, P. Krüger, C. Kürbis, C.J. Mellor, F. Pereira Dos Santos, A. Peters, N. Poli, M. Popp, M. Prevedelli, E.M. Rasel, J. Rudolph, F. Schreck, K. Sengstock, F. Sorrentino, S. Stellmer, G.M. Tino, T. Valenzuela, T.J. Wendrich, A. Wicht, P. Windpassinger, and P. Wolf. iSense: A portable ultracold-atom-based gravimeter. *Procedia Computer Science*, 7:334–336, 2011.
- [51] L. de Broglie. Waves and quanta. *Nature*, 112:540, 1923.
- [52] C.L. Degan, F. Reinhard, and P. Cappellaro. Quantum sensing. *Review of Modern Physics*, 89:035002, 2017.
- [53] N.H. Dekker, C.S. Lee, V. Lorent, J.H. Thywissen, S.P. Smith, M. Drndić, R.M. Westervelt, and M. Prentiss. Guiding neutral atoms on a chip. *Physical Review Letters*, 84(6):1124–1127, 2000.

- [54] Y.N. Demkov and P.B. Kurasov. von Neumann-Wigner theorem: level repulsion and degenerate eigenvalues. *Theoretical and Mathematical Physics*, 15:1407–1422, 2007.
- [55] J. Denschlagm, D. Cassettari, A. Chenet, S. Schneider, and J. Schmiedmayer. A neutral atom and a wire: towards mesoscopic atom optics. *Applied Physics B*, 69:291–301, 1999.
- [56] R. Descartes. *Discours de la méthode pour bien conduire sa raison et chercher la vérité dans les sciences [Discourse on the Method of Rightly Conducting One’s Reason and of Seeking Truth in the Sciences]*. Imprimerie de Ian Marie, Leiden, 1637.
- [57] M.R. Dietrich, N. Kurz, T. Noel, G. Shu, and B.B. Blinov. Hyperfine and optical barium ion qubits. *Physical Review A*, 81:052328, 2010.
- [58] P.A.M. Dirac and F.R. Howard. On the theory of quantum mechanics. *Proceedings of the Royal Society A*, 112(762):661–677, 1926.
- [59] E.A. Donley, T.P. Heavner, F. Levi, M.O. Tataw, and S.R. Jefferts. Double-pass acousto-optic modulator system. *Review of Scientific Instruments*, 76:063112, 2005.
- [60] A.R. Edmonds. *Angular Momentum in Quantum Mechanics*. Princeton University Press, Princeton, 1996.
- [61] A. Einstein. Ist die trägheit eines körpers von seinem energieinhalt abhängig? [Does the inertia of a body depend upon its energy-content?]. *Annalen der Physik*, 18(13):639–641, 1905.
- [62] A. Einstein. Über einen die erzeugung und verwandlung des liches betreffenden heuristischen gesichtspunkt [On a heuristic point of view about the creation and conversion of light]. *Annalen der Physik*, 17(6):132–148, 1905.
- [63] A. Einstein. *Quantentheorie des einatomigen idealen Gases [Quantum Theory of a Monoatomic Ideal Gas]*. Sitzungsberichte der Preussischen Akademie der Wissenschaften, 1925.
- [64] U. Ernst, A. Marte, F. Schreck, J. Schuster, and G. Rempe. Bose-Einstein condensation in a pure Ioffe-Pritchard field configuration. *Europhysics Letters*, 41:1–6, 1998.

- [65] H. Fan, S. Kumar, J. Sedlacek, H. Kübler, S. Karimkashi, and J.P. Shaffer. Atom based RF electric field sensing. *Journal of Physics B: Atomic, Molecular and Optical Physics*, 48(20):202001, 2015.
- [66] D. Favre, F. Guen and J. Simon. Optical feedback effects upon laser diode oscillation field spectrum. *IEEE Journal of Quantum Electronics*, 18(10):1712 – 1717, 1982.
- [67] E. Feenberg and K.C. Hammack. Nuclear shell structure. *Physical Review*, 75:1877–1893, 1949.
- [68] T. Fernholz, R. Gerritsma, P. Krüger, and R.J.C. Spreeuw. Dynamically controlled toroidal and ring-shaped magnetic traps. *Physical Review A*, 75(6):063406, 2007.
- [69] C.J. Foot. *Atomic Physics*. Oxford Master Series in Physics. Oxford University Press, Oxford, 2004.
- [70] B. Foxon. Stabilisation of a frequency doubled source for laser cooling. Master’s thesis, University of Birmingham, 2016. (Formerly B. Cook).
- [71] B. Foxon, S. Jammi, and T. Fernholz. Multi order controlled synthetic clock transitions. *In preparation*.
- [72] A. Fresnel. *Oeuvres Complètes d’Augustin Fresnel [Complete Works of Augustin Fresnel]*. Imprimerie Nationale, Paris, 1868.
- [73] P. Gassendi. *Syntagma Philosophicum [Philosophical Treatise]*. Brepol, Turnhour, 1657.
- [74] R. Geiger, V. Ménoiret, G. Stern, N. Zahzam, P. Cheinet, B. Battelier, A. Villing, M. Moron, F. Lours, Y. Bidel, A. Bresson, A. Landragin, and P. Bouyer. Development of compact cold-atom sensors for inertial navigation. *Nature Communications*, page 424, 2011.
- [75] F. Gentile. *Towards an atomic Sagnac interferometer with full dynamical control of atoms in ring waveguides*. PhD thesis, University of Nottingham, 2018.
- [76] W. Gerlach and O. Stern. Der experimentelle nachweis der richtungsquantelung im magnetfeld [The experimental proof of directional quantization in the magnetic field]. *Zeitschrift für Physik*, 9:349–352, 1922.

- [77] T. Gherman and D. Romanini. Mode-locked cavity-enhanced absorption spectroscopy. *Optics Express*, 10(19):1033–1042, 2002.
- [78] M. Gildemeister, E. Nugent, B.E. Sherlock, M. Kubasik, B.T. Sheard, and C.J. Foot. Trapping ultracold atoms in a time-averaged adiabatic potential. *Physical Review A*, 81:031402, 2010.
- [79] D. Giulini, E. Joos, C. Kiefer, J. Kupsch, I.O. Stamatescu, and H.D. Zeh. *Decoherence and the Appearance of a Classical World in Quantum Theory*. Springer, Berlin/Heidelberg, 2013.
- [80] R.G. Gould. The LASER, light amplification by stimulated emission of radiation. *The Ann Arbor Conference on Optical Pumping*, 1959.
- [81] G. Gräff, H. Kalinowsky, and J. Traut. A direct determination of the proton electron mass ratio. *Zeitschrift für Physik A*, 297:35–39, 1980.
- [82] S. Granieri, A. Siahmakoun, and D. Thelen. Optical modulation with a single sideband and suppressed carrier. In R.A. Lessard, G.A. Lampropoulos, and G.W. Schinn, editors, *Applications of Photonic Technology 5*, volume 4833, pages 1154–1158. International Society for Optics and Photonics, SPIE, 2003.
- [83] R. Grimm, M. Weidemüller, and Y.B. Ovchinnikov. Optical dipole traps for neutral atoms. *Advances in Atomic, Molecular and Optical Physics*, 42:95–170, 2000.
- [84] D. Hanneke, S. Fogwell, and G. Gabrielse. New measurement of the electron magnetic moment and the fine structure constant. *Physical Review Letters*, 100:120801, 2008.
- [85] T.W. Hänsch and A.L. Schawlow. Cooling of gases by laser radiation. *Optics Communications*, 13(1):68–69, 1975.
- [86] W. Harper. Optical pumping. *Review of Modern Physics*, 44:169–249, 1972.
- [87] M.L. Harris, C.S. Adams, S.L. Cornish, I.C. McLeod, E. Tarleton, and I.G. Hughes. Polarization spectroscopy in rubidium and cesium. *Physical Review A*, 73:062509, 2006.
- [88] T.L. Harte, E. Bentine, K. Luksch, A.J. Barker, D. Trypogeorgos, B. Yuen, and C.J. Foot. Ultracold atoms in multiple radio-frequency dressed adiabatic potentials. *Physical Review A*, 97:013616, 2018.

- [89] E. Hecht. *Optics*. Addison-Wesley, Boston, 2002.
- [90] W. Heisenberg. Über quantentheoretische umdeutung kinematischer und mechanischer beziehungen [Quantum theoretical re-interpretation of kinematic and mechanical relations]. *Zeitschrift für Physik*, 33(1):879–893, 1925.
- [91] S. Hofferberth, I. Lesanovsky, B. Fischer, J. Verdu, and J. Schmiedmayer. Radiofrequency-dressed-state potentials for neutral atoms. *Nature Physics*, 2:710–716, 2006.
- [92] R. Hooke. *Micrographia: or Some Physiological Descriptions of Minute Bodies Made by Magnifying Glasses. With Observations and Inquiries Thereupon*. J. Martyn and J. Allestry, London, 1665.
- [93] M. Hosseini, B.M. Sparkes, G. Campbell, P.K. Lam, and B.C. Buchler. High efficiency coherent optical memory with warm rubidium vapour. *Nature Communications*, 2:174, 2011.
- [94] R. Hui and M. O’Sullivan. *Fiber Optic Measurement Techniques*. Academic Press, Cambridge, Massachusetts, 2009.
- [95] C. Huygens. *Traité de la Lumière [Treatise on Light]*. Pieter van der Aay, Leiden, 1690.
- [96] G. Jäger, T. Berrada, J. Schmiedmayer, T. Schumm, and U. Hohenester. Parametric-squeezing amplification of bose-einstein condensates. *Physical Review A*, 92:053632, 2015.
- [97] S. Jammi. *Towards quantum optics experiments with trapped atoms in a hollow-core fibre*. PhD thesis, University of Nottingham, 2017.
- [98] S. Jammi, T. Pyragius, M.G. Bason, H.M. Florez, and T. Fernholz. Dispersive detection of radio-frequency-dressed states. *Physical Review A*, 97(4):043416, April 2018.
- [99] K.N. Jarvis, J.A. Devlin, T.E. Wall, B.E. Sauer, and M.R. Tarbutt. Blue-detuned magneto-optical trap. *Physical Review Letters*, 120:083201, 2018.
- [100] K. Jensen, R. Budvytyte, R.A. Thomas, T. Wang, A.M. Fuchs, M.V. Balabas, G. Vasilakis, L.D. Mosgaard, H.C. Stærkind, J.H. Müller, T. Heimburg, S.-P. Olesen, and E.S. Polzik. Optically pumped magnetometers: From quantum origins to multi-channel magnetoencephalography. *Scientific Reports*, 6:29638, 2016.

- [101] K. Jensen, R. Budvytyte, R.A. Thomas, T. Wang, M.V. Fuchs, A.M. Balabas, G. Vasilakis, L.D.M. Hans, C. Stærkind, J.H. Müller, T. Heimburg, S.-P. Olesen, and E.S. Polzik. Non-invasive detection of animal nerve impulses with an atomic magnetometer operating near quantum limited sensitivity. *Scientific Reports*, 6:169–172, 2016.
- [102] J.R. Johansson, P.D. Nation, and F. Nori. QuTiP 2: A Python framework for the dynamics of open quantum systems. *Computer Physics Communications*, 184:1234–1240, 2013.
- [103] J. Johnson, B. Foxon, V. Atkocius, F. Gentile, S. Jammi, K. Poullos, and T. Fernholz. Hafele and Keating on a chip: Sagnac interferometry with a single clock. In S.M. Shahriar and J. Scheuer, editors, *Optical, Opto-Atomic, and Entanglement-Enhanced Precision Metrology II*, volume 11296, pages 224 – 237. International Society for Optics and Photonics, SPIE, 2020.
- [104] B. Julsgaard. *Entanglement and Quantum Interactions with Macroscopic Gas Samples*. PhD thesis, University of Aarhus, 2003.
- [105] R. Kaiser, C. Westbrook, and F. David. *Ondes de matiere coherentes [Coherent atomic matter waves]*. Springer, Amsterdam, 1999.
- [106] G. Kazakov and T. Schumm. Magic radio-frequency dressing for trapped atomic microwave clocks. *Physical Review A*, 91:023404, 02 2015.
- [107] D.W. Keith, C.R. Ekstrom, Q.A. Turchette, and D.E. Pritchard. An interferometer for atoms. *Physical Review Letters*, 66:2693–2696, 1991.
- [108] A. Kersey and D. Jackson. Current sensing utilizing heterodyne detection of the Faraday effect in single-mode optical fiber. *Journal of Lightwave Technology*, 4(6):640–644, 1986.
- [109] G. Kirchoff and R. Bunsen. Chemische analyse durch spectralbeobachtungen [Chemical analysis through spectral observations]. *Annalen der Physik*, 186(6):161–189, 1860.
- [110] E. Koukharenko, Z. Moktadir, M. Kraft, M.E. Abdelsalamc, D.M. Bagnall, C. Vale, M.P.A. Jones, and E.A. Hinds. Microfabrication of gold wires for atom guides. *Sensors and Actuators A*, 115:600–607, 2004.
- [111] A. Kuzmich, N.P. Bigelow, and L. Mandel. Atomic quantum non-demolition measurements and squeezing. *Europhysics Letters*, 42(5):481–486, 1998.

- [112] A. Lavoisier. *Traité élémentaire de chimie [Elementary treatise on chemistry]*. Cuchet, Paris, 1789.
- [113] P. Lebedev. Untersuchungen über die druckkräfte des liches [Studies on the pressure forces of light]. *Annalen der Physik*, 311(11):433–458, 1901.
- [114] I. Lesanovsky and W. von Klitzing. Time-averaged adiabatic potentials: Versatile matter-wave guides and atom traps. *Physical Review Letters*, 99:083001, 2007.
- [115] P.D. Lett, R.N. Watts, C.I. Westbrook, W.D. Phillips, P.L. Gould, and H.J. Metcalf. Observation of atoms laser cooled below the doppler limit. *Physical Review Letters*, 61:169–172, 1988.
- [116] F. Levi, J. Camparo, B. Francois, C.E. Calosso, S. Micalizio, and A. Godone. Precision test of the AC Stark shift in a rubidium atomic vapor. *Physical Review A*, 93:023433, 2016.
- [117] R. Löw, H. Weimer, J. Nipper, J.B. Balewski, B. Butscher, H.P. Büchler, and T. Pfau. An experimental and theoretical guide to strongly interacting Rydberg gases. *Journal of Physics B*, 45:113001, 2012.
- [118] A.D. Ludlow, M.M. Boyd, J. Ye, E. Peik, and P.O. Schmidt. Optical atomic clocks. *Reviews of Modern Physics*, 87:637–701, 2015.
- [119] N. Lundblad, S. Ansari, Y. Guo, and E. Moan. Observations of $\lambda/4$ structure in a low-loss radio-frequency-dressed optical lattice. *Physical Review A*, 90:053612, 2014.
- [120] N. Lundblad, R.A. Carollo, C. Lannert, M.J. Gold, X. Jiang, D. Paseltiner, N. Sergay, and D.C. Aveline. Shell potentials for microgravity Bose–Einstein condensates. *Nature Partner Journals: Microgravity*, 5:30, 2019.
- [121] N. Lundblad, P.J. Lee, I.B. Spielman, B.L. Brown, W.D. Phillips, and J.V. Porto. Atoms in a radio-frequency-dressed optical lattice. *Physical Review Letters*, 100:150401, 2008.
- [122] T.A. Maldonado. Electro-optic modulators. In M. Bass, editor, *Handbook of Optics*, volume 2. McGraw Hill Professional, Orlando, 1995.
- [123] W. Markowitz, R. Glenn Hall, L. Essen, and J.V.L. Parry. Frequency of cesium in terms of ephemeris time. *Physical Review Letters*, 1:105–107, 1958.

- [124] H. Mas, S. Pandey, G. Vasilakis, and W. von Klitzing. Bi-chromatic adiabatic shells for atom interferometry. *New Journal of Physics*, 21(12):123039, 2019.
- [125] D.D. McCarthy and P.K. Seidelmann. *Time – From Earth Rotation to Atomic Physics*. Wiley-VCH, Weinheim, 2009.
- [126] S.T. Merkel, P.S. Jessen, and I.H. Deutsch. Quantum control of the hyperfine-coupled electron and nuclear spins in alkali-metal atoms. *Physical Review A*, 78:023404, 2008.
- [127] A. Messiah. *Mécanique Quantique [Quantum Mechanics]*. North Holland Publishing Company, Amsterdam, 1961.
- [128] H.J. Metcalf and P. van der Straten. *Laser Cooling and Trapping*. Springer Science and Business Media, Berlin, 2001.
- [129] A.A. Michelson and E.W. Morely. On the relative motion of the Earth and of the luminiferous ether. *Sidereal Messenger*, 6:306–310, 1887.
- [130] M.A. Morrison and G.A. Parker. A guide to rotations in quantum mechanics. *Australian Journal of Physics*, 40:465–97, 1987.
- [131] W. Nagourney, J. Sandberg, and H. Dehmelt. Shelved optical electron amplifier: Observation of quantum jumps. *Physical Review Letters*, 56:2797–2799, 1986.
- [132] P. Navez, S. Pandey, H. Mas, K. Poulios, T. Fernholz, and W. von Klitzing. Matter-wave interferometers using TAAP rings. *New Journal of Physics*, 18:075014, 2016.
- [133] I. Newton. *Philosophiæ Naturalis Principia Mathematica [Mathematical Principles of Natural Philosophy]*. Benjamin Motte, London, 1687.
- [134] A. Nicolas, L. Veissier, L. Giner, E. Giacobino, D. Maxein, and J. Laurat. A quantum memory for orbital angular momentum photonic qubits. *Nature Photonics*, 8:234–238, 2014.
- [135] H. Perrin and B.M. Garraway. Trapping atoms with radio frequency adiabatic potentials. *Advances In Atomic, Molecular, and Optical Physics*, 66:181–262, 2017.
- [136] W. Petrich, M.H. Anderson, J.R. Ensher, and E.A. Cornell. Behavior of atoms in a compressed magneto-optical trap. *Journal of the Optical Society of America B*, 120:1332–1335, 1994.

- [137] M. Planck. Ueber das gesetz der energieverteilung im normalspectrum [On the law of energy distribution in the normal spectrum]. *Annalen der Physik*, 4:553, 1901.
- [138] S. Pradhan and B.N. Jagatap. Measurement of temperature of laser cooled atoms by one-dimensional expansion in a magneto-optical trap. *Review of Scientific Instruments*, 79:013101, 2008.
- [139] D.W. Preston. Doppler-free saturated absorption: Laser spectroscopy. *American Journal of Physics*, 64:1432, 1996.
- [140] J.D. Pritchard, A.N. Dinkelaker, A.S. Arnold, P.F. Griffin, and E. Riis. Demonstration of an inductively coupled ring trap for cold atoms. *New Journal of Physics*, 13:103047, 2012.
- [141] T. Pyragius. *Quantum Vector Magnetometry based on the Voigt Effect*. PhD thesis, University of Nottingham, 2019.
- [142] T. Pyragius, H.M. Florez, and T. Fernholz. A Voigt effect based 3D vector magnetometer. *Physical Review A*, 100:023416, 2019.
- [143] E.L. Raab, M. Prentiss, A. Cable, S. Chu, and D.E. Pritchard. Trapping of neutral sodium atoms with radiation pressure. *Physical Review Letters*, 59:2631–2634, 1987.
- [144] G. Racah. Theory of complex spectra II. *Physical Review*, 62:438–462, 1942.
- [145] N.F. Ramsey. A molecular beam resonance method with separated oscillating fields. *Physical Review*, 78:695–699, 1950.
- [146] J.W. Rayleigh. Note on the pressure of radiation, showing an apparent failure of the usual electromagnetic equations. *The London, Edinburgh, and Dublin Philosophical Magazine and Journal of Science*, 45(277):522–525, 1898.
- [147] J. Reichel and V. Vuletić. *Atom Chips*. North Holland Publishing Company, Weinheim, 2011.
- [148] G. Reinaudi, T. Lahaye, Z. Wang, and D. Guéry-Odelin. Strong saturation absorption imaging of dense clouds of ultracold atoms. *Optics Letters*, 32(21):3143–3145, 2007.

- [149] P. Ripka. Magnetic sensors: Principles and applications. In K.H.J. Buschow, R.W. Cahn, M.C. Flemings, B. Ilshner, E.J. Kramer, S. Mahajan, and P. Veyssi re, editors, *Encyclopedia of Materials: Science and Technology*, pages 1–11. Elsevier, Oxford, 2007.
- [150] H. R mer. *Theoretical Optics: An Introduction*. Wiley-VCH, Weinheim, 2005.
- [151] M.E. Rose. *Elementary Theory of Angular Momentum*. John Wiley and Sons, New Jersey, 1957.
- [152] E. Rutherford. The scattering of α and β particles by matter and the structure of the atom. *The London, Edinburgh, and Dublin Philosophical Magazine and Journal of Science*, 21(125):669–688, 1911.
- [153] G. Sagnac. Sur la preuve de la r alit e de l’ ther lumineux par l’exp erience de l’interf erographe tournant [On the proof of the reality of the luminiferous aether by the experiment with a rotating interferometer]. *Comptes-Rendus de l’Acad mie des Sciences*, 157:1410–1413, 1913.
- [154] S.D. Saliba, M. Junker, L.D. Turner, and R.E. Scholten. Mode stability of external cavity diode lasers. *Applied Optics*, 48(35):6692–6700, 2009.
- [155] S. Sanna and W.G. Schmidt. LiNbO₃ surfaces from a microscopic perspective. *Journal of Physics: Condensed Matter*, page 413001, 2017.
- [156] A. Sargsyan, G. Hakhumyan, C. Leroy, Y. Pashayan-Leroy, A. Papoyan, and D Sarkisyan. Hyperfine Paschen-Back regime realized in Rb nanocell. *Optics Letters*, 37(8):1379–1381, 2012.
- [157] L. S rk ny, P. Weiss, H. Hattermann, and J. Fort gh. Controlling the magnetic field sensitivity of atomic clock states by microwave dressing. *Physical Review A*, 90:053416, 10 2014.
- [158] M. Sasaki, M. Fujiwara, and M. Takeoka. Magnetic sensors: Principles and applications. In Y. Yamamoto and K. Semba, editors, *Principles and Methods of Quantum Information Technologies*, pages 33–51. Springer, Tokyo, 2016.
- [159] P.N. Schatz and A.J. McCaffery. The Faraday effect. *Quarterly Reviews, Chemical Society*, 4(23):552–584, 1969.

- [160] J. Scherschligt, J.A. Fedchak, D.S. Barker, S. Eckel, N. Klimov, C. Makrides, and E. Tiesinga. Development of a new UHV/XHV pressure standard (cold atom vacuum standard). *Metrologia*, 54(6):S125, 2017.
- [161] E. Schrödinger. Quantisierung als eigenwertproblem [Quantization as an eigenvalue problem]. *Annalen der Physik*, 384(4):361–376, 1926.
- [162] F. Schuller, M.J.D. Macpherson, D.N. Stacey, R.B. Warrington, and K.P. Zetie. The Voigt effect in a dilute atomic vapour. *Optics Communications*, 86(2):123–127, 1991.
- [163] T. Schumm, S. Hofferberth, L.M. Andersson, S. Wildermuth, S. Groth, I. Bar-Joseph, J. Schmiedmayer, and P. Krüger. Matter-wave interferometry in a double well on an atom chip. *Nature Physics*, 1:57–62, 2005.
- [164] I. Serre, L Pruvost, and H.T. Duong. Fluorescence imaging efficiency of cold atoms in free fall. *Applied Optics*, 37(6):1016–1021, 1998.
- [165] G.A. Sinuco-León and B.M. Garraway. Radio-frequency dressed lattices for ultracold alkali atoms. *New Journal of Physics*, 17:053037, 2015.
- [166] G.A. Sinuco-León and B.M. Garraway. Addressed qubit manipulation in radio-frequency dressed lattices. *New Journal of Physics*, 18:035009, 2016.
- [167] G.A. Sinuco-León, B.M. Garraway, H. Mas, S. Pandey, G. Vasilakis, V. Bolpasi, W. von Klitzing, B. Foxon, S. Jammi, K. Poulios, and T. Fernholz. Microwave spectroscopy of radio-frequency-dressed ^{87}Rb . *Physical Review A*, 100:053416, 2019.
- [168] G.A. Sinuco-Léon, H. Mas, S. Pandey, G. Vasilakis, B. M. Garraway, and W. von Klitzing. Decoherence-free radiofrequency dressed subspaces. *arXiv*, 2020.
- [169] C. Specht, H.P. Nölleke, A. Reiserer, M. Uphoff, E. Figueroa, S. Ritter, and G. Rempe. A single-atom quantum memory. *Nature*, 473:190–193, 2011.
- [170] J. Stark. Beobachtungen über den effekt des elektrischen felde auf spektrallinien I. quereffekt [Observations of the effect of the electric field on spectral lines I. transverse effect]. *Annalen der Physik*, 43:956–983, 1913.

- [171] D.A. Steck. Rubidium 87 D line data. <http://steck.us/alkalidata>.
- [172] R. Stevenson, M.R. Hush, T. Bishop, I. Lesanovsky, and T. Fernholz. Sagnac interferometry with a single atomic clock. *Physical Review Letters*, 115:163001, Oct 2015.
- [173] O. Svelto. *Principles of Lasers*. Springer Science and Business Media, Berlin, 2010.
- [174] B. Szigeti. Polarisability and dielectric constant of ionic crystals. *Transactions of the Faraday Society*, 45:155–166, 1949.
- [175] J.J. Thomson. On the emission of negative corpuscles by the alkali metals. *The London, Edinburgh, and Dublin Philosophical Magazine and Journal of Science*, 10(59):584–590, 1905.
- [176] M. Thorpe and J. Ye. Cavity-enhanced direct frequency comb spectroscopy. *Applied Physics B*, 91:347–414, 2002.
- [177] S. Tolansky. Negative nuclear spins and a proposed negative proton. *Zeitschrift für Physik A*, 134:26, 1934.
- [178] M. Trinker, S. Groth, S. Haslinger, S. Manz, T. Betz, I. Bar-Joseph, T. Schumm, and J. Schmiedmayer. Multi-layer atom chips for versatile atom micro manipulation. *Applied Physics Letters*, 92:254102, 2008.
- [179] I. Ushijima, M. Takamoto, M. Das, T. Ohkubo, and H. Katori. Cryogenic optical lattice clocks. *Nature Photonics*, 9:185–189, 2015.
- [180] A.G. van Melsen. *From Atoms to Atom: The History of the Concept Atom*. Dover, New York, 2004.
- [181] N.V. Vitanov, B.W. Shore, L. Yatsenko, K. Böhmer, T. Halfmann, T. Rickes, and K. Bergmann. Power broadening revisited: theory and experiment. *Optics Communications*, 199(1):117 – 126, 2001.
- [182] J. R. Weber, W. F. Koehl, J. B. Varley, A. Janotti, B. B. Buckley, C. G. Van de Walle, and D. D. Awschalom. Quantum computing with defects. *Proceedings of the National Academy of Sciences*, 107(19):8513–8518, 2010.
- [183] M. Weidemüller and C. Zimmermann, editors. *Cold Atoms and Molecules: Concepts, Experiments and Applications to Fundamental Physics*. Wiley-VCH, Weinheim, 2009.

- [184] G.F. Weston. *Ultrahigh Vacuum Practice*. Butterworth and Co., London, 1985.
- [185] S. Weyers, U. Hübner, R. Schröder, C. Tamm, and A. Bauch. Uncertainty evaluation of the atomic caesium fountain CSF1 of the PTB. *Metrologia*, 38(4):343–352, 2001.
- [186] M. Wilkinson. Narrowly avoided crossings. *Journal of Physics A: Mathematical and General*, 20:635–645, 1986.
- [187] D.J. Wineland, R.E. Drulliner, and F.L. Wall. Radiation-pressure cooling of bound resonant absorbers. *Physical Review Letters*, 40(25):1639–1642, 1978.
- [188] T. Young. The Bakerian Lecture: On the theory of light and colours. *Philosophical Transactions*, 92, 1802.
- [189] B. Yuen, I.J.M. Barr, J.P. Cotter, E. Butler, and E.A. Hinds. Enhanced oscillation lifetime of a Bose-Einstein condensate in the 3D/1D crossover. *New Journal of Physics*, 17(9):093041, 2015.
- [190] P. Zeeman. Over de invloed eener magnetisatie op den aard van het door een stof uitgezonden licht [On the influence of magnetism on the nature of the light emitted by a substance]. *Verslagen van de Gewone Vergaderingen der Wis- en Natuurkundige Afdeling*, 5:181–184 and 242–248, 1896.
- [191] Y.-C. Zhang, Z. Xu, and S. Zhang. Topological superfluids and the BEC-BCS crossover in the attractive Haldane-Hubbard model. *Physical Review A*, 95:043640, 2017.
- [192] M.-K. Zhou, Z.-K. Hu, X.-C. Duan, B.-L. Sun, L.-L. Chen, Q.-Z. Zhang, and J. Luo. Performance of a cold-atom gravimeter with an active vibration isolator. *Physical Review A*, 86:043630, 2012.
- [193] Y. Zhou, I. Lesanovsky, T. Fernholz, and W. Li. Controlling the dynamical scale factor in a trapped atom Sagnac interferometer. *Physical Review A*, 101:012517, 2020.
- [194] O. Zobay and B.M. Garraway. Two-dimensional atom trapping in field-induced adiabatic potentials. *Physical Review Letters*, 86:1195–1198, 2001.
- [195] W.H. Zurek. Decoherence, einselection, and the quantum origins of the classical. *Review of Modern Physics*, 75:715–775, May 2003.